Henrik Høstmark

# Transient Stability Assessment of Virtual Synchronous Machine based Wind Energy Conversion System

**Master's thesis**

**NTNU**

Norwegian University of
Science and Technology

Henrik Høstmark

# Transient Stability Assessment of Virtual Synchronous Machine based Wind Energy Conversion System

Master's thesis in Energy and Environmental Engineering
Supervisor: Mohammad Amin
June 2020

Norwegian University of Science and Technology
Faculty of Information Technology and Electrical Engineering
Department of Electric Power Engineering

**NTNU**
Norwegian University of
Science and Technology

# Summary

In recent years there has been an increased focus on the environmental crisis, forcing a drastic change in the energy landscape. Renewable generation is integrated into the grid with unprecedented speed, and the transition from conventional generation to renewable generation is bringing new challenges to the safe operation of the energy system. In this transition, one of the most promising and fastest-growing energy sources is wind power, which is often connected to the grid using power electronic converters.

Many different techniques exist for controlling such converters. This thesis is based on an adaptation of the Synchronverter virtual synchronous machine (VSM) to control a large-scale wind energy conversion system connected through back-to-back converters. The use of virtual synchronous machines has been proven to be a promising method of enabling such converter connected generation to provide the grid with ancillary services such as inertial response, frequency control, and voltage regulation, formerly only provided by conventional synchronous machines. With the potential to constitute a large share of grid-connected generation in the future, it is of interest to further examine the transient behaviour and stability of the VSM.

The main objectives of this thesis have been to analyse the transient rotor angle stability of the Synchronverter VSM using both traditional stability analysis methods, known from the conventional synchronous generator, and modified analysis methods, and to improve the stability by introducing enhanced control loops to the Synchronverter control system. These objectives are motivated by the ongoing energy transition where easy determination- and improvement of stability limits, without adding large costs, would simplify the introduction of VSM to the grid, and thus further motivate utility companies to make use of the new technology.

The Synchronverter control structures and their mathematical models have been used to derive a dynamical system that can be used to investigate the Synchronverter analytically. Based on a comprehensive literature study, both the equal area criterion (EAC) and transient energy function (TEF) have been adapted to the analytically modelled Synchronverter dynamical equations to obtain the critical clearing angle (CCA) and critical clearing time (CCT) of the system. This was done using different analytical models such as the classical model of an unregulated system and a model including the effect of the voltage regulating loop. The TEF has also been used to derive a quasi-steady approximate Lyapunov method for predicting the stability of the VSM. The analytical system and related results were then compared to simulation results of a hypothetical wind energy conversion system that was tested for a severe voltage contingency in the MATLAB/Simulink environment.

The results of the stability analysis of the original system showed large variations in the performance of the different analysis methods. While the EAC and TEF utilising the classical model without damping gave a far too conservative result for the stability, deviating with $88.47\%$ from the real CCT, the TEF including the damping term gave a too high prognosis, $57.45\%$ above the real CCT, and thus predicted an unstable system to be stable. The derived quasi-steady approximate Lyapunov method was, however, able to incorporate the deteriorating effect that

the reactive power loop of the VSM has on the system stability, while also considering the large impact damping has on system stability for a VSM with a relatively small virtual inertia. As such, the quasi-steady method yielded very precise estimates of both the CCT and CCA, having a deviation of only two cycles from the system CCT of 386.1 ms. When compared to the responses of the simulated system, the dynamic responses of the derived analytical system were shown to be practically identical. The analytical stability investigations were therefore concluded to be based on a well-functioning analytical model, and any deviations in the results were attributed to the method used.

An unfeasible high post-fault current was identified when clearing the fault at the CCT. To mitigate this current and improve the transient stability, three enhanced Synchronverter control topologies were derived based on the current state-of-the-art for dynamic control of VSMs and methods known from the conventional Synchronous generator; a power correction loop (PCL), a virtual resistor (VR) loop, and a system equipped with both a virtual resistor and artificial damper windings (VR/DW).

Simulation results show that all three systems drastically advance the stability limits, with improvements of $66.9\%$ and $97.00\%$ for the PCL and VR systems respectively. The VR/DW system is however found to be stable even for a clearing time of $1.5$ s, and no CCT was found within the first $4$ seconds after fault initiation. While all three enhanced topologies improved the CCT, only the VR/DW system was demonstrated to satisfyingly mitigate the post-fault current to acceptable levels at all possible clearing times. Furthermore, the VR/DW controller yielded fast and well-dampened tracking of references, demonstrating elegant controller responses that actively mitigated high-frequent oscillations and achieved all controller objectives.

Based on the results, the applicability of traditional stability analysis when analysing the VSM, and the performance of the different enhanced loops added to the Synchronverter controller, were thoroughly analysed and discussed. It is concluded that traditional stability analysis methods using the classical model are no longer viable for the VSM, but that the derived quasi-steady method shows excellent ability in predicting the stability limits also for the virtual synchronous machine.

Moreover, the novel enhanced Synchronverter controller, equipped with both a virtual resistor and artificial damper windings, is concluded to be a far superior controller implementation compared to both the original Synchronverter and the two other investigated enhanced control topologies. Its demonstrated capabilities related to both stability improvement and post-fault current mitigation are concluded to be exceptionally good, yielding results far beyond what would typically be demanded in the power system, and it can therefore be considered to constitute a significant advancement over the state-of-art for the Synchronverter control system.

Lastly, possible ideas for future work have been discussed to enable both the author and other members of the scientific community to easily identify tasks that are of academic interest in future research. Some of the more prominent tasks discussed include expanding the system to include inter-area connections and multiple machines, modifying the system to comprise a fully equipped microgrid with energy storage solutions, and comparison between different types of virtual synchronous machines and droop control for better understanding of their respective characteristics related to power system stability.

# Sammendrag

De senere års fokus på klimaendringene har tvunget frem et skifte i energisystemet. Fornybare energikilder blir integrert i stadig større grad, og omveltningen fra tradisjonell kraftproduksjon til fornybar kraftproduksjon fører med seg en rekke nye utfordringer knyttet til sikker drift av kraftsystemet. En av de mest lovende, og raskest økende, energikildene i denne overgangen er vindkraft, som med sin egenskap av å ikke være regulerbar ofte er koblet til nettet ved bruk av kraftomformere og kraftelektronikk.

Det eksisterer mange ulike teknikker for å kontrollere kraftelektronikk. Denne avhandlingen er basert på en tilpasning av en virtuell synkronmaskin (VSM), kalt en "Synchronverter", for å kontrollere et storskala vindkraftverk koblet til kraftsystemet via en likeretter-likestrømsbro-vekselsretter topologi. Bruken av virtuelle synkronmaskiner har vist seg å være en lovende metode å sørge for at også kraftproduksjon tilkoblet via kraftelektronikk evner å støtte nettet med systemtjenester som frekvensregulering, spenningsregulering og virtuell treghet, tidligere kun levert av tradisjonelle synkronmaskiner. Med potensiale til å utgjøre en stor andel av nett-tilkoblet kraftproduksjon i fremtiden, er det av interesse å undersøke den transiente atferden og stabiliteten til en VSM.

Hovedmålsettingene for denne masteroppgaven har vært å analysere den transiente rotorvinkel-stabiliteten til Synchronverteren ved bruk av både klassiske stabilitetsanalysemetoder, kjent fra den tradisjonelle synkrongeneratoren, samt tilpassede analysemetoder for en VSM, og å forbedre stabiliteten i systemet ved å introdusere nye, forbedrede kontrollsløyfer til Synchronverter-kontrollsystemet. Disse målsettingene er motivert av den pågående omveltningen i energisystemet, hvor enkel identifisering og forbedring av systemets stabilitetsgrenser, uten store tilleggskostnader, vil forenkle introduksjonen av VSM som et konkurransedyktig alternativ og videre motivere kraftselskaper til å ta i bruk teknologien.

Kontrollstrukturene, og de matematiske modellene, som beskriver kontrollsystemet har blitt brukt til å utlede en dynamisk modell som kan brukes til å analysere Synchronverteren analytisk. Basert på en omfattende litteraturgjennomgang har både "like arealers metode" (EAC) og Lyapunov's direkte metode (TEF) blitt tilpasset de analytiske modellene som beskriver kontrollsystemets dynamiske respons. Dette har blitt gjort for å finne systemets kritiske feilrettingsvinkel (CCA) og den tilhørende kritiske feilrettingstiden (CCT). De ulike metodene benytter ulike analytiske modeller, som den klassiske modellen av et uregulert system og en modell som innkluderer effekten av den spenningsregulerende kontrollsløyfen. TEF har også blitt brukt til å utlede en kvasi-stabil tilnærmet Lyapunovmetode for å analysere stabiliteten til en VSM. Det analytiske systemet og relaterte resultater ble deretter sammenlignet med simuleringsresultater av et hypotetisk vindkraftverk simulert for en alvorlig kortslutningsfeil i MATLAB/Simulink.

Resultatene fra stabilitetsanalysen av det originale systemet viste store variasjoner i nøyaktigheten, og dermed ytelsen, til de forskjellige analysemetodene. Både EAC og TEF ga et altfor konservativt resultat av stabilitetsgrensene ved bruk av den klassiske modellen uten demping, med et avvik på $88.47\%$ fra den virkelige CCT. TEF ved bruk av den klassiske modellen inkludert

demping ga derimot et for høyt estimat, $57.45\%$ over den reelle CCT, og anslo dermed et ustabilt system som stabilt. Den kvasi-stabile tilnærmede Lyapunov metoden var imidlertid i stand til å inkorporere den negative effekten spenningsreguleringssløyfen har på stabiliteten til en VSM, og samtidig ta i betraktning den store påvirkningen dempingen har på systemstabiliteten for en VSM med en relativt liten virtuell treghet. I egenskap av dette ga metoden et særdeles presist resultat av både CCA og CCT, med et avvik på 2 perioder fra systemets faktiske CCT på $386.1$ ms. Sammenlignet med responsen fra det simulerte systemet ble den dynamiske responsen til det modellerte analytiske systemet vist å være identisk, sett bort ifra neglisjerbare avvik. De analytiske analysemetodene ble derfor konkludert med å være basert på en velfungerende analytisk modell, og eventuelle avvik i resultatene av stabilitetsanalysen ved bruk av den fulle analytiske modellen ble derfor tilskrevet analysemetoden.

Når feilen ble rettet ved CCT ble det identifisert en uanvendelig høy strøm umiddelbart etter feilretting. Basert på state-of-art innenfor dynamisk kontroll av VSM og metoder kjent fra den tradisjonelle synkrongeneratoren ble tre ulike forbedrede kontrollstrukturer foreslått implementert i Synchronverteren for å dempe den uanvendelige strømmen og forbedre den transiente stabiliteten; en effektkorrigerende sløyfe (PCL), en sløyfe med en virtuell motstand (VR), og en topologi utstyrt med både en virtuell motstand og virtuelle dempeviklinger (VR/DW).

Simuleringsresultatene viser at alle tre systemene drastisk forbedrer stabilitetsgrensene, med forbedringer på henholdsvis $66.9\%$ og $97.00\%$ for PCL og VR systemene. VR/DW systemet ble imidlertid funnet til å være stabilt selv ved en feilrettingstid på $1.5$ s, og ingen CCT ble funnet i løpet av de første 4 sekundene etter at feilen ble initiert. Mens alle de tre forbedrede kontrollstrukturene forbedret CCA/CCT, var det kun VR/DW systemet som i tilfredsstillende grad dempet strømmen umiddelbart etter feilretting til et akseptabelt nivå ved alle de aktuelle feilrettingstidene. Videre ga VR/DW kontrolleren en rask og veldempet følging av system-referansene, samt demonstrerte en elegant evne til å dempe også høyfrekvente oscillasjoner.

Basert på resultatene ble anvendbarheten av klassisk stabilitetsanalyse for gransking av en VSM, samt ytelsen til de ulike forbedrede kontrolltopologiene, grundig analysert og diskutert. Det konkluderes med at tradisjonelle stabilitetsanalysemetoder ved bruk av den klassiske modellen ikke lenger er gyldige for en VSM, men at den utledede kvasi-stabile metoden viser en utmerket evne til å forutsi stabilitetsgrensene også for den virtuelle synkronmaskinen. Videre konkluderes det med at den nye, forbedrede Synchronverter-kontrolleren, implementert med både en virtuell motstand og virtuelle dempeviklinger, i stor grad er overlegen både det originale kontrollsystemet og de to andre forbedrede topologiene. De påviste egenskapene relatert til både stabilitetsfor-bedring og strømforbedring blir trukket frem som eksepsjonelt gode ved å gi resultater langt utover det som typisk vil kreves i kraftsystemet. VR/DW-kontrollsystemet anses derfor som en betydelig forbedring av det eksisterende systemet.

Til slutt ble mulige ideer for fremtidig arbeid diskutert for å gjøre det mulig for både forfatteren og andre medlemmer av det vitenskapelige samfunnet å enkelt identifisere oppgaver som er av faglig interesse i fremtidig forskning. Noen av de mer vesentlige oppgavene som diskuteres inkluderer utvidelse av systemet til å omfatte mellomområdeforbindelser og flere maskiner, modifisering av systemet til å omfatte et fullt utstyrt mikronett med energilagringsløsninger, og sammenligning mellom forskjellige typer virtuelle synkronmaskiner og droop-kontroll for bedre forståelse av deres respektive egenskaper relatert til kraftsystemets stabilitet.

# Preface

This report is the final product of the master's thesis course TET4900 at the Norwegian University of Science and Technology (NTNU) and equals the workload of 30 ECTS-credits. The thesis is written during the spring of 2020 and was carried out at the Department of Electrical Power Engineering as the final part of fulfilling the requirements for the grade of Master of Technology in Energy and Environmental Engineering. The thesis serves as a continuation of a specialisation project conducted during the fall of 2019 and is contributing to the field of power system stability.

The process of working with the thesis has, like everything else in society, been impacted by the outbreak of the COVID-19 virus. As the NTNU campus closed for students, and we all had to find new methods of working from home, the already challenging work of getting acquainted with new, complex topics, such as power system stability, got even more challenging. As a novice to many of the concepts used, many hours have been spent acquiring the knowledge necessary to adequately perform the investigations lying within the scope of the thesis. This has led to many moments of frustration, a lot of ups and downs, and a distinctive sense of achievement when things finally came together. As the spring flew by and the world around came to a stand-still, the work carried on, resulting in this thesis, and I can honestly say it has been a fun and meaningful experience altogether.

I would like to extend my profound gratitude towards my supervisor, Associate Professor Mohammad Amin. His deep theoretical insight, as well as the ability to answer even my most banal questions with patience, have been key to making this a great learning experience. The difference between dropping by the office across the hallway and having to maintain contact via Skype, when working on complex problems and novel implementations improving on the state-of-art, has been diminished thanks to his true interest in my work. During our meetings, both via Skype and at the office, he always had an educational approach and willingness to help, even though the circumstances were somewhat special.

In addition, I would like to thank my friends and family for keeping me motivated during the entire process. Their ability to help me keep focused on both the thesis and the life outside of school has been vital, especially in these strange times of COVID-19. Last but not least, I would especially like to thank Trine Mathisen for helping me with the proofreading of the thesis and for keeping up with me during my most frustrated working periods. Her encouraging and supporting words have pushed me through periods of low motivation, and she has truly been invaluable to the success of my study efforts throughout the last five years.

Henrik Høstmark
Trondheim, June 26th 2020

Dept. of Electric Power Engineering

# Contents

# List of Figures

# List of Tables

# Abbreviations

**AC**  Alternating Current.

**ADC**  Analog to Digital Converter.

**APL**  Active Power Loop.

**AVR**  Automatic Voltage Regulator.

**BESS**  Battery Energy Storage System.

**CAPEX**  Capital Expenditures.

**CCA**  Critical Clearing Angle.

**CCT**  Critical Clearing Time.

**CO$_2$**  Carbon Dioxide.

**DAC**  Digital to Analog Converter.

**DC**  Direct Current.

**DFIG**  Doubly Fed Induction Generator.

**DSP**  Digital Signal Processor.

**DWs**  Damper Windings.

**e.p.**  equilibrium point.

**EAC**  Equal Area Criterion.

**EMF**  Electromotive Force.

**ESS**  Energy Storage System.

**EU**  European Union.

**EU ETS**  EU Emission Trading System.

**FACTS**  Flexible AC Transmission Systems.

**FCR** Frequency Containment Reserves.

**FRC-WT** Fully-Rated Converter Wind Turbines.

**FRR** Frequency Restoration Reserves.

**FRT** Fault Ride Through.

**HVDC** High Voltage Direct Current.

**IEA** International Energy Agency.

**IEEE** Institute of Electrical and Electronics Engineers.

**IFD** Instantaneous Frequency Deviation.

**IGBTs** Insulated-Gate Bipolar Transistors.

**LCOE** Levelized Cost of Electricity.

**MPPT** Maximum Power Point Tracking.

**O&G** Oil and Gas.

**OPEX** Operational Expenditures.

**PCC** Point of Common Coupling.

**PCL** Power Correction Loop.

**PI** Proportional/Integral.

**PLL** Phase Locked Loop.

**PMSG** Permanent Magnet Synchronous Generator.

**PSS** Power System Stabiliser.

**PV** Photo Voltaic.

**PWM** Pulse Width Modulation.

**RES** Renewable Energy Sources.

**RMS** Root Mean Square.

**RPL** Reactive Power Loop.

**s.e.p.** stable equilibrium point.

**SG** Synchronous generator.

**SMIB** Single-Machine-Infinite-Bus.

**SPWM** Sinusoidal Pulse Width Modulation.

**STA** Sinusoidal Tracking Algorithm.

**TEF**  Transient Energy Function.

**TSO**  Transmission System Operator.

**u.e.p.**  unstable equilibrium point.

**UN**  United Nations.

**VR**  Virtual Resistor.

**VSC**  Voltage Source Converter.

**VSM**  Virtual Synchronous Machine.

**WECS**  Wind Energy Conversion System.

# Nomenclature

**Units**

| | |
|---|---|
| $\Omega$ | Ohm |
| ° | Degree |
| A | Ampere |
| C | Celsius |
| F | Farad |
| g | gram |
| H | Henry |
| Hz | Hertz |
| m | meter |
| N | Newton |
| p.u. | per unit |
| rad | Radian |
| s | second |
| V | Volt |
| VA | Volt Ampere |
| VAr | Volt Ampere reactive |
| W | Watt |

**Metric Prefix**

| | | |
|---|---|---|
| $\mu$ | micro | $10^{-6}$ |
| m | milli | $10^{-3}$ |
| k | kilo | $10^{3}$ |
| M | mega | $10^{6}$ |
| G | giga | $10^{9}$ |

# Introduction

*This introductory chapter serves to give the reader a better understanding of the framework which the thesis is built upon. First, the motivation behind the thesis work is elaborated, before the specific objectives are presented. The targeted contribution, as well as the thesis' relation to the specialisation project, is elaborated, and the method, scope and structure of the report are outlined.*

## 1.1   Background and Motivation

The global demand for electricity has grown rapidly as the global economy has developed over the last decades, and according to the International Energy Agency (IEA), the demand rose to $25606$ TWh annually in 2017[1]. The rising demand for energy has been followed by an increased focus on the environmental challenges related to $CO_2$ emissions, where electricity production is a key driver. The energy industry has therefore been forced into an energy transition where renewables are at the centre of technological development. This transition is clearly visible when looking at the global energy mix, where the share of global electricity generation in 2018 coming from renewables was $26\%$, with an estimated increase to $49\%$ in 2030[2].

To ensure the transition into a sustainable future, both the European Union (EU) and the United Nations (UN) have enacted different policy frameworks describing climate and energy policies and targets going forward. The EU passed a framework containing EU-wide targets for the year 2030 stating that the EU as a whole should achieve at least 32% share of renewable energy, and be climate neutral in 2050[3]. In 2016 the UN also came to a new agreement meant to replace the Kyoto Protocol from 1997. The Paris Climate Agreement, ratified by 187 party-members of the UN, sets a target of keeping the global temperature increase below 2°C and pursue efforts to keep it to 1.5°C within the current century[4]. These two accords, as well as other national climate policy frameworks, have led to the need for significant changes in the power system, integrating even more Renewable Energy Sources (RES). Here, wind power is highlighted as one of the primary solutions to reduce the environmental footprint, as well as emissions of greenhouse gases, coming from power generation.

The increased focus on RES has also made an impact on the economical landscape governing the investments of energy companies. Technologies such as wind and solar have now matured enough to be able to compete with conventional energy sources such as coal and gas without the

need of heavy subsidies[5], making them more attractive to the energy companies. Combining this with stricter policies related to the quotas for the EU Emission Trading System (EU ETS) and short gestation times from investment decision to full operation, the Levelized Cost of Electricity (LCOE) for wind energy has become lower than coal-fired electricity[6]. Based on this, wind power was presumed to pass natural gas in 2019, becoming the leading energy technology in Europe measured by installed capacity[7].

However, Renewable Energy Sources (RES) like wind and solar are intermittent and not necessarily generating electricity that is directly compatible with the parameters of the grid. This is especially true for Photo Voltaic (PV) systems which generate Direct Current (DC), and wind power which often generate variable frequency Alternating Current (AC). Thus, these intermittent sources have to be connected to the grid using power electronic converters which effectively decouples the properties of the electric machine from the grid properties such as frequency and voltage. In addition, the system will to a large degree transition from having centralised generation to distributed generation[8].

This new system topology dominated by converter connected generation may bring challenges to the conventional operation of the power system when the share of RES becomes significantly large. Challenges may include problems related to the security of supply, capacity adequacy, power system stability and reliability. The conventional operation of the grid has until now been based on highly controllable rotating machines using either thermal energy from fossil fuels or hydropower to drive a turbine that in turns drive a generator that is directly coupled to the grid at the synchronous speed/frequency, i.e. the generator stator frequency is equal to the grid frequency. This topology has made it relatively easy to adjust and balance the grid in case of contingencies, in addition to being able to support the grid with an inertial response and ancillary services such as voltage support and frequency support.

However, as the frequency of the converter connected generation is effectively decoupled from the grid, so is the available inertia of the generator/turbine. In addition, converter connected generation is often controlled to inject all power available from the source, and is less likely to be able to participate in frequency control such as Frequency Containment Reserves (FCR) and Frequency Restoration Reserves (FRR)[9], which may be a threat to the secure system operation. Transmission System Operators (TSOs) have therefore implemented new grid code requirements that power generation connected through converters must comply with to be allowed to connect to the grid. Notable requirements include the ability to provide frequency- and voltage support, have adequately fault ride-through (FRT) capabilities, and easy determination of stability limits and operating range[10]. It is therefore of interest to develop technologies that equip also converter connected generation with these abilities, and a method that has been shown to be very promising is the Virtual Synchronous Machine (VSM) control technology. A Virtual Synchronous Machine is a control method used to control converters in such a way that many of the attributes of the conventional Synchronous generator (SG) are preserved, i.e. the converter can be seen as an SG by the grid. Thus, VSMs are designed to possess many of the characteristics inherently found in conventional SGs, and are therefore also, to a certain degree, capable of providing the grid with ancillary services. This is vital to facilitate an accelerated integration of renewables. It is therefore of academic interest to study different aspects related to the VSM, and to validate its performance under different operating conditions. Through this research, the academic society can motivate utilities and energy companies to increase their investments in renewables and to trust that the new technologies introduced, such as the VSM, does not put system integrity at risk.

Many studies have been performed to prove the effectiveness and the functioning of the VSM concept for providing ancillary services to the grid, but very few studies look into the subjects related to VSM and transient power system stability. Furthermore, one of the main challenges with VSM controlled voltage source converters is that they lack the ability to limit the current, possibly leading to excessively high currents both during- and after a fault has occurred. This can be extremely harmful to the converters, which in most cases disconnect to minimise damage. As such, converters are known to have very poor Fault Ride Through (FRT) capabilities.

In this thesis, a transient stability analysis will be carried out using classical power system stability tools for a system consisting of a VSM. The study will assess the applicability of classical stability analysis methods, known from conventional SG, when analysing VSM-controlled converters. If the classical analysis is shown to be unfeasible, a modified analysis method also applicable to the VSM should be outlined, thus drastically simplifying their introduction to the grid. Furthermore, the thesis will look into how modifications to the VSM control system can enhance system stability using very little effort and without changes to the power system topology. These modifications to the control system will aim at both improving the transient stability and reducing the possibility of operating at too high converter currents.

This is motivated by the ongoing energy transition described above, where VSMs are considered a key solution to the successful integration of renewables. In addition, easy determination of stability limits is specifically mentioned as a key characteristic of the VSM to comply with new grid codes, and it is therefore of interest to investigate whether methods known from the SG can be applied also to the VSM. Also, it will be of importance to demonstrate that VSMs can be analysed analytically when investigating their stability, and that they can actually increase stability limits without adding the large costs normally required when enhancing the stability of a system consisting of conventional SGs.

## 1.2   Objectives

The objectives of this master's thesis are to investigate the transient stability of a power system consisting of a Virtual Synchronous Machine (VSM) based Wind Energy Conversion System (WECS), propose methods of improving the stability of the system if possible, and to simulate both the original system, as well as the improved system, in the MATLAB/Simulink environment to verify the functioning of both the stability analysis and the proposed enhanced system controls.

As such, the thesis consists of two main research objectives plus some add-on objectives, where the two main objectives are; perform a stability analysis of the original system, and improve the control structure to achieve enhanced stability. The stability analysis aims at investigating the applicability of well-known analytical stability assessment methods from the conventional synchronous generator when analysing the *virtual* synchronous generator, and comparing the analytical results with simulation results. The objective of improving the system stability revolves around adding new control loops to the VSM control algorithm to improve the dynamic response when subjected to large disturbances, thus improving the transient stability and mitigating high converter currents.

These objectives are largely motivated by the factors outlined in Section 1.1 and are thus seen in the context of the technological advancements and state-of-art of the energy system. In addition, the thesis objectives are motivated by the recommendations for future work pointed out in the preliminary study preceding this thesis, and the fundamental drive behind any research, which is to advance on the state-of-art within a given field of study.

More specifically, the objectives can be divided into five parts listed as follows:

- Acquire sufficient knowledge on the complex theory related to power system stability and associated methods of stability assessments.

- Perform an investigation into the transient stability of a given VSM system using related theory known from classical stability analysis. The objective aims at investigating whether classical stability analysis known from the conventional synchronous generator is also applicable to the VSM. If this is not the case, a method also applicable to the Synchronverter should be derived for easy identification of stability limits.

- Propose new control loops that can be added to the Synchronverter VSM to enhance the system stability and improve the dynamic response of the Synchronverter control system, with a special focus on mitigating the converter current without affecting the steady-state characteristics.

- Construct a test-bed in the MATLAB/Simulink environment to test- and validate the theoretical concepts and analytical results, and to verify the effectiveness of the proposed enhanced control structure.

- Put forward well-judged tasks that should be further investigated in future research based on the experience and results obtained from the thesis work.

## 1.3   Contribution

This thesis's contribution to the already established research on the topic will be to create an analytical model that can be used to investigate the Synchronverter dynamical response, and provide a detailed comparison between the simulated system and the obtained analytical model. The analytical model will further be utilised in a modified Lyapunov method for investigating the transient stability of the VSM.

Furthermore, a novel, enhanced Synchronverter control structure will be proposed, drastically improving the dynamic response of the Synchronverter control system when subjected to a contingency and thus advancing the transient stability of a power system consisting of a VSM-connected wind turbine. More precisely, the use of a virtual resistor and artificial damper windings will be adapted to the Synchronverter control system, yielding both a dynamical response and stability limits far superior to the original system.

The proposed control structure will require a minimum amount of both tuning and increase in controller complexity. Furthermore, it will be easily implemented, and thus make the VSM an even more attractive solution in the energy transition by simplifying the adaption of the VSM to systems that dictate high demands related to power system stability and security.

In addition, parallel to the thesis work, a scientific paper has been written and submitted for publication based on the results of the specialisation project. The paper, having the title *Small-signal Modelling and Tuning of Synchronverter-based wind energy conversion systems*, is currently in major revision, and is attached in Appendix E for the completeness of the contribution of the specialisation project and the master's thesis as a whole.

## 1.4   Relation to the Specialisation Project

A specialisation project was conducted during the autumn of 2019 with the title *'Virtual Synchronous Machine Based Wind Energy Conversion System'* ([5]), and this master's thesis serves as a continuation of the work carried out in said project. The main objectives of the specialisation project were to investigate the Synchronverter Virtual Synchronous Machine control technique for power electronics connecting wind power to the grid. More specifically the objectives were to propose a tuning procedure for the control parameters, tune the controls to a specific system and to simulate the technique in the MATLAB/Simulink environment to verify both the performance of the proposed tuning procedure and the Synchronverter's ability to deliver ancillary services such as frequency and voltage support to the grid.

The results showed great performance by the Synchronverter-controlled converters under both frequency- and voltage disturbances, and both active- and reactive power injection were adjusted based on the situation at the grid and the available power from the wind turbine. The proposed tuning procedure yielded well-tuned controller parameters, enabling the controller to have fast and accurate responses to contingencies and changes in power set-points, without steady-state deviations.

However, it was specifically mentioned when defining the scope of the specialisation project that a notable limitation was that no stability analysis of the proposed system was performed. Furthermore, as a part of suggestions for future work, it was explicitly stated that an investigation into the control topology's behaviour related to system stability should be carried out. As such, a direct link between the specialisation project and this thesis has been established.

The experience and results obtained from working on the specialisation project will therefore be of importance when further investigations are done into the concept of Virtual Synchronous Machines in this thesis. Parts of the specialisation project report will also be used as background material and serve as important parts of the theory this thesis is based on, and are thus included also in this thesis. In addition, parts of the simulation model that will be introduced later in this thesis were first developed for the specialisation project and later modified for the study carried out here.

## 1.5   Method

An introductory study of VSMs and their functioning was carried out in [5] ahead of this thesis. This study, as well as an in-depth literature review of relevant articles and papers related to power system stability and stability of VSMs, will be used to explain the necessary theory required to grasp the study that is to be carried out. The required mathematical modelling given in the specialisation project will be provided, including the working principles of a wind turbine, the mathematical modelling of a synchronous generator and the Synchronverter control system.

The mathematical foundation of dynamical systems and the link to power system stability will be explained, before relevant theory, investigated literature and papers will be used to analyse the transient stability of the Synchronverter VSM. When the stability limits of the original system have been determined, new control loops will be proposed based on a literature review of the current state-of-the-art for dynamic control of VSMs and methods known from the dynamic response of the conventional Synchronous generator.

A Simulink model was developed for the introductory study in the specialisation project, and

this model will be modified and adapted to the study in this thesis. The simulations will include both the original system and the proposed enhanced system, and the VSM-based WECS will be tested for a large contingency making the dynamic responses of the different control topologies clearly visible and comparable. The investigations will also include analysis and discussion of all obtained results so that conclusion can be drawn.

## 1.6   Scope and limitations

The scope of the thesis work can be summarised in the following:

- Get up to date on classical power system stability theory and power system developments.

- Model the dynamics of the Synchronverter VSM analytically.

- Adapt classical stability analysis methods to the Synchronverter VSM using the obtained dynamics, resulting in stability limits that can be verified or refuted using a simulation model.

- If necessary, modify the classical stability analysis to better reflect the dynamics of the Synchronverter VSM.

- Perform a comprehensive, yet focused literature review on the state-of-art for dynamic control of VSM and classical SG control.

- Put forward new control implementations to the Synchronverter VSM to enhance the transient stability margins of the system. Compare the different control implementations in their effectiveness.

- Use simulation results to validate and discuss the different approaches to enable a well-substantiated conclusion to the different thesis objectives.

- Propose adjustments and requirements for future research based on the obtained results and experience.

Notable limitations include the following:

- Simulations will only be carried out on a hypothetical system using MATLAB/Simulink, meaning all system parameters are hypothetical and no physical hardware implementations will be done. Furthermore, an aggregated wind farm model is used.

- The focus of the thesis is on controller dynamic performance and power system stability, and therefore the details related to choosing specific parameters for the WECS used for testing are not emphasised.

- Stability of the VSM control system in the sense of control theory through terms such as phase margins, gains, Nyquist diagrams and pole placement is not discussed.

- Wind energy in detail, such as pitch control, other types of turbine control, foil-theory and turbine behaviour are outside the scope of this thesis.

- Only one type of virtual synchronous machine will be subject for investigation, and no comparison to other types of VSM will be performed.

- Only transient angular stability is considered, and investigations into frequency- and voltage stability are thus not carried out.

## 1.7   Structure

The report is based on a four-level structure using the form **A.B.C.D**. Here **A** is the number of the chapter, **B** is the section number within chapter **A** and so forth. Equations, figures an tables are enumerated on the form **A.B** according to their number **B** within chapter **A**.

The bibliography provided at the end of the thesis uses the citation style defined by the Institute of Electrical and Electronics Engineers (IEEE), and references used throughout the thesis can be recognised by their reference number inside square brackets. The reference number will match the number in the bibliography and follow a chronological order based on when in the thesis the reference is first cited.

Sections from the specialisation project ([5]) that are found to be relevant for the master's thesis will be included either in their original form or in a modified, redrafted version. Redrafted sections may include new parts added during the work with this thesis or just be updated with the latest information.

If a section is included in its original form or redrafted from the specialisation project it will be clearly stated. The sections these notes applies to are also summarised here for easy identification by the reader:

- Sections included in their original form include: *2.1*, 2.3, *3.1* (except *3.1.5* which was added during the thesis work), *3.2* and *3.3*.

- Sections included in a modified form include: *2.2*.

This master's thesis consists of six chapters including the introduction chapter, plus five appendices. The structure, and a summary, of the remaining five chapters and appendices, are outlined below to give a compact overview of the content of each of the following chapters. The compact overviews will also be repeated at the beginning of each chapter for easy navigation in the thesis.

**Chapter 2** provides an introduction to the basic theory needed to form the foundation required before the study carried out in this thesis can be started. The chapter contains both new material as well as sections originally written for the specialisation project. First, an introduction to wind power is given, before the wind turbine and permanent magnet synchronous generator are modelled mathematically. Then, a brief explanation of power electronic converters is provided. The synchronous machine is then modelled and the swing equation is introduced. Also, a short introduction to the concept of virtual synchronous machines is given, and an in-depth introduction to dynamical systems is presented. Lastly, an introduction to power system stability is given, and rotor angle stability is discussed.

**Chapter 3** models the Synchronverter VSM control technique for both inverter control and rectifier control. The system topology is also described in detail.

**Chapter 4** describes the investigation into the transient angular stability of a VSM connected to an infinite bus using different methods of stability analysis. First, the type of contingency is defined along with a problem formulation. Then, the differential equations describing the dynamics of the Synchronverter using different assumptions are obtained, before the concepts of the equal area criterion and transient energy function are introduced. Using these concepts, different methods of analysing the stability of the given system are described in detail. Furthermore, results and simulations providing insight into the system stability are provided, before being thoroughly discussed.

**Chapter 5** puts forward a set of additional control loops that can be introduced to the Synchronverter control system to increase the stability margins, and thus enhance the system stability. First, an introduction into methods of improving the transient stability of conventional power systems is given, before how to quantify the improvement is established. Then, the concept of a power correction loop is introduced, before the use of both a virtual resistor and artificial damper windings are proposed for the Synchronverter VSM. Lastly, simulations are carried out to validate the effectiveness and functioning of the proposed enhanced control systems. The performance of each method is then discussed and compared to the other methods.

**Chapter 6** will outline conclusions for both the stability analysis carried out on the original system and the proposed control loops improving the transient stability. The conclusions will be tied to the objectives and targeted contribution of the project. Lastly, recommendations for future research will be put forward based on the findings and discussions provided by the investigations carried out in this thesis.

**Appendix A** contains the per unit system used in this thesis.

**Appendix B** provides all the system parameters needed to carry out the investigations and simulations of the thesis.

**Appendix C** provides figures depicting all the Simulink models used for the simulations carried out in this thesis.

**Appendix D** provides figures depicting additional simulation results that provide further insight into system behaviour beyond what is being discussed in detail.

**Appendix E** contains the full version of the scientific paper that was written based on the specialisation project. The paper was written parallel to the thesis work to form the contribution to the scientific community from the work carried out in the specialisation project. The paper is attached in its entirety with both appendices and it own bibliography.

# Chapter 2

# Background Theory

*This chapter provides an introduction to the basic theory needed to form the foundation required before the study carried out in this thesis can be started. The chapter contains both new material as well as sections originally written for the specialisation project. First, an introduction to wind power is given, before the wind turbine and permanent magnet synchronous generator are modelled mathematically. Then, a brief explanation of power electronic converters is provided. The synchronous machine is then modelled and the swing equation is introduced. Also, a short introduction to the concept of virtual synchronous machines is given, and an in-depth introduction to dynamical systems is presented. Lastly, an introduction to power system stability is given, and rotor angle stability is discussed.*

## 2.1 Introduction to Wind Power

*A presentation of the Wind Energy Conversion System (WECS) was included in the specialisation project preceding this thesis. The model of the system under investigation is the same as in the specialisation project and the presentation from the project report ([5]) is therefore included below in its original version.*

### 2.1.1 Wind Turbines and Their Topologies

A wind turbine is a machine which converts the energy in the wind into electricity[11]. Blades creating aerodynamic lift force are mounted to a rotor shaft which then experiences a net positive torque from the blades. The mechanical power applied to the shaft can be converted to electricity by use of a generator, and it can be noted that the maximum possible mechanical power that can be extracted from the power in the airflow is limited to $59.3\%$ according to Betz limit[12].

Wind turbines can have several different blade topologies such as single blade, double blade and bicycle multi-blade, but the most common type used today is the three-bladed turbine [11]. Modern wind turbines are divided into two categories based on the operating type; fixed speed wind turbines and variable speed wind turbines. Variable speed turbines are preferred due to more control flexibility and improved system efficiency and power quality[13]. It is also worth mentioning that a wind turbine can be directly driven or have a gearbox that enables mechanical speed conversion between the turbine and generator.

The most used topologies for variable speed wind turbines are Doubly Fed Induction Generators (DFIG) and Fully-Rated Converter Wind Turbines (FRC-WT) with synchronous generators (SG). In the DFIG topology, the variable speed operation is achieved by the use of a controllable voltage in the rotor which decouples the electrical speed of the machine from the mechanical speed of the rotor[13]. This is done by adjusting the slip of the induction machine.

The FRC-WT topology on the other hand decouples the whole generator completely from the utility grid, enabling the electrical speed of the generator to deviate completely from the nominal grid frequency. Several different generator technologies can be applied to the FRC-WT topology, and for the application in this thesis the Permanent Magnet Synchronous Generator (PMSG) will be used. The simple mathematical model of the PMSG is therefore outlined in Section 2.1.2.4.

### 2.1.2   Modelling the Wind Energy Conversion System

A MATLAB/Simulink model was built from ground up as a part of the specialisation project. The model is to a large extent based on the mathematical description of a Wind Energy Conversion System (WECS) laid out in this section.

#### 2.1.2.1   Wind Turbine

Foil theory and wind turbine aerodynamics are described in detail in [11], but for the applications in this thesis the simplified turbine model from [14] will be utilised. The kinetic energy in the airflow that can be converted into mechanical power, $P_m$, is given by (2.1) where $\rho$ is the density of the air, $R$ is the turbine radius, $v_w$ is the wind speed and $C_p$ is the power coefficient.

$$P_m = \frac{1}{2}\rho\pi R^2 v_w^3 C_p(\lambda, \beta) \qquad (2.1)$$

The power coefficient, $C_p$, is dependent on the pitch angle of the turbine blades, $\beta$, and the tip speed ratio $\lambda$. $\lambda$ is defined in (2.2), where $\omega_m$ is the rotational speed of the rotor.

$$\lambda = \frac{\omega_m R}{v_w} \qquad (2.2)$$

All wind turbine designs have specific expression describing $C_p$. However, according to [15], these expressions do not have large differences and can therefore be approximated by an analytic function. Therefore the expression in (2.3) is used[14].

$$C_p(\lambda, \beta) = 0.5(\frac{116}{\lambda_i} - 0.4\beta - 5)e^{\frac{-21}{\lambda_i}} \qquad (2.3)$$

Here $\lambda_i$ is defined as in (2.4).

$$\frac{1}{\lambda_i} = \frac{1}{\lambda + 0.08\beta} - \frac{0.035}{\beta^3 + 1} \qquad (2.4)$$

Based on the model outlined above, the turbine needs to maintain its optimal tip speed ratio, $\lambda_{opt}$, at any given wind speed to extract maximum power out of the airflow. Therefore, based on (2.2),

the rotational speed of the rotor must be adjusted based on the wind speed. This can be shown by utilising (2.1), (2.2) and (2.3) to plot the power curve of a turbine for different wind speeds and rotor speeds, as depicted in Figure 2.2 where the power curves of a turbine operating at rated power at $v_w = 12$ m/s is shown. In this figure, it can be seen that the maximum power extracted from the airflow for a given wind speed is achieved for a specific $\omega_m$. This will be the $\omega_m$ that gives $\lambda = \lambda_{opt}$ for that given wind speed. This knowledge will be used to design the Maximum Power Point Tracking (MPPT) algorithm in Section 2.1.2.2, which will enable the turbine to operate at maximum efficiency.

The power coefficient can be plotted for different $\lambda$ and $\beta$, yielding the curves depicted in Figure 2.1. From this figure the maximal power coefficient, $C_{p,max}$ and the optimal tip speed ratio $\lambda_{opt}$, can be easily found.
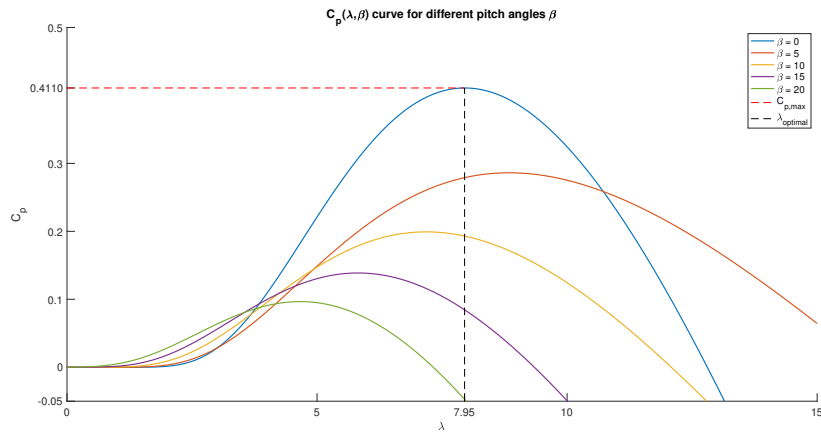


Figure 2.1: $C_p(\lambda, \beta)$ curve based on (2.3)

The wind turbine in the Simulink model used for simulation purposes is based on the mathematical modelling in Section 2.1.2.1. In addition, the pre-made model from [16] is used as a reference for the implementation, with modifications related to the analytic expression used for the power coefficient.

### 2.1.2.2   Maximum Power Point Tracking

To ensure that the WECS is operating at $\lambda_{opt}/C_{p,max}$ for maximum power efficiency, an MPPT algorithm has to be modelled. The MPPT algorithm is implemented to adjust the power set-point, i.e. the load, which would effectively change the speed of the generator, ultimately adjusting $\omega_m$ to the optimal point where $\lambda_{opt}$ is achieved. Many different MPPT techniques have been proposed in the literature, and the optimal torque control proposed in [17] will be presented here using modifications from [18].

The first step is to rewrite (2.2) into:

$$v_w = \frac{\omega_m R}{\lambda} \tag{2.5}$$

Equation (2.5) can then be substituted into (2.1) which yields:

$$P_m = \frac{1}{2}\rho\pi R^5 \frac{\omega_m^3}{\lambda^3} C_p(\lambda, \beta) \tag{2.6}$$

The objective is to run the WECS at $\lambda_{opt}$, giving $C_{p,max}$, and (2.6) is therefore adjusted to reflect this as in (2.7a) where $P_{m,opt}$ is the maximum power of the wind turbine and thus the optimal power set-point for the given turbine speed. Using the fact that $P_m = \omega_m T_m$, (2.7a) can also be expressed as the maximum torque from the turbine as in (2.7b). In both equations, $K_{p,opt}$ is defined as in (2.7c).

$$P_{m,opt} = \frac{1}{2}\rho\pi R^5 \frac{C_{p,max}}{\lambda_{opt}^3}\omega_m^3 = K_{p,opt}\omega_m^3 \tag{2.7a}$$

$$T_{m,opt} = \frac{K_{p,opt}\omega_m^3}{\omega_m} = K_{p,opt}\omega_m^2 \tag{2.7b}$$

$$K_{p,opt} = \frac{1}{2}\rho\pi R^5 \frac{C_{p,max}}{\lambda_{opt}^3} \tag{2.7c}$$

We can use this knowledge to plot the MPPT curve in the same figure as the power curve of the turbine for different wind speeds and rotor speeds, as seen in Figure 2.2. The advantage of this method is that only a measurement of the turbine speed is necessary, i.e. no additional sensors measuring the wind speed is required. Note that in Figure 2.2 the MPPT curve is depicted with a limit at the rated mechanical power of the turbine. However, with no additional control, such as pitch control for the turbine blades or limitations in the power set-point, the MPPT curve will continue upwards for wind speeds higher than the rated wind speed. It can be noted that the turbine's torque curves can be plotted using the same method as for the power curve in Figure 2.2. This is however not done here.

The maximum power of the turbine can also be calculated directly based on the wind speed if this measurement is available, as the maximum power coefficient is already known. $P_{m,opt}$ can then calculated using (2.8).

$$P_{m,opt} = \frac{1}{2}\rho\pi R^2 v_w^3 C_{p,max} \tag{2.8}$$
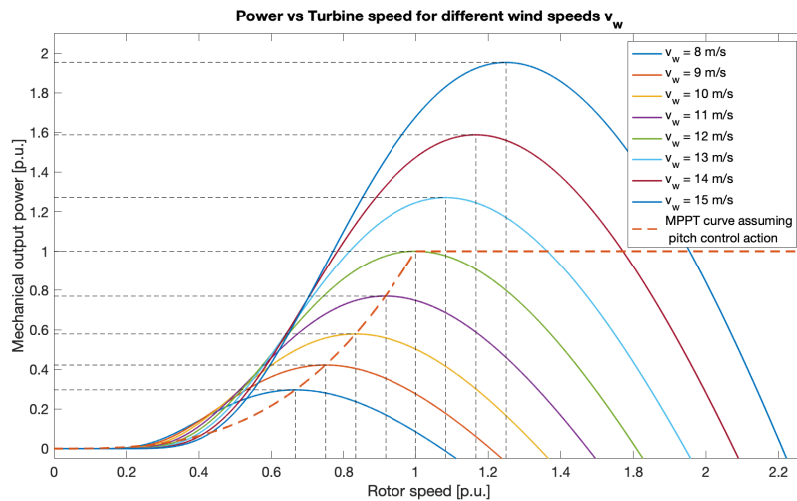


Figure 2.2: Power curve, including MPPT curve, for a turbine rated at $v_w = 12$ m/s.

### 2.1.2.3  De-Rated Operation

Another method of operating the WECS is in de-rated operating mode, also known as de-loaded operating mode[19]. In contrast to the MPPT operating mode, a de-rated operation is an operating mode which is not utilising the full potential of the wind speed, and thus the wind turbine is not operating at the optimal operating point. In the de-rated operating mode, the turbine keeps a margin that can be utilised in the event of a sudden drop in frequency, by increasing the power output.

There are in reality two different methods of de-loading a wind turbine; balancing de-loading and delta de-loading[19]. Balancing de-loading is achieved by setting a maximum power output regardless of wind speed, enabling a constant power output from the turbine. Delta de-loading is achieved by setting the power reference to a certain percentage of the MPPT set point, and the two different methods are visualised in Figure 2.3 for a wind turbine rated at 2 MW.
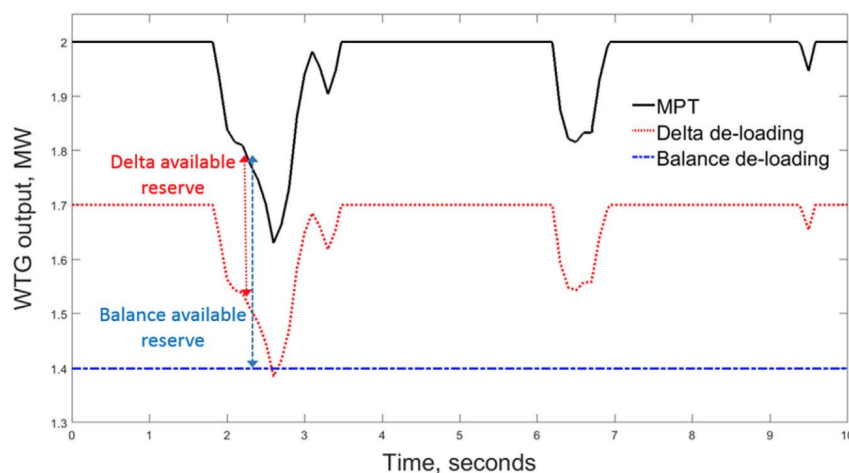


Figure 2.3: Methods of de-rating[19].

Different techniques can be used to alter the operating point of the turbine, and the two most common will be covered here. For fixed speed wind turbines it is most common to adjust the pitch angle of the blades to decrease the torque of the turbine[20]. If more power is needed the pitch angle can be changed, thus increasing the torque. However, pitch control can be slow as it requires large turbine blades to rotate. Therefore, for variable speed wind turbines such as the one used in this thesis, a more common approach is to change the power set-point of the controllers. This will force the wind turbine to operate at a point away from the MPPT curve in Figure 2.2, enabling the power set-point to be instantly increased e.g. for provision of primary frequency control.

### 2.1.2.4  Permanent Magnet Synchronous Generator

The permanent magnet synchronous generator is a simplified version of the synchronous generator, which will be modelled mathematically in Section 2.3.1, where the rotor flux is provided by permanently installed magnets. This means that there is no need for an external excitation current for the rotor flux, which is a major advantage when it comes to both efficiency, reliability and cost[21]. It must however be noted that the cost of the magnetic material for large scale PMSGs can be quite high.

Since the PMSG is a version of the SG the mathematical model is to a large extent the same as for the SG. However, since the flux is created by the permanently installed magnets, $\Psi$ is

introduced as the flux generated by the permanent magnets. The mathematical model used for the PMSG is obtained as follows:

$$e = \Psi \dot{\theta}_e \widetilde{\sin} \theta_e \tag{2.9a}$$

$$T_e = p \Psi \langle i, \widetilde{\sin} \theta_e \rangle \tag{2.9b}$$

$$P_g = \dot{\theta}_e \Psi \langle i, \widetilde{\sin} \theta_e \rangle \tag{2.9c}$$

$$Q_g = -\dot{\theta}_e \Psi \langle i, \widetilde{\cos} \theta_e \rangle \tag{2.9d}$$

Here, $\dot{\theta}_e = \omega_e$ is the electrical speed of the generator which is related to the mechanical speed of the rotor by the number of pole pairs, $p$, in the generator as shown in (2.10).

$$\omega_e = p \omega_m \tag{2.10}$$

The model presented above is based on equations (2.16), (2.18), (2.19a) and (2.19b) which will be more thoroughly discussed in Section 2.3.1.

## 2.2   Power Electronic Converters

*A presentation of the necessary background material related to power electronic converters was included in the specialisation project preceding this thesis. This presentation is deemed valuable also for this thesis, and the presentation from the project report ([5]) is therefore included below in a redrafted version.*

Power electronic converters are used to change the characteristics of a voltage/current to better fit the requirements of a system, and typical converters include rectifiers, inverters and DC-DC converters. Furthermore, power electronic converters are often divided into two parts; the power part and the electronic part.

**The power part** consists of the physical switching devices and electrical components such as diodes, thyristors, capacitors and inductors. For the application discussed in this thesis, the type of semi-conductor used in the power converters is often chosen to be Insulated-Gate Bipolar Transistors (IGBTs) due to their high current and voltage ratings.

**The electronic part** of the power electronic converter consists of the controller in the Digital Signal Processor (DSP), signal condition unit, sensors and Pulse Width Modulation (PWM) drivers[22]. It also contains an Digital to Analog Converter (DAC) and Analog to Digital Converter (ADC), with additional output ports for monitoring purposes. The control system controlling the converter is implemented in the electronic part.

### 2.2.1   Back-to-Back Converters

This thesis will use mainly two types of power electronic converters, namely *rectifiers* and *inverters*. Rectifiers convert AC signals into DC signals, inverters convert signals from DC to AC, and when the two types are operated in series to make an AC-DC-AC connection it is called

back-to-back converters. An example of this is shown in Figure 2.4, where a wind turbine is connected to a grid using back-to-back converters. There exist several variations of converters within these two types, but in this study, only controllable three-phase rectifiers and inverters will be used. The term controllable here means that the output from the converter can be adjusted by applying control signals to the semi-conductors inside the converter, creating any desired frequency and voltage on the output. Such a controlled converter is therefore also often called a Voltage Source Converter (VSC).
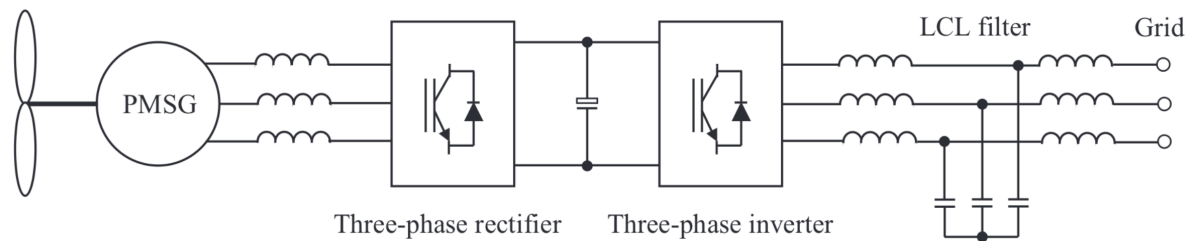


Figure 2.4: Connection of wind power with a Permanent Magnet Synchronous Generator (PMSG), using back-to-back converters[18].

## 2.2.2   The Pulse Width Modulation Technique

The control signals used to control the IGBTs in the power part of the converter are often created by use of the Pulse Width Modulation (PWM) technique. There exist different PWM techniques, and the Sinusoidal Pulse Width Modulation (SPWM) technique is explained here. A comprehensive explanation of the SPWM technique can be found in [23] and [24], but for explanatory reasons, a short introduction is given here.

A modulating signal, hereby called the reference, is compared to a triangular carrier signal having a frequency equal to the switching frequency $f_s$ used in the IGBTs. This generates a sequence of pulses called the drive signals. The frequency of the output voltage will be controlled by the frequency of the reference, and the amplitude of the output voltage will be controlled by the modulation index which is depending on the peak voltage of the reference[24]. The same applies to three-phase systems where three reference voltages are compared to the carrier signal, creating three sets of pulses to drive the three different legs of the converter.

Using a three-phase reference and a triangular carrier signal, the resulting control signals can be seen in Figure 2.5. Note that control signal T1 denotes the control signal for IGBT 1 etc., and that T1 and T4 are linked to phase $a$ and are thus not operating at the same time to avoid short-circuiting the converter. From Figure 2.5 it can be seen that the control signal for T1 is on when phase $a$ of the reference signal exceeds the carrier signal, and off when the carrier signal is higher than the reference signal. The PWM method can be implemented in Simulink using a pre-made 2-level PWM Generator from Mathworks[25].
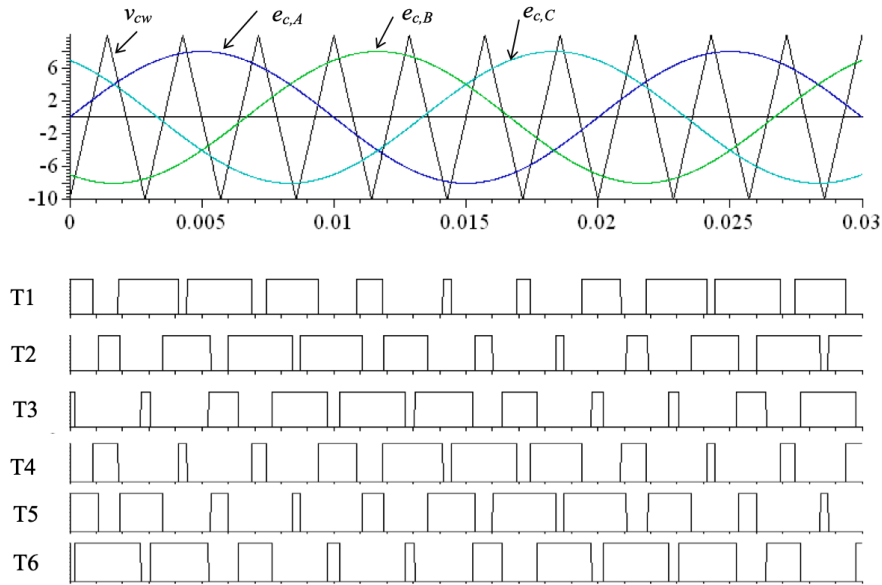
Figure 2.5: A three phase reference signal compared to a triangular carrier signal, and the resulting control signals[26].

## 2.3   Modelling the Synchronous Machine

*The necessary modelling of the Synchronous Machine was presented in the specialisation project preceding this thesis. The modelling method used here remains unchanged and the presentation from the project report ([5]) is therefore included below in its original version.*

To be able to understand the control scheme that will be explained in Chapter 3, the model of a synchronous machine must be described. The mathematical models of a synchronous generator and a synchronous motor have some slight differences, and will therefore be described separately. The topology used for this application will be an idealised three-phase round-rotor machine, meaning that all stator inductances can be considered constant. In addition, a model without damper windings, only one pole pair per phase, and no magnetic saturation effects in the core is assumed[27].

### 2.3.1   Synchronous Generator

A graphic representation of a synchronous generator is depicted in Figure 2.6, and the model outlined here will be the model used in [27]. Since the assumption of an idealised round-rotor machine is made, the air gap is considered to be uniform. The three stator windings are placed in the periphery around the air gap and are regarded as concentrated coils with self-inductance $L$ and mutual inductance $-M$ where $(M > 0)$[27]. Also, the resistance of the windings is denoted $R_s$ while the rotor winding's self-inductance is denoted $L_f$.

The rotor angle $\theta$ varies as the rotor turns, making the mutual inductance between the rotor and the stator windings to vary along with it. $M_f$ is therefore defined as in (2.11) for the three different phases[28].

$$M_{af} = M_f \cos(\theta)$$
$$M_{bf} = M_f \cos(\theta - \frac{2\pi}{3})$$
$$M_{cf} = M_f \cos(\theta + \frac{2\pi}{3})$$

(2.11)

As the generator has three phases equally separated by an angle of $\frac{2\pi}{3}$ it is convenient to define the vectors $\widetilde{\cos}\,\theta$ and $\widetilde{\sin}\,\theta$ in (2.12). Further, the flux linkages of the stator windings $\Phi$, the phase currents $i$, the back-Electromotive Force (EMF) $e$ and the terminal phase voltages $v$ are denoted as in (2.13).

$$\widetilde{\cos}\,\theta = \begin{bmatrix} \cos(\theta) \\ \cos(\theta - \frac{2\pi}{3}) \\ \cos(\theta + \frac{2\pi}{3}) \end{bmatrix}, \qquad \widetilde{\sin}\,\theta = \begin{bmatrix} \sin(\theta) \\ \sin(\theta - \frac{2\pi}{3}) \\ \sin(\theta + \frac{2\pi}{3}) \end{bmatrix}$$

(2.12)

$$\Phi = \begin{bmatrix} \Phi_a \\ \Phi_b \\ \Phi_c \end{bmatrix}, \qquad i = \begin{bmatrix} i_a \\ i_b \\ i_c \end{bmatrix}, \qquad e = \begin{bmatrix} e_a \\ e_b \\ e_c \end{bmatrix}, \qquad v = \begin{bmatrix} v_a \\ v_b \\ v_c \end{bmatrix}$$

(2.13)

In (2.13) we have the following definitions of the specific flux linkages

$$\Phi_a = Li_a - Mi_b - Mi_c + M_{af}i_f$$
$$\Phi_b = -Mi_a + Li_b - Mi_c + M_{bf}i_f$$
$$\Phi_c = -Mi_a - Mi_b + Li_c + M_{cf}i_f$$
$$\Phi_f = M_{af}i_a + M_{bf}i_b + M_{cf}i_c + L_f i_f$$

(2.14)

Note that we have expressions for the rotor, subscript $f$, as well as the stator, subscript $abc$. In a balanced three-phase machine with no neutral line $i_a + i_b + i_c = 0$ holds. In addition $L_s$ is defined as $L_s = L + M$. By taking this into consideration and using (2.12), the flux linkages from (2.14) can be rewritten into equations (2.15a) and (2.15b). Note that $\langle \cdot, \cdot \rangle$ is defined as the conventional inner product, i.e. dot product, of two matrices in $\mathbb{R}^3$.

$$\Phi = L_s i + M_f i_f \widetilde{\cos}\,\theta$$

(2.15a)

$$\Phi_f = L_f i_f + M_f \langle i, \widetilde{\cos}\,\theta \rangle$$

(2.15b)

Now, based on the the explanation above, the back-EMF and the terminal voltage in (2.13) can be defined in (2.16) and (2.17) respectively.

$$e = M_f i_f \dot{\theta} \widetilde{\sin}\,\theta - M_f \frac{di_f}{dt} \widetilde{\cos}\,\theta = M_f i_f \dot{\theta} \widetilde{\sin}\,\theta \,|_{constant\ i_f}$$

(2.16)

$$v = -R_s i - \frac{d\Phi}{dt} = -R_s i - L_s \frac{di}{dt} + e$$

(2.17)

Lastly, the electromagnetic torque generated by the machine is defined as in (2.18).

$$T_e = M_f i_f \langle i, \widetilde{\sin \theta} \rangle \tag{2.18}$$

For the control applications, it will be useful to also define the real and reactive power based on the model outlined above. We therefore define $P$ and $Q$ in equations (2.19a) and (2.19b).

$$P_g = \dot{\theta} M_f i_f \langle i, \widetilde{\sin \theta} \rangle \tag{2.19a}$$

$$Q_g = -\dot{\theta} M_f i_f \langle i, \widetilde{\cos \theta} \rangle \tag{2.19b}$$
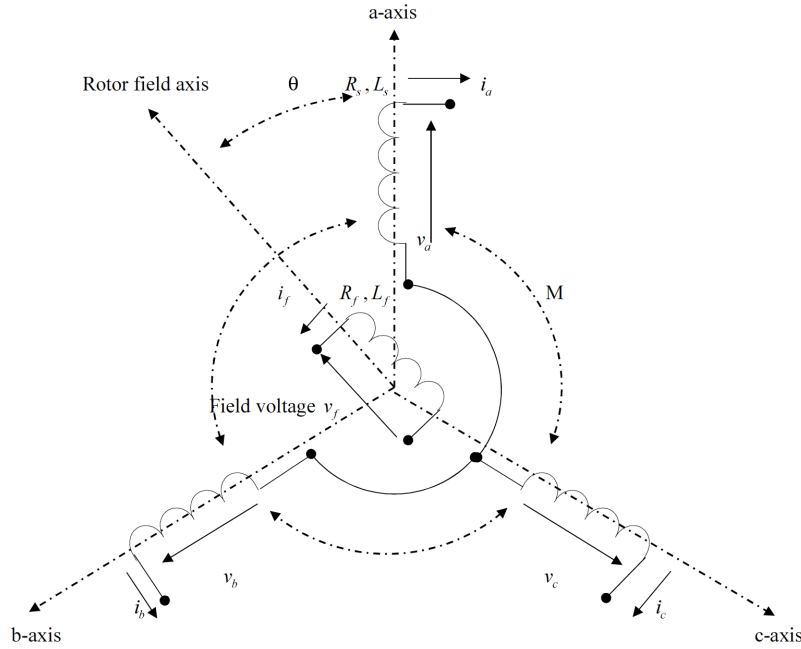


Figure 2.6: Structure of an idealised three-phase round-rotor synchronous generator[29].

## 2.3.2 Synchronous Motor

A graphic representation of a synchronous motor is depicted in Figure 2.7, and as can be seen from this figure, the model of the motor is very similar to the model of the generator in Figure 2.6. More specifically the back-electromotive force in the motor, $e_m$, and the electromagnetic torque in the motor, $T_{me}$, are still calculated based on equations (2.16) and (2.18) respectively[30]. However there are some very important differences that must be pointed out, and the following discussion will follow the model outlined in [31] and [18]. Based on the depicted model in Figure 2.7 let us first define the vector of currents flowing into the motor, $i_r$, and the vector of voltages applied to the motor terminals, $v_r$, as in (2.20).

$$i_r = \begin{bmatrix} i_{ra} \\ i_{rb} \\ i_{rc} \end{bmatrix}, \qquad v_r = \begin{bmatrix} v_{ra} \\ v_{rb} \\ v_{rc} \end{bmatrix} \tag{2.20}$$

We can now, based on the direction of the currents which are now flowing into the machine as opposed to the case with the generator, make the following re-definitions[31];

$$v_r = e + R_s i_r + L_s \frac{d i_r}{dt} \tag{2.21}$$

$$\frac{d\,\omega_e}{dt} = \frac{1}{J}(T_{me} - T_{mm} - D\omega_e) \tag{2.22}$$

where it can be seen from the modified swing equation in (2.22) that the electromagnetic torque and the mechanical torque have switched signs compared to the swing equation that will be further explained in Section 2.4. This means that if the load torque, $T_{mm}$, is higher than the electromagnetic torque $T_{me}$ the motor will slow down. The active and reactive powers are still calculated based on (2.19a) and (2.19b), however now with the current as defined in this section[30]. This will result in a negative injected power calculated by (2.19a), i.e. power is consumed by the motor.
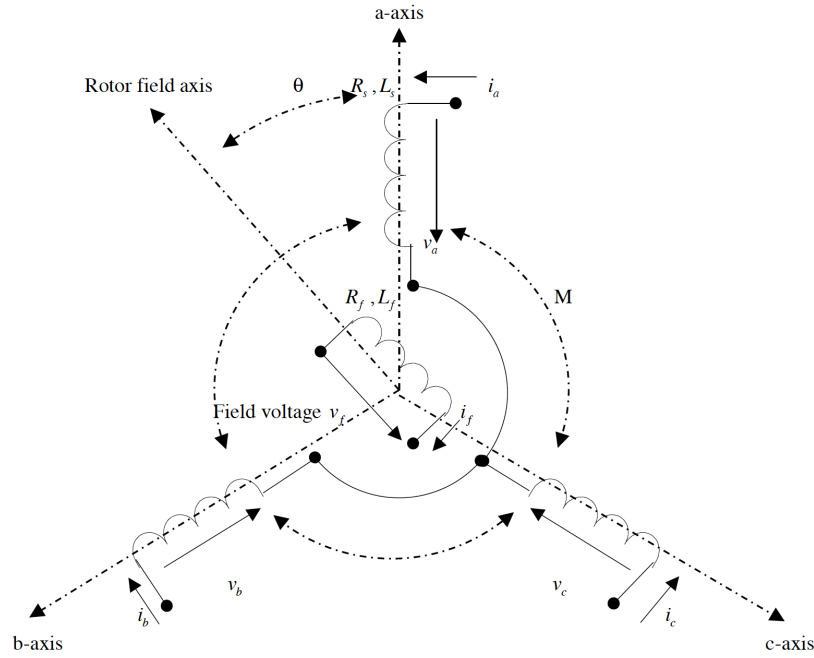


Figure 2.7: Structure of an idealised three-phase round-rotor synchronous motor[29].

## 2.4   The Swing Equation

A thorough introduction to the swing equation is given in [32], and the explanation here will follow that introduction. The explanation will be related to a normal synchronous machine so that the swing equation can be easily modified and adapted to the virtual synchronous machine. A typical synchronous generator is driven by a turbine through a shaft. This shaft is typically called the drive train, and assuming free-body rotation where the turbine and generator inertia move together, the shaft can be modelled a rigid. Using the assumption of a rigid, ideally stiff shaft, the turbine, drive train, and generator can be modelled as a single mass model[33], and the sum of the individual inertias can be regarded as one inertia $J$. The turbine-generator system can thus be treated as one unit, and any unbalance in the applied torques on the rotor shaft will lead to a dynamic following Newton's second law in (2.23).[32]

$$J\frac{d\,\omega_m}{dt} + D_d\,\omega_m = \tau_t - \tau_e \tag{2.23}$$

Newton's second law relates the rate of change of rotational speed, $\omega_m$, to the balance between the torque from the turbine, $\tau_t$, and the electrical torque from the generator, $\tau_e$, taking into account

the dampening torque coefficient $D_d$ and the moment of inertia $J$[34]. During synchronous operation, the speed is equal to the synchronous speed and the torques are in balance, i.e.

$$\omega_m = \omega_{sm} \qquad \tau_t = \tau_e + D_d\,\omega_{sm} \qquad \tau_m = \tau_t - D_d\,\omega_{sm} = \tau_e$$

where $\tau_m$ is the net mechanical torque applied to the shaft when subtracting rotational losses during synchronous operation. The rotor position can be defined based on a synchronously rotating reference frame so that the rotor angle $\delta_m$ denotes the angle of the rotor with respect to the rotating reference frame.

$$\omega_m = \omega_{sm} + \Delta\omega_m = \omega_{sm} + \frac{d\delta_m}{dt} \tag{2.24}$$

Equation (2.24) can then be deduced and inserted into (2.23) yielding (2.25). Note that $\Delta\omega_m = \omega_m - \omega_{sm} = \frac{d\delta_m}{dt}$ is the speed deviation of the shaft from the synchronous speed. Equation (2.25) can again me modified to include the powers instead of the torques using that $P = \omega\tau$ and that $\omega_m \approx \omega_{sm}$. Multiplying both sides of (2.25) with $\omega_{sm}$ and rearranging thereby results in the well known *swing equation* governing rotor dynamics in (2.26). Note that $M_m = J\omega_{sm}$ is the angular momentum of the rotor at synchronous speed, $D_m = \omega_{sm}D_d$ is the dampening coefficient, and $P_m$ and $P_e$ are the net mechanical power input to the generator and the electrical air-gap power respectively.

$$J\frac{d^2\delta_m}{dt^2} + D_d\frac{d\delta_m}{dt} = \tau_m - \tau_e \tag{2.25}$$

$$M_m\frac{d^2\delta_m}{dt^2} = P_m - P_e - D_m\frac{d\delta_m}{dt} \tag{2.26}$$

The angle and speed used for the swing equation in (2.26) are related to the mechanical properties. However, as the mechanical and electrical properties of angle and speed are connected trough the number of pole pairs $p$ in the generator, the power angle $\delta$ and angular speed $\omega$ can also be expressed in electrical radii and radii per second respectively.

## 2.5   Virtual Synchronous Machines

The concept of Virtual Synchronous Machines is relatively new in the energy industry and revolves around controlling power electronics to emulate the behaviour of the conventional synchronous machine with all the inherent benefits related to inertia, drooping, synchronisation and voltage regulation. The VSM was first proposed in [35], [36] and has later been the subject to a large amount of research, leading also to the introduction of the Synchronverter VSM in [28]. With this further research, even control systems based on the induction machine have been proposed to ease the integration of power electronics into the conventional power grid[37], and VSMs are now likely to be dominating the future grid consisting of a large share of converter connected generation.

Several different versions of VSMs exist in the literature, and a thorough examination is given in [38]. The main difference lies in the mathematical model used, additional control loops, and the order of the model, which all have different pros and cons. As pointed out in [38] a low-order

VSM algorithm is more stable than a high-order VSM algorithm, partially due to the possibility of numerical instability.

Also, VSMs and droop controlled converters share many of the same characteristics, as the idea behind droop control is to emulate the drooping function of the conventional SG. As such, many studies have been devoted to comparing the VSM to droop control. Reference [39] points out that the VSM has a larger inertia than droop control and therefore better frequency stability, but that a delay in the virtual governor of the VSM reduces the inertia and amplifies oscillation. Therefore, [39] proposed an inertial droop control that inherits the advantages of conventional droop control, and in addition provides inertia support for the system. Furthermore, the comparison and examination of both a VSM and droop control is treated extensively in [8], where two technical routes, one based on the Synchronverter technology and the other based on the robust droop control technology, are investigated.

However, as pointed out in [40], also VSM-controlled Voltage Source Converters are prone to angular instability. Furthermore, it is concluded that when the DC link voltage was constant, VSM-controlled voltage source inverters had the same angle stability criterion as conventional SGs, making the study carried out in this thesis even more relevant. The VSM under investigation in this thesis will be presented in Chapter 3.

## 2.6   Differential Equations of Dynamical Systems

To fully grasp the extent of the analysis that is to be carried out in this thesis, a theoretical foundation related to mathematical modelling of dynamical systems is required. This is because power systems are inherently dynamical systems that can be modelled using many of the same concepts as any other dynamical system. Generally, the dynamic of a system can be described by a set of differential equations normally represented as[41]

$$\frac{d}{dt}\boldsymbol{x}(t) = \dot{\boldsymbol{x}} = f(\boldsymbol{x}) \tag{2.27}$$

In (2.27) $\boldsymbol{x}$ is the state vector, i.e. the vector containing the state variables, $\dot{\boldsymbol{x}}$ is its derivative and $f$ is a vector-valued function. The dimension of $\boldsymbol{x}$ is given by the number of state variables $n_x$, and as $\boldsymbol{x}$ belongs to the Euclidean space $R^{n_x}$ we have that $f : \mathcal{D} \to R^{n_x}$ is a function that is both continuous and has continuous first-order partial derivatives with respect to $\boldsymbol{x}$ on the domain $\mathcal{D} \subset R^{n_x}$ into $R^{n_x}$[34]. The set of differential equations can be solved, yielding the solution $\boldsymbol{x}$(t). When solving differential equations, knowing the initial states of the state variables is of importance. The initial states are denoted $\boldsymbol{x}(t_0)$ where $t_0$ is the initial time.

Based on the above defined dynamical system, further important clarifications can be made. First, an equilibrium point (e.p.) can be defined as any point $\boldsymbol{x}_0$ yielding $\dot{\boldsymbol{x}} = f(\boldsymbol{x}_0) = 0$. If, at any time, the system has settled at an equilibrium point, the system is defined to be in *steady-state*. Opposite, if $\dot{\boldsymbol{x}} = f(\boldsymbol{x}) \neq 0$, the system is defined to be in a *dynamic state*.

Furthermore, equilibrium points can be divided into stable and unstable equilibrium points. It is therefore necessary to have methods that identify whether an e.p. is stable or not. A well-known framework for stability analysis of equilibrium points is the Lyapunov framework[42]. This framework includes mainly three different methods of characterising the stability of an e.p., each of which will be explained her based on the derivations given in [34], [43] and [42].

### 2.6.1   Stability in the Sense of Lyapunov

An equilibrium point (e.p.) can be said to be stable in the sense of Lyapunov, and thus defined as an stable equilibrium point (s.e.p.), if the solutions of the system starting in the vicinity of the e.p. will continue to exist in the direct vicinity of the e.p. at all times. This definition can be described mathematically using the notation for initial states and equilibrium points as follows.

The equilibrium point $\boldsymbol{x}_0$ is stable if, for each $\epsilon > 0$ there can be found a $\gamma = \gamma(\epsilon) > 0$ so that

$$||\boldsymbol{x}(t_0) - \boldsymbol{x}_0|| < \gamma \qquad \Rightarrow \qquad ||\boldsymbol{x}(t) - \boldsymbol{x}_0|| < \epsilon \qquad , \qquad \forall t \geq t_0$$

A graphic interpretation of stability in the sense of Lyapunov is depicted in Figure 2.8[34].
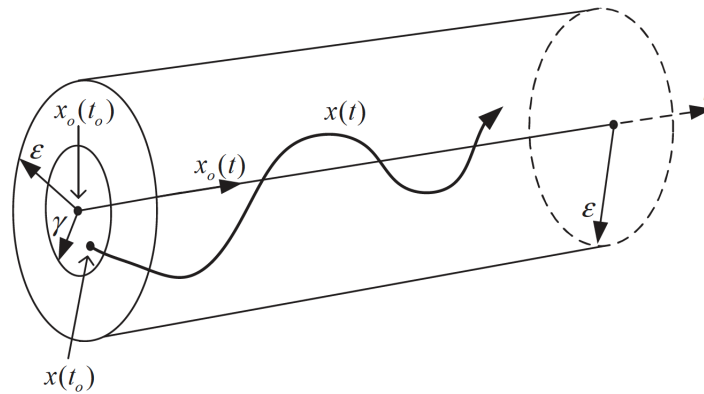


Figure 2.8: A stable equilibrium point $\boldsymbol{x}_0$ in the sense of Lyapunov[34].

Moreover, the e.p. can also be asymptotically stable, meaning the solutions converge to the e.p as time goes to infinity. This can be mathematically described using the following method:

The equilibrium point $\boldsymbol{x}_0$ is asymptotically stable if stability has been proven as described above, and in addition, it is possible to choose $\gamma$ so that

$$||\boldsymbol{x}(t) - \boldsymbol{x}_0|| \to 0 \quad as \quad t \to \infty$$

A graphic interpretation of asymptotic stability is depicted in Figure 2.9[34].
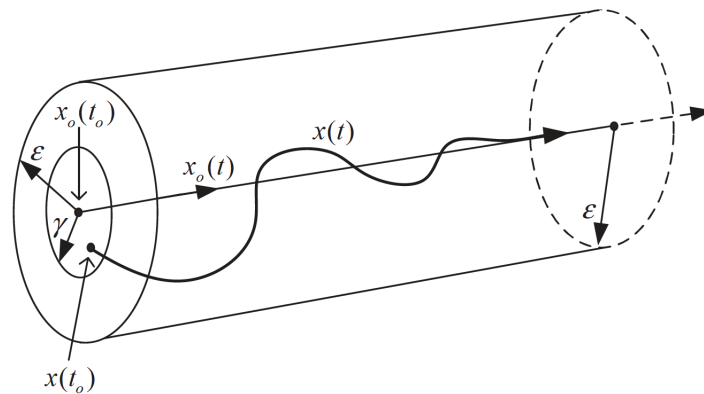


Figure 2.9: An asymptotically stable equilibrium point $\boldsymbol{x}_0$ in the sense of Lyapunov[34].

Otherwise, if the equilibrium point is not stable, the equilibrium point is unstable, and defined as an unstable equilibrium point (u.e.p.)[42].

## 2.6.2 Lyapunov's Indirect Method

The next method of analysing the stability of an equilibrium point $x_0$ belonging to the system in (2.27) is based on Lyapunov's indirect method. Lyapunov's indirect method utilises linearization of the non-linear system equations around $x_0$ so that (2.27) can be rewritten as in (2.28).

$$\Delta\dot{x} = A\Delta x \tag{2.28}$$

In (2.28) $A$ is the state matrix, and using (2.27) it can be found that $A = \left[\frac{\partial f(x)}{\partial x}\right]$. By further developing this insight the general expression in (2.29) is obtained, where the system is linearized around its equilibrium point $x_0$.

$$A = \left[\frac{\partial f(x)}{\partial x}\right]_{x=x_0} = \begin{bmatrix} \frac{\partial f_1}{\partial x_1} & \cdots & \frac{\partial f_1}{\partial x_{n_x}} \\ \vdots & \ddots & \vdots \\ \frac{\partial f_{n_x}}{\partial x_1} & \cdots & \frac{\partial f_{n_x}}{\partial x_{n_x}} \end{bmatrix}_{x=x_0} \tag{2.29}$$

Lyapunov's indirect method revolves around analysing the Eigenvalues of the state matrix $A$ to check if they belong to the stable domain. The Eigenvalues $\lambda$ of $A$ can be found using (2.30), where $I$ is the identity matrix.

$$|A - \lambda I| = 0 \tag{2.30}$$

$x_0$ is then characterised as asymptotically stable if all Eigenvalues $\lambda$ have negative real parts, i.e. $\Re(\lambda) < 0$ for all $\lambda$. Opposite, if any $\lambda$ has a positive real part, the equilibrium point is unstable. It is from these definitions evident that if a complex Eigenvalue has a real part equalling zero, other methods are more suitable to determine the stability of the e.p., leading to Lyapunov's direct method which will be explained next.

## 2.6.3 Lyapunov's Direct Method

Lastly, the stability of an equilibrium point $x_0$ belonging to the system in (2.27) can be determined based on Lyapunov's direct method. The direct method revolves around analysing a *Lyapunov function*, which is a continuously differential scalar function that satisfies a set of conditions. Let us denote this function as $\mathcal{V}(x)$. The equilibrium point $x_0$ is then stable if[34], [42]

1. $\mathcal{V}(x_0) = 0$

2. $\mathcal{V}(x) > 0$ for all $x \in \mathcal{D}$, except at $x_0$

3. $\dot{\mathcal{V}}(x) = \frac{\partial\mathcal{V}(x)}{\partial x} \cdot f(x) \leq 0$ for all $x \in \mathcal{D}$

Moreover, $x_0$ can be said to be asymptotically stable if the conditions above hold and condition 3 is further restricted, yielding conditions 4/5, i.e. $x_0$ is stable if conditions 1, 2, and 3 holds, and asymptotically stable if conditions 1, 2, and 4/5 holds.

4. $\dot{\mathcal{V}}(\boldsymbol{x}) < 0$ for all $\boldsymbol{x} \in \mathcal{D}$ except at $\boldsymbol{x}_0$ where $\dot{\mathcal{V}}(\boldsymbol{x}_0) = 0$

5. $\dot{\mathcal{V}}(\boldsymbol{x}) \leq 0$ as long as $\dot{\mathcal{V}}(\boldsymbol{x})$ is not 0 on any $\boldsymbol{x} \in \mathcal{D}$ except at $\boldsymbol{x}_0$.

Lyapunov's direct method of stability is heavily used in determining the stability of power systems, and one of the methods used to assess the stability of the Virtual Synchronous Machine (VSM) in this thesis will be based on the direct method. This will be further explained in Chapter 4.

## 2.7  Introduction to Power System Stability

Today's society is to a large extent dependent on the continued supply of electricity to uphold critical functions. However, the nature of electricity and related costs make it difficult to store electricity in large quantities, thus making the balance between generation and demand vital. Transmission System Operators (TSOs) are therefore continuously assessing the robustness of the power system by performing mainly two different types of analysis.

***Static*** analysis revolves around analysing the system during normal operation. This includes making sure that the system is operating within certain constraints to avoid overloading components[34].

***Dynamic*** analysis revolves around analysing the power system's dynamic response to a disturbance[34], and it is this type of analysis that will be the focus here.

The modern electric power system is often regarded as the largest, most complex machine ever created. By interconnecting different components over a large geographical area, the system generates, transmits and distributes electricity to end-users, maintaining a real-time balance between production and generation. Such a complex structure is prone to experience several dynamic interactions, and a good understanding of how the power system behaves when exposed to a contingency is therefore crucial to the system operator[34]. How the system behaves will depend on both the nature of the disturbance and the initial operating conditions of the system. While most instabilities are caused by large disturbances, such as tripping of large generators or short-circuit faults, the system is also continuously experiencing small disturbances in the form of load variations.[5]

To obtain a good understanding of how disturbances affect the operating conditions, an analysis of the *power system stability* where the dynamics are studied is necessary. To further explain the meaning of power system stability the definition put forward by the IEEE/CIGRE Joint Task Force in [43] can be used:

> *"Power system stability is the ability of an electric power system, for a given initial operating condition, to regain a state of operating equilibrium after being subjected to a physical disturbance, with most system variables bounded so that practically the entire system remains intact."*[43]

It can be argued that the concept of power system stability for all intentional purposes can be condensed down to one single problem. However, due to the large variety and complexity of possible instabilities that can occur, the concept cannot be treated as such. It is therefore necessary to make appropriate simplifications and assumptions so that any given problem can be dealt with using the appropriate degree of detail when creating the mathematical system model. The IEEE/CIGRE Task Force therefore divides power system stability into *rotor angle stability, frequency stability* and *voltage stability* to better facilitate stability analysis, identification of key

factors causing instabilities, and improvement of stability. This categorisation is done based on the simplifications, devices and processes, time frame, size of disturbance and detail necessary to investigate the different stability phenomena.

***Rotor angle stability*** is concerned with the ability of a synchronously connected machine to remain in synchronism with the system both in steady-state and after a contingency. The mechanism governing this type of stability is the equilibrium between mechanical- and electromagnetic torque, and a detailed overview will be given in Section 2.8.

***Frequency stability*** is concerned with the ability of a power system to maintain a steady frequency after being subjected to a contingency resulting in a significant imbalance between generation and load. The power system frequency is the real-time frequency of the AC voltage/current and is an appropriate indicator of the balance between active power generation and consumption including losses. As long as this balance is kept level, the frequency will remain constant. The mechanism governing this type of stability is the ability to restore equilibrium between system generation and load with minimum unintentional loss of load.

***Voltage stability*** is concerned with the ability of a power system to maintain the nominal voltage at any given bus in the system both in steady-state and after a contingency, given a set of initial operating conditions. The mechanism governing this type of stability is the equilibrium between load demand and load supply.

Further sub-classifications as defined by the Task Force are shown in Figure 2.10.
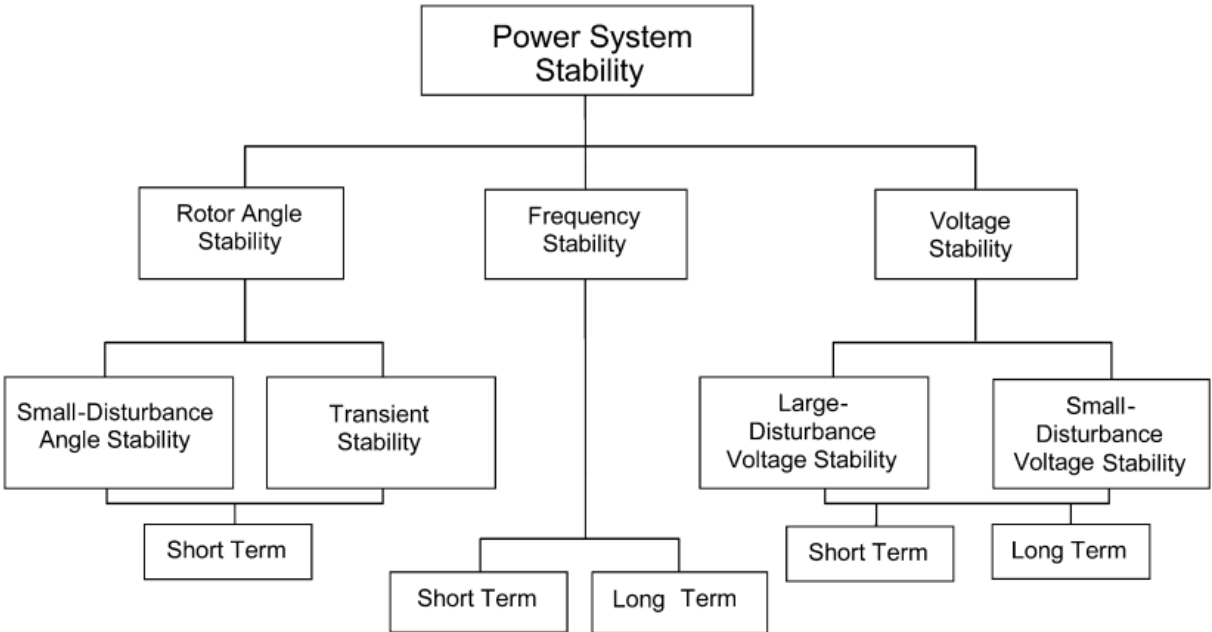


Figure 2.10: Classification of stability based on IEEE/CIGRE Joint Task Force[43].

As mentioned above, it is common to adopt analytical, mathematical models to analyse the system dynamic response, and the categorisation makes it easier to derive the appropriate model for the specific dynamic response that is investigated. It is however important to note that a contingency in many cases eventually will trigger the dynamics of all three categories, even though these are not covered by the model used in the stability analysis. The differentiation related to mathematical models is therefore only a tool to ease the analysis that is to be performed.

## 2.8    Rotor Angle Stability

In this thesis, the main focus will be on the rotor angle stability, defined in by the IEEE/CIGRE Task Force as:

> *"Rotor angle stability refers to the ability of synchronous machines of an interconnected power system to remain in synchronism after being subjected to a disturbance. It depends on the ability to maintain/restore equilibrium between electromagnetic torque and mechanical torque of each synchronous machine in the system. The instability that may result occurs in the form of increasing angular swings of some generators leading to their loss of synchronism with other generators."*[43]

By the definition above it is evident that the instability can both be due to the loss of synchronism between one specific machine and the rest of the synchronised system, or between separate groups of machines that are synchronised within their respective groups but where the groups have lost synchronism with other groups[34]. The study of rotor angle stability is in its essence a study of the electromechanical oscillations that can occur in grid-connected machines, and the key factor of interest is how the power output and rotor angle of the machine are connected. This will be further explained in Section 2.8.2.

As seen from Figure 2.10, rotor angle stability is divided further into *Small-disturbance/small-signal rotor angle stability* and *Large-disturbance/transient rotor angle stability*. Small-signal stability has to do with the ability to remain in synchronism after being subject to a small disturbance. For a disturbance to be considered as small, it should be possible to adequately carry out a stability analysis using a linearized system model[44].

Transient stability analysis examines the system's ability to remain in synchronism after a large disturbance. Such faults often yield large fluctuations in the rotor angle of generators, and the ability of a generator to maintain in synchronism with the system is largely influenced by the initial operating conditions and severity of the fault. Common for both small-signal and transient rotor angle stability is that they are studied as short term phenomena, having a period of interest between a few milliseconds up to a few seconds following the disturbance.

### 2.8.1    Root Causes for Rotor Angle Instability

The typical root causes to rotor angle instability depend on whether small-signal stability or transient stability is of interest. Two situations often resulting in what can be categorised as small disturbances are lack of synchronising torque and insufficient damping torque. These disturbances often manifest themselves through increased non-oscillatory rotor angle or rotor oscillations with increasing amplitude[43]. However, increased use of continuously working Automatic Voltage Regulators (AVRs) has almost eliminated the non-oscillatory instability problem, leading to insufficient damping of oscillations being the major concern in small-signal stability. However, AVRs may in certain cases also deteriorate the stability of the system, and a common solution to this problem is the use of a Power System Stabiliser (PSS) as an added input to the AVR system.

For large disturbances, the recurring issues of short circuit faults and tripping of transmission lines are the dominating instability causes. Short circuit faults are often divided into different types based on the nature of the fault, and the different types of faults have different severity. Most severe is the balanced three-phase-to-ground fault, but also faults such as two-phase-to-ground, phase-to-phase and single-phase to ground are serious threats to system stability. These

large disturbances almost always manifest themselves as instability in the form of aperiodic angular separation and thus first swing instability. This is due to insufficient synchronising torque[43].

## 2.8.2   Power-Angle Curve and Swing Equation Analysis

Until now, dynamic systems and equilibrium points have been discussed on a general basis. This theory will now be applied to power systems. From Section 2.4 it became evident that the equation governing the rotor dynamics is given by (2.26). This equation will now be further investigated for the simple Single-Machine-Infinite-Bus (SMIB) system depicted in Figure 2.11, and the variables will now belong to the electrical domain, i.e. angle and speed of the generator. In Figure 2.11 the synchronous generator is modelled as a constant back-EMF behind its impedance.
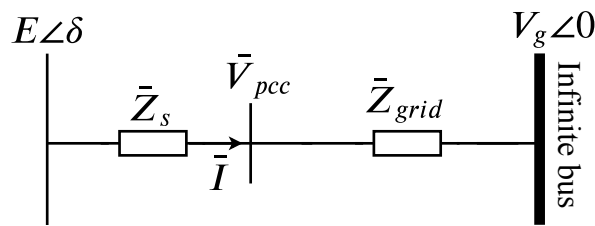


Figure 2.11: Example Single-Machine-Infinite-Bus system.

Here, $E$ is the amplitude of the generator back-EMF, $\delta$ is the angle of the generator with respect to a rotating reference frame, $\bar{I}$ is the injected current, $\bar{Z}_s = R_s + jx_s$ is the impedance containing the resistance of the generator windings and the synchronous reactance, $\bar{V}_{pcc}$ is the voltage at the Point of Common Coupling (PCC), $\bar{Z}_{grid} = R_g + jX_g$ is the grid impedance and $V_g$ is the grid voltage amplitude with its angle set to zero due to being used as reference. The total impedance can thus be defined as $\bar{Z}_{tot} = \bar{Z}_s + \bar{Z}_{grid} = R_{tot} + jX_{tot}$ with amplitude $Z_{tot} = |\bar{Z}_{tot}|$. When all these quantities are known, the active and reactive powers delivered by the machine can be calculated using (2.31a) and (2.31b) respectively[45].

$$P_e = \left(\frac{E}{Z_{tot}}\right)^2 R_{tot} + \frac{E V_g}{Z_{tot}} \sin\left(\delta - \arctan\left(\frac{R_{tot}}{X_{tot}}\right)\right) \tag{2.31a}$$

$$Q = \left(\frac{E}{Z_{tot}}\right)^2 X_{tot} - \frac{E V_g}{Z_{tot}} \cos\left(\delta - \arctan\left(\frac{R_{tot}}{X_{tot}}\right)\right) \tag{2.31b}$$

Equation (2.31a) represents the power-angle characteristic of the generator, and assuming constant back-EMF and grid voltage, the power-angle characteristic becomes strictly a function of $\delta$. A typical power-angle characteristic is depicted in Figure 2.12, and this depiction will now be used to explain the equilibrium points of the system by looking more closely at the swing equation. Substituting $P_e = P_e(\delta)$ into (2.26) yields (2.32).

$$M_m \frac{d^2 \delta_m}{dt^2} = P_m - P_e(\delta) - D_m \frac{d\delta_m}{dt} \tag{2.32}$$

It is known that during steady-state operation, the power system is in equilibrium. It is also known that during steady-state the generator is operating at the synchronous speed meaning

both of the derivative parts in (2.32) can be set to zero. This reveals that when operating at the equilibrium, the mechanical power and electrical power must be identical, i.e. $P_m = P_e(\delta)$.

Assuming constant mechanical power applied to the generator, the mechanical power can be plotted along with the electrical power-angle characteristic in Figure 2.12. Here, the maximum value of $P_e(\delta)$ is denoted the critical power $P_{e,cr}$ having a corresponding critical angle $\delta_{cr}$. Using the power-angle characteristic, the equilibrium points of the system can be easily identified, and three possible scenarios depending on the mechanical power become evident.
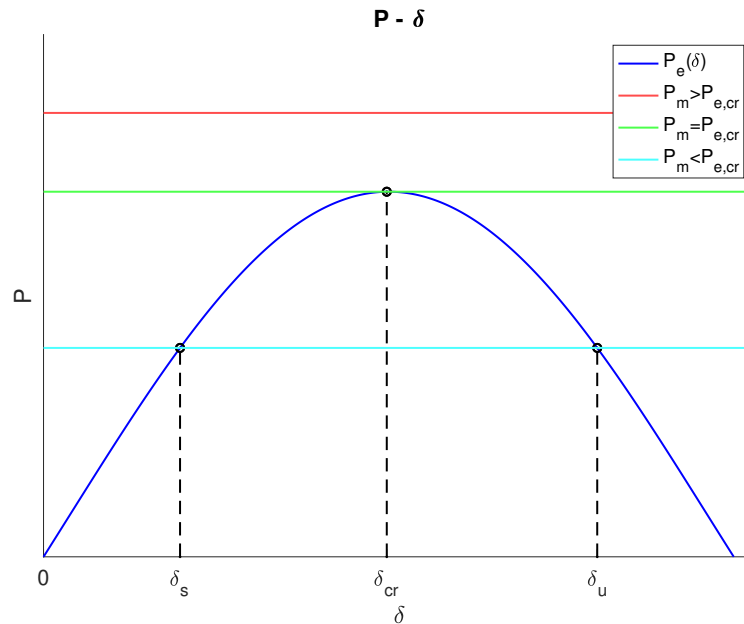


Figure 2.12: Power-Angle curve for the SMIB system based on eq. (2.31a)

1. $P_m > P_{e,cr}$ yields no intersections between the mechanical and electrical powers meaning no equilibrium points exist.

2. $P_m = P_{e,cr}$ yields exactly one intersection between the mechanical and electrical powers meaning one equilibrium point exists at the angle $\delta_{cr}$.

3. $P_m < P_{e,cr}$ yields two intersections between the mechanical and electrical powers meaning two equilibrium points exist at the angles $\delta_s$ and $\delta_u$ .

During normal operation, situation 3 is most common and will therefore be investigated further to determine the stability of the two equilibrium points $\delta_s$ and $\delta_u$. This can be done mathematically using any of the elaborated Lyapunov methods, but can also be explained visually using Figure 2.13 to facilitate a better understanding of the physical system.

Assume that the power system operates at $\delta_s$ and then experience a contingency causing a shift in $\delta$ from $\delta_s$ to $\delta_1$. At $\delta_1$ we have $P_e < P_m$ causing the system to enter the dynamic state with dynamics governed by the swing equation. According to the swing equation, the generator will then speed up, increasing the rotor angle $\delta$ back to $\delta_s$.

Opposite, if the system experience a contingency causing a shift in $\delta$ from $\delta_s$ to $\delta_2$. we have $P_e > P_m$. According to the swing equation, the generator will then decelerate, decreasing the rotor angle $\delta$ back to $\delta_s$. As the angle moves towards $\delta_s$, the powers re-enter equilibrium. It should be noted that if there were no damping in the system, the rotor angle would enter periodic

oscillating swings around the equilibrium point, i.e. the e.p. $\delta_s$ is stable, while if damping is present the rotor angle will settle back to the equilibrium point, i.e. the e.p. $\delta_s$ is asymptotically stable.

Now assume that the power system operates at $\delta_u$ and then experience a contingency causing a shift in $\delta$ from $\delta_u$ to $\delta_3$. Again $P_e > P_m$ and according to the swing equation the generator will then decelerate, decreasing the rotor angle $\delta$. However, as can be seen in Figure 2.13, decreasing the rotor angle from $\delta_3$ moves the operating point away from the e.p. $\delta_u$.

Opposite, assuming that the power system operates at $\delta_u$ and then experience a contingency causing a shift in $\delta$ from $\delta_u$ to $\delta_4$ yields $P_e < P_m$. According to the swing equation the rotor will accelerate, increasing $\delta$, which again moves the operating point away from the e.p. $\delta_u$. It can therefore be concluded that the e.p. $\delta_u$ is an unstable equilibrium point (u.e.p.).
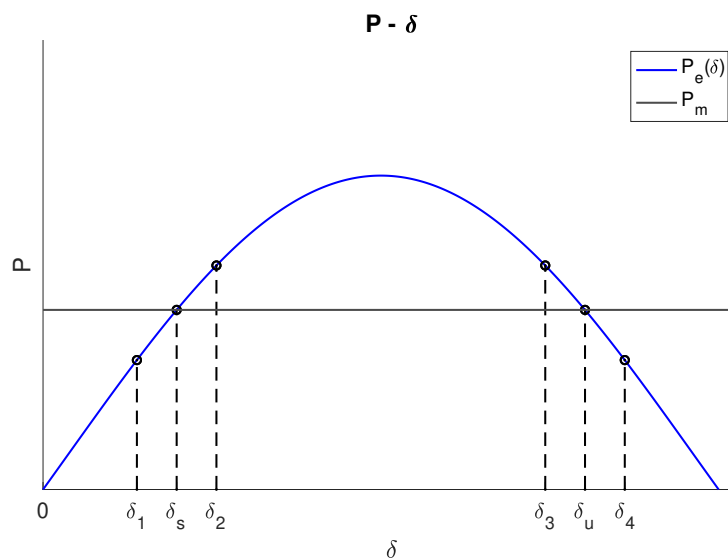


Figure 2.13: Power-angle curve showing small deviations in $\delta$.

### 2.8.3   Stability Analysis Methods for Power System Applications

Several different methods exist for analysing the stability of power systems. Firstly, a division between numerical simulation and analytical formulation can be made[46]. Numerical simulation is known to be time-consuming, but will in most cases yield the most accurate result, while analytical formulations render possible the use of much faster methods of determining the stability of the system. Furthermore, analytical models can be sub-divided into average models and discrete-time models, where average models are most common today.

Depending on the scope of the analysis that is to be carried out, the domain of the analysis will vary. For small-signal stability, the use of frequency-domain based methods such as Eigenvalue analysis, impedance-based analysis using Nyquist and transfer function based analysis are commonly used. For large disturbances, the use of time-domain based methods such as state-space modelling, Lyapunov's indirect and direct method and bifurcation analysis are commonly used, but these methods are also applicable for small-signal analysis[46]. In this thesis, what is commonly referred to as classical stability analysis will be used. This includes the time-domain based Lyapunov method, but also an analysis of the $P - \delta$ curve introduced above. Also numerical simulation will be adopted, and the stability analysis will be explained in detail in Chapter 4.

# The Synchronverter Control Technique

*This chapter models the Synchronverter VSM control technique for both inverter control and rectifier control. Also, the system topology is described in detail. As the thesis revolves around analysing the transient stability of the Synchronverter control system adopted for a WECS in the specialisation project, the chapter is included in its entirety from [5], except for Section 3.1.5 which was added during the thesis work.*

## 3.1 Grid Side - Inverter Control strategy

The Synchronverter control technology is based on the mathematical model of a synchronous machine, and a Synchronverter is thus defined in [27] and [28] as a converter that mimics a synchronous machine. It is therefore considered as a way of implementing a Virtual Synchronous Machine. The power part of a typical three-phase inverter is depicted in Figure 3.1, where the inverter is connected to a stiff grid.
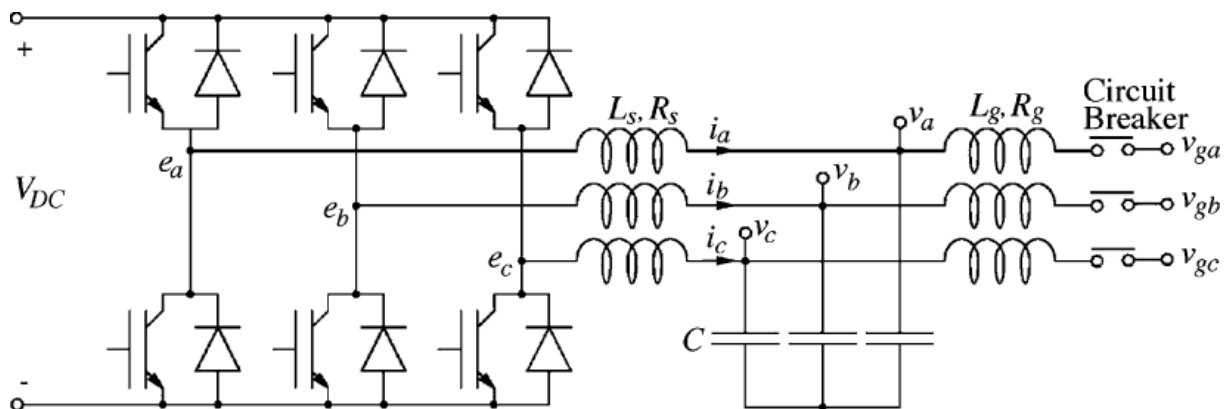


Figure 3.1: Power part of a typical controllable inverter[27].

From Figure 3.1 it can be seen that $L_s$ and $R_s$ represents the inductance and resistance of the stator windings of the imaginary synchronous generator[27]. This means that the terminal voltages of the Synchronverter VSM are the capacitor voltages in Figure 3.1, and the output of the actual inverter will represent the back-Electromotive Force (EMF) $e$ of the VSM due to the imaginary rotor movement. $L_s$ and $C$ in additions functions as a filter to attenuate ripples due to the PWM switching.

The Synchronverter controller is located in the electronic part of the power electronic converter, where the mathematical model used is derived in Section 2.3.1. More specifically equations (2.16), (2.18) and (2.19b) will constitute the core of the controller along with the swing equation[27]. Ultimately the control system will generate the reference for the PWM signals used to control the physical IGBTs in the power part of the converter. The objective of the grid side converter is to inject the correct amount of power to the grid when taking into account both the MPPT set-point from the turbine and the grid voltage and frequency. This should be achieved for the entire operating range of the wind turbine.

The control topology of the grid side controller in the Laplace domain is depicted in Figure 3.2. As can be seen, the inputs to the controller are the active power reference $P_{ref}$, the reactive power reference $Q_{ref}$, the converter current $i_{c,grid}$, and the voltage $v_{pcc}$, which will be the voltage at the Point of Common Coupling (PCC). When the Synchronverter is utilised in a WECS, $P_{ref}$ will be set by the MPPT of the turbine and thus follow (2.8) which gives the maximum power delivered by the wind turbine for a given wind speed. Usually, the power reference is set slightly below maximum to account for losses[30]. It is also possible to operate the turbine in a de-rated mode and thus further decrease the power set-point to an even lower percentage of the MPPT.

$P_{ref}$ is divided by the nominal speed of the system, $\omega_n$, to obtain the mechanical torque reference. Note that $\omega_n$ can be used in this division instead of the virtual frequency of the converter $\omega$ as the relative difference between them is negligible[27]. $Q_{ref}$ can be set based on the operator's needs, making the utility achieve reactive power support if needed. $i_{c,grid}$ and $v_{pcc}$ are obtained through measurements using sensors. For easy interpretation of the control system depicted in Figure 3.2, the equations constituting the core of the controller are repeated here, using that the number of pole pairs in the imaginary machine is 1:

$$\dot{\omega} = \frac{1}{J}(T_m - T_e - D_p\omega) \tag{3.1a}$$

$$e = M_f i_f \omega \widetilde{\sin}\theta \tag{3.1b}$$

$$T_e = M_f i_f \langle i_{c,grid}, \widetilde{\sin}\theta \rangle \tag{3.1c}$$

$$P = \omega M_f i_f \langle i_{c,grid}, \widetilde{\sin}\theta \rangle \tag{3.1d}$$

$$Q = -\omega M_f i_f \langle i_{c,grid}, \widetilde{\cos}\theta \rangle \tag{3.1e}$$

### 3.1.1   Active Power Control and Frequency Droop

It is clear that the controller consists of two control channels; one for the active power and one for the reactive power[29]. The Active Power Loop (APL) is the upper loop in Figure 3.2 and is governed by the swing equation using the mechanical torque reference, electrical torque and drooping torque. The mechanical torque reference is calculated as

$$T_{m,ref} = \frac{P_{ref}}{\omega_n} \tag{3.2}$$
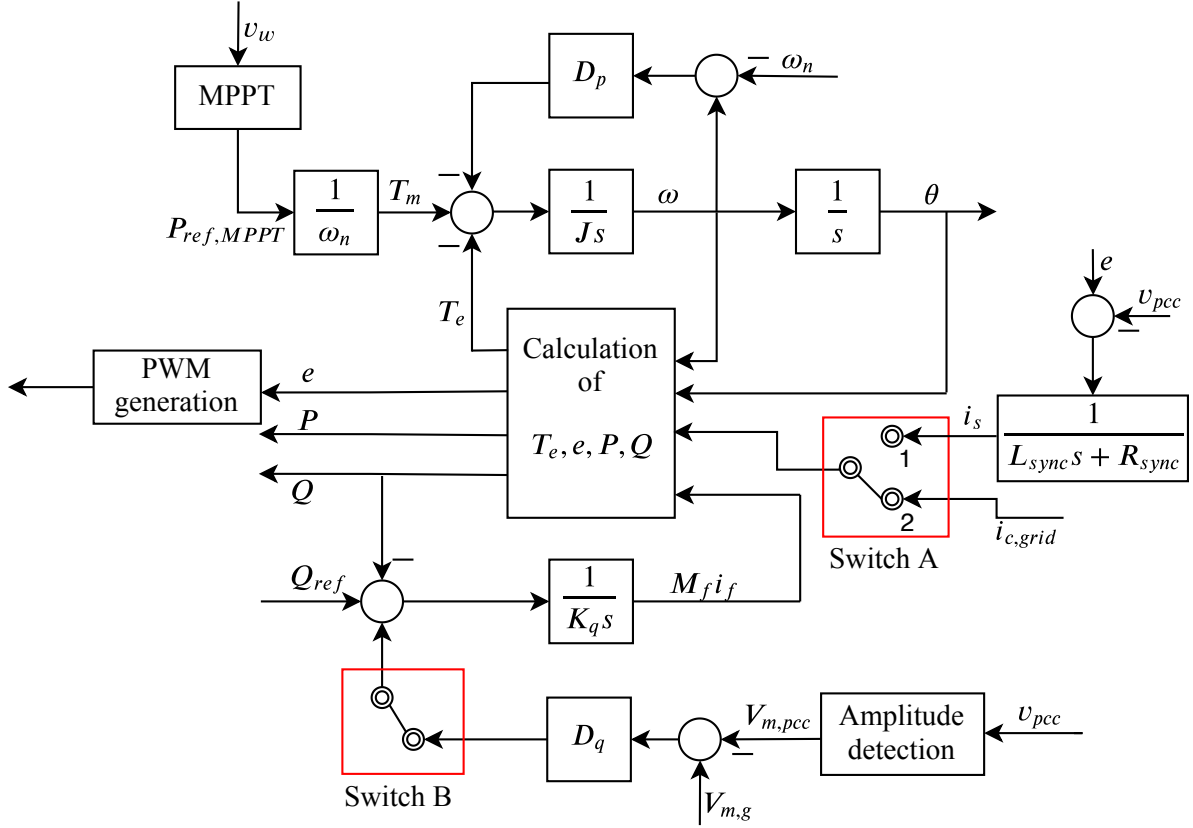
Figure 3.2: Synchronverter control topology for inverter, modified from [27].

where $P_{ref}$ is slightly below the value calculated by (2.8) as explained above. The electromagnetic torque is calculated using (3.1c). The frequency drooping is implemented by comparing the virtual frequency of the converter $\omega$ to the system frequency reference $\omega_n$, yielding $\Delta\omega$ which is then multiplied with the frequency droop coefficient $D_p$. $D_p$ is here representing both the mechanical friction coefficient, i.e. the damping, and the drooping coefficient of a real synchronous generator[29], and is in [27] defined as

$$D_p = -\frac{\Delta T}{\Delta\omega} \qquad (3.3)$$

where $\Delta T$ is the change in mechanical torque applied to the imaginary rotor and $\Delta\omega$ is the change in frequency. The deviation between $(T_{m,ref} + \Delta T)$ and $T_e$ is then fed through an integrator via the inertia gain $\frac{1}{J}$, yielding the speed of the converter.

Using this implementation method it can be seen that if the active power consumption decreases in the grid, resulting in a lower $T_e$, the speed of the converter will initially increase. However, by comparing the increased speed of the converter to the frequency reference, the drooping feedback will be negative and thus result in a reduced net mechanical torque set-point for the VSM. Thereby achieving the desired frequency control.

The active power loop ultimately controls the speed $\omega$ of the VSM which again, by integration, yields the phase angle $\theta$ of the back-EMF $e$ of the VSM. $e$ is the control signal used as reference for the PWM.

### 3.1.2  Reactive Power Control and Voltage Droop

The Reactive Power Loop (RPL) is the lower loop in Figure 3.2 and consists of the reactive power reference, actual reactive power injected and the voltage drooping. The reactive power reference is set by the operator, and the actual reactive power is calculated by use of (3.1e). The voltage drooping is implemented by comparing the amplitude of the voltage at the Point of Common Coupling (PCC), $V_{m,pcc}$, to the grid voltage reference $V_{m,g}$, giving the voltage error $\Delta V$ which is then multiplied with the voltage droop coefficient $D_q$. This term is then added to the reactive power deviation and fed through an integrator via the gain $\frac{1}{K_q}$, creating the virtual $M_f i_f$ of the VSM. $D_q$ is in [27] defined as

$$D_q = -\frac{\Delta Q}{\Delta V} \qquad (3.4)$$

where $\Delta Q$ is the required change in reactive power needed to change the voltage $\Delta V$ volts. Note that the voltage droop in Figure 3.2 can be disabled by opening switch B.

Using this method it can be seen that if the grid voltage decreases, the drooping term will be positive and thus add to the net reactive power reference. This will, in turn, increase the reactive power injected to the grid by the converter, increasing the grid voltage. The desired voltage support is thus achieved.

The reactive power loop ultimately controls the amplitude $E$ of $e$ by adjusting the virtual $M_f i_f$. This means that $e$, which is used as reference signal for the PWM signals, now can be fully computed using (3.1b) as the controls governing both the amplitude and angle have been described. This completes the Synchronverter control technique for inverters.

### 3.1.3  Amplitude Detection

To successfully implement the control technique described above, some additional functionality needs to be introduced. In Section 3.1.2 the voltage drooping was implemented by comparing the amplitude of $v_{pcc}$ to the grid voltage reference. However, to do this, an amplitude detector have to be implemented. Different methods exists in the literature to obtain the amplitude of the voltage, such as utilising a Phase Locked Loop (PLL), or the fact that in balanced systems we can write[47][27]:

$$v_a v_b + v_b v_c + v_c v_a = -\frac{3}{4} v_m$$

where $v_{a,b,c}$ are the phase voltages and $v_m$ is the amplitude.

However, for the application in this thesis the Clarke transformation, also known as $\alpha - \beta$ transformation, will be used to determine the amplitude of the grid voltage. The Clarke transformation is a mathematical transformation that transforms the $abc$ components in the time domain of the three phase system into $\alpha\beta\gamma$ components, and is given as[48]:

$$v_{\alpha\beta\gamma} = \begin{bmatrix} v_\alpha \\ v_\beta \\ v_\gamma \end{bmatrix} = \frac{2}{3} \begin{bmatrix} 1 & -\frac{1}{2} & -\frac{1}{2} \\ 0 & \frac{\sqrt{3}}{2} & -\frac{\sqrt{3}}{2} \\ \frac{1}{2} & \frac{1}{2} & \frac{1}{2} \end{bmatrix} \begin{bmatrix} v_a \\ v_b \\ v_c \end{bmatrix} \qquad (3.5)$$

When assuming a balanced three phase system it is known that $v_a + v_b + v_c = 0$ yielding the result that $v_\gamma = 0$[48]. Equation (3.5) can therefore be rewritten as

$$v_{\alpha\beta} = \begin{bmatrix} v_\alpha \\ v_\beta \end{bmatrix} = \frac{2}{3} \begin{bmatrix} 1 & -\frac{1}{2} & -\frac{1}{2} \\ 0 & \frac{\sqrt{3}}{2} & -\frac{\sqrt{3}}{2} \end{bmatrix} \begin{bmatrix} v_a \\ v_b \\ v_c \end{bmatrix} \tag{3.6}$$

ultimately yielding the following definitions of the $\alpha$- and $\beta$ components:

$$v_\alpha = \frac{2}{3} v_a - \frac{1}{3}(v_b + v_c) \tag{3.7a}$$

$$v_\beta = \frac{1}{\sqrt{3}}(v_b - v_c) \tag{3.7b}$$

It is now possible to calculate the amplitude of the voltage, $v_m$, using (3.8), and this will be the method used to obtain $V_{m,pcc}$ in Figure 3.2.

$$v_m = \sqrt{v_\alpha^2 + v_\beta^2} \tag{3.8}$$

### 3.1.4   Self Synchronisation

Another functionality that needs to be introduced is a way of synchronising the inverter controller with the grid before connection. This is important to avoid large transients that can damage the converters and to ensure a stable and secure connection.

The synchronisation is usually achieved by implementing a dedicated synchronisation unit, and many different methods for obtaining synchronisation exists in the literature. For example [49] outlines the use of Zero-Crossing detection, PLLs and Sinusoidal Tracking Algorithms (STA). However, in almost all power electronic equipment connected to the grid today, a basic PLL is used to obtain an accurate synchronisation[50]. The objective of the synchronisation unit is to provide the frequency, phase and amplitude of the fundamental component of the grid voltage, for which the PLL is well suited.

However, synchronisation units can have a negative impact on controller performance[51], and the PLL is in addition non-linear, making it difficult and time-consuming to tune the PLL parameters. It is therefore preferable, if possible, to omit the synchronisation unit altogether and instead implement the synchronisation functionality into the core of the controller. The method that will be used in this thesis was first proposed in [51] and utilises the inherent capabilities of the synchronous machine to synchronise with the grid. A slightly modified version will be explained here.

The active and reactive powers delivered to the grid by a synchronous machine can be approximated, using amplitudes instead of RMS values, as[51]:

$$P = \frac{3V_g E}{2X} \sin(\theta - \theta_g) \tag{3.9a}$$

$$Q = \frac{3V_g}{2X}[E\cos(\theta - \theta_g) - V_g] \tag{3.9b}$$

where $V_g$ is the amplitude of the grid voltage, $E$ is the amplitude of the synchronous machines back-EMF, $\theta$ is the angle of the machine and $\theta_g$ is the angle of the grid. $X$ is the synchronous reactance of the machine. The objective is to synchronise the converter with the grid, i.e.:

$$E\angle\theta = V_g\angle\theta_g \implies \begin{cases} E = V_g \\ \theta = \theta_g \end{cases} \tag{3.10}$$

and from (3.9a) and (3.9b) it can quickly be deduced that if the criteria in (3.10) is fulfilled, the active and reactive power injected into the grid will both be zero. This can be utilised in the synchronisation procedure for the Synchronverter as it will imply $e = v_g$. Setting the power set-points $P_{ref} = 0$ and $Q_{ref} = 0$ during the initial synchronisation therefore means that the Synchronverter will control itself into synchronisation with the grid. As the synchronverter will be connected at the Point of Common Coupling the voltage at the PCC will be the voltage that the converter should be synchronised with, and therefore $v_{pcc}$ will be used in the procedure.

However, during the synchronisation process, i.e. before the converter is connected to the grid, the circuit breaker will be open, meaning the current $i_{c,grid}$ will be zero. The Synchronverter will therefore not be able to achieve synchronisation using $i_{c,grid}$ as feedback current to the controller as no regulation process is possible when the current is zero. Therefore, to overcome this problem, a synchronising loop will be implemented, injecting a virtual current into the controller so that the desired synchronisation is achieved. This means that during the synchronisation process the virtual current

$$i_s = \frac{e - v_{pcc}}{L_{sync} \cdot s + R_{sync}} \tag{3.11}$$

will be the input to the control system[51]. Here, $L_{sync}$ is a virtual inductor, $s$ is the Laplace operator and $R_{sync}$ is a virtual resistor used to create the virtual current. $i_s$ can then be used in (3.1c) and (3.1e), along with $P_{ref} = 0$ and $Q_{ref} = 0$ so that $e$ is controlled to be synchronised with the grid voltage. This will also imply that $i_s$ is controlled to be zero and that the converter can be connected to the grid, i.e. the breaker can be closed, without large transients. After connection to the grid the real current $i_{c,grid}$ will be fed into the controller instead of the virtual current by switching switch A in Figure 3.2 from position 1 to position 2. The active and reactive power set-points will also be changed to reflect the desired operation. The part of the controller implementing the synchronisation capability is depicted in the far right of Figure 3.2. Using this type of synchronisation greatly reduces controller complexity and increases overall efficiency and performance[51].

### 3.1.5   Set-Point Limiter and Saturation

To ensure that the control system does not operate the system at an operating point beyond the capabilities of the converters, limitations and saturation should be implemented to limit the active- and reactive power set-points. This will be done using a strategy which is prioritising

active power over reactive power. The power set-points are based on the reference power and the drooping so that

$$P_{set} = T_{set}\,\omega_n = \Big(T_m - D_p(\omega - \omega_n)\Big)\,\omega_n \tag{3.12a}$$

$$Q_{set} = Q_{ref} + D_q(V_{m,g} - V_{m,pcc}) \tag{3.12b}$$

Firstly, the set-points are saturated so that $T_{set} \in [0, \frac{S_n}{\omega_n}]$ and $Q_{set} \in [0, S_n]$, where $S_n$ is the rated apparent power. In addition, the total apparent power set-point of the inverter should not exceed the rated apparent power, i.e.

$$\sqrt{P_{set}^2 + Q_{set}^2} \le S_n \tag{3.13}$$

A check is therefore implemented so verify that the criterion in (3.13) is satisfied. If this is not the case $P_{set}$ remains unchanged while $Q_{set}$ is set as

$$Q_{set} = \sqrt{S_n^2 - P_{set}^2} \tag{3.14}$$

Note that if the original $Q_{set}$ is negative, i.e. the voltage at the PCC is sufficiently high so that the voltage drooping brings the reactive power set-point below zero, the check in (3.13) may give a wrong result. Therefore, if $Q_{set} < 0$, $Q_{set} = 0$ is used. The actual set-point limiter implemented into the Simulation model can be found in Appendix C.1, Figure C.6.

## 3.2  Rotor Side - Rectifier control strategy

The Synchronverter technology will also be used to control the rectifier side of the back-to-back converters connecting the WECS to the grid. This will also be a PWM controlled three-phase converter for which a typical power part is depicted in Figure 3.3. The three-phase generator to the far left of the figure will for this thesis constitute the PMSG driven by the wind turbine. The method of using the Synchronverter control technology to operate a rectifier was first proposed in [31], and builds on the idea from [27]. Instead of operating the converter as a synchronous generator, as is the case for the inverter side explained in Section 3.1, the converter will now be operated as a synchronous *motor*, and it is therefore yet again a way of implementing a virtual synchronous machine.

From Figure 3.3 it can be seen that also for the rectifier side $L_s$ and $R_s$ will represent the inductance and resistance of the windings of the imaginary synchronous motor, meaning the voltage at the converter terminals constitute the back-EMF $e$ of the VSM. The mathematical model used for the Synchronverter controlled rectifier is derived in Section 2.3.2, and as previously explained it bears much resemblance to the model used for the synchronous generator, except that the inductor currents are defined in the opposite direction, flowing into the machine.

The core of the controller will therefore be exactly the same as for the inverter, leading to negative power and electrical torque. This is due to the fact that with the mathematical model used, the power is defined positive for a generating unit, i.e. currents flowing out of the machine, and negative for a consuming unit such as the motor, based on the direction of the currents. Based on these definitions the swing equation in the controller core can also be kept unchanged using
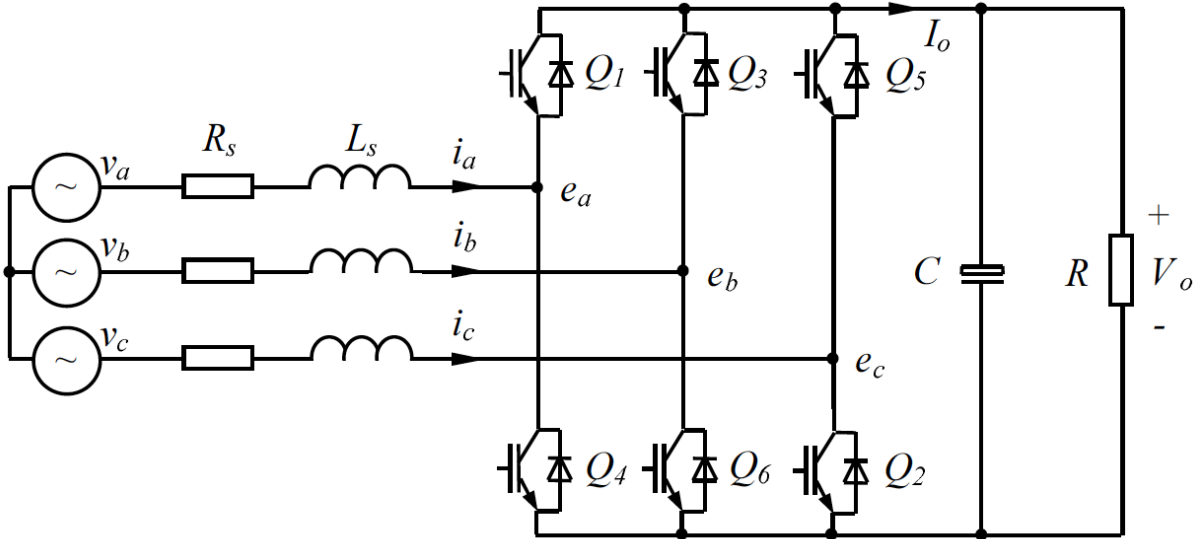
Figure 3.3: Power part of a typical three-phase rectifier[29].

(3.1a), as the redefined signs of the electrical and mechanical torques will ultimately lead to the desired swing equation representing a motor in (2.22).

Also for the rotor side, the control system will generate the reference for the PWM signals used to control the physical IGBTs in the power part. The objective of the rotor side converter is to maintain the DC link voltage at the reference level, while sending the correct amount of power to the grid side as demanded by the grid side converter. This should be achieved for the entire operating range of the wind turbine, and the converter frequency should follow the variable frequency of the PMSG. The control topology of the rotor side controller in the Laplace domain is depicted in Figure 3.4.

As can be seen, the inputs to the controller are the DC voltage reference $V_{DC,ref}$, the reactive power reference $Q_{ref}$, the converter current $i_{c,rotor}$, the mechanical rotation of the turbine shaft $\omega_m$, and during the synchronisation process, the voltage of the PMSG $v_{pmsg}$ is required. $Q_{ref}$ is usually set to zero to obtain unity power factor. $i_{c,rotor}$, $v_{pmsg}$ and $\omega_m$ are obtained through measurements coming from sensors.

### 3.2.1   DC Voltage Control and Frequency Droop

The control structure depicted in Figure 3.4 also consists of two control channels; an upper channel for the DC voltage control and a lower channel for the reactive power control. In addition, the upper channel has an outer and an inner loop denoted the DC voltage loop and the power loop respectively for which the power loop has an additional inner frequency loop.

The DC voltage control loop is the upper loop in Figure 3.4 and is governed by the swing equation using the mechanical torque reference, electrical torque and the frequency drooping. As seen from Figure 3.4, the DC voltage deviation is passed through a Proportional/Integral (PI) controller to create the mechanical torque reference for the virtual synchronous machine. The PI controller consist of a proportional gain and an integral gain, having the expression $K_{p,dc} + \frac{K_{i,dc}}{s}$. The electrical torque is calculated using (3.1c).

The drooping torque is created by comparing the frequency of the converter $\omega$ to the electrical
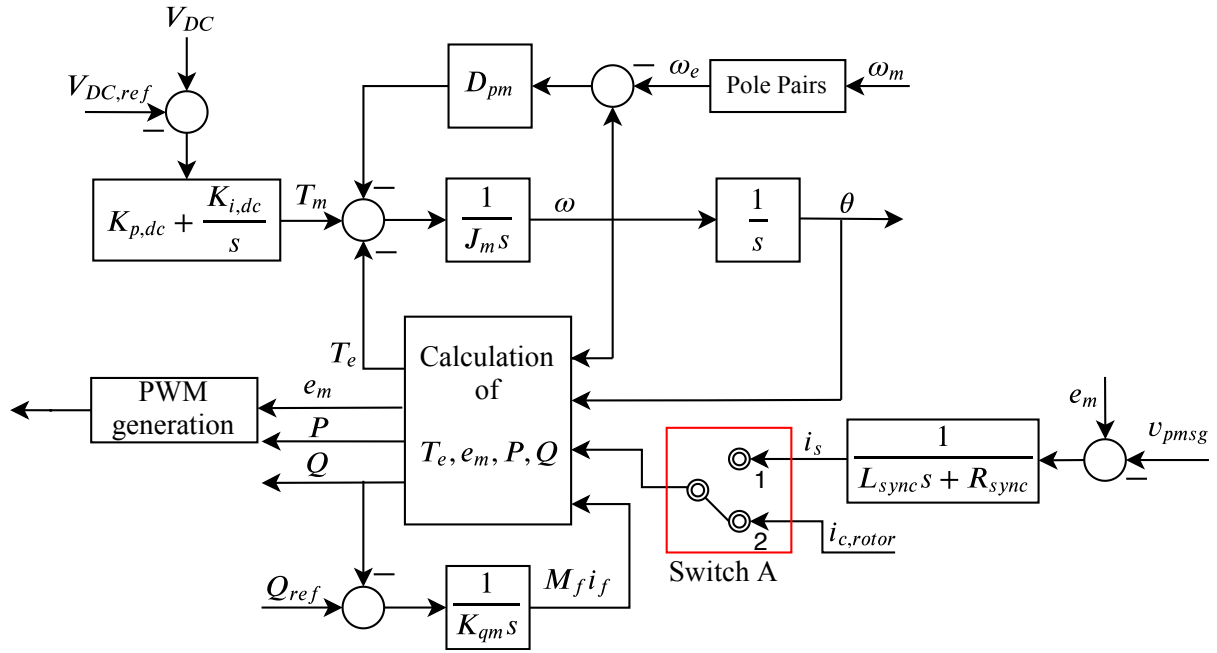
Figure 3.4: Synchronverter control topology for rectifier, modified from [31].

frequency of the PMSG, $\omega_e$, giving $\Delta\omega$. Note that the electrical frequency of the PMSG is obtained using the mechanical speed of the shaft and the number of pole pairs in the PMSG. $\Delta\omega$ is then multiplied with the frequency droop coefficient $D_{pm}$. $D_{pm}$ is here representing the mechanical friction coefficient of a real synchronous motor[29], and will in this thesis have the same definition as $D_p$, i.e. calculated using (3.3).

The deviation between $T_{m,ref} + \Delta T$ and $T_e$ is sent through an integrator with the gain $\frac{1}{J_m}$. This in turn controls the speed of the converter $\omega$. As for the grid side converter, the speed $\omega$ of the VSM yields, by integration, the angle of the control signal $e$ used for the PWM signals. $J_m$ is the virtual inertia of the synchronous motor.

### 3.2.2   Reactive Power Control

The reactive power loop is the lower loop in Figure 3.4 and consists of the reactive power reference and actual reactive power. The reactive power reference is set by the operator and is for the rectifier often set to zero to obtain unity power factor. The actual reactive power is calculated by use of (3.1e). The reactive power deviation is fed through an integrator with the gain $\frac{1}{K_{qm}}$, creating the virtual $M_f i_f$.

As for the grid side converter, the reactive power loop ultimately controls the amplitude of the control signal $e$ by adjusting $M_f i_f$. Therefore, with the angle controlled by the DC voltage loop and the amplitude coming from the reactive power loop, the control signal for the PWM signals can be calculated based on (3.1b), completing the Synchronverter control technique for rectifiers.

### 3.2.3   Self Synchronisation

Before the PWM signals are released to the IGBTs the controller needs to synchronise with the grid frequency and voltage governed by the PMSG. During this period the rectifier works as an uncontrolled three-phase diode rectifier. The synchronisation is important to limit high inrush

currents to the rectifier, and the procedure used here is modified from the procedure proposed in [52]. The synchronisation follows to a great extent the method in Section 3.1.4. Both the torque reference and the reactive power reference is set to zero, and a virtual current, $i_s$, is introduced as feedback to the controller. The virtual current is necessary during the synchronisation because the rectifier is operating in an uncontrolled mode[52], i.e. the current $i_{c,rotor}$ cannot be controlled by the controller as no signals are sent to the IGBTs.

The virtual current $i_s$ can be calculated as

$$i_s = \frac{v_{pmsg} - e}{L_{sync} \cdot s + R_{sync}} \tag{3.15}$$

however based on the previously defined direction of currents for the rectifier control system, the virtual current used as the feedback will be $-i_s$, resulting in the virtual current in (3.16).

$$i_{s,feedback} = \frac{e - v_{pmsg}}{L_{sync} \cdot s + R_{sync}} \tag{3.16}$$

When synchronisation is achieved the PWM signals can be released to the IGBTs, the mechanical reference torque can be set to the output from the PI controller, and switch A in Figure 3.4 can be thrown into position 2 so that the real current $i_{c,rotor}$ can be fed into the controller as feedback instead of the virtual current.

## 3.3  System Topology

The two control strategies explained in Sections 3.1 and 3.2 are used to control the back-to-back converters connecting a large-scale Wind Energy Conversion System to the grid. Therefore, to provide the reader with a visual context, the full control strategy for use in a wind power application will be outlined in this section. The full system topology of the system that is investigated in this thesis is depicted in Figure 3.5, showing both the physical electrical system and the control structures.

The topology consists of a wind turbine driving a PMSG. A three-phase grid is then connecting the PMSG to the rectifier, implementing the inductor $L_s$ and the resistor $R_s$. Between the two converters, the DC link consists of a capacitor, $C_{DC}$, and a resistor known as the chopper resistor, $R_{chopper}$. The chopper resistor is connected using a controlled IGBT, and the objective of $R_{chopper}$ is to protect the DC link from overvoltages. This is done by connecting the resistor when the DC voltage passes a given threshold so that excess energy can be dissipated in the chopper resistor to avoid damaging the converters. In addition, the chopper resistance is used to obtain the desired DC voltage before connecting the grid/load to the inverter. $R_{chopper}$ is designed based on the rated power of the system and can be calculated as[53]:

$$R_{chopper} = \frac{V_{DC,ref}^2}{P_{rated}} \tag{3.17}$$

After the DC link, the inverter is connected to the three-phase grid via $L_s$, $R_s$ and the filter capacitance $C$. The circuit breakers indicate the Point of Common Coupling and gives the measuring point of the voltage $v_{pcc}$. The final parts of the system are the grid inductance $L_g$, grid

resistance $R_g$ and the infinite bus with the voltage $v_g$. The idea behind the system topology is to a large extent based on the system investigated in [18] and [30], with modifications.
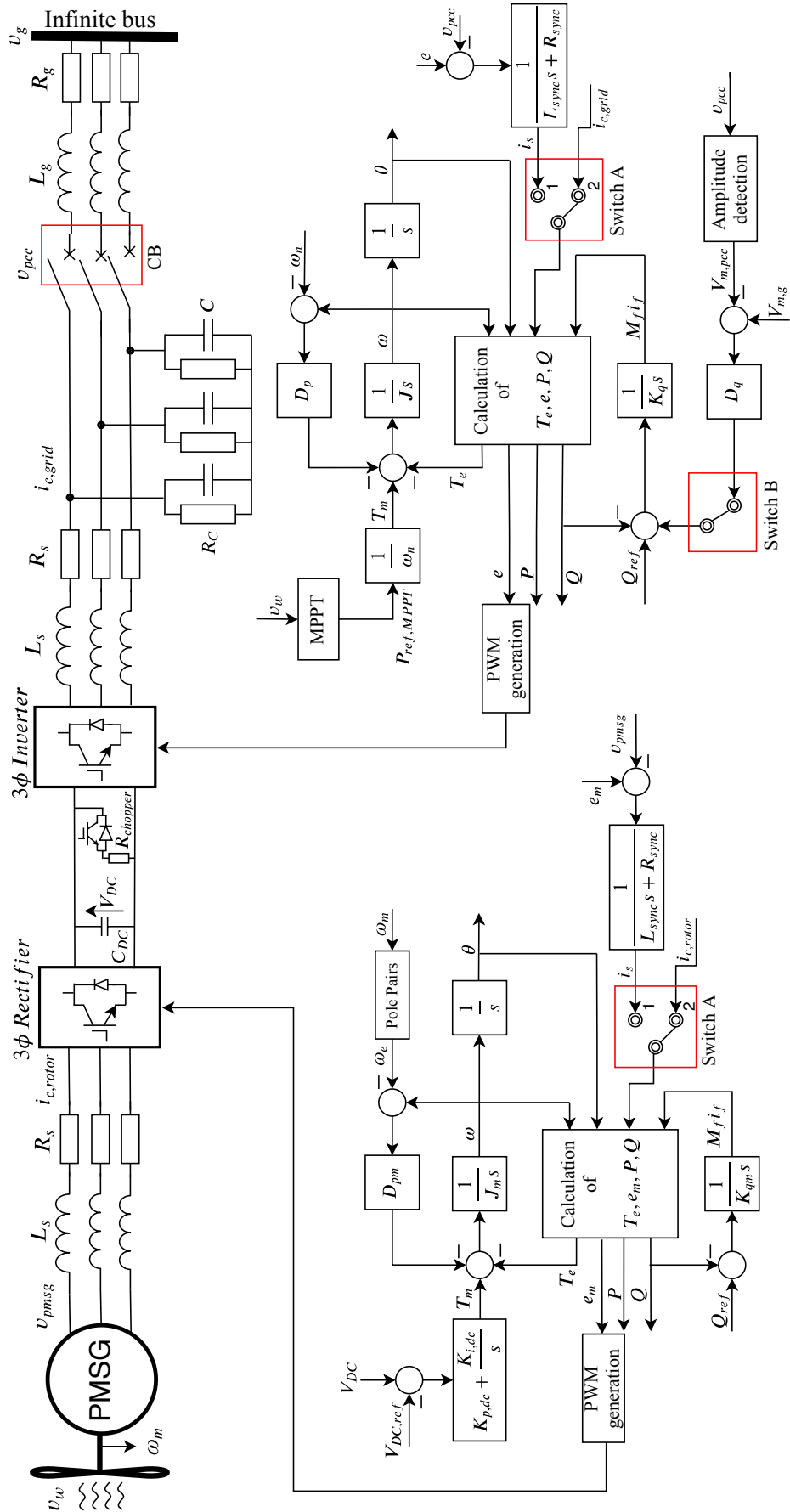
Figure 3.5: Full system topology of a Wind Energy Conversion System.

# Chapter 4

# Understanding the Transient Stability by Analysing the Original System

*This chapter describes the investigation into the transient angular stability of a VSM connected to an infinite bus using different methods of stability analysis. First, the type of contingency is defined along with a problem formulation. Then, the differential equations describing the dynamics of the Synchronverter using different assumptions are obtained, before the concepts of the equal area criterion and transient energy function are introduced. Using these concepts, different methods of analysing the stability of the given system are described in detail. Furthermore, results and simulations providing insight into the system stability are provided, before being thoroughly discussed.*

## 4.1   Introduction

Before an analytical stability analysis can be performed, the system under investigation must be laid out so that appropriate assumptions can be made throughout the analysis. This is also necessary to be able to find the correct initial-, fault- and post-fault states of the system. For the initial stability analysis, consider the system in Figure 3.5, for which the power part is depicted in Figure 4.1. The fault scenario that will be used is that a three-phase grounded fault will occur at the grid, reducing the amplitude of the grid voltage $V_g$ to a certain level. After the fault is cleared, the grid voltage will return to its nominal value without any changes in the network configuration, i.e. disconnections of lines or reduction of loads. Moreover, the wind speed is assumed to be sufficiently constant so that a constant power reference can be assumed for the inverter. Also, assuming the rectifier to be able to control the DC voltage so that the grid side will not be affected by the responses of the rotor side, only the grid side converter must be considered.

Based on the problem formulation, three states are defined for the system:

1. Pre-fault state: The operating state of the system before the contingency takes place.

2. Fault state: The operating state of the system during the fault.

3. Post-fault state: The operating state of the system after the fault has been cleared

and variables with superscripts $pre$, $f$ and $post$ thus belong to the states as indicated by the superscript.

Using the control topology described in Chapter 3 it is possible to describe the dynamics of the Synchronverter VSM using many of the same approaches as are common for normal synchronous generators. These dynamics, as well as a comprehensive presentation of methods used in power system stability analysis, can be found in numerous textbooks such as [32], [34], [44], [54], [55]. However, these textbooks use lengthy mathematical derivations to explain the complex topics and methods used, and not all derivations are relevant for the virtual synchronous generator. Therefore, using these textbooks and relevant papers as background material, traditional stability analysis as well as a modified analysis method will be adapted to the Synchronverter VSM to perform a transient stability analysis of the system.
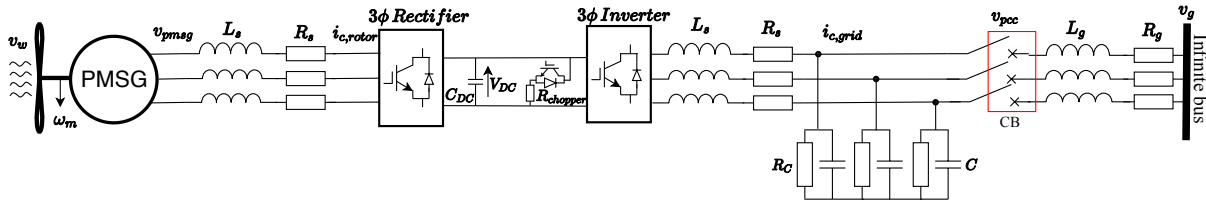


Figure 4.1: Network topology of the investigated system.

## 4.2    Analytical Model of the System

### 4.2.1    The Synchronverter Dynamics

The back-to-back converters in Figure 4.1 are controlled as virtual synchronous machines. As explained in Chapter 3, the rotor side converter is controlled to mimic a synchronous motor, while the grid side converter is controlled to mimic a synchronous generator. As such, the grid side converter will represent the generator of interest in the transient stability analysis, as this will be the unit governing the WECS's synchronism with the grid and thus is the unit that may lose synchronism with the grid due to a contingency.

Traditionally, when analysing the transient stability of the synchronous generator, the generator's sub-transient-, transient- and synchronous reactances are of crucial importance. The different values of this reactance for different time periods are founded in the complex interactions between generator components such as armature windings and damper windings. However, as the VSM has no physical generator windings, the modelling of the Synchronverter does not include such changes in winding reactance. From Section 3.1 it is known that the inverter voltage represents the VSM's back-EMF and the filter reactance represents the VSM's winding reactance, which is assumed to be constant.

When modelling the dynamics of the Synchronverter-controlled inverter analytically, the control structure in Figure 3.2 will be used. As the VSM studied is connected to an infinite bus with constant frequency $\omega_n$, the bus voltage is used as a reference, i.e. having an angle of $0°$.

Using a common reference frame rotating at the nominal grid frequency means that the angle of the converter with respect to the common reference frame can be defined as the power angle $\delta$, i.e. the angle between the VSM reference frame and the common reference frame. A visual representation of the reference frames are provided in Figure 4.2 where the $D - Q$ axis is the common reference frame rotating at $\omega_n$ and $d-q$ axis is the reference frame of the Synchronverter rotating at $\omega$. Remember that $\omega$ is the virtual electrical angular speed of the VSM as defined in Section 3.1.
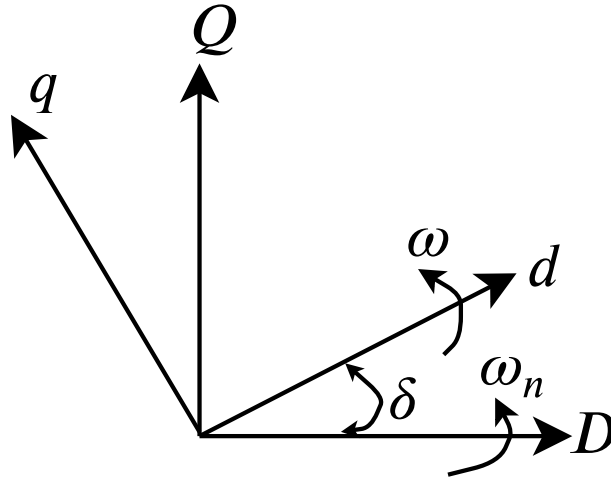
Figure 4.2: A typical reference frame transformation, modified from [56].

Using the reference frame transformation, the dynamics of the Virtual Synchronous Machine
can be found. First, from Figure 4.2, it is evident that the power angle $\delta$ changes according to
(4.1a) where $\Delta\omega = \omega - \omega_n$. As $\omega_n$ is constant, differentiating (4.1a) yields (4.1b).

$$\frac{d\delta}{dt} = \omega - \omega_n = \Delta\omega \tag{4.1a}$$

$$\frac{d^2\delta}{dt^2} = \frac{d\Delta\omega}{dt} = \frac{d\omega}{dt} \tag{4.1b}$$

Next, by looking at Figure 3.2 the swing equation of the Synchronverter control structure can be
identified as

$$\frac{d^2\theta}{dt^2} = \frac{d\omega}{dt} = \frac{1}{J}(T_m - T_e - D_p\Delta\omega) \tag{4.2}$$

and by comparing (4.1b) and (4.2) it becomes clear that the second order differentiation of the
power angle can be written as in (4.3). Note that all variables belonging to the Synchronverter
are defined as in Section 3.1.

$$\frac{d^2\delta}{dt^2} = \frac{1}{J}(T_m - T_e - D_p\Delta\omega) \tag{4.3}$$

Due to convenience, it is practical to have (4.3) represented with powers instead of torques, and
both sides are therefore multiplied with $\omega_n$ yielding

$$\omega_n\frac{d^2\delta}{dt^2} = \frac{1}{J}(P_{ref} - P_e - \omega_n D_p\Delta\omega) \implies \frac{d^2\delta}{dt^2} = \frac{1}{\omega_n J}(P_{ref} - P_e - \omega_n D_p\Delta\omega) \tag{4.4}$$

where $P_{ref}$ is the constant power reference. Above, the dynamics governed by the active power
control loop has been obtained. To have the full dynamics of the control structure, also the

dynamics governed by the reactive power control loop must be included. The mathematical equation of the lower control loop can be found from Figure 3.2 as

$$\frac{dM_f i_f}{dt} = \frac{1}{K_q}\left(Q_{ref} - Q + D_q(V_{m,g} - V_{m,pcc})\right) \tag{4.5}$$

Equation (4.5) represents the voltage regulator of the VSM, which can be treated as the Automatic Voltage Regulator (AVR) of a conventional SG. It is now possible to represent the dynamic of the system as a set of differential equations using the same form as in (2.27). Choosing $\delta$, $\Delta\omega$, and $M_f i_f$ as state variables the state vector can be defined as

$$\boldsymbol{x} = \begin{bmatrix} x_1 \\ x_2 \\ x_3 \end{bmatrix} = \begin{bmatrix} \delta \\ \Delta\omega \\ M_f i_f \end{bmatrix} \tag{4.6}$$

and by utilising equations (4.1a), (4.1b), (4.4) and (4.5), the full Synchronverter dynamics on the form $\dot{\boldsymbol{x}} = f(\boldsymbol{x})$ is given by (4.7).

$$\dot{\boldsymbol{x}} = \begin{bmatrix} \dot{x}_1 \\ \dot{x}_2 \\ \dot{x}_3 \end{bmatrix} = \begin{bmatrix} \frac{d\delta}{dt} \\ \frac{d\Delta\omega}{dt} \\ \frac{dM_f i_f}{dt} \end{bmatrix} = \begin{bmatrix} \Delta\omega \\ \frac{1}{\omega_n J}\left(P_{ref} - P_e - \omega_n D_p \Delta\omega\right) \\ \frac{1}{K_q}\left(Q_{ref} - Q + D_q(V_{m,g} - V_{m,pcc})\right) \end{bmatrix} \tag{4.7}$$

When neglecting the filter capacitance and the associated parallel resistor in Figure 4.1 the active and reactive powers delivered by the VSM can be calculated as a function of $\delta$ using (2.31a) and (2.31b). To simplify the notation, (2.31a) and (2.31b) can be redefined in (4.8a) and (4.8b) respectively with the different $K$'s defined in(4.8c)[34].

$$P_e = K_{1p} + K_2 \sin(\delta - K_3) \tag{4.8a}$$

$$Q = K_{1q} - K_2 \cos(\delta - K_3) \tag{4.8b}$$

$$K_{1p} = \left(\frac{E}{Z_{tot}}\right)^2 R_{tot} \quad , \quad K_{1q} = \left(\frac{E}{Z_{tot}}\right)^2 X_{tot} \quad , \quad K_2 = \left(\frac{E V_g}{Z_{tot}}\right)$$
$$K_3 = \arctan\left(\frac{R_{tot}}{X_{tot}}\right) \tag{4.8c}$$

Equations (4.8a) and (4.8b) can now be substituted into the set of differential equations in (4.7). Based on the method used for analysing the stability, different parts of the dynamics explained above will typically be used, and three different versions are therefore defined here.

#### 4.2.1.1   The Classical Model Without Damping

The first version of the dynamics to be defined is what is know as *the classical model* of an unregulated system for the conventional Synchronous generator (SG), here defined without the damping/frequency-drooping term. In this model, the back-EMF of the generator is assumed to be constant, $E = constant$, meaning the dynamic of the Reactive Power Loop (RPL) of the VSM is omitted. This means that the classical model describes the dynamics using only the swing equation.

In addition, a common simplification is to neglect the dampening term of the swing equation, and the classical model without dampening can thus be derived in (4.9). Note that the differential equations in (4.9b) are expressed based on the common three-phase base power $S_b$, with the power calculated using per unit (p.u.) values of $E$, $V_g$ and $Z_{tot}$ in the $K$'s. The per unit values are calculated according to the explanation in Appendix A, and it should be mentioned that $\delta$ and $\Delta\omega$ are still given in rad and rad/s respectively, and that $K_3$ is always given in rad.

$$\boldsymbol{x} = \begin{bmatrix} x_1 \\ x_2 \end{bmatrix} = \begin{bmatrix} \delta \\ \Delta\omega \end{bmatrix} \tag{4.9a}$$

$$\dot{\boldsymbol{x}} = \begin{bmatrix} \dot{x}_1 \\ \dot{x}_2 \end{bmatrix} = \begin{bmatrix} \Delta\omega \\ \frac{S_b}{\omega_n J}\left( P_{ref} - \left( K_{1p} + K_2\sin(\delta - K_3) \right) \right) \end{bmatrix} \tag{4.9b}$$

Equation (4.9b) can also be expressed using the state variables, i.e.

$$\dot{\boldsymbol{x}} = \begin{bmatrix} \dot{x}_1 \\ \dot{x}_2 \end{bmatrix} = \begin{bmatrix} x_2 \\ \frac{S_b}{\omega_n J}\left( P_{ref} - \left( K_{1p} + K_2\sin(x_1 - K_3) \right) \right) \end{bmatrix} \tag{4.10}$$

#### 4.2.1.2   The Classical Model Including Dampening

When including the dampening term, the classical model in (4.9) is expanded, yielding (4.11).

$$\boldsymbol{x} = \begin{bmatrix} x_1 \\ x_2 \end{bmatrix} = \begin{bmatrix} \delta \\ \Delta\omega \end{bmatrix} \tag{4.11a}$$

$$\dot{\boldsymbol{x}} = \begin{bmatrix} \dot{x}_1 \\ \dot{x}_2 \end{bmatrix} = \begin{bmatrix} \Delta\omega \\ \frac{S_b}{\omega_n J}\left( P_{ref} - \left( K_{1p} + K_2\sin(\delta - K_3) \right) - \frac{\omega_n D_p}{S_b}\Delta\omega \right) \end{bmatrix} \tag{4.11b}$$

Again, equation (4.11b) can also be expressed using the state variables, i.e.

$$\dot{\boldsymbol{x}} = \begin{bmatrix} \dot{x}_1 \\ \dot{x}_2 \end{bmatrix} = \begin{bmatrix} x_2 \\ \frac{S_b}{\omega_n J}\left( P_{ref} - \left( K_{1p} + K_2\sin(x_1 - K_3) \right) - \frac{\omega_n D_p}{S_b}x_2 \right) \end{bmatrix} \tag{4.12}$$

### 4.2.1.3   Model Including AVR

The Automatic Voltage Regulator (AVR) is the unit that regulates the field excitation in a rotating SG[57], and thus regulates the amplitude of the back-EMF. The dynamical model which includes the RPL of the Synchronverter can be interpreted as a VSM version of the flux-decay model, i.e one-axis model, for a conventional SG, although the physical foundations for the two cases are very much not the same. In this model, the back-EMF is no longer considered constant, $E \neq constant$, but instead regulated by the lower control loop of the Synchronverter, and the full dynamics in (4.7) are therefore considered. As the back-EMF is no longer constant, an investigation into how $E$ changes is required. From (3.1b) it is recalled that the amplitude of the back-EMF is calculated as

$$E = \omega \cdot M_f i_f$$

and when taking into account the chosen state variables in (4.6) and using the definition of $\Delta\omega$ from (4.1a), the back-emf $E$ can be calculated as

$$E = \omega \cdot M_f i_f = (\Delta\omega + \omega_n)M_f i_f = (x_2 + \omega_n)x_3 \tag{4.13}$$

As for the active power in the classical model, the reactive power used in the voltage dynamics will be calculated in per unit, i.e. the $K$'s in the expression for power are calculated using per unit values. This means that it is preferable to have $E$ calculated directly in per unit as

$$E_{pu} = \omega_{pu} \cdot M_f i_{f,pu} = (\Delta\omega_{pu} + 1)M_f i_{f,pu} = (x_2 + 1)x_3 \tag{4.14}$$

Note that $\omega_{n,pu} = 1$ as per the defined base values. As seen from (4.14), both $x_2 = \Delta\omega$ and $x_3 = M_f i_f$ need to be expressed in per unit, and some modifications must therefore be applied to the dynamics to reflect this. Also, to clearly show that the $K$'s are no longer constants, but instead functions of state variables due to their dependency on $E$, the full expressions for the $K$'s used in the AVR model in (4.15b) are included in (4.15d). Thus the system dynamics of the Synchronverter including the RPL is represented in (4.15). Note that $V_{b,pu} = 1$ has been substituted into the voltage drooping term for $V_{m,g}$ as the grid nominal voltage is also used as base voltage. The AVR model is entirely in per unit values except for $\delta$ and $K_3$ which are always given in rad.

$$\boldsymbol{x} = \begin{bmatrix} x_1 \\ x_2 \\ x_3 \end{bmatrix} = \begin{bmatrix} \delta \\ \Delta\omega \\ M_f i_f \end{bmatrix} \tag{4.15a}$$

$$\dot{\boldsymbol{x}} = \begin{bmatrix} \dot{x}_1 \\ \dot{x}_2 \\ \dot{x}_3 \end{bmatrix} = \begin{bmatrix} \Delta\omega \cdot \omega_n \\ \frac{S_b}{\omega_n^2 J}\left(P_{ref} - (K_{1p} + K_2\sin(\delta - K_3)) - \frac{\omega_n^2 D_p}{S_b}\Delta\omega\right) \\ \frac{S_b}{M_f i_{fb} \cdot K_q}\left(Q_{ref} - (K_{1q} - K_2\cos(\delta - K_3)) + \frac{D_q V_b}{S_b}(1 - V_{m,pcc})\right) \end{bmatrix} \tag{4.15b}$$

Equation (4.15b) can also be expressed using the state variables, i.e.

$$\dot{\boldsymbol{x}} = \begin{bmatrix} \dot{x}_1 \\ \dot{x}_2 \\ \dot{x}_3 \end{bmatrix} = \begin{bmatrix} x_2 \cdot \omega_n \\ \frac{S_b}{\omega_n^2 J} \left( P_{ref} - (K_{1p} + K_2 \sin(x_1 - K_3)) - \frac{\omega_n^2 D_p}{S_b} x_2 \right) \\ \frac{S_b}{M_f i_{f,b} \cdot K_q} \left( Q_{ref} - (K_{1q} - K_2 \cos(x_1 - K_3)) + \frac{D_q V_b}{S_b}(1 - V_{m,pcc}) \right) \end{bmatrix} \quad \text{(4.15c)}$$

$$K_{1p} = \left( \frac{(x_2 + 1)x_3}{Z_{tot}} \right)^2 R_{tot} \quad , \quad K_{1q} = \left( \frac{(x_2 + 1)x_3}{Z_{tot}} \right)^2 X_{tot}$$

$$K_2 = \left( \frac{(x_2 + 1)x_3 \, V_g}{Z_{tot}} \right) \quad , \quad K_3 = \arctan\left( \frac{R_{tot}}{X_{tot}} \right) \quad \text{(4.15d)}$$

To follow common power system analysis practice, the per unit system will be used for the different models as described above. Therefore, to ease notation, the subscript $pu$ will be omitted.

## 4.2.2 Defining The States

Based on the problem formulation in Section 4.1 and the described dynamics, some conclusions can be drawn related to the parameters and variables during the pre-fault, fault, and post-fault states for both the classical model (with/without dampening) and the AVR model. The superscript definitions from Section 4.1 are therefore applied to the parameters and variables so that easy distinction between them can be made. The network impedance between the VSM and the grid is independent of the chosen model describing the dynamics, and as the fault happens somewhere at the grid, the total impedance between the generator and the grid remains constant before, throughout, and after the contingency, i.e.

$$Z_{tot}^{pre} = Z_{tot}^{f} = Z_{tot}^{post} \Rightarrow K_3^{pre} = K_3^{f} = K_3^{post}$$

The notation $Z_{tot}$ and $K_3$ will therefore be used independent of system state.

### 4.2.2.1 Using the Classical Model

In the classical model, $E$ is considered constant. This, as well as the conclusion regarding $Z_{tot}$, can be used to deduce that

$$K_{1p}^{pre} = K_{1p}^{f} = K_{1p}^{post} \quad , \quad K_2^{pre} = K_2^{post}$$

by looking at (4.8c). With constant power reference and all $K$'s being identical in the pre-fault and post-fault states, it is evident that $P_e^{pre} = P_e^{post}$. During fault the grid voltage is reduced from its nominal value to $V_g^{f}$, and thus

$$K_2^{f} < K_2^{pre,post} \Rightarrow P_e^{f} < P_e^{pre,post}$$

where $K_2^{f}$ is calculated using $V_g^{f}$.

It is of interest to find the steady-state equilibrium points of the dynamical system presented above in the pre-fault and post-fault states, and to define the initial conditions for the state variables as this will represent the operating conditions at the time of fault-initiation. From Section 2.6 it is known that the equilibrium points can be found by setting $\dot{\boldsymbol{x}} = 0$. In addition, it is known that in steady-state the VSM is synchronised with the grid, i.e. $\Delta \omega_0 = 0$, which is also

correct according to $\dot{x}_1 = 0$. Furthermore, in steady-state the injected powers follow the power reference of the Synchronverter so that

$$P_{ref} = P_e^{pre} = K_{1p}^{pre} + K_2^{pre}\sin(\delta_{s0}^{pre} - K_3)$$

The stable equilibrium point (s.e.p.) $\delta = \delta_{s0}^{pre}$ can then be found through the following steps, resulting in (4.16).

$$P_{ref} = K_{1p}^{pre} + K_2^{pre}\sin(\delta_{s0}^{pre} - K_3)$$

$$\frac{P_{ref} - K_{1p}^{pre}}{K_2^{pre}} = \sin(\delta_{s0}^{pre} - K_3)$$

$$\delta_{s0}^{pre} = \arcsin\left(\frac{P_{ref} - K_{1p}^{pre}}{K_2^{pre}}\right) + K_3 \tag{4.16}$$

Using $\delta_{s0}^{pre}$ the unstable equilibrium point (u.e.p.) $\delta_{u0}^{pre}$ can be found as

$$\delta_{u0}^{pre} = \pi + K_3 - \arcsin\left(\frac{P_{ref} - K_{1p}^{pre}}{K_2^{pre}}\right) = \pi - \delta_{s0}^{pre} + 2K_3 \tag{4.17}$$

From the conclusions related to the $K$'s it is evident that the pre- and post-fault states are identical when using the classical model, and thus the equilibrium points of the two states are also identical as long as the power reference $P_{ref}$ is constant, i.e.

$$\delta_{s0}^{pre} = \delta_{s0}^{post}$$

$$\delta_{u0}^{pre} = \delta_{u0}^{post}$$

### 4.2.2.2   Using the AVR Model

When using the AVR model the pre-fault system will be identical to the pre-fault system when using the classical model and thus the pre-fault e.p.'s are still calculated using (4.16) and (4.17). However, as $E$ is now changing, the $K$'s need to be continuously updated with $E$ given by the dynamics both during fault and post-fault, and the known pre-fault value of $E$ is therefore denoted $E^{pre}$. This also implies that the e.p.'s of the post fault system will depend on $E$ as given by the dynamics. Lastly, since $E$ is a known quantity in the pre-fault state and $\omega = \omega_n$ in steady-state, the initial value of $M_f i_f^{pre}$ is found as

$$M_f i_f^{pre} = \frac{E^{pre}}{\omega} \tag{4.18}$$

## 4.3   Equal Area Criterion

With the system dynamics modelled analytically, it is possible to start the stability investigation. Such an investigation typically seeks to determine two parameters that is of particular interest, namely the Critical Clearing Angle (CCA), $\delta_{cc}$, and the corresponding Critical Clearing Time

(CCT) $t_{cc}$. The critical clearing time is the maximum permissible duration a fault can last for which the system will remain stable after the fault. As such it is the time it takes from the initialisation of the fault until $\delta$ reaches the critical angle $\delta_{cc}$, after which the system will not be able to regain steady-state. To determine $\delta_{cc}$ and the corresponding $t_{cc}$, mainly two methods are used in the classical stability assessment, and the first method that will be adopted to the VSM is known as the Equal Area Criterion (EAC).

The EAC is commonly adopted in transient stability analysis of SG's by using the classical model without dampening, and the dynamics in (4.9) will therefore be considered in this section.

### 4.3.1 Introduction to the EAC

The Equal Area Criterion can be explained intuitively using the $P - \delta$ curve depicted in Figure 4.3, where the pre- and post-fault states are identical as per the problem formulation and the chosen dynamics. A more in-depth explanation can be found in [58].

During pre-fault the system is steady, operating at $\delta_{s0}$ in point 1. A fault then lowers the grid voltage, and the operating point moves from point 1 on curve I to point 2 on curve II. By recalling the analysis in Section 2.8.2, as $P_{ref} > P_e$ the virtual rotor will accelerate according to the swing equation. The operating point will then move along curve II from point 2 to point 3 where the fault is cleared at $\delta = \delta_c$. The operating point then jumps to point 4 on curve I, where $P_{ref} < P_e$. Again, recalling the analysis in Section 2.8.2, the rotor angle will decelerate until point 5 where $\Delta\omega = 0$ and $\delta = \delta_{max}$, before accelerating back towards $\delta_{s0}$ in point 1. The angle $\delta_{max}$ is thus the maximum angle of the post-fault system, and it is known that $\delta_{max} < \delta_{u0}$ yields a stable post-fault system as $\delta$ moves back towards the s.e.p. instead of diverging.
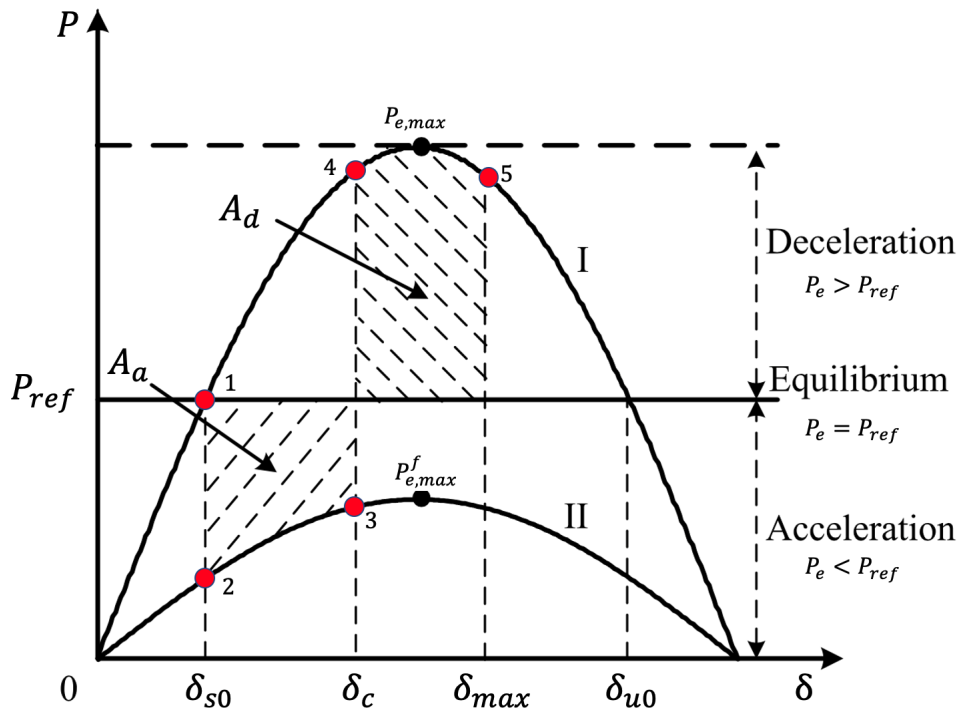


Figure 4.3: Typical $P - \delta$ curve, modified from [56].

As will be shown, the mathematical derivation of the EAC involves integration of powers. As such, it is evident that the EAC uses energy as an instrument to determine for which clearing

angles $\delta_c$ the system will remain stable. Using the discussion above we define the areas $A_a$ and $A_d$ in Figure 4.3 as the acceleration area and the deceleration area respectively. $A_a$ will then represent the injected kinetic energy during fault, while $A_d$ will represent the ability of the system to absorb energy. For the system to remain stable, it should be able to absorb all the power that is being injected during fault. This can be used to define the EAC; the system will remain stable as long as the deceleration area is equal to, or larger, than the acceleration area, i.e $A_d \geq A_a$.

The mathematical derivation used to perform a stability analysis using the above-explained concept of the Equal Area Criterion is provided in Section 4.3.2.

### 4.3.2   Mathematical Derivation

From the introduction to the EAC it is evident that a condition for the system to remain stable is that at at some time $t_a$ after the fault has been cleared the system reaches a state where $\frac{d\delta}{dt} = \Delta\omega(t_a) = 0$ before reaching the unstable angle. This can be used to derive the EAC mathematically, and the following derivations will largely follow the discussion in [34].

With the dynamics given by the classical model without dampening from (4.9), the swing equation is given as

$$\frac{d\Delta\omega}{dt} = \frac{S_b}{\omega_n J}\Big(P_{ref} - P_e(\delta))\Big)$$

It is now possible to multiply both sides with $\frac{d\delta}{dt} = \Delta\omega$ yielding

$$\Delta\omega\frac{d\Delta\omega}{dt} = \frac{S_b}{\omega_n J}\Big(P_{ref} - P_e(\delta)\Big)\frac{d\delta}{dt}$$

Next, by integrating this expression, $\Delta\omega(t_a)$ can be found in (4.19) through the following steps:

$$\int_0^{\Delta\omega(t_a)} \Delta\omega \, d\Delta\omega = \frac{S_b}{\omega_n J}\int_{\delta_{s0}^{pre}}^{\delta_{max}}\Big(P_{ref} - P_e(\delta)\Big)d\delta$$

$$\frac{1}{2}(\Delta\omega(t_a))^2 = \frac{S_b}{\omega_n J}\int_{\delta_{s0}^{pre}}^{\delta_{max}}\Big(P_{ref} - K_{1p} + P_e(\delta)\Big)d\delta$$

$$\Delta\omega(t_a) = \sqrt{\frac{2S_b}{\omega_n J}\int_{\delta_{s0}^{pre}}^{\delta_{max}}\Big(P_{ref} - P_e(\delta)\Big)d\delta} \tag{4.19}$$

Recalling that $\frac{d\delta}{dt} = \Delta\omega(t_a) = 0$ must be satisfied for the system to remain stable yields equation (4.20). The system can then be classified as stable if there exists an angle $\delta = \delta_{max}$ so that the condition in (4.20) holds[34].

$$\int_{\delta_{s0}^{pre}}^{\delta_{max}}\Big(P_{ref} - P_e(\delta)\Big)d\delta = 0 \tag{4.20}$$

Equation 4.20 can be used to define the previously explained acceleration- and deceleration areas. This is done by defining $\delta = \delta_c$ as the clearing angle of the VSM when clearing the fault at the clearing time $t_c$. Equation (4.20) is then reformulated as in (4.21) using the fault- and post-fault quantities, where $A_a$ represents the acceleration area and $A_d$ represents the deceleration area.

$$\int_{\delta_{s0}^{pre}}^{\delta_c} \Big(P_{ref} - P_e^f(\delta)\Big)d\delta + \int_{\delta_c}^{\delta_{max}} \Big(P_{ref} - P_e^{post}(\delta)\Big)d\delta = 0$$

$$\int_{\delta_{s0}^{pre}}^{\delta_c} \Big(P_{ref} - K_{1p}^f - K_2^f \sin(\delta - K_3)\Big)d\delta = \int_{\delta_c}^{\delta_{max}} \Big(K_{1p}^{post} + K_2^{post} \sin(\delta - K_3) - P_{ref}\Big)d\delta$$

$$\Rightarrow A_a = A_d$$

(4.21)

If there can be found an angle $\delta_{max}$ making $A_d = A_a$ the system is stable by the Equal Area Criterion. From Section 4.3.1 and Figure 4.3 it is clear that the maximum deceleration area available is obtained when the maximum angle is the unstable e.p. of the post-fault system, i.e. $\delta_{max} = \delta_{u0}^{post}$. The critical clearing angle $\delta_{cc}$ can then be found as the angle fulfilling the condition in (4.22) with $\delta_{max} = \delta_{u0}^{post}$.

$$\int_{\delta_{s0}^{pre}}^{\delta_{cc}} \Big(P_{ref} - K_{1p}^f - K_2^f \sin(\delta - K_3)\Big)d\delta = \int_{\delta_{cc}}^{\delta_{max}^{post}} \Big(K_{1p}^{post} + K_2^{post} \sin(\delta - K_3) - P_{ref}\Big)d\delta$$

$$A_a = A_{d,max}$$

(4.22)

The critical clearing angle fulfilling the above condition is then found by solving $f(\delta_{cc}) = A_a - A_{d,max} = 0$, typically by using software such as MATLAB. The expressions in (4.23a) and (4.23b) are therefore derived from (4.22) to simplify software implementation.

$$A_a = (P_{ref} - K_{1p}^f)(\delta_{cc} - \delta_{s0}^{pre}) + K_2^f \Big[ \cos(\delta_{cc} - K_3) - \cos(\delta_{s0}^{pre} - K_3)\Big] \qquad (4.23a)$$

$$A_{d,max} = (K_{1p}^{post} - P_{ref})(\delta_{max} - \delta_{cc}) - K_2^{post} \Big[ \cos(\delta_{max} - K_3) - \cos(\delta_{cc} - K_3)\Big] \quad (4.23b)$$

With $\delta_{cc}$ found, it is of interest to find the corresponding $t_{cc}$. However, using the EAC, this will only be possible if the electrical power is constant during the fault, i.e. $P_e^f = constant$. This will only be the case if $K_2^f = 0$. Otherwise $P_e^f$ will vary with $\delta$ which is changing according to the dynamics. As $E$ is considered constant in the classical model, the only scenario yielding $K_2^f = 0$ is a fault where $V_g^f = 0$. If this is the case, the electrical power during fault is given by $K_{1p}^f$ and the critical clearing time $t_{cc}$ can be found analytically using (4.24) which is derived by using the the swing equation in the following way:

$$\frac{d\Delta\omega}{dt} = \frac{S_b}{\omega_n J}\Big(P_{ref} - P_e^f\Big) \Longrightarrow \int d\Delta\omega = \frac{S_b}{\omega_n J} \int \Big(P_{ref} - P_e^f\Big)dt$$

$$\Rightarrow \Delta\omega = \frac{d\delta}{dt} = \frac{S_b}{\omega_n J} \int \Big(P_{ref} - P_e^f\Big)t \Longrightarrow \int_{\delta_{s0}^{pre}}^{\delta_{cc}} d\delta = \frac{S_b}{\omega_n J} \int_0^{t_{cc}} \Big(P_{ref} - P_e^f\Big)t \, dt$$

$$\Rightarrow \delta_{cc} - \delta_{s0}^{pre} = \frac{S_b}{2\omega_n J}\left(P_{ref} - P_e^f\right)t_{cc}^2$$

$$t_{cc} = \sqrt{\frac{2\omega_n J}{S_b(P_{ref} - P_e^f)}(\delta_{cc} - \delta_{s0}^{pre})} \qquad (4.24)$$

For situations where $K_2^f \neq 0$ the critical clearing time cannot be found analytically using the EAC, and other methods must therefore be applied. Thus the Equal Area Criterion has been adopted to the Synchronverter VSM to find the critical clearing angle and, if possible, the critical clearing time. This concludes the stability analysis using the EAC.

## 4.4   Transient Energy Function - The Lyapunov Function

The second method that will be adopted to the VSM is Lyapunov's direct method, i.e. using a Lyapunov function to determine the stability of the dynamical system. The Lyapunov function that is commonly used in power system analysis is also known as the Transient Energy Function (TEF)[32]. This is because an energy function is used as a candidate Lyapunov function, and a thorough study and explanation of the method is given in [59].

The TEF is widely used for assessing power system transient stability due to its speed and reduced processing requirements by computer software. This is because stability can be investigated without the need to solve the system differential equations of the post-fault system, and in contrast to the Equal Area Criterion, the TEF method can also be used to find the CCT in cases where the electric power during fault is not constant. Still, it can be shown that the TEF and EAC are, for all intentional purposes, investigating the same thing, namely the kinetic- and potential energy of the system. This will however not be done here, and interested readers are therefore referred to [32].

### 4.4.1   TEF Without Damping

First, the TEF will be derived for the Synchronverter VSM using the classical model without dampening, and the derivations will to a large extent follow the discussion in [32]. With the dynamics given by (4.9), the swing equation is given as

$$\frac{d\Delta\omega}{dt} = \frac{S_b}{\omega_n J}\left(P_{ref} - P_e(\delta))\right)$$

which during normal operation has one stable and one unstable equilibrium point; $(\delta_{s0}; \Delta\omega = 0)$ and $(\delta_{u0}; \Delta\omega = 0)$. By rearranging and multiplying both sides with $\frac{d\delta}{dt} = \Delta\omega$ we obtain

$$\frac{\omega_n J}{S_b}\Delta\omega\frac{d\Delta\omega}{dt} - \left(P_{ref} - P_e(\delta))\right)\frac{d\delta}{dt} = 0$$

The TEF will investigate the stability of the post-fault system, and substituting for $P_e$ yields

$$\frac{\omega_n J}{S_b}\Delta\omega\frac{d\Delta\omega}{dt} - \left(P_{ref} - K_{1p}^{post} - K_2^{post}\sin(\delta - K_3)\right)\frac{d\delta}{dt} = 0 \qquad (4.25)$$

Integrating (4.25) from the stable post-fault e.p. to any point$(\delta; \Delta\omega)$ on the system trajectory during fault results in the following integral equation, where $W_k$ is the system kinetic energy, and $W_p$ is the system potential energy with respect to the s.e.p..

$$\mathcal{V} = \int_0^{\Delta\omega} \frac{\omega_n J}{S_b} \Delta\omega \, d\Delta\omega - \int_{\delta_{s0}^{post}}^{\delta} \left( P_{ref} - K_{1p}^{post} - K_2^{post} \sin(\delta - K_3) \right) d\delta = W_k + W_p = \text{constant}$$

As the left side of (4.25) is equal to zero, the integral of the left side must be constant, meaning the sum of kinetic and potential energy in the system is constant when the damping has been neglected. It is now possible to evaluate the integrals to find the candidate Lyapunov function in equation (4.26).

$$\mathcal{V} = \frac{1}{2} \frac{\omega_n J}{S_b} (\Delta\omega)^2 - \int_{\delta_{s0}^{post}}^{\delta} \left( P_{ref} - K_{1p}^{post} - K_2^{post} \sin(\delta - K_3) \right) d\delta$$

$$= \frac{1}{2} \frac{\omega_n J}{S_b} (\Delta\omega)^2 - \left( P_{ref}(\delta - \delta_{s0}^{post}) - K_{1p}^{post}(\delta - \delta_{s0}^{post}) + K_2^{post} \cos(\delta - K_3) - K_2^{post} \cos(\delta_{s0}^{post} - K_3) \right)$$

$$\mathcal{V}(\boldsymbol{x}) = \frac{1}{2} \frac{\omega_n J}{S_b} (\Delta\omega)^2 + K_{1p}^{post}(\delta - \delta_{s0}^{post}) + K_2^{post} \cos(\delta_{s0}^{post} - K_3)$$
$$- K_2^{post} \cos(\delta - K_3) - P_{ref}(\delta - \delta_{s0}^{post}) \tag{4.26}$$

The derived candidate function must be shown to be a true Lyapunov function satisfying the criteria set out in Section 2.6.3. As the post-fault system is investigated, the e.p.'s of the post-fault system

$$\boldsymbol{x}_0 = \boldsymbol{x}_{s0}^{post} = \left[ \delta_{s0}^{post} \; \Delta\omega_0 \right]^T = \left[ \delta_{s0}^{post} \, 0 \right]^T$$

will be used to show that the TEF in (4.26) is a Lyapunov function for the system in question, and thus can be used in the stability analysis.

The first criterion in Section 2.6.3 is easily satisfied by evaluating $\mathcal{V}(\boldsymbol{x}_{s0}^{post})$. Substituting $\delta = \delta_{s0}^{post}$ and $\Delta\omega = 0$ into (4.26), it is found that $\mathcal{V}(\boldsymbol{x}_{s0}^{post}) = 0$, satisfying criteria 1. The remaining conditions seek to establish that the stationary point for which the candidate function is derived is indeed a minimum point, and not a maximum point or a saddle point as defined in Figure 4.4.

To show that (4.26) satisfies condition 2, i.e.

$$\mathcal{V}(\boldsymbol{x}) > 0 \text{ for all } \boldsymbol{x} \in \mathcal{D} \text{ except at } \boldsymbol{x}_0$$

both the gradient and Hessian matrix must be investigated. First, the gradient must be shown to be zero, and the gradient is therefore calculated using (4.27).

$$\nabla\mathcal{V}(\boldsymbol{x}) = \frac{\partial \mathcal{V}(\boldsymbol{x})}{\partial \boldsymbol{x}} = \left[ \frac{\partial \mathcal{V}(\boldsymbol{x})}{\partial \delta} \quad \frac{\partial \mathcal{V}(\boldsymbol{x})}{\partial \Delta\omega} \right] = \left[ K_{1p}^{post} + K_2^{post} \sin(\delta - K_3) - P_{ref} \quad \frac{\omega_n J}{S_b} \Delta\omega \right] \tag{4.27}$$

By evaluating the gradient at the stable equilibrium point it is shown that the gradient is indeed zero as the electric power and the reference power are equal at the equilibrium, making the s.e.p. an extrema of the energy function.
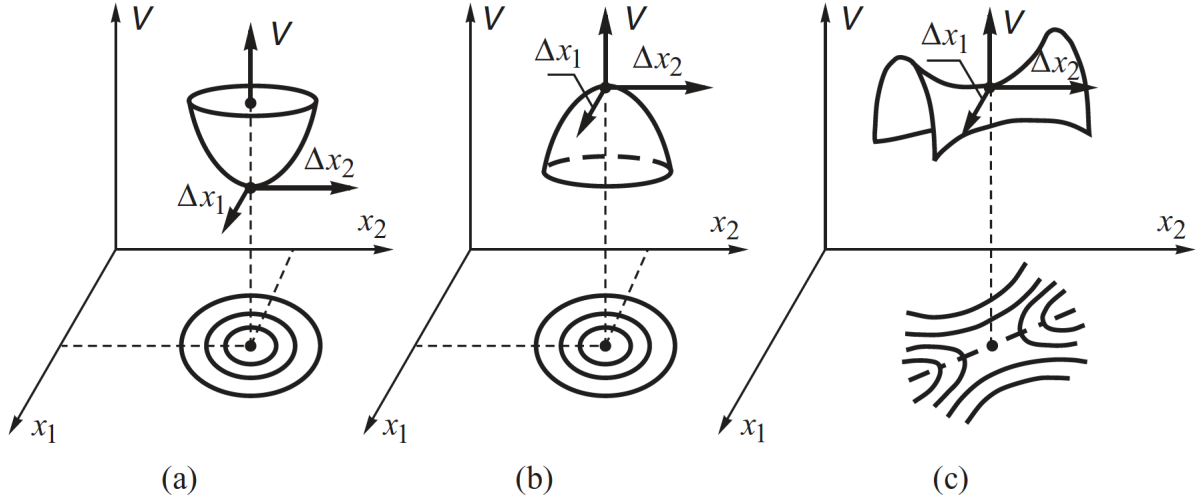
Figure 4.4: Different types of stationary points for a scalar function of two variables[32]; (a) minimum, (b) maximum, (c) saddle point

$$\nabla\mathcal{V}(\boldsymbol{x})\bigg|_{\delta=\delta_{s0}^{post},\,\Delta\omega=0} = \begin{bmatrix} 0 & 0 \end{bmatrix} \tag{4.28}$$

Next, the Hessian matrix, $\mathcal{H}$, is calculated in (4.29), and the objective is to show that the Hessian is positive definite for the stable e.p., which if shown means that $\boldsymbol{x}_{s0}^{post}$ is a minimum.

$$\mathcal{H} = \frac{\partial^2\mathcal{V}(\boldsymbol{x})}{\partial x^2} = \begin{bmatrix} \frac{\partial^2\mathcal{V}(\boldsymbol{x})}{\partial\delta^2} & \frac{\partial^2\mathcal{V}(\boldsymbol{x})}{\partial\delta\partial\Delta\omega} \\ \frac{\partial^2\mathcal{V}(\boldsymbol{x})}{\partial\Delta\omega\partial\delta} & \frac{\partial^2\mathcal{V}(\boldsymbol{x})}{\partial(\Delta\omega)^2} \end{bmatrix} = \begin{bmatrix} K_2^{post}\cos(\delta - K_3) & 0 \\ 0 & \frac{\omega_n J}{S_b} \end{bmatrix} \tag{4.29}$$

The Hessian is found to be a $2 \times 2$ diagonal matrix, and the elements on the diagonal is therefore also found to be the Eigenvalues $\lambda$ of $\mathcal{H}$. For a $2 \times 2$ matrix it can be concluded that the matrix is positive definite if the Eigenvalues are positive[41][60]. The Hessian $\mathcal{H}$ will therefore be positive definite when

$$K_2^{post}\cos(\delta - K_3) > 0 \tag{4.30a}$$

$$\frac{\omega_n J}{S_b} > 0 \tag{4.30b}$$

The condition in (4.30a) can be shown to hold for

$$-\frac{\pi}{2} + K_3 < \delta < \frac{\pi}{2} + K_3$$

while the condition in (4.30b) is always satisfied. $\mathcal{H}$ is thus shown to be positive definite on the interval governed by $\delta$ above, and as long as $\delta_{s0}^{post}$ is within this interval, the Hessian will be positive definite at the e.p. $\boldsymbol{x}_{s0}^{post}$, making the extrema a minimum. The second condition is thus satisfied.

Finally, it must be shown that

$$\dot{\mathcal{V}}(\boldsymbol{x}) = \frac{\partial\mathcal{V}(\boldsymbol{x})}{\partial\boldsymbol{x}} \cdot f(\boldsymbol{x}) \leq 0 \text{ for all } \boldsymbol{x} \in \mathcal{D}$$

Substituting using (4.27) and the chosen dynamics $\dot{x} = f(x)$ yields

$$\left[K_{1p}^{post} + K_2^{post} \sin(\delta - K_3) - P_{ref} \quad \frac{\omega_n J}{S_b} \Delta\omega\right] \cdot \left[\begin{array}{c} \Delta\omega \\ \frac{S_b}{\omega_n J}\left(P_{ref} - K_{1p}^{post} - K_2^{post} \sin(\delta - K_3)\right) \end{array}\right]$$

(4.31)

and applying some mathematical derivations to (4.31) the third condition is found to be satisfied in (4.32) through he following step:

$$\dot{\mathcal{V}}(x) = (K_{1p}^{post} + K_2^{post} \sin(\delta - K_3) - P_{ref})\Delta\omega + \frac{\omega_n J}{S_b}\Delta\omega \cdot \frac{S_b}{\omega_n J}\left(P_{ref} - K_{1p}^{post} - K_2^{post} \sin(\delta - K_3)\right)$$

$$\dot{\mathcal{V}}(x) = \left(K_{1p}^{post} + K_2^{post} \sin(\delta - K_3) - P_{ref}\right)\Delta\omega + \left(P_{ref} - K_{1p}^{post} - K_2^{post} \sin(\delta - K_3)\right)\Delta\omega = 0$$

(4.32)

The candidate Lyapunov function has thus been shown to be a true Lyapunov function for the s.e.p. $x_{s0}^{post}$, and can therefore be used for the stability analysis that is to be performed. The idea behind the Transient Energy Function is to check whether the initial conditions of the post-fault state, i.e. the values of the state variables at $t_c$, $x_c$, lies within the stability region, also known as the attraction region, of the stable post-fault equilibrium point. Such an attraction region is depicted in Figure 4.5, where it can be seen that if the initial condition is inside the region, the system states either oscillates around the s.e.p. if neglecting dampening (Fig. 4.5a) or converges to the s.e.p. if including dampening (Fig. 4.5b), while if the initial condition is outside the region, the system states diverge.



(a) Typical attraction region of undampened system[34].

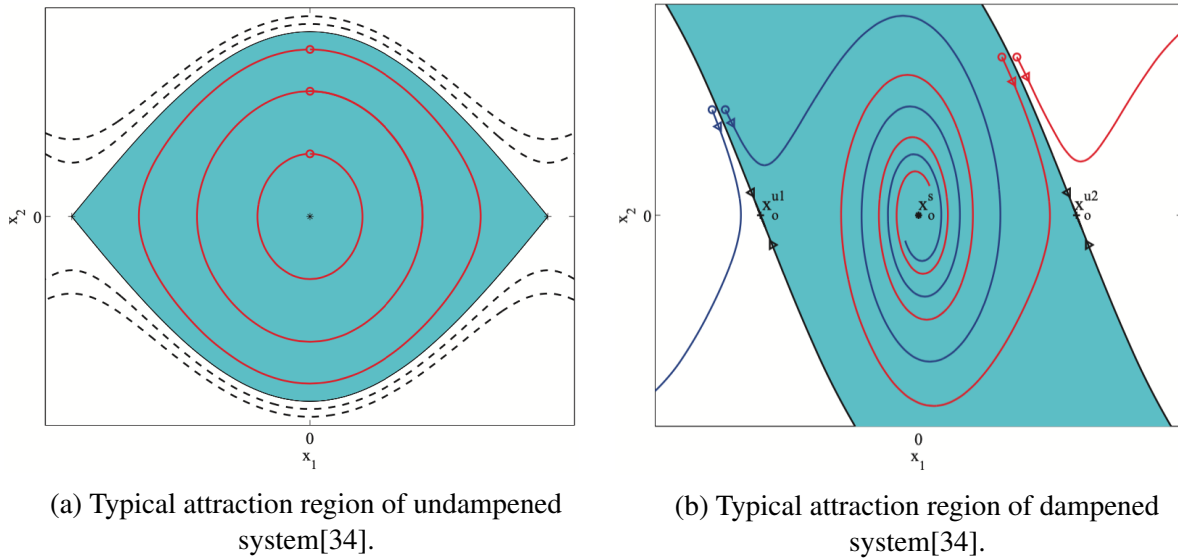(b) Typical attraction region of dampened system[34].

Figure 4.5: Typical attraction regions of undampened and dampened systems[34].

Checking whether the initial conditions are inside or outside the attraction region can be done by investigating whether the value of $\mathcal{V}(x_c)$ is less than some critical value indicating the border of the attraction region, i.e

$$\mathcal{V}(x_c) < \mathcal{V}_{cr}$$

If this is the case, the system will remain stable after the fault. The time where $\mathcal{V}(\boldsymbol{x}_c) = \mathcal{V}_{cr}$ will thus yield the CCT, $t_{cc}$. The critical value $\mathcal{V}_{cr}$ is found by evaluating the TEF in (4.26) at the unstable post-fault e.p., $\boldsymbol{x}_{u0}^{post}$. Doing this, the critical value of the Lyapunov function is found using (4.33).

$$\mathcal{V}_{cr} = K_{1p}^{post}(\delta_{u0}^{post} - \delta_{s0}^{post}) + K_2^{post}\cos(\delta_{s0}^{post} - K_3) - K_2^{post}\cos(\delta_{u0}^{post} - K_3) - P_{ref}(\delta_{u0}^{post} - \delta_{s0}^{post})$$
(4.33)

The stability analysis is then carried out using numerical integration of the faulted system, using the dynamics in (4.9), where $K_2$ is calculated using $V_g^f$. For each step in the numerical integration, the TEF is evaluated at the solution of the dynamic system at that time step and then compared to the critical value. The critical clearing time is then found as the time where $\mathcal{V}(\boldsymbol{x}_{t_{cc}}) = \mathcal{V}_{cr}$, where the critical clearing angle is found as $x_{1,t_{cc}}$. This concludes the stability analysis using the TEF based on the classical model when neglecting dampening.

## 4.4.2 TEF Including Damping

When neglecting the damping, the stability analysis is likely to yield a conservative result with a critical clearing time far below the actual value. A more correct value can however be obtained by using a dynamic model that more precisely mirrors the system. As such, the classical model including dampening from (4.11b) can be used for the analysis. The dampening term $\frac{\omega_n D_p}{S_b}\Delta\omega$ must also be incorporated into the Lyapunov function so that the decaying energy of the system after the fault has been cleared is considered in the analysis. The damping term can be incorporated into $\mathcal{V}$ in (4.26) using the procedure in [61], where the terms

$$\frac{\omega_n D_p}{S_b}\kappa(\delta - \delta_{s0}^{post})\Delta\omega + \frac{\left(\frac{\omega_n D_p}{S_b}\right)^2}{2\left(\frac{\omega_n J}{S_b}\right)}\kappa(\delta - \delta_{s0}^{post})^2$$

are added, yielding the candidate Lyapunov function including dampening in (4.34).

$$\mathcal{V}(\boldsymbol{x}) = \frac{1}{2}\frac{\omega_n J}{S_b}(\Delta\omega)^2 + K_{1p}^{post}(\delta - \delta_{s0}^{post}) + K_2^{post}\cos(\delta_{s0}^{post} - K_3) - K_2^{post}\cos(\delta - K_3)$$
$$-P_{ref}(\delta - \delta_{s0}^{post}) + \frac{\omega_n D_p}{S_b}\kappa(\delta - \delta_{s0}^{post})\Delta\omega + \frac{\omega_n D_p^2}{2S_b J}\kappa(\delta - \delta_{s0}^{post})^2$$
(4.34)

It can be shown that the candidate Lyapunov function in (4.34) satisfies the criteria necessary to be a true Lyapunov function. This is done in [56], [61] and will not be repeated here. Applying the the same approach as in Section 4.4.1, evaluating (4.34) at the u.e.p. of the post-fault system, the critical value of the TEF can be found using (4.35).

$$\mathcal{V}_{cr} = K_{1p}^{post}(\delta_{u0}^{post} - \delta_{s0}^{post}) + K_2^{post}\cos(\delta_{s0}^{post} - K_3) - K_2^{post}\cos(\delta_{u0}^{post} - K_3)$$
$$-P_{ref}(\delta_{u0}^{post} - \delta_{s0}^{post}) + \frac{\omega_n D_p^2}{2S_b J}\kappa(\delta_{u0}^{post} - \delta_{s0}^{post})^2$$
(4.35)

In (4.34) and (4.35) $\kappa$ is a constant between 0 and 1, i.e. $0 \leq \kappa \leq 1$. Reference [62] sets $\kappa = 1$, and this will also be done for the applications of this thesis. Having both the TEF in (4.34) and the critical value in (4.35), the stability analysis can be carried out using the same method as in

Section 4.4.1. Numerical integration of the faulted system using the dynamics in (4.11) is to be performed, where $K_2$ is calculated using $V_g^f$. For each step of the numerical integration, the TEF is evaluated at the solution of the dynamic system at that time step and then compared to the critical value. The critical clearing time is then found as the time where $\mathcal{V}(\boldsymbol{x}_{t_{cc}}) = \mathcal{V}_{cr}$, where the critical clearing angle is found as $x_{1,t_{cc}}$. This concludes the stability analysis using the TEF based on the classical model including dampening.

### 4.4.3  Quasi-Steady Approximate Lyapunov Approach

In Sections 4.3, 4.4.1, and 4.4.2 the three most common methods of analysing the transient stability of a Synchronous generator have been adopted to the Synchronverter Virtual Synchronous Machine. However, non of these methods consider the effect of the RPL governing the back-EMF amplitude of the VSM, which in many cases can have a significant impact on stability.

During a contingency as the one described in Section 4.1 the voltage difference between the faulted end and the VSM will result in a sudden increase of reactive power injected by the VSM. The reactive power control loop will then react by drastically decreasing $M_f i_f$ resulting in a sudden drop in the amplitude of the VSM back-EMF $E$. This drop in $E$ effectively reduces the stability margin of the system by increasing the acceleration area during fault and decreasing the deceleration area of the $P - \delta$ curve after the fault, as depicted in Figure 4.6.

In Figure 4.6, the dashed curves represent the electric power when considering the RPL, $P_e$' and $P_e^f$', which are clearly below the curves representing the case with constant $E$. In reality, the RPL would lead to a family of curves as $E$ would continuously be changing. However, for the depiction in Figure 4.6 only a snapshot of how the system behaviour would change is included to give the reader with some visual context.

The stability analysis using the classical model including dampening, which is viable for the large majority of cases concerning the conventional SG, is thus no longer viable for the VSM in the form of yielding a too optimistic result of the CCA and CCT.
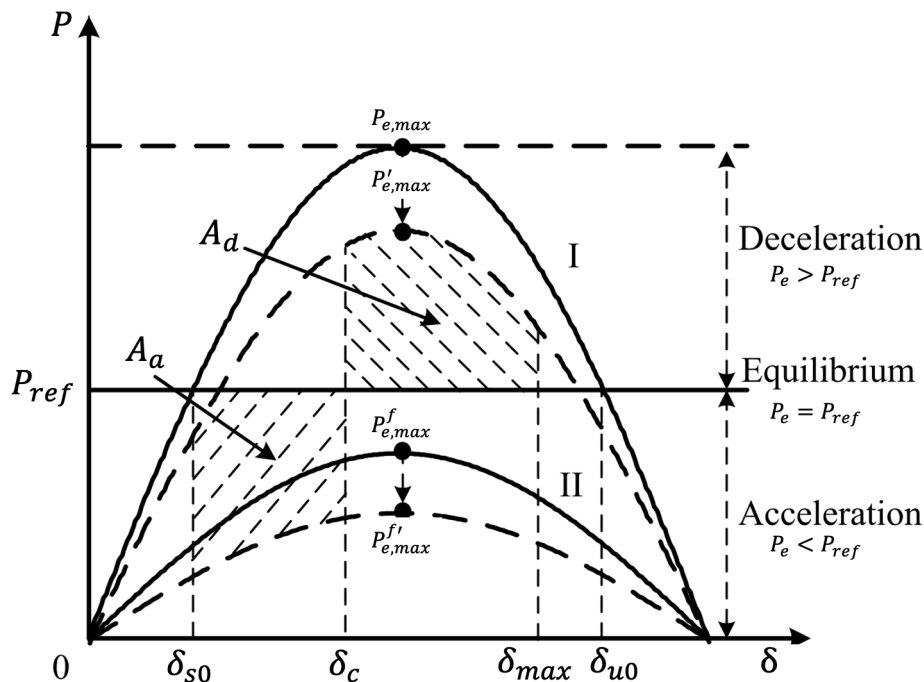


Figure 4.6: $P - \delta$ curve including effects of RPL, modified from [56].

It has been proven extremely difficult to construct a Lyapunov function that includes the dynamic of the voltage loop, or field flux decay in the case of the conventional SG[42][63]. Therefore, to overcome the difficult problem of creating a Lyapunov function based on the highly non-linear dynamics in (4.15), a *quasi-steady* approach was suggested for a general VSM in [56]. Here, instead of considering the changes in the post-fault voltage as a state variation, the changes are instead treated as parameter variations.

As pointed out in [56], the back-EMF $E$ cannot immediately restore to its rated value after the fault is cleared. This is due to the presence of an integrator in the control loop, but more so due to $\delta_c$ being much higher than $\delta_{s0}^{post}$, yielding operation far from the stable equilibrium point. This has a major impact on how the system behaves post-fault, as the large $\delta_c$ may lead to the back-EMF of the VSM actually *decreasing* immediately after clearing the fault, which would impact stability margins. This is not taken into consideration in the quasi-steady approach in [56]. Some changes have therefore been applied to the approximate Lyapunov method proposed in [56] to accommodate the possibility of worsened operating conditions immediately after fault-clearing.

The quasi-steady approach is based on the knowledge about the RPL's time constant being sufficiently small so that the assumption of the RPL instantly reaching steady-state can be considered to be true. It is this assumption that makes it possible to change the differential equation describing the RPL in (4.15b) into the quasi-steady equation in (4.36) where $E$ is considered as a parameter instead of a function of $\omega$ and $M_f i_f$ in the post-fault system.

$$0 = Q_{ref} - \left(\frac{E}{Z_{tot}}\right)^2 X_{tot} + \left(\frac{E\,V_g}{Z_{tot}}\right)\cos(\delta - K_3) + \frac{D_q V_b}{S_b}(1 - V_{m,pcc}) \qquad (4.36)$$

This translation of the voltage dynamics makes it possible to utilise the TEF described in Section 4.4.2 for the post-fault system, and the stability analysis is thus still based on investigating whether the post-fault system is within the attraction region of the post-fault s.e.p.. It is therefore still essential to perform numerical integration of the faulted system. As the main problem relates to incorporating the changes of $E$ into the TEF of the post-fault system, the full system dynamics can still be used for the forward numerical integration of the faulted system. This will be done using the full dynamics repeated in (4.37a). Note that the PCC voltage used in the RPL differential equation is calculated at each time step using (4.37c) where $Z_c$ is the filter impedance plus the breaker impedance and $\bar{I}_c$ is the converter current as per the system topology in Figure 4.1.

$$\dot{\boldsymbol{x}} = \begin{bmatrix} \dot{x}_1 \\ \dot{x}_2 \\ \dot{x}_3 \end{bmatrix} = \begin{bmatrix} x_2 \cdot \omega_n \\ \frac{S_b}{\omega_n^2 J}\left(P_{ref} - (K_{1p} + K_2\sin(x_1 - K_3)) - \frac{\omega_n^2 D_p}{S_b}x_2\right) \\ \frac{S_b}{M_f i_{f,b}\cdot K_q}\left(Q_{ref} - (K_{1q} - K_2\cos(x_1 - K_3)) + \frac{D_q V_b}{S_b}(1 - V_{m,pcc})\right) \end{bmatrix} \qquad (4.37a)$$

$$K_{1p} = \left(\frac{(x_2+1)x_3}{Z_{tot}}\right)^2 R_{tot} \quad , \quad K_{1q} = \left(\frac{(x_2+1)x_3}{Z_{tot}}\right)^2 X_{tot}$$

$$K_2 = \left(\frac{(x_2+1)x_3\,V_g^f}{Z_{tot}}\right) \quad , \quad K_3 = \arctan\left(\frac{R_{tot}}{X_{tot}}\right) \qquad (4.37b)$$

$$S = P + jQ$$

$$\bar{E} = (x_2 + 1)x_3 * e^{jx_1} \quad \rightarrow \bar{I}_c = \left(\frac{S}{\bar{E}}\right)^* \quad \rightarrow \bar{V}_{pcc} = \bar{E} - \bar{I}_c Z_c \quad \rightarrow V_{m,pcc} = |\bar{V}_{pcc}| \quad \text{(4.37c)}$$

For each step of the numerical integration of the faulted system, $E^{post}$, which will be the quasi-steady value of $E$ after the fault has been cleared, is recalculated using (4.36). Here all parameters belong to the post-fault system and $\delta$ is coming from the numerical integration, i.e. solution of $x_1 = \delta$ at that time step. As $E^{post}$ will change, so will the post-fault s.e.p., u.e.p. and the critical energy $\mathcal{V}_{cr}$. Therefore, $\delta_{s0}^{post}$, $\delta_{u0}^{post}$ and $\mathcal{V}_{cr}$ must be updated using the calculated $E^{post}$ at each time step, before the TEF is evaluated at the time step and compared to the updated $\mathcal{V}_{cr}$.

The steps in the analysis can be listed as follows:

1. Forward numerical integration of faulted system using (4.37a) and the pre-fault steady-state values as initial conditions.

2. At each time step, $E^{post}$, i.e. the value $E$ will reach immediately after fault-clearing if cleared at this time step, is calculated using (4.36) with $\delta$ being the angle at the given time step.

3. Using the newly updated $E^{post}$ to calculate $K_{1p}^{post}$ and $K_2^{post}$, $\delta_{s0}^{post}$ and $\delta_{u0}^{post}$ are calculated using

$$\delta_{s0}^{post} = \arcsin\left(\frac{P_{ref} - K_{1p}^{post}}{K_2^{post}}\right) + K_3$$

$$\delta_{u0}^{post} = \pi - \delta_{s0}^{pre} + 2K_3$$

4. Calculate $\mathcal{V}_{cr}(\delta_{s0}^{post}, \delta_{u0}^{post}, \Delta\omega_0^{post} = 0, E^{post})$ using (4.35).

5. Calculate $\mathcal{V}(\delta, \Delta\omega, E^{post})$ using (4.34).

6. Compare $\mathcal{V}_{cr}$ to $\mathcal{V}$. If $\mathcal{V} = \mathcal{V}_{cr}$ the critical clearing angle is found as $x_1 = \delta$ and the critical clearing time will be the time step of the integration.

As seen above, the proposed method is not actually an original Lyapunov method using the initial values of the post-fault system coming from the forward integration. This because the initial conditions of the post-fault system are not necessarily representative as a starting point of the actual post-fault state-variable trajectories due to the post-fault voltage drop when cleared at high angles. Therefore, the actual operating conditions immediately after fault-clearing is calculated based on the clearing angle, using the assumption that the voltage loop will reach steady-state instantly after fault-clearing. The method is therefore named an *approximate* Lyapunov method, modified from the quasi-steady method proposed in [56].

## 4.5   Full-Forward Numerical Integration

In addition to the methods explained above, another possible method of analysing the stability is to perform full-forward numerical integration of the system both during fault and post-fault. This is a time-consuming process which is rarely used for large, complex systems, but which, for the system in question, can be performed without putting too much strain on the computing hardware/software and thus get results without disproportionate long computation times. The procedure for this kind of analysis will follow the following steps:

1. Start an iterative loop iterating on the clearing time $t_c$ from $0$ to some maximum time using a fixed time step.

2. Perform forward numerical integration of the faulted system until $t = t_c$ using the steady pre-fault states as initial conditions. Save the values of the state variables $\boldsymbol{x}_{t_c}$ at $t = t_c$.

3. Perform forward numerical integration of the post-fault system until some end-time $t = t_e$ using $\boldsymbol{x}_{tc}$ as initial conditions.

4. Check if the system stabilises by investigating the end values $\boldsymbol{x}_{t_e}$. If for example $x_{1,t_e} = \delta > \pi$ the system can be deemed unstable, and the critical clearing time will be $t_c$ minus one time step. If the system is found to be stable, move to the next iteration of $t_c$ and repeat the process.

An advantage of performing full-forward numerical integration is that the analytical equations, describing the dynamics of the system, can be compared to the simulation model by plotting the results of the forward integration against the Simulink response. Thus it would be possible to identify possible modelling errors related to e.g. which simplifications that have been made. In addition, it would be possible to determine the exact CCA and CCT of the analytic system which can be compared to the results gotten using any of the methods above to verify their performance.

## 4.6 Simulations and Results

*This Section provides results and discussions of the analytical stability analysis outlined in Chapter 4 for a given Wind Energy Conversion System (WECS). The simulation model used for simulations is described, and the simulation procedure is outlined. Further, results obtained from simulating the system is provided and discussed.*

### 4.6.1 Simulation Model and Fault Scenario

A Simulink model of a WECS, of which the topology is depicted in Figure 3.5, was built for the specialisation project in [5]. This model will form the foundation, with slight modifications, for the simulations also in this thesis, and is implemented in the MATLAB/Simulink environment using version R2019a(9.6).

The system consists of an aggregated wind farm model capable of delivering $1.0603$ MW of mechanical power, and the nominal base power for the electrical system is set to $1$ MVA of rated power. To simplify the comparison between analytical results and simulation results, the wind turbine is operated in de-loaded mode using balancing de-loading. Thus, when operating at the rated wind speed $v_w = 12$ m/s, the active power reference for the grid side converter is limited to be constant $0.8$ p.u. $= 800$ kW. The reactive power reference is set to zero. Using a constant wind speed of $v_w = 12$ m/s is an obvious simplification as the wind speed in a real application would be continuously changing, having variations that could drastically impact system stability. Assuming a constant wind speed is however convenient when applying theory known from conventional, easily regulated generation, while also making for a good basis upon which comparison between systems can be adequately performed.

As in [5], the rated voltage of both the PMSG and the infinite bus is $690V$ line-to-line, and the rated grid frequency is $50$ Hz. In addition, the DC link reference voltage is set to $2\sqrt{2}V_{gn,L-G}$, i.e. two times the nominal peak phase voltage. Using the system parameters described above,

the base values used for per unit calculations are obtained using the equations in Appendix A. The base values are listed in Appendix B, Table B.1.

Details revolving the tuning of the controller parameters such as $D_p$, $D_q$, $J$ etc. are outside the scope of this thesis, but was treated extensively in the specialisation project ([5]). The results of the tuning will not be presented in detail, but interested readers are referred to the scientific paper attached in Appendix E for details revolving how the Synchronverter parameters can be tuned. It is however mentioned that $D_p$ is tuned to increase the active power set-point by a $100\%$ of base power for $2\%$ reduction in frequency, while $D_q$ tuned to increase the reactive power set-point by a $100\%$ of base power for $10\%$ reduction in PCC voltage.

The system parameters can be found in Appendix B, Tables B.2, B.3, B.4 and B.5. Also, the controller parameters of the inverter controller and rectifier controller are listed in Tables B.6 and B.7 respectively.

The Simulink model of the full system is depicted Appendix C.1, Figure C.1, with further details in Figures C.2, C.3 and C.4. In addition, Simulink models of the control systems controlling the inverter and the rectifier are provided in Figures C.5 and C.8 respectively, with additional sub-models in Figures C.6 and C.7.

The fault scenario that is to be analysed is the occurrence of a balanced three-phase-to-ground fault at the grid, reducing the amplitude of the voltage of the infinite bus to $0.1$ per unit. As stated in Section 4.1, after the fault is cleared, the grid voltage will return to its nominal value without any changes in the network configuration, i.e. disconnections of lines or reductions of loads. A symmetric grid fault was chosen as it is known to yield the worst voltage drops, and thus represent the most severe contingencies. This does however mean that the control systems are not tested for unbalanced voltages, which may produce very different responses than the ones seen here.

### 4.6.2   Pre-Fault Equilibrium Points

With the system and fault scenario defined, the stability analysis can be initiated. Using the system parameters in Appendix B, the first step is to find the pre-fault stable- and unstable equilibrium points $\boldsymbol{x}_{s0}^{pre}$ and $\boldsymbol{x}_{u0}^{pre}$. Before the fault occurs, $E^{pre}$ is controlled to be 1 p.u., and the grid voltage is set to be 1 p.u.. Furthermore, the power reference is $P_{ref} = 0.8$ per unit.

The base values and the system parameters in Appendix B, as well as $E^{pre} = V_g^{pre} = 1$ p.u., can now be used to calculate the total impedance between the converter and the grid when neglecting the filter capacitor, which again can be used to find $K_{1p}^{pre}$, $K_2^{pre}$ and $K_3$ using (4.8c). The results, plus the power reference, are given in Table 4.1.

Table 4.1: Network Impedance and Pre-Fault $K$'s.

| Parameter | Value | Parameter | Value |
|-----------|-------|-----------|-------|
| $R_{tot}$ | 0.1031 p.u. | $K_{1p}^{pre}$ | 0.1585 p.u. |
| $X_{tot}$ | 0.8000 p.u. | $K_2^{pre}$ | 1.2397 p.u. |
| $\bar{Z}_{tot}$ | $0.1031 + j0.8000$ p.u. | $K_3$ | 0.1282 rad |
| $Z_{tot}$ | 0.8066 p.u. | $P_{ref}$ | 0.8 p.u. |

Using the values in Table 4.1, equations (4.16) and (4.17) can be utilised to calculate $\delta_{s0}^{pre}$ and $\delta_{u0}^{pre}$ respectively. Furthermore, as previously explained, $\Delta\omega = 0$ in steady-state. The stable and unstable e.p. of the pre-fault system when considering the classical model are then found as in Table 4.2.

Table 4.2: Equilibrium points of pre-fault system assuming $E = constant$.

| Stable e.p. | Value | Unstable e.p. | Value |
|---|---|---|---|
| $\delta_{s0}^{pre}$ | 0.6721 rad = 38.5065° | $\delta_{u0}^{pre}$ | 2.7259 rad = 156.1805° |
| $\Delta\omega$ | 0 rad/s | $\Delta\omega$ | 0 rad/s |

When considering the AVR-model, $M_f i_{f0}^{pre} = 1$ p.u. is added to the e.p., and $\Delta\omega$ is given in p.u instead of rad/s. This yields the results in in Table 4.3.

Table 4.3: Equilibrium points of pre-fault system assuming $E \neq constant$.

| Stable e.p. | Value | Unstable e.p. | Value |
|---|---|---|---|
| $\delta_{s0}^{pre}$ | 0.6721 rad = 38.5065° | $\delta_{u0}^{pre}$ | 2.7259 rad = 156.1805° |
| $\Delta\omega$ | 0 p.u. | $\Delta\omega$ | 0 p.u. |
| $M_f i_{f0}^{pre}$ | 1.0 p.u. | $M_f i_{f0}^{pre}$ | 1.0 p.u. |

The analytically found pre-fault equilibrium points in Tables 4.2 and 4.3 can be compared to the pre-fault steady-state values of the simulated system in Section 4.6.6, Figures 4.14a, 4.14b and 4.14c. While $\Delta\omega = 0$ represents an exact equality between the analytical and simulated system, $\delta_{s0,sim}^{pre} = 38.1°$ is slightly lower than the analytical $\delta_{s0}^{pre} = 38.5065°$. The difference of $0.4065°$ is however considered negligible. From Figure 4.14c it is evident that $E_{sim}^{pre} = 1$. As $E^{pre} = \omega^{pre} M_f i_f^{pre} = (\Delta\omega + 1) \cdot M_f i_{f,0}^{pre}$ and it has been concluded that $\Delta\omega = 0$, it is found that $M_f i_{f,0}^{pre} = 1.0$ p.u. which is identical to the value in Table 4.3.

The values of the analytically found pre-fault equilibrium points are thus found to be identical, or very close, to the equilibrium points of the actual system, and the initial conditions used for the numerical integration in the subsequent analysis is therefore deemed as valid.

### 4.6.3 Results Using Classical Model Without Damping

#### 4.6.3.1 Equal Area Criterion

When using the Equal Area Criterion (EAC) derived in Section 4.3, the classical model is used, i.e. $E$ is considered constant. Thus, the post-fault $K$'s are equal to their pre-fault counterparts in Table 4.1, meaning also the post-fault equilibrium points are identical to the pre-fault equilibrium points in Table 4.2. During fault, the grid voltage is $0.1$ p.u. yielding the calculated $K_{1p}^f$, $K_2^f$ and $K_3^f$ in Table 4.4.

The Critical Clearing Angle (CCA), $\delta_{cc}$, is then found by solving $g(\delta_{cc}) = A_a - A_{d,max} = 0$ using the fsolve function in MATLAB. Here $A_a$ and $A_{d,max}$ are calculated using equations (4.23a) and (4.23b) respectively with $\delta_{max} = \delta_{u0}^{post} = \delta_{u0}^{pre}$.

Table 4.4: Fault $K$'s assuming $E = constant$.

| $K$'s during fault | Value |
|---|---|
| $K_{1p}^f$ | 0.1585 p.u. |
| $K_2^f$ | 0.1240 p.u. |
| $K_3^f = K_3^{post} = K_3$ | 0.1282 rad |

Using the EAC, the CCA is found to be $\delta_{cc} = 89.5836°$. The $P - \delta$ curve for both the pre/post-fault state and the fault-state are depicted in Figure 4.7. Here, also the stable and unstable equilibrium points are plotted, in addition to the critical clearing angle. The two areas, i.e. the acceleration area and the deceleration area, that are equal at the critical clearing angle, are also indicated as $A_a$ and $A_d$ respectively. As seen in Figure 4.7, $P_e^f$ is dependant on $\delta$, i.e. $P_e^f \neq constant$. The critical clearing time can therefore not be found analytically using (4.24), and the result of the stability analysis using the EAC is thus summarised in Table 4.5.

Table 4.5: Results of stability analysis using EAC.

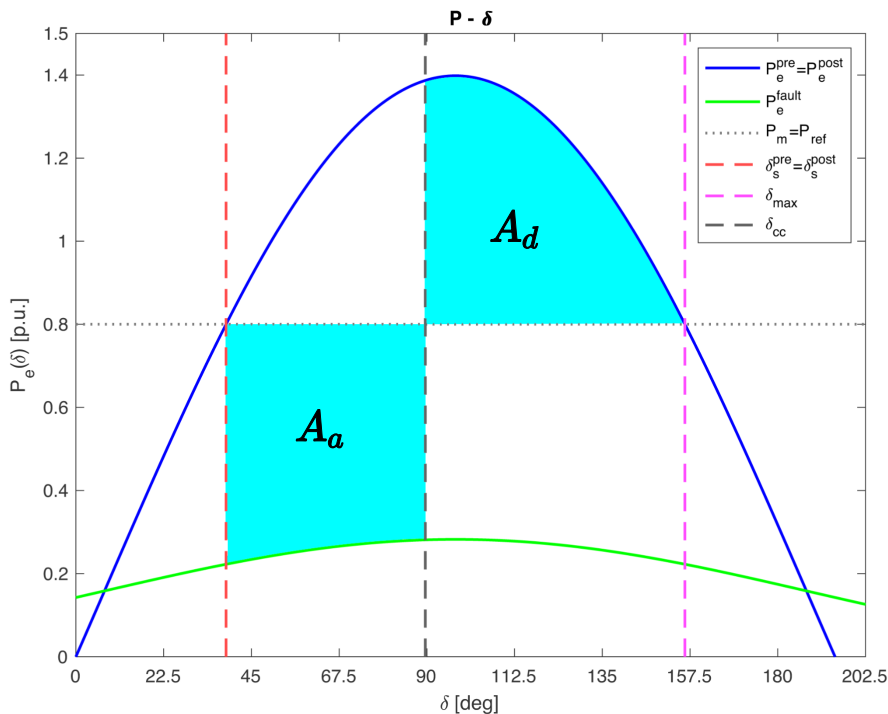| Parameter | Value |
|---|---|
| CCA, $\delta_{cc}$ | 89.5836° |



Figure 4.7: $P - \delta$ curve for the system, including critical clearing angle and indicated areas.

#### 4.6.3.2 Transient Energy Function Without Damping

The TEF method without damping uses the same system dynamics as the EAC, and the pre-, fault- and post-fault $K$'s are therefore the same as in Tables 4.1 and 4.4, with subsequent equilibrium points as in Table 4.2. Using (4.33), the critical value of the TEF is calculated to be $\mathcal{V}_{cr} = 0.8041$.

Forward integration is then performed on the set of differential equations in (4.10) inserted for the $K$'s in Table 4.4 and using the stable e.p. from Table 4.2 as initial conditions. The integration is carried out using the `ode45` solver for differential equations in MATLAB. For each solution of $\delta$ and $\Delta\omega$ of the integration, the value of the TEF is calculated by (4.26) and compared to $\mathcal{V}_{cr}$. A graphic illustration of the results is given in Figure 4.8, where the critical clearing time is found to be $t_{cc} = 0.0445$ s. At the time step of the integration corresponding to the critical clearing time, the solution of $\delta$ is obtained as $\delta = \delta_{cc} = 89.3926°$. The results of the stability analysis using the TEF without damping are summarised in Table 4.6.

Table 4.6: Results of stability analysis using TEF without damping.

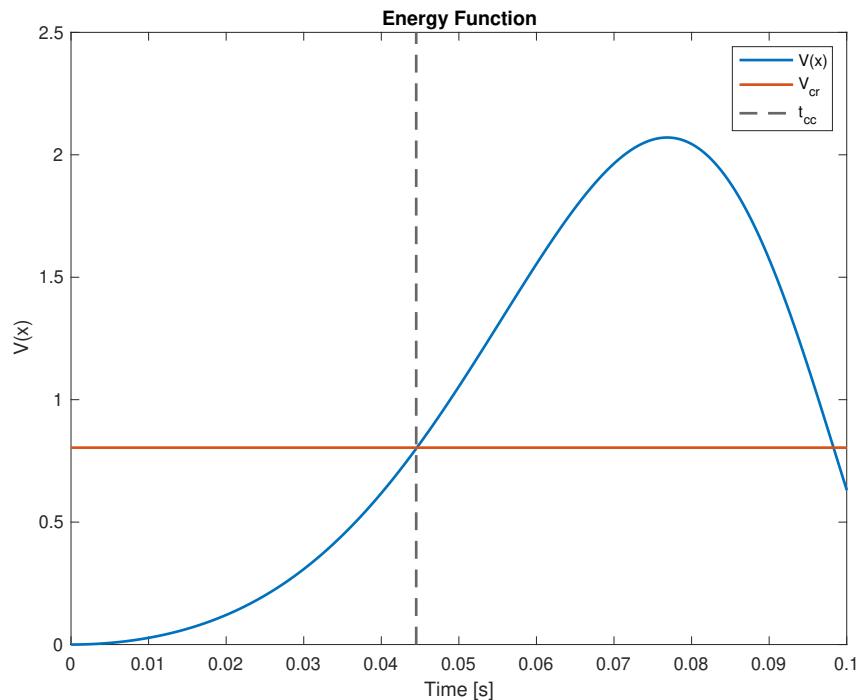| Parameter | Value |
| --- | --- |
| $\mathcal{V}_{cr}$ | 0.8041 |
| CCA, $\delta_{cc}$ | 89.3926° |
| CCT, $t_{cc}$ | 0.0445 s = 44.5 ms |



Figure 4.8: Energy function vs. clearing time for classical model without damping.

The dynamical system when using the classical model without damping is forwardly integrated for a clearing time 1 ms below and 1 ms above the CCT found by the stability assessment above, for a fault initiated at $t = 0.1\,s$. The response of $\delta$ is depicted in Figure 4.9.
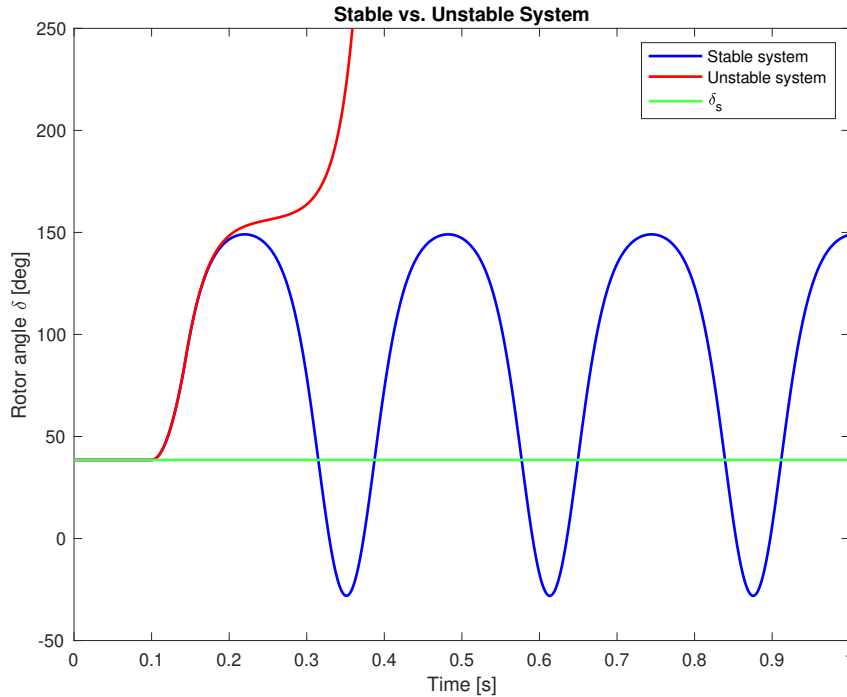
Figure 4.9: $\delta$ for stable and unstable system when neglecting damping.

### 4.6.3.3  Performance of the Classical Model Without Damping

The Equal Area Criterion and the Transient Energy Function without damping both use the same mathematical model as a foundation for analysing the system stability. As such, it is expected that the two methods should yield very similar results for system stability limits. Comparing the CCA found in Tables 4.5 and 4.6, the results confirms this similarity with a difference in CCA of only $0.191°$, which for this application is considered negligible. The results do however emphasise the large drawback of the EAC method, as no CCT can be found for the given fault scenario using the EAC. With this said, the EAC as depicted in Figure 4.7 serves as an intuitive method of finding the critical clearing angle when that is the parameter of interest. Furthermore, the curves in Figure 4.7 reaffirms the equilibrium points as the intersections between the power reference $P_{ref}$ and the electrical power $P_e$.

The limitation related to finding the CCT is clearly overcome by the transient energy function method, which by means of the critical value of $\mathcal{V}$ is able to determine the CCT as visualised in Figure 4.8. Here, as expected from the theory, the critical clearing time is found as the time when the value of the TEF exceeds the critical value. As such, it can be argued that the EAC serves as a good introduction to understanding the core problem of transient angular instability, using visual representation as an aid, but that the TEF method is a better approach to determining the actual stability limit of the system when the critical clearing time is of interest.

With that being said, the CCT $t_{cc} = 44.5$ ms identified in Figure 4.8 is considered a very short clearing time compared to typical clearing times for power systems, equalling approximately 2 cycles. Furthermore, looking at Table 4.11 in Section 4.6.7 and comparing the limits as found by the EAC and TEF without dampening to the simulation results, the deviation from the actual CCT is found to be 88.47% which is a substantial divergence.

Even though this seems like a large difference, the deviation is expected considering two major

aspects impacting the results. Firstly, neglecting the damping is expected to negatively impact the stability results. This is natural as the acceleration and deceleration of the rotor angle are increased and decreased respectively. While this is true also for the conventional SG, the effect of neglecting the damping when analysing the VSM can be particularly large as the VSM can have a tuned inertia $J$ that is way smaller than what typically found in the conventional SG. This makes the dampening/frequency-droop govern a significant part of the dynamic response. As such, neglecting the damping when analysing the VSM could potentially yield a much larger deviation from the actual system than when neglecting the damping when analysing the conventional SG.

Secondly, the transient energy function is expected to yield a conservative result. This attribute is inherent to the method and comes from the fact that for any dynamic system there exists a set of potential Lyapunov functions that can be utilised. All of these Lyapunov functions have their own attraction regions for which a set of initial conditions will render the system stable, i.e. satisfy the stability requirements. Thus, each Lyapunov function that can be found for a given system usually only covers a sub-set of the actual stability area, and thereby tends to yield a pessimistic assessment of the system stability. This attribute can however be argued to be positive in the sense that the analysis is less likely to yield a stable result for an unstable situation, which in worst case could jeopardise system integrity. A too conservative result on the other hand can be argued to be negative as it might lead to protections systems being set to trip prematurely, which may affect customers and increase the risk of major disruptions in the power supply.

According to the theory in Section 2.8.2, the rotor angle would enter periodic oscillating swings around the equilibrium point if damping is neglected. This is due to the value of $\mathcal{V}(\delta, \Delta\omega)$ being constant after fault-clearing so that the state trajectory depicted in Figure 4.5a becomes a closed curve around the s.e.p.. Recalling Section 2.8.2, the system is then considered stable but not asymptotically stable. The dynamic response depicted in Figure 4.9 is completely in accordance with this theory, where it is clearly visible that the rotor angle of the stable system starts to oscillate with constant swings around the stable e.p., while the rotor angle of the unstable system diverges.

Furthermore, the rotor angle of the stable system in Figure 4.9 continues to increase after the fault is cleared as the deceleration process takes some time. However, $\Delta\omega = 0$ is achieved at $\approx 150°$, just before the u.e.p. at $156.1805°$ as per the requirement for stability, and the rotor angle then accelerates back towards the s.e.p.. The rotor angle of the unstable system on the other hand is seen decelerating until reaching the point where $\Delta\omega$ is the smallest, which coincides with the u.e.p. at $156.1805°$. When the rotor angle passes $156.1805°$, the mechanical power is again larger than the electrical, as per the $P - \delta$ curve, and the rotor angle can be seen to start accelerating again, thus diverging from the stable state.

### 4.6.4   Results Using Transient Energy Function With Damping

The TEF added with the damping term is based on the classical model with damping. Here, $E$ is still considered constant and the pre-, fault- and post-fault $K'$ are therefore the same as in Tables 4.1 and 4.4, with subsequent equilibrium points as in Table 4.2. Using (4.35), the critical value of the TEF is calculated to be $\mathcal{V}_{cr} = 85.8290$.

Forward integration is then carried out on the set of differential equations in (4.12) inserted for the $K$'s in Table 4.4 and using the stable e.p. from Table 4.2 as initial conditions. The integration is carried out using the `ode45` solver for differential equations in MATLAB. For each solution of $\delta$ and $\Delta\omega$ of the integration, the value of the TEF is calculated by (4.34) and compared to $\mathcal{V}_{cr}$.

A graphic illustration of the results is given in Figure 4.10, where the critical clearing time is
found to be $t_{cc} = 0.6079$ s. At the time step of the integration corresponding to the critical
clearing time, the solution of $\delta$ is obtained as $\delta = \delta_{cc} = 155.3479°$. The results of the stability
analysis using the TEF with damping are summarised in Table 4.7.

Table 4.7: Results of stability analysis using TEF with damping.

| Parameter | Value |
| --- | --- |
| $\mathcal{V}_{cr}$ | 85.8290 |
| CCA, $\delta_{cc}$ | 155.3479° |
| CCT, $t_{cc}$ | $0.6079\,\text{s} = 607.9\,\text{ms}$ |
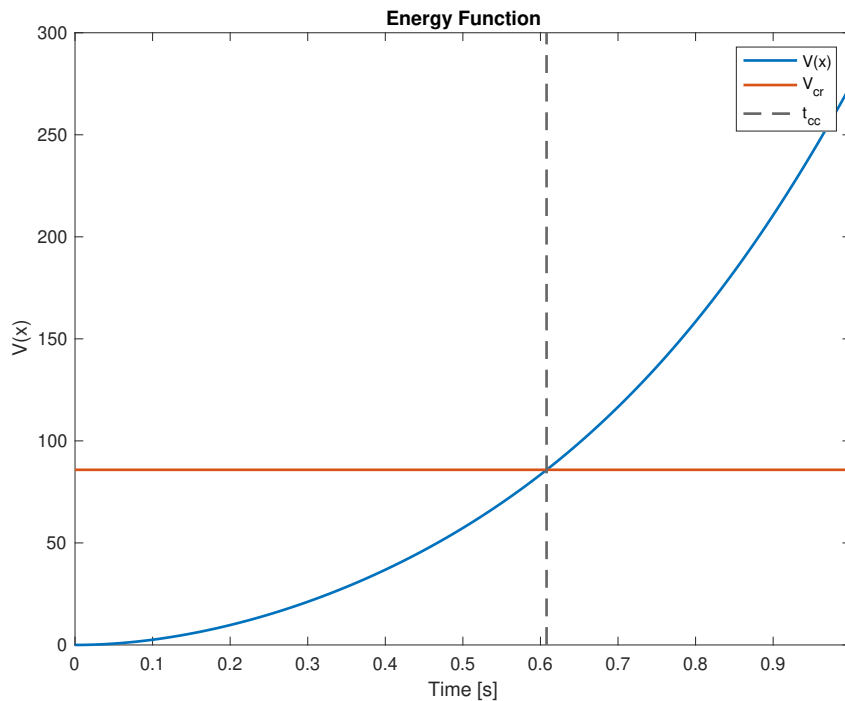


Figure 4.10: Energy function vs. clearing time for classical model with damping.

The dynamic system when using the classical model with damping was forwardly integrated for
a clearing time 1 ms below and 1 ms above the CCT found by the stability assessment above, for
a fault initiated at $t = 0.1\,s$. The response of $\delta$ is depicted in Figure 4.11.

The Transient Energy Function including damping yielded, as seen in Table 4.7, a much more
optimistic result of the system stability. As the classical model with damping has the same stable
and unstable equilibrium points as the classical model without damping, the first observation that
can be discussed is that the critical clearing angle $\delta_{cc} = 155.3479°$ in Table 4.7 is dramatically
close to the unstable post-fault e.p. $\delta_{s0}^{post} = 156.1805°$. This implies that the full deceleration of
the rotor angle takes place in the course of less than $1°$.

The possibility of such an event can be explained using two different factors, both contributing to
the result. Firstly, the damping clearly restrains the acceleration of the rotor angle, as the slope in

Figure 4.11: $\delta$ for stable and unstable system when including damping.

Figure 4.11 is much more gradual than for the case without damping. As such, less deceleration is required. Secondly, a large damping coefficient along with relatively small inertia for the VSM makes the damping govern the response. The larger the damping/droop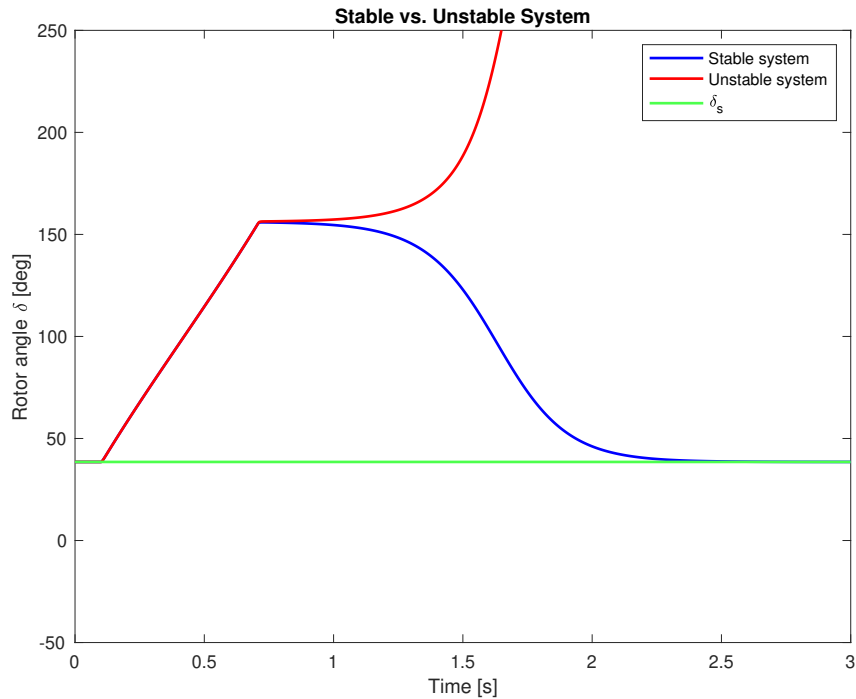ing, or smaller the inertia, the faster the speed of the VSM will be able to change. Thus, for the full deceleration process to take place in the course of $1°$, the influence of the damping on the dynamic response is very large, further emphasising the impact of damping when analysing the VSM with small inertia, as discussed for the model neglecting the damping.

Again, by comparing $\mathcal{V}$ to the critical value $\mathcal{V}_{cr}$, the critical clearing time was obtained as visualised in Figure 4.10. The CCT of $607.9$ ms is, in sharp contrast to the CCT of the system without damping, considered very high. This is also confirmed when looking at Table 4.11 in Section 4.6.7, where it is evident that the TEF with damping has yielded a CCT $57.45\%$ above the CCT of the simulated system, and thereby deemed an unstable system as stable. The analysis has thus failed its main purpose of obtaining the stability limits to ensure the safe operation of the power system. Using the classical model including damping for a Synchronverter with relatively small inertia and relatively large damping coefficient could therefore involve rather large deviations in the "*wrong*" direction from the actual stability limits, making the method less suitable for such a stability analysis. This emphasises the need for the quasi-steady method tested in the next section.

When looking at Figure 4.11, two large differences from Figure 4.9 can be noticed. The first one is the already discussed slope of the rotor angle during fault, which in addition to being much more gradual, seems to be linear. This linearity can be explained by the large damping limiting $\Delta\omega$ to reach its maximum value almost instantly before restraining $\Delta\omega$ at this constant maximum level for the duration of the fault, making the increase in $\delta$ linear.

The second large difference is seen in the rotor angle for the stable system, which, for the model

including damping, falls back to the s.e.p. after the fault-clearing. This is in line with the described theory in Section 2.8.2, stating that if damping is present, the rotor angle will settle back to the equilibrium point. This is because the value of $\mathcal{V}(\delta, \Delta\omega)$ decreases after clearing the fault due to the damping so that the state trajectories depicted in Figure 4.5b spirals back to the s.e.p.. Recalling Section 2.8.2, the system is then considered asymptotically stable. For the unstable system, the response is identical to that in 4.9 with the rotor angle accelerating fast after passing the u.e.p..

### 4.6.5 Results Using Quasi-Steady Approach

The analysis using the quasi-steady approximate Lyapunov approach is carried out according to Section 4.4.3, and $E$ is no longer considered constant. The pre-fault operating condition is however the same, yielding the pre-fault $K$'s and the initial conditions given by Tables 4.1 and 4.3 respectively.

Forward integration is then performed on the set of differential equations in (4.37a), inserted for (4.37b) and (4.37c). The stable e.p. from Table 4.3 is used as initial conditions, and the integration is carried out using the `ode45` solver for differential equations in MATLAB. For each solution of $\delta$, $E^{post}$ is to be calculated by (4.36).

At this point, some additional computational assumptions are made. At the time of fault-clearing, the magnitude of the PCC voltage is assumed to be less than $0.94$ p.u., and with $D_q$ tuned to increase the reactive power set-point by 100 percent for a 10 percent reduction in voltage, the magnitude $V_{m,pcc} < 0.94$ p.u. implies $Q_{set} > 0.6$ per unit. Also, it is assumed that when the fault is cleared, the active power set-point returns to $P_{set} = P_{ref} = 0.8$ p.u.. The stipulated $P_{set} = 0.8$ p.u. and $Q_{set} > 0.6$ p.u. yields a violation of the criterion in (3.13) for a total power rating $S_n = 1$ p.u., thus activating the reactive power set-point limitation in (3.14) which dictates $Q_{set} = 0.6$ p.u.. Therefore, as

$$\left( Q_{set} = Q_{ref} + \frac{D_q V_b}{S_b}(1 - V_{m,pcc}) \right) > \left( \sqrt{S_n^2 - P_{set}^2} = 0.6 \right) \implies Q_{set} = 0.6$$

equation (4.36) simplifies to (4.38).

$$0.6 - \left( \frac{E}{Z_{tot}} \right)^2 X_{tot} + \left( \frac{E V_g}{Z_{tot}} \right) \cos(\delta - K_3) = 0 \tag{4.38}$$

Equation (4.38) is a second-order equation that can be solved for $E$ at a given $\delta$. Therefore, for each solution of $\delta$, $E^{post}$ is calculated using (4.38), always choosing the positive solution. With $E^{post}$ obtained, the new post-fault $K$'s are calculated and used to find the new post-fault e.p., before the new $\mathcal{V}_{cr}$ is obtained by using (4.35). The value of the TEF is then calculated by (4.34) and compared to $\mathcal{V}_{cr}$.

A graphic illustration of the results is given in Figure 4.12, where the critical clearing time is found to be $t_{cc} = 0.3450$ s. At the time step of the integration corresponding to the critical clearing time, the solution of $\delta$ is obtained as $\delta = \delta_{cc} = 108.3287°$. The results of the stability analysis using the quasi-steady approximate Lyapunov approach are summarised in Table 4.8.

The dynamic system when using the AVR model is forwardly integrated for a clearing time both equal to- and 10 ms above the CCT found by the stability assessment above, for a fault initiated at $t = 0.3\,s$. The response of $\delta$ is depicted in Figure 4.13.

Table 4.8: Results of stability analysis using quasi-steady approximate Lyapunov approach.

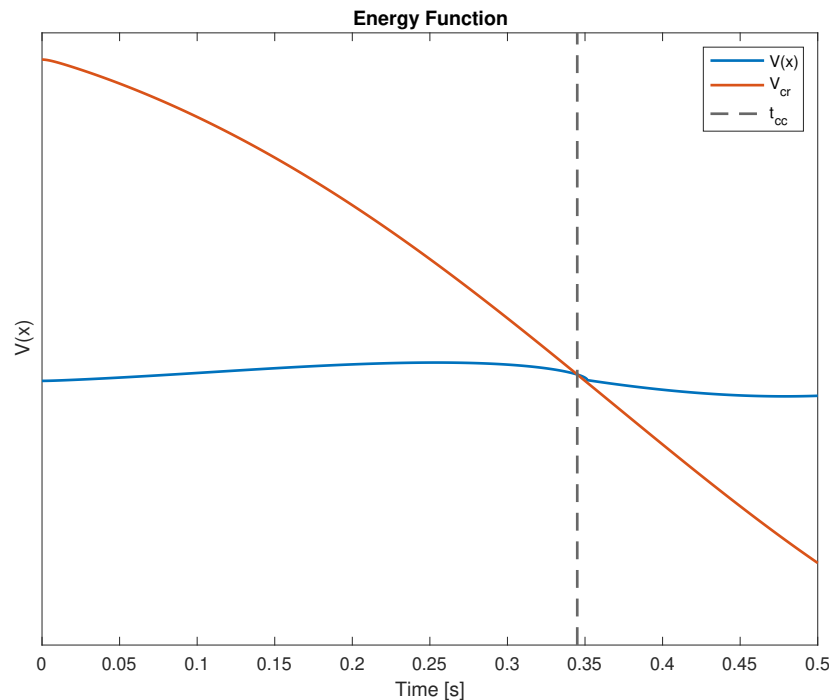| Parameter | Value |
|---|---|
| CCA, $\delta_{cc}$ | 108.3287° |
| CCT, $t_{cc}$ | $0.3450\,\mathrm{s} = 345.0\,\mathrm{ms}$ |



Figure 4.12: Energy function vs. clearing time for AVR model using the quasi-steady approximate Lyapunov method.

The need for the quasi-steady approximate Lyapunov approach when analysing the transient stability of the VSM was dedicated in Section 4.4.3 to the deteriorating effect of the AVR/RPL loop of the VSM. This was emphasised by the possibility of the back-EMF actually decreasing after the fault is cleared instead of increasing back to the nominal value, and thus contribute to further deteriorate the conditions. The argumentation above is confirmed to be valid for both the analytical system and the simulated system, as will be seen in Section 4.6.6, Figure 4.14c, where $E$ actually stabilises as low as $0.61$ p.u. after the fault has been cleared, dropping from around $0.9$ p.u. at the time of the fault-clearing. As such, an original Lyapunov method using the initial $E$ of the post-fault system to assess the stability would yield a too optimistic result as the voltage drop of the post-fault system would not be considered. Thus, the theoretical need for the quasi-steady method is well confirmed also by simulation results.

However, before any analytical results were obtained using the quasi-steady method, some assumptions were made for the calculations, and it is therefore of interest to discuss these assumptions in light of the simulation results that will be provided in Section 4.6.6 before discussing the results. The first assumption is related to the PCC voltage being less than $0.94$ p.u. at the time of fault-clearing. Looking at Figure 4.14c, this assumption is clearly justified with the PCC voltage of both the analytical system and the simulated system dropping below $0.9$ p.u.
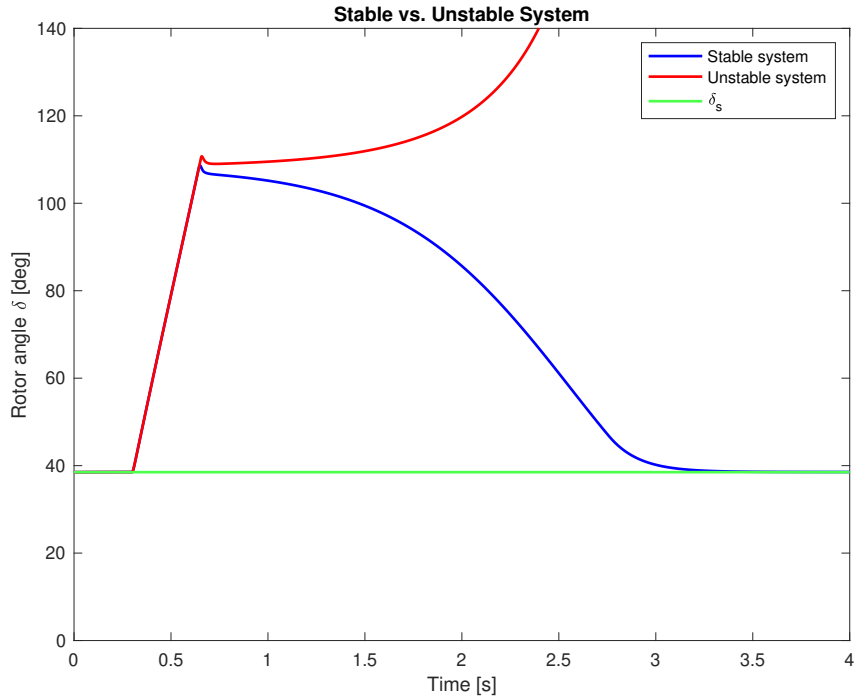
Figure 4.13: $\delta$ for stable and unstable system when using AVR model.

immediately after fault-initiation and continues to decrease during fault.

The second assumption revolves around the post-fault active power returning to $0.8$ p.u. immediately after clearing the fault. This assumption is justified by looking at Figure 4.14d, where $P$ returns to $0.8$ p.u. after a very short transient reaching higher than $0.8$ p.u. The final assumption of $Q_{set}$ being limited to $0.6$ p.u., which is truly at the core of the calculations carried out by (4.38), is confirmed looking at Figure 4.14e. Here, it is observed that $Q$ immediately follows the set-point and settles at $0.6$ p.u. directly after clearing the fault.

As the calculations are shown to be based on well-founded assumptions, the results can be more thoroughly discussed. From Figure 4.12 it is observable that, in contrast to what was the case for the classical model, the critical value of the Lyapunov function, $\mathcal{V}_{cr}$, is no longer constant but decreases with the clearing time. This is expected as a new critical value is calculated for each new post-fault $E$ resulting from (4.38). The decrease can be explained by the fact that a longer clearing time, i.e. a higher $\delta$, yields a lower post-fault $E$ by (4.38) and thus worsened stability conditions. Thus, it is seen that the stability is limited not so much by the increased value of $\mathcal{V}$, but rather the rapid decrease in $\mathcal{V}_{cr}$. This is in accordance with the theory which states that a lower $E^{post}$ yields a lower $P_e$ curve with a subsequent smaller deceleration area, meaning that the system can go unstable for an angle that the system would have remained stable at if the back-EMF was constant at the pre-fault value.

The found CCT of $345.0$ ms is to a larger extent inside the expected range of what a critical clearing time might be for a typical power system, and is thus deemed more credible than the previously found critical clearing times. Furthermore, when comparing the CCA and CCT in Table 4.8 with the results of the Simulink simulation in Table 4.11 in Section 4.6.7, two observations can be made. Firstly, the deviation from the CCT of the simulated system is only $41.1\,\mathrm{ms} = 10.64\%$ or approximately two cycles. This is quite small considering the

simplifications of the model/procedure, such as neglecting the filter capacitance of the system. This simplification will however be addressed later. With an error of approximately 2 cycles, the functioning of the method can be said to be very good, clearly taking into account the rapid response of the Reactive Power Loop. It can therefore be argued that a method of analysing the transient stability of a VSM analytically has been established in a satisfactory manner, partly based on classical stability analysis added with modifications to accommodate the distinctive characteristic of the Synchronverter VSM.

Secondly, the stability limits found by the quasi-steady method can be compared to the stability limits of the analytical system as found by the full-forward numerical integration. Such a comparison is of interest as it will provide insight into the quasi-steady method's performance related to the system it is actually analysing, i.e. the full Synchronverter dynamics without the filter capacitance as modelled in (4.15). Using the results in Table 4.11 in Section 4.6.7 it can be calculated that the discrepancy between the quasi-steady approximate Lyapunov method and the full-forward numerical integration is only $7.2\,\text{ms} = 2.04\%$ for the CCT and $\approx 1.5°$ for the CCA. This is a highly accurate prediction for such a dynamical system, and testifies further to the functioning of the modified, quasi-steady approximate Lyapunov method for analysing the stability of a VSM which is particularly influenced by the reactive power loop, i.e. the Automatic Voltage Regulator (AVR) of the VSM. It can thus be argued that by including the filter capacitance into the analytical model, the deviation towards the simulated system can be further decreased from $41.1\,\text{ms}$.

Looking at Figure 4.13, it is clear that the responses of the stable and unstable system share many of the characteristics with the responses depicted in Figure 4.11. Both of the unstable power angles quickly accelerates and diverges from the stable state, while both of the stable power angles settles back to the s.e.p.. A notable difference is however that while the stable system in Figure 4.11 settles back from a clearing angle around $150°$ in approximately 2 seconds from the time of clearing, the stable system in Figure 4.13 uses almost 3 seconds to settle back down from a clearing angle of approximately $109°$. The system in Figure 4.13 is thereby using a longer time to settle back with fewer degrees to go. This means that a side effect of the RPL is not only to worsen the stability conditions, but also to slow down the process of returning the power angle to the s.e.p. after fault-clearing.

A final observation/clarification that should be discussed regarding the quasi-steady method relates to the post-fault equilibrium points. Recalling the procedure explained in Section 4.4.3, each newly calculated $E$ is used to re-calculate the $K$'s with subsequent new post-fault equilibrium points. However, as seen in Figure 4.13, also the dynamics including the AVR will return to the same post-fault e.p. as the other models. This is as expected, due to the AVR eventually bringing $E$ back to its nominal value, yielding the same post-fault e.p. as if $E$ had been constant all along. With this in mind, the new post-fault e.p. found, and used, by the quasi-steady method only relates to the $E$ that the VSM settles at immediately after fault-clearing as calculated by (4.38).

As such, this newly calculated e.p. is only used to assess the operating conditions immediately after fault-clearing, and thus has nothing to to with the post-fault e.p. in the long term. This is important to bear in mind if e.g. calculations related to the N-1 criterion are of interest, where the post-fault e.p. could have a large influence on the system's ability to remain stable for the next contingency. This is however more relevant to other types of system/fault configurations than the one discussed in this thesis.

### 4.6.6   Results Using Full Forward Integration and Simulink Simulation

The stability assessment utilising full forward numerical integration of the system in (4.15) inserted for (4.37c) is carried out according to Section 4.5 using the `ode45` solver. A `for`-loop iterating over the clearing time is implemented, and a `break` function stops the iteration if the angle at the end of the forward integration of the post-fault system, $\delta_{end}$, is larger than $\pi$, i.e. iteration stops when $\delta_{end} > \pi$. The results of the stability analysis using full forward numerical integration are summarised in Table 4.9.

Table 4.9: Results of stability analysis using full forward numerical integration of the system.

| Parameter | Value |
|---|---|
| CCA, $\delta_{cc}$ | 109.8395° |
| CCT, $t_{cc}$ | $0.3522\,\text{s} = 352.2\,\text{ms}$ |

To find the actual CCA and CCT of the investigated system, simulations in MATLAB/Simulink were carried out. Trial and error were used to iterate on clearing times to find the actual CCT of the system, while the CCA was determined by investigating plots of the power angle at the fault-clearing time. Simulations were then carried out with a new clearing time for each simulation until the CCT was determined. The results of the stability analysis using simulations of the actual system in MATLAB/Simulink are summarised in Table 4.10.

Table 4.10: Results of stability analysis by simulating the system in MATLAB/Simulink.

| Parameter | Value |
|---|---|
| CCA, $\delta_{cc}$ | 112.2520° |
| CCT, $t_{cc}$ | $0.3861\,\text{s} = 386.1\,\text{ms}$ |

Before discussing the results, it must be mentioned that both the full-forward numerical integration method and running simulations are considerably more time consuming than any of the other discussed methods. Even for the dynamical system investigated here, which can be argued to have relatively little complexity in being a SMIB system, the analysis using full forward integration could be very time-consuming. This will of course vary depending on hardware capabilities, but with more complex systems including e.g. inter-area connections and multiple machines, the analysis quickly becomes unfeasible.

With that being said, the CCT $t_{cc} = 352.2\,\text{ms}$ of the analytical system was found to have a deviation from the simulated system of only $33.9\,\text{ms} = 8.78\%$ or approximately 1.7 cycles, while the deviation of the CCA is around 2.5°. Interestingly the CCA of 109.8995° is on the right-hand side of the power angle curve. Taking into account the diminished deceleration area due to the lowered $E$, a CCA on the right-hand side of the power angle curve further highlights the large impact damping has on the stability and dynamic response of the VSM system.

As previously discussed, a conservative result is expected when using the Lyapunov method. However, when using full forward numerical integration, the results should in theory, when ignoring numerical inaccuracies, be identical to the simulation results if the analytical model models the system of interest perfectly. This is however not the case for the analytical model of the full Synchronverter dynamics used in this thesis, as both the filter capacitance $C$ and

the associated parallel resistance $R_C$ are neglected when setting up the expressions for $P$ and $Q$ injected by the VSM. Including $R_C$ in the model would yield a higher power consumption during fault, thereby decreasing the power imbalance accelerating the rotor. Including $C$ in the model would decrease the required reactive power injection from the VSM, thereby improving the regulation of the PCC voltage and potentially yielding a faster return of $E$ to its nominal value. As such, obtaining stability limits slightly below the actual stability limits is also expected when using the full-forward numerical integration method on the simplified dynamics modelled in this thesis.

Based on the above, it is beyond doubt that the analytical approach of full-forward numerical integration can yield viable results with a high degree of precision. The results place the full-forward integration closest to the simulated system when comparing the four different methods utilising analytical models, making the full integration method a feasible option depending on the system configuration, time available, and scope/purpose of the analysis that is to be carried out. A quick investigation into system stability can for example be carried out using a less exact method, while an analysis serving as a basis for decisions revolving trip-settings for protection systems etc. should be carried out with higher precision.

The responses of the analytical system used for the full-forward numerical integration can be plotted against the responses of the simulated system. This will be done using their respective critical clearing times as clearing times. Therefore, to compare the two responses when the systems are pushed to their stability limits, the response of the analytical system is plotted for a $t_{cc} = 352.2$ ms, while the response of the simulated system is plotted for a $t_{cc} = 386.1$ ms. To obtain the responses of the simulated system, simulations were carried out using the fixed step Simulink solver `ode3` with a sample time $T_s = 1 \cdot 10^{-6} s = 1\mu s$, and had the following sequence of events:

1. The simulation was started at $t = 0$ with all IGBTs off and the circuit breaker in the open position. The wind speed is $12$ m/s. In the DC link, a resistor equal to $1.7 \cdot R_{chopper}$ was connected to obtain the DC voltage, and the virtual synchronisation currents were fed to the controllers.

2. The IGBTs on the rotor side was started at $t = 0.2$ with $V_{DC,ref} = 1126.8$ V and $Q_{ref,rotor} = 0$. Switch A in the rotor side controller was turned to position 2 to feed the real current to the controller.

3. The IGBTs on the grid side was started at $t = 0.5$ with $P_{ref} = Q_{ref} = 0$, and the voltage droop disabled, i.e. switch B open. Switch A in the grid side controller was turned to position 2 to feed the real current to the controller.

4. The circuit breaker was closed at $t = 0.8$ connecting the grid side converter to the grid.

5. $P_{ref}$ was changed to reflect the balancing de-loading of $0.8$ p.u. at $t = 1.5$, and the chopper resistance was disconnected. At the same time, switch B was closed at to activate the voltage droop loop of the grid side controller.

6. The grid voltage was decreased by $0.9$ p.u. to $0.1$ p.u. at $t = 6.0$.

7. The fault was cleared at $t = 6.3861$, bringing the grid voltage back to $1$ p.u..

8. Simulation was ended at $t = 12$

The plots depicting the response belonging to the grid side are shown in Figure 4.14 where the analytical system and the simulated system are plotted together. The plots depicting the response

belonging to the rotor side for the simulated system are shown in Figure 4.15. Note that the first
3 seconds representing the synchronisation period and period needed to reach steady-state after
simulation initialisation is omitted from the plots. Furthermore, a simulation using a clearing
time $0.5$ ms above the CCT, i.e. $t_c = 0.3866$ s, was conducted to provide interested readers with
the response of an unstable system. The results are attached in Appendix D.1.



(a) Power angle $\delta$

(b) Speed deviation $\Delta\omega$ of the VSM from the
nominal grid frequency.

(c) Amplitudes of $E$ and $V_{pcc}$.

(d) Active power injection $P$ by inverter.

(e) Reactive power injection $Q$ by inverter.

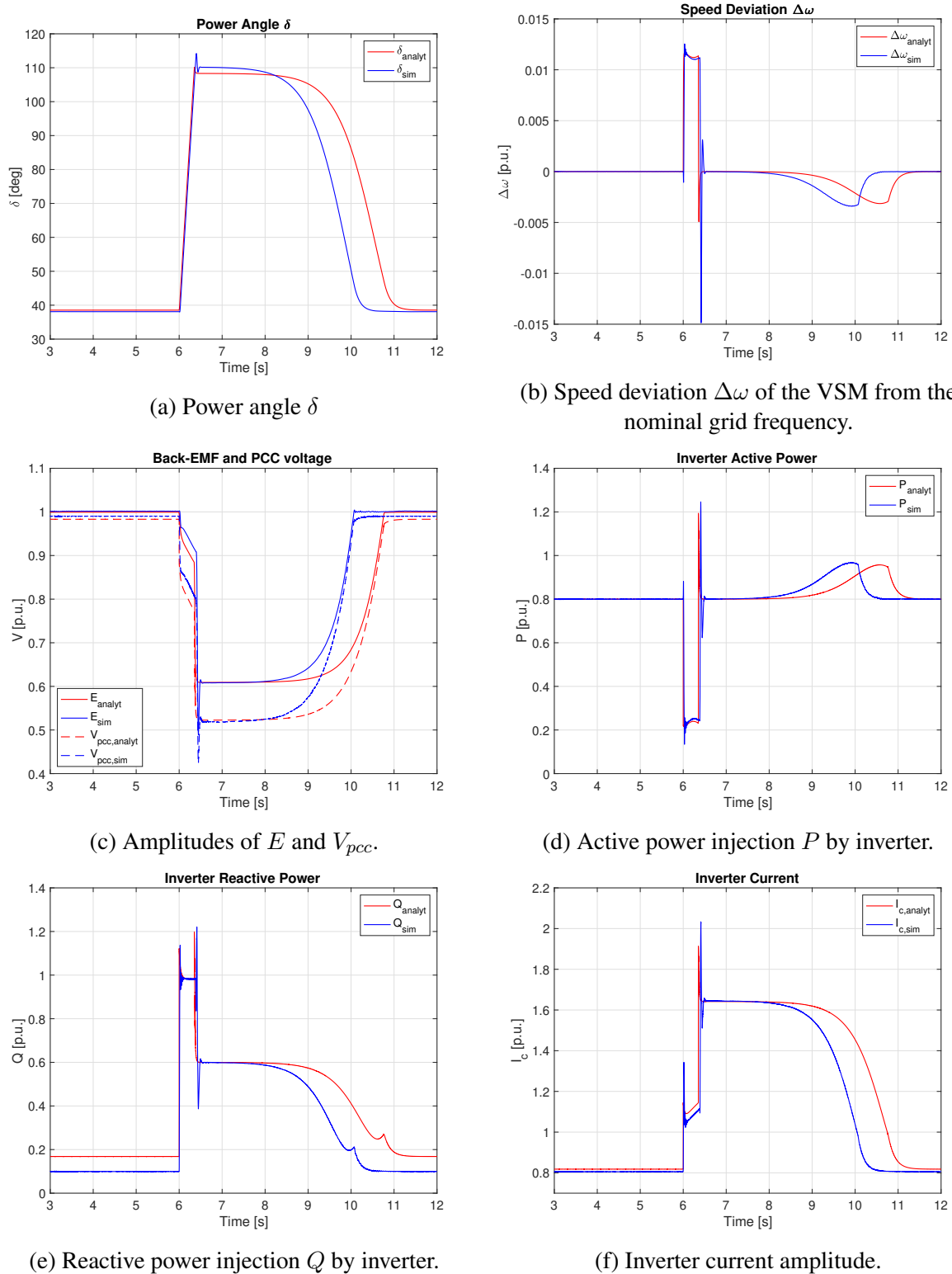(f) Inverter current amplitude.

Figure 4.14: Grid side system responses of analytical system and Simulink system.

The dynamic responses of both the analytical system and the simulated system will now be treated in detail, and compared, to further discuss the functioning of the modelled dynamics. When comparing the response of the analytical system to the response of the Simulink system it is important to remember that the two responses are related to the critical clearing times of each of the systems, i.e. the analytical system is depicted using a clearing time $t_c = 0.3522$ s, while the Simulink system is depicted using $t_c = 0.3861$ s. It has been chosen to display it this way to compare the characteristics of the responses of the two systems when pushed to their respective stability limits.

Figure 4.14a depicts the power angle of the Synchronverter VSM around the fault. It is clear that during the fault, the rotor accelerations of the two systems are nearly identical as $\delta_{analyt}$ and $\delta_{sim}$ lies on top of each other. This is confirmed looking at Figure 4.14b, where the responses of $\Delta\omega$ during fault are practically identical except for very small oscillations seen for the simulated system. Looking more closely at Figure 4.14a, a small dip can be seen for $\delta_{sim}$ immediately after fault-clearing. This dip can be seen in relation to the large transient seen in $\Delta\omega_{sim}$, which again is caused by the slightly higher transient in $P_{sim}$ immediately after clearing the fault. Even with the fault being cleared slightly after the analytical system, $\delta_{sim}$ returns to the s.e.p. faster than $\delta_{analyt}$, something which is a recurring observation valid for all the responses depicted in Figure 4.14. It is evident that the simulated system returns to its nominal steady-state operation faster than the analytical system, and it is reasonable to dedicate this difference in the responses to $C$ and $R_C$.

Small discrepancies between the analytical system and the Simulink system can be found in the responses of $E$ and $V_{pcc}$ in Figure 4.14c, where the analytical values seem to be slightly lower than the simulated ones. These discrepancies are however very small, lying between $0.005$ and $0.01$ p.u. or around $2.5$ to $5$ volts. The large difference is therefore, as for the other responses, the time it takes for the system to regain steady-state at the nominal values. This is especially important for the back-EMF $E$, as a low $E$ yields a too high current $I_c$ if injecting the rated power.

As expected from the theory, the active power during fault drops drastically, initiating the angular acceleration. Comparing Figures 4.14d and 4.14b it is observed that the responses of $P$ and $\Delta\omega$ mirror each other. This is as expected, and can be seen in relation to the swing equation where $\Delta\omega$ is inversely dependant on $P_e - P_{set}$, i.e. increased active power consumption above the power set-point decreases the speed of the VSM from the nominal speed. Furthermore, all the responses shown in Figures 4.14a, 4.14b, and 4.14d are connected through the swing equation.

Regarding the reactive power Q in Figure 4.14e, the effect of neglecting the filter capacitor $C$ is truly visualised. The analytical system can be seen to have a reactive power injection close to two times $Q_{sim}$ in steady-state due to not having the capacitor injecting reactive power at the PCC. The deviation is however fairly small during, and immediately after, the fault, which helps to justify neglecting the filter capacitance when modelling the system analytically. Also, as previously mentioned, the assumption in the quasi-steady method of $Q = 0.6$ p.u. immediately after the fault is shown to be valid.

Lastly, the inverter current is depicted in Figure 4.14f. The steady-state current of the analytical system is seen to be slightly higher than for the Simulink system, which is a direct consequence of $Q_{analyt}$ being higher than $Q_{sim}$. The amplitude of the current during fault is of particular interest, as one could normally expect this current to be way above rated values. However, looking at Figure 4.14f the current during fault is not distressingly high, being below $1.2$ p.u. during the entire fault after a small transient. The real problem of a VSC not having the capability

of limiting the current does however appear when the fault is cleared and the VSM reduces the back-EMF while increasing the power injection at the same time.

This is the case directly after the fault is cleared, with $P \approx 0.8$ p.u. and $Q \approx 0.6$ p.u. yielding $S \approx 1$ p.u.. However, with $E \approx 0.6$ p.u, $I_c$ is pushed to $\approx 1.65$ p.u. so that the VSM still injects $S = EI_c \approx 1$ p.u.. Such a high current for a prolonged period of time (several seconds as seen in Figure 4.14f) could, as previously explained, damage the converters and such an operation of the system is therefore not feasible. The need for additional control loops is thereby emphasised to mitigate the excessively high post-fault currents.

As seen from the discussion above, the responses of the Simulink system and the analytical system are to a large extent identical in their appearances, with minor discrepancies. These discrepancies have for the most part been attributed to the absence of the filter capacitor in the analytical model, further yielding a slower return to steady-state for the analytical model after clearing the fault. This can be identified by the clearly visible time delay between the two responses post fault. However, as the dynamical response during fault, which is of particular interest when using the quasi-steady method, can be argued to be very much the same for the two systems, the performance of the analytical equations used to describe the full dynamics of the Simulink system is concluded to be beyond sufficient for the applications in this thesis.

It must also be mentioned that even though the stability limit in the sense of the transient rotor angle stability was found to be $t_{cc} = 0.3861$ s, the dynamic responses show that clearing at this CCT would yield an unfeasible operating scenario due to the high post-fault current. This could potentially lead to the disconnection of the converter due to thermal capacity protection systems. The actual stability limit of the converter as a whole can therefore be argued to be lower than what is found by investigating only the rotor angle stability, as clearing at a lower clearing angle would yield a more feasible post-fault operating scenario.

The rotor side of the back-to-back converters, including the rectifier, has not been discussed or treated in detail in the stability analysis so far. It was however assumed in Chapter 4 that the rectifier would be able to control the DC voltage also during the fault, so that only the grid side needed to be investigated in the analytical analysis. Also, as the stability analysis revolves around the entire WECS and not only the inverter, plots are provided in Figure 4.15 depicting the responses of some key rotor side variables for the same simulation as the one providing the grid side results in Figure 4.14. Therefore, a brief explanation and discussion revolving the rotor side will be given here.

The DC link voltage is depicted in Figure 4.15a where it is clear that the assumption of constant DC voltage is not entirely justified. A large spike occurs at the initiation of the fault, while a large dip occurs at the time of fault-clearing. These two large deviations are caused by the sudden changes in active power consumption at the grid side, where a large drop in $P$ yields a spike in $V_{DC}$ and vice versa. This is because a large drop in active power consumption at the grid side results in a large drop in the DC current. The response is however dampened by the well-tuned PI controller of the rectifier control system, which quickly controls the DC voltage to track the reference value again after the contingency, with some small deviations also during the process of decreasing the power angle around $t = 10$ s. The large deviation of up to $\pm 0.25$ p.u. in the DC voltage does however seem to not influence the response of the grid side inverter.
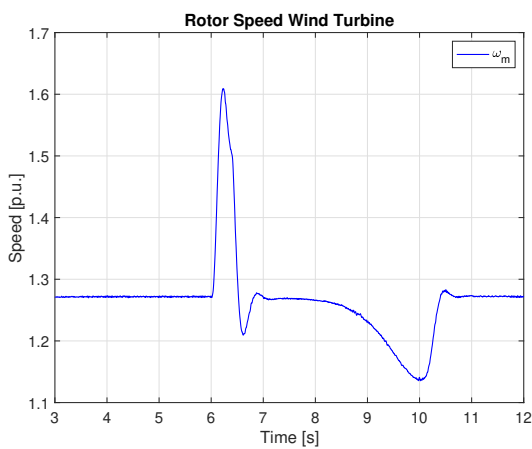
With that being said, a simplification that may affect the stability should be mentioned when discussing the DC link voltage. While the chopper resistance in the DC link is implemented in the simulation model and used during the initialisation process, it is not implemented in such
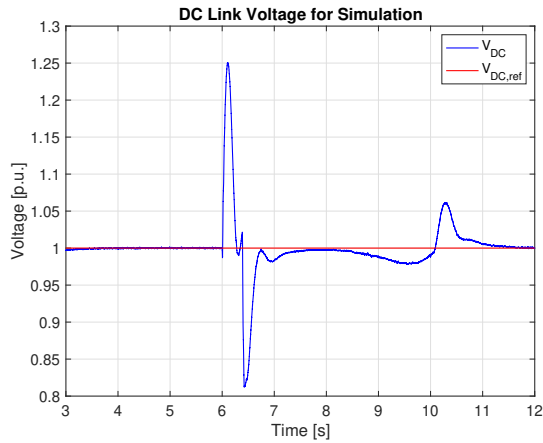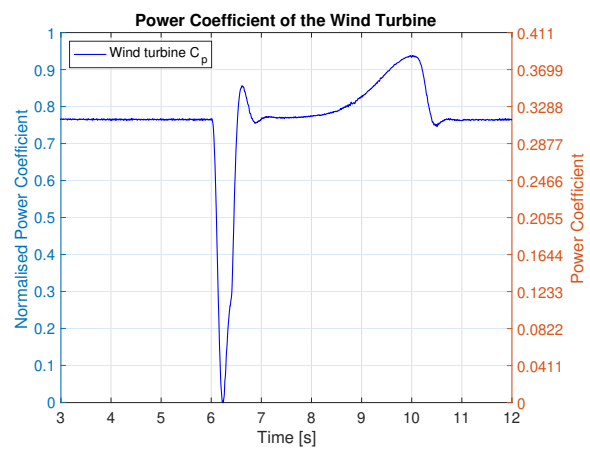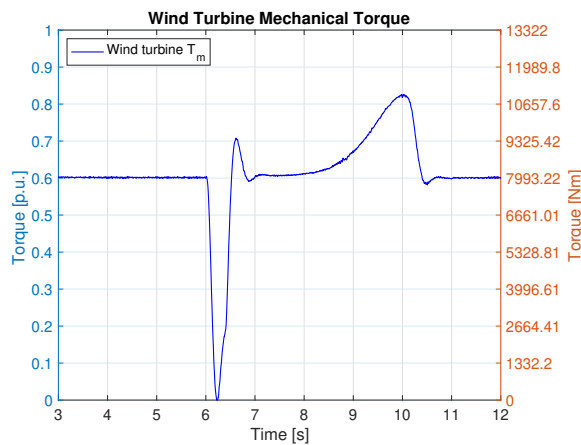
(a) DC link voltage.
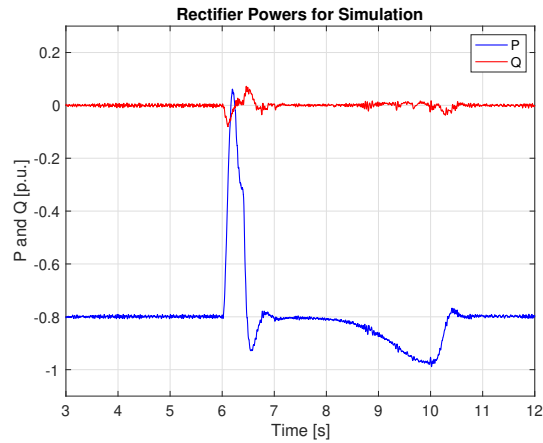
(b) Powers calculated by the rectifier control system.



(c) Mechanical rotor speed of the wind turbine.

(d) Power coefficient of the wind turbine.



(e) Mechanical torque of the wind turbine.

Figure 4.15: Rotor side response of original Simulink system when fault is cleared at the CCT $t_{cc} = 386.1 \, \text{ms}$.

a way that it serves its designed purpose, i.e. being switched in if the DC voltage exceeds a given value. As such, the transients in the DC link voltage, reaching up to $1.25$ p.u. at the time of fault-initiation, could potentially have triggered the chopper in a real application, something which is not considered in the stability analysis.

Looking at the rectifier $P$ and $Q$ in Figure 4.15b it is evident that the rectifier controller is able to maintain a power factor close to 1 due to $Q$ being controlled to zero, which is one of its controller objectives. Note that, as per the convention explained in Section 2.3.2, the rectifier powers are calculated to be negative. During the fault, $P$ calculated by the inverter changes drastically to the point where, according to Figure 4.15b, the rotor side actually consumes power, i.e. $P_{rectifier} > 0$. However, it is known from Figure 4.14d that the inverter at the grid side injects just above 0.2 p.u. of active power. The fact that for a very small time period $P_{rectifier} > 0$ should therefore be discussed more in detail. Especially since this will be a recurring observation for all the rotor side results seen throughout the thesis.

One explanation for $P_{rectifier} > 0$ could be that the plot depicts the instantaneous powers and not the line frequency average powers. This means that while the instantaneous $P$ might be positive, the average $P$ over the period will still be negative, i.e. the active power flowing from the rotor side to grid side. Another explanation can be found by taking a closer look at the wind turbine model used in the Simulation. The power curves for the wind turbines used in the aggregated model is depicted in Figure 2.2, and it is known that the torque curves have a similar appearance. As the rotor speed increases excessively, the output mechanical power, and torque, of the turbine decreases to a point where the torque actually can become negative. If the turbine torque drops below zero for just a couple of milliseconds, the torque applied to the PMSG would be negative and the PMSG would operate as a motor, driving the turbine. This can also be seen in Figure 4.15e where the mechanical output torque of the turbine drops instantly, also followed by the drastic drop in the power coefficient as see in Figure 4.15d.

The very short period of $P_{rectifier} > 0$ is thus attributed as a consequence of the simplifications of not including turbine control such as pitch control in the scope of the thesis. This has the direct consequence of yielding excessively high rotor speeds to the point where the mechanical torque becomes negative and the PMSG starts to act as a motor driving the turbine. This would never happen in a real WECS application, as rotor breaks or pitch control would have kicked in, keeping the turbine within an admissible area on the torque curve, also limiting wear and tear on turbine components.

Lastly, the mechanical speed of the rotor of each wind turbine of the aggregated model is seen to experience large variations in Figure 4.15c. The large variations are caused by the changing electromagnetic torque applied to the PMSG, which can be clearly seen by comparing the plot of $P$ in Figure 4.15b with the speed variations in Figure 4.15c.

To summarise, the steady-state performance of the rotor side is as excepted, with the rectifier controller achieving all of its control objectives and the wind turbine operating at expected values considering the de-rated power set-point. During the fault, the rotor side of the WECS does experience large variations but is nicely controlled back to steady-state again after the contingency has been resolved. Moreover, even though the rotor side has these large variations, the stability of the grid side does not seem to be affected, meaning the simplification of only considering the grid side in the analytical analysis can be justified. As such, the rotor side performance is considered more than adequate for the scope and applications of this thesis.

### 4.6.7  Summary of Stability Analysis for Original System.

The stability limits obtained by the stability analysis carried out in this chapter, including their deviation from the actual critical clearing time of the simulated system, are summarised in Table 4.11. Note that a negative deviation from the real CCT denotes that the prediction is too high, thus predicting an unstable system to be stable. The table is added here to provide the reader with easy identification and comparison between the methods. The Table further emphasises the large differences in performance already discussed for the different methods.

Table 4.11: Stability limits using different assessment methods.

| Method | CCA | CCT | $\Delta$CCT [%] |
|---|---|---|---|
| Equal Area Criterion | 89.5836° | Not applicable | Not applicable |
| TEF w/o Damping | 89.3926° | $0.0445\,\text{s} = 44.5\,\text{ms}$ | 88.47% |
| TEF w Damping | 155.3479° | $0.6079\,\text{s} = 607.9\,\text{ms}$ | -57.45% |
| Quasi-steady approx. Lyapunov | 108.3287° | $0.3450\,\text{s} = 345.0\,\text{ms}$ | 10.64% |
| Full Forward Integration | 109.8395° | $0.3522\,\text{s} = 352.2\,\text{ms}$ | 8.78% |
| Simulink Simulation | 112.2520° | $0.3861\,\text{s} = 386.1\,\text{ms}$ | 0% |

# Methods to Improve the System Stability

*This chapter puts forward a set of additional control loops that can be introduced to the Synchronverter control system to increase the stability margins, and thus enhance the system stability. First, an introduction into methods of improving the transient stability of conventional power systems is given, before how to quantify the improvement is established. Then, the concept of a power correction loop is introduced, before the use of a virtual resistor and artificial damper windings are proposed for the Synchronverter VSM. Lastly, simulations are carried out to validate the effectiveness and functioning of the proposed enhanced control systems. The performance of each method is then discussed and compared to the other methods.*

## 5.1   Introduction

There exist several different methods of improving the transient stability of the conventional power system. Common equipment such as fast circuit breakers with automatic re-closing after fault-clearing can improve the stability by reducing the acceleration area and $t_c$, in addition to increasing the deceleration area when re-connecting load faster[34]. More expensive- and equipment-intensive methods requiring investment in additional infrastructure include, but are not limited to, braking resistors, shunt capacitor devices and series compensation[32].

Braking resistors, or shunt resistors, are switched in close to the generating unit during, and after, a fault to increase the electric power consumption and thus decrease, or brake, rotor acceleration due to the imbalance of powers in the swing equation. This effectively reduces the acceleration area and increases the available deceleration area of the $P - \delta$ curve, thus increasing the CCA/CCT. The use of shunt capacitors effectively increase the loading capability, i.e. maximum power transfer capability, of transmission lines and thus increase the potential acceleration area. However, shunt capacitors are mainly used for maintaining an acceptable voltage profile[34], and series capacitor compensation is therefore a much more effective way of increasing the power transfer capability by reducing the line reactance.

Another method adopted to improve transient stability is fast valving, which rapidly decreases the mechanical input torque, and thus the acceleration torque applied to the machine. However, to ensure stability, the reduction in acceleration torque should take place during the first few tenths of a second following a disturbance, and restoring the power to the required post-fault value should take less than a second[32]. With current technology, the pressure changes and

---

huge torques involved for such control actions in hydro turbines makes it unfeasible. Steam turbines on the other hand are capable of responses very close the required control action time. Thus, fast valving is extensively used in modern steam turbines.

Lastly, even the tripping of one or more generating units operating in parallel on a common bus bar has been used to improve stability. This by rapidly changing the torque balance on the remaining generators to ensure that they don't lose synchronism. The use of this method in the modern power system is achieved without the need of going through the lengthy shutdown and start-up cycles common to generators. This is done by disconnecting the unit from the grid, but continue running the generator in island mode supplying the power station and related facilities. The generator can then be re-synchronised to the grid and brought back to full power in only a couple of minutes. The method does however involve some large disadvantages such as frequency and power variations between synchronised, interconnected systems.[32]

As explained above, several methods are used in the conventional power system to improve transient stability. However, it has been argued that these methods either involve extra costs, are not applicable to some turbine types, or have other disadvantages. The use of power electronics does however open up a new landscape of possible methods of improving the transient stability in the modern power system. It is therefore of interest to find new implementations that can be introduced into the controls of power electronics to drastically improve the stability without adding large Capital Expenditures (CAPEX) and Operational Expenditures (OPEX). Adding control loops that can apply appropriate control signals to improve stability requires practically no additional costs as everything is implemented electronically. This will therefore be the objective of this Chapter.

Furthermore, the switching devices of converters have limited thermal capacity[64]. It is therefore common to disconnect converters if the current rises to high to avoid high currents damaging the converters. Thus, converters are traditionally known to have very poor Fault Ride Through (FRT) capabilities. This is further emphasised by the fact that the original Synchronverter VSM does not have the ability to limit the inverter current due to being a voltage-controlled, not current-controlled, control system[65].

As such, current limitation of VSC by use of inner current loops has been the topic of several studies, but many of them show that current limitation makes the converter more prone to lose synchronous stability[66], and thus reduces the transient stability. Recent research however, has proposed to include virtual impedances in the controls to limit fault currents and inrush currents of voltage-controlled VSMs, and the results are quite promising[67].

From the discussion in Section 4.4.3 and the results in Section 4.6.6 it is known that the back-EMF of the VSM, $E$, will not return to its nominal value immediately after clearing the fault due to the high power angle and the integrator. As such, the low $E$ may result in an undesirable high current when the converter injects the rated power immediately after the fault has been cleared. Based on this, it will be advantageous to achieve a high electromagnetic torque, or a significantly improved damping effect, to both slow down the acceleration of the rotor angle and return the power angle to the stable e.p. as soon as possible after the fault is cleared. This will facilitate that $E$ can be controlled back up to its nominal value, reducing the time operating with a high post-fault current.

This advanced electromagnetic torque, or improved damping, can be realised in different ways, such as control loops making the power injection seem higher than what it actually is to slow down the VSM, a VSM version of fast valving known as a power correction loop, or even by

introducing virtual damper windings known from the conventional SG.

Two main controller objectives are therefore defined for the enhanced control loops that will be investigated here:

1. Improve the system stability.

2. Mitigate the post-fault current, i.e. limit the time operating at excessively high converter currents.

The improvement in stability can be measured in a couple of different ways, and two methods will be presented and used here. First, the improvement in the stability limit, i.e. CCT $t_{cc}$, can be measured in percent using (5.1). Here, $t_{cc,enhanced}$ is the new critical clearing time using enhanced control loops and $t_{cc,orig}$ is the CCT of the original system.

$$\mathcal{I} = \left( \frac{t_{cc,enhanced} - t_{cc,orig}}{t_{cc,orig}} \right) \cdot 100\% \tag{5.1}$$

Second, the stability margin, i.e. margin between the clearing time and the critical clearing time, of the enhanced system when the fault is cleared at the critical clearing time of the original system can be calculated using (5.2).

$$\mathcal{M}_{stab} = \left( \frac{t_{cc,enhanced} - t_{cc,orig}}{t_{cc,enhanced}} \right) \cdot 100\% \tag{5.2}$$

## 5.2   Enhanced Control Loops

### 5.2.1   Power Correction Loop

From the analysis in Chapter 4 it is evident that the angular instability of the VSM is due to sustained imbalance between the power set-point and the actual delivered power, causing the virtual angle of the VSM to accelerate. It is known from conventional Synchronous generators that the transient stability can be improved by governor action, i.e. fast valving explained in Section 5.1, reducing the mechanical power applied to the turbine during fault[44]. However, this process involves mechanical parts and thus may have some time delay which will impact the ability to improve stability for the conventional SG. This is not the case for the VSM which can change its power set-point instantly.

It is therefore of interest to introduce a new control loop that reduces the power set-point of the converter if subjected to a severe voltage fault. This will be an adoption of fast valving to the VSM. A Power Correction Loop (PCL) was proposed for a general VSM in [56], and this loop will now be adapted to the Synchronverter control structure. First, the grid voltage amplitude, $V_{g,meas}$, is measured. If the grid voltage decreases below a pre-defined set-value, $V_{set}$, an additional loop is activated, altering the input torque by subtracting a torque $\Delta T_{m,corr}$ from the reference torque. The torque $\Delta T_{m,corr}$ will be calculated using (5.3), where $M$ is a constant coefficient that governs the correction torque based on difference between the nominal voltage $V_n$ and the measured grid voltage $V_{g,meas}$.

$$\Delta T_{m,corr} = M(V_n - V_{g,meas}) \tag{5.3}$$

The constant $M$ can be tuned according to (5.4) where $\Delta V = V_n - V_{g,meas}$. This will set how large the correction in the reference torque will be for a given decrease in grid voltage.

$$M = \frac{\Delta T_{m,corr}}{\Delta V} = \frac{\Delta P_{m,corr}}{\omega_n \Delta V} \tag{5.4}$$

The PCL is added to the Synchronverter control structure as depicted in the blue box in Figure 5.1, and will effectively reduce the rotor angle acceleration.
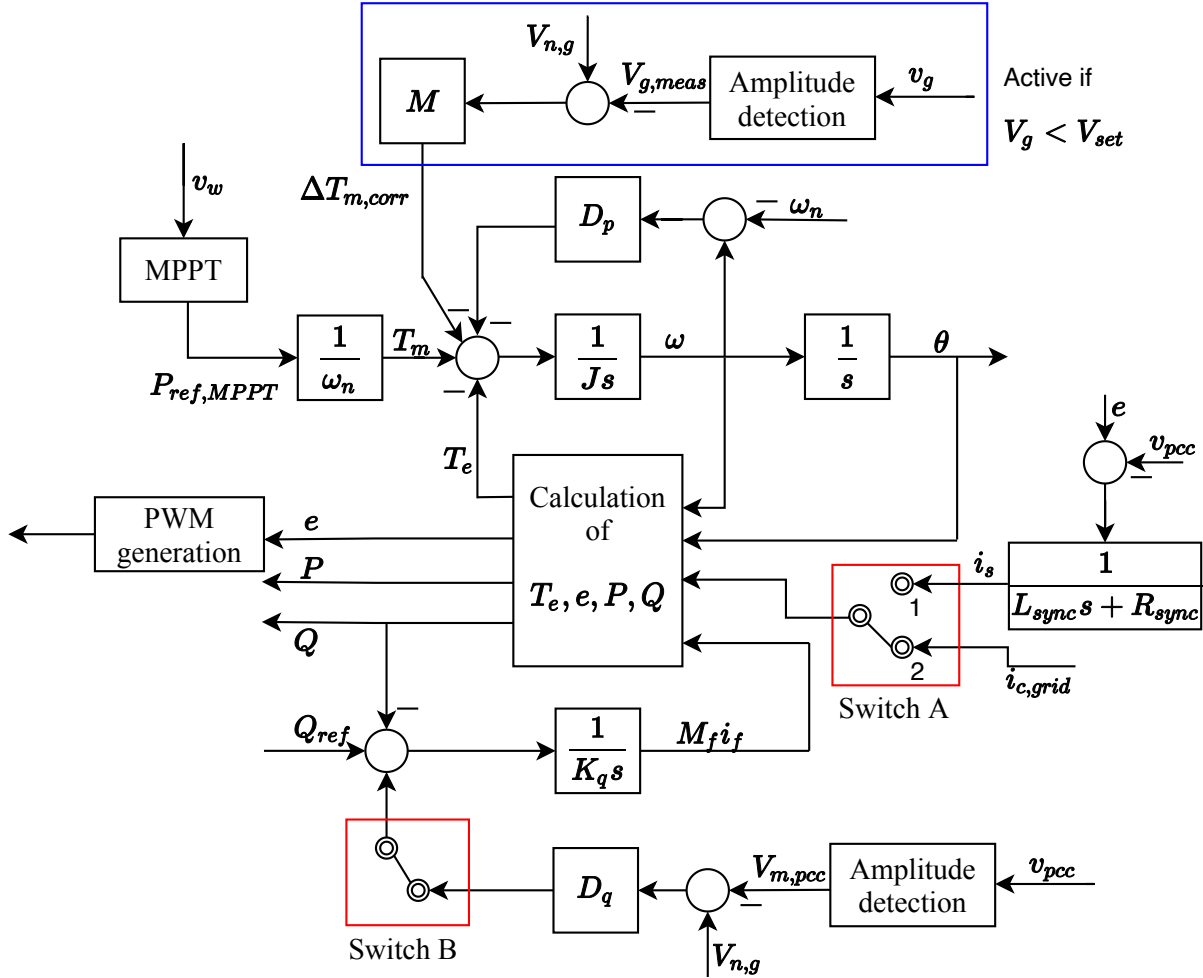


Figure 5.1: Enhanced control structure including power correction loop.

Furthermore, the added control loop can easily be added to the analytical dynamics and subsequent stability analysis of the Synchronverter system by use of the quasi-steady approximate Lyapunov approach in Section 4.4.3. This is because the modified set-point during fault does not affect the post-fault system, and therefore the derived quasi-steady method does not need to be modified. To accommodate the PCL in the quasi-steady approach, the dynamics of the fault system in (4.37a) is added with the term $\Delta P_{m,corr}$ calculated as

$$\Delta P_{m,corr} = \frac{M\omega_n \Delta V}{S_b}$$

in per unit. This yields the fault dynamics given by (5.5) to be used in the analytical stability assessment of the system added with the PCL.

$$\dot{\boldsymbol{x}} = \begin{bmatrix} \dot{x}_1 \\ \dot{x}_2 \\ \dot{x}_3 \end{bmatrix} = \begin{bmatrix} x_2 \cdot \omega_n \\ \frac{S_b}{\omega_n^2 J}\left(P_{ref} - \Delta P_{m,corr} - (K_{1p} + K_2 \sin(x_1 - K_3)) - \frac{\omega_n^2 D_p}{S_b} x_2\right) \\ \frac{S_b}{M_f i_{f,b} \cdot K_q}\left(Q_{ref} - (K_{1q} - K_2 \cos(x_1 - K_3)) + \frac{D_q V_b}{S_b}(1 - V_{m,pcc})\right) \end{bmatrix} \tag{5.5}$$

## 5.2.2  Virtual Resistor

The power correction loop in Section 5.2.1 has the obvious drawback of needing an additional measurement of the grid voltage, implying the need for extra equipment with associated costs that may be impractical or even unfeasible to the operator. It is therefore of interest to find additional methods of enhancing the system stability, which can be implemented without adding any new hardware, such as sensors and communication devices, that are not already needed for the original Synchronverter control system.

As implementing a virtual impedance to limit the fault current has been investigated by the scientific community already, a hybrid method will be proposed here, adding a Virtual Resistor (VR) if the current is too high. The idea behind the Virtual Resistor is to synthesise a higher active power injection than what is actually the case when the current is too high. This will be done by decreasing the back-EMF through a virtual voltage drop, and will subsequently yield a smaller imbalance between the power set-point and the calculated injected power, reducing the acceleration of the power angle during the fault. After the fault has been cleared, the large synthesised active power should yield a faster deceleration of the power angle, returning the power angle to its s.e.p. value faster, making it possible for $E$ to return faster to its nominal value.

It is important to note that this is not a current limiting method meant to limit the current to some set maximum value, but instead manipulate the active power injection calculated by the inverter. This will manipulate the electromagnetic torque working on the power angle through the swing equation. Therefore, the highly inductive fault current and the reactive power injection will to a large extent remain unchanged as no modifications are done to alter the reactive power/current.

The voltage drop $v_{vr}$ across the virtual resistor $R_{vr}$ will be calculated using (5.6) where $i_{c,grid}$ is the measured converter current.

$$v_{vr} = R_{vr} i_{c,grid} \tag{5.6}$$

Having the voltage drop $v_{vr}$, the reference signals, $e_{ref}$, sent to the PWM module can be calculated as

$$\begin{aligned} e_{ref} &= e \quad , \quad |i_{c,grid}| \leq I_{set} \\ e_{ref} &= e - v_{vr} \quad , \quad |i_{c,grid}| > I_{set} \end{aligned} \tag{5.7}$$

where $e$ is the back-emf calculated by (3.1b), and $I_{set}$ is a pre-defined current magnitude which serves as the threshold triggering the virtual resistor. For simplicity and to limit the scope of the thesis, the fine-tuning of $R_{vr}$ is left for later research. The virtual resistor loop is added to the Synchronverter control structure as depicted in the blue box in Figure 5.2.
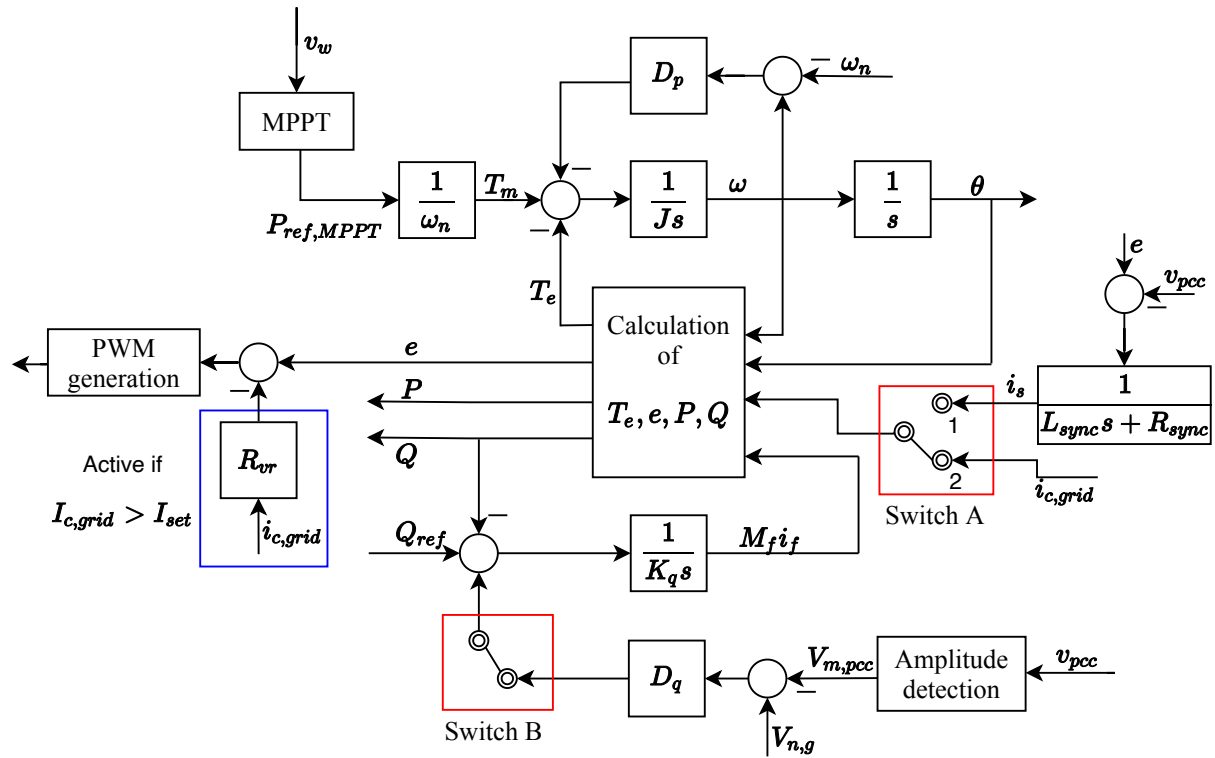
Figure 5.2: Enhanced control structure including virtual resistor.

## 5.2.3   Virtual Damper Windings

The original Synchronverter from [27][28] combines the governor droop function with the damping, purely based on the VSM's speed deviation from the nominal frequency. However, as pointed out in [68], this may lead to poorly damped dynamics when the frequency droop rate is chosen sufficiently large, i.e. $D_p$ is tuned to be small. Therefore, [68] lists several other possible implementations of damping to the VSM found in the literature, including the use of frequency measurement by use of PLL, using the frequency derivative, and even implementing a power forward term. In addition, a simple, yet challenging, implementation of a Power System Stabiliser (PSS) to dampen the voltage amplitude is proposed.  However, all of the proposed damping methods have the inherent property of requiring tuning which in many cases can be both challenging and time-consuming.

Therefore, to further improve the controller performance when subjected to a large contingency, a novel implementation of virtual damper windings to the Synchronverter VSM will be invest-igated. Damper windings are well-known to reduce mechanical oscillations and hunting in the conventional Synchronous generator[44] without the need of additional tuning, and the method proposed here will add the damping power to the power set-points of the Synchronverter. The derivation of the electrical equations revolving around the damping power in the conventional SG are long and tedious. Therefore, only the essential parts needed to derive the control method are included here. The explanation of the damper windings will largely follow the derivations in [34], and is based on the same assumptions as was used in Section 2.3, except that damper windings are now included.

It is known that the stator of a Synchronous generator is represented by the three magnetic axes $a$, $b$ and $c$, corresponding to the phase windings, while the rotor is represented by the pole axis ($d$-axis) and the inter-pole axis ($q$-axis)[34]. The rotor will be equipped with two short-circuited

damper windings, one in the *d-axis* and one in the *q-axis* as depicted in Figure 5.3. In Figure 5.3, $\beta_m$ is the angle of the rotor with respect to the stationary reference *a*-axis, and equals the angle $\theta$ of the of the Synchronverter. Furthermore, $L_{aa}$, $L_{bb}$, and $L_{cc}$ are the self-inductances of the stator windings, while $L_{ff}$, $L_{DD}$, and $L_{QQ}$ are the self-inductances of the field- and damper windings respectively. $r_a$, $r_b$, $r_c$, $r_f$, $r_D$ and $r_Q$ are the related resistance of each of the windings.
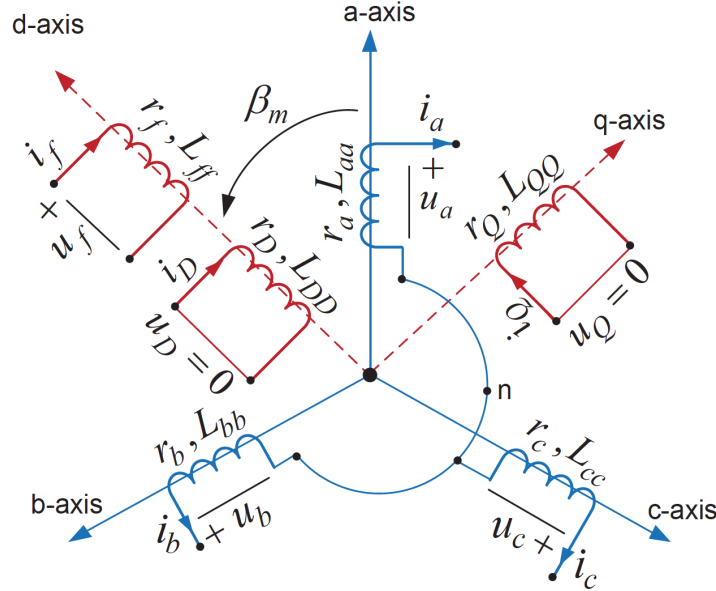


Figure 5.3: Structure of a synchronous generator including damper windings[34].

Since the windings are magnetically coupled, the flux linkages are given by

$$
\begin{bmatrix}
\Phi_a \\
\Phi_b \\
\Phi_c \\
-- \\
\Phi_f \\
\Phi_D \\
\Phi_Q
\end{bmatrix}
=
\begin{bmatrix}
L_{aa} & L_{ab} & L_{ac} & | & L_{af} & L_{aD} & L_{aQ} \\
L_{ba} & L_{bb} & L_{bc} & | & L_{bf} & L_{bD} & L_{bQ} \\
L_{ca} & L_{cb} & L_{cc} & | & L_{cf} & L_{cD} & L_{cQ} \\
-- & -- & -- & | & -- & -- & -- \\
L_{fa} & L_{fb} & L_{fc} & | & L_{ff} & L_{fD} & L_{fQ} \\
L_{Da} & L_{Db} & L_{Dc} & | & L_{Df} & L_{DD} & L_{DQ} \\
L_{Qa} & L_{Qb} & L_{Qc} & | & L_{Qf} & L_{QD} & L_{QQ}
\end{bmatrix}
\begin{bmatrix}
i_a \\
i_b \\
i_c \\
-- \\
i_f \\
i_D \\
i_Q
\end{bmatrix}
\tag{5.8}
$$

where $L_{mn} = L_{nm}$ is the mutual inductance between winding *m* and *n*. It can be shown that when neglecting the two damper windings, the linkages in (5.8) are identical to the flux linkages derived in (2.14). Since many of the inductance elements vary with the angle, it is common to transform the flux linkages from the stator reference frame to the rotor reference frame, i.e. from *abc*-components to *dq0*-components which rotate together with the rotor. This can be done by using the well-known Park's coordinate transformation in (5.9) and (5.10).

$$
\boldsymbol{P} = \sqrt{\frac{2}{3}}
\begin{bmatrix}
\cos(\theta) & \cos(\theta - \frac{2\pi}{3}) & \cos(\theta + \frac{2\pi}{3}) \\
\sin(\theta) & \sin(\theta - \frac{2\pi}{3}) & \sin(\theta + \frac{2\pi}{3}) \\
\frac{1}{\sqrt{2}} & \frac{1}{\sqrt{2}} & \frac{1}{\sqrt{2}}
\end{bmatrix}
\tag{5.9}
$$

$$\boldsymbol{v}_{dq0} = \boldsymbol{P}\,\boldsymbol{v}_{abc}$$
$$\boldsymbol{i}_{dq0} = \boldsymbol{P}\,\boldsymbol{i}_{abc} \tag{5.10}$$
$$\boldsymbol{\Phi}_{dq0} = \boldsymbol{P}\,\boldsymbol{\Phi}_{abc}$$

Using Park's coordinate transformation and applying mathematical derivation, the flux linkages in (5.8) are rewritten into three magnetically decoupled winding sets as in (5.11)[34].

$$
\begin{bmatrix} \Phi_d \\ \Phi_f \\ \Phi_D \end{bmatrix} =
\begin{bmatrix} L_d & kM_f & kM_D \\ kM_f & L_{ff} & L_{fD} \\ kM_D & L_{fD} & L_{DD} \end{bmatrix}
\begin{bmatrix} i_d \\ i_f \\ i_D \end{bmatrix}
$$
$$
\begin{bmatrix} \Phi_q \\ \Phi_Q \end{bmatrix} =
\begin{bmatrix} L_q & kM_Q \\ kM_Q & L_{QQ} \end{bmatrix}
\begin{bmatrix} i_q \\ i_Q \end{bmatrix} \tag{5.11}
$$
$$
\Phi_0 = L_0 i_0
$$

Here the notation is changed so that $M$ represents the mutual inductance and $k = \sqrt{\frac{3}{2}}$. Recalling that for balanced three-phase systems $i_0 = 0$ yields $\Phi_0 = 0$. It is now possible to extract the parts of (5.11) that are of interest for the introduction of virtual damper windings to the VSM. Only the flux linkages of the $d$- and $q$-axis are of interest, i.e. $\Phi_d$ and $\Phi_q$, which can be found from (5.11) as

$$\Phi_d = L_d i_d + kM_f i_f + kM_D i_D \tag{5.12a}$$

$$\Phi_q = L_q i_q + kM_Q i_Q \tag{5.12b}$$

Using (5.12a) and (5.12b), the PCC voltage, i.e. the terminal voltage of the VSM, in *dq* coordinates can be expressed as in (5.13a) and (5.13b) where $R_s$ is the resistance of the filter inductance $L_s$, $L_d = L_q = L_s$ for the VSM and $\omega$ is the converter speed.

$$v_d = -\omega\Phi_q - R_s i_d = -\omega L_q i_q - \omega kM_Q i_Q - R_s i_d \tag{5.13a}$$

$$v_q = \omega\Phi_d - R_s i_q = \omega L_d i_d + \omega kM_f i_f + \omega kM_D i_D - R_s i_q \tag{5.13b}$$

Equations (5.13a) and (5.13b) can now be used to find expressions for calculating $M_D i_D$ and $M_Q i_Q$ which are the flux contributions from the damper windings onto the *d*- and *q* voltages.

$$M_D i_D = \frac{v_q - \omega L_d i_d + R_s i_q - \omega kM_f i_f}{\omega k} \tag{5.14a}$$

$$M_Q i_Q = \frac{v_d + \omega L_q i_q + R_s i_d}{-\omega k} \tag{5.14b}$$

Thus, utilising the already available measurements of $v_{pcc}$ and $i_{c,grid}$ and applying the Park transformation, both $M_D i_D$ and $M_Q i_Q$ can be calculated using (5.14a) and (5.14b). Both $M_D i_D$

and $M_Q i_Q$ are zero in steady-state and will therefore not change the steady-state characteristic of the converter. As soon as a transient occurs, $M_D i_D$ and $M_Q i_Q$ becomes non-zero and can thus be used to implement damping power into the set-points of the VSM. The expression for $M_D i_D$ will however need some slight adjustments to serve the desired purpose for the applications in this thesis. In its current form, $M_D i_D$ will return to zero even before the fault is cleared if the fault clearing time is long, yielding a good response to small-signal disturbances but limited effect during large, longer-lasting disturbances. Moreover, it is desired to have the effect of the damper windings also after the fault has been cleared, until the system has again reached its nominal operating points.

In (5.14a), the expression for $E$ is recognised as the last part. Looking more closely it can be deduced that as long as $v_q$ plus the voltage drop across the filter resistance and inductance equals the back-EMF of the VSM, $M_D i_D$ will be zero. As described above, we want to have a contribution from the virtual damper windings as long as the VSM does not operate at its nominal set-points. Therefore, the actual back-EMF, $E = \omega M_f i_f$, is replaced with the nominal back-EMF $E_n = \omega_n M_f i_{f,n}$ in the expression for $M_D i_D$ yielding (5.15), where both the measured PCC voltage and the measured converter current have been transformed using Park's transformation.

In theory, this will yield a contribution from the artificial damper windings, i.e. $M_D i_D \neq 0$, for as long as $E \neq E_n$, due to the fact that $v_q$ plus the voltage drop across the filter inductance, and related resistance, will not be equal to $E_n$. This is beneficial considering the dynamic of $E$ when operating far from the equilibrium point immediately after the fault has been cleared. The modifications will not impact the steady-state characteristic of the VSM as $M_D i_D$ will still be zero in steady-state when $E = E_n$.

$$M_D i_D = \frac{v_q - \omega L_d i_d + R_s i_q - \omega_n k M_f i_{f,n}}{\omega k} \tag{5.15}$$

Having calculated both $M_D i_D$ and $M_Q i_Q$ using (5.15) and (5.14b) respectively, the damper windings contribution to the VSM set-points can be calculated using (5.16a), (5.16b) and (5.16c), where $i$ is the measured three-phase converter current and $\widetilde{\cos}\,\theta$ and $\widetilde{\sin}\,\theta$ are still defined as in (2.12). Again, $\langle \cdot, \cdot \rangle$ denotes the inner product in $\mathbb{R}^3$.

$$T_D = -M_D i_D \langle i, \widetilde{\sin}\theta \rangle + M_Q i_Q \langle i, \widetilde{\cos}\theta \rangle \tag{5.16a}$$

$$P_D = -\omega M_D i_D \langle i, \widetilde{\sin}\theta \rangle + \omega M_Q i_Q \langle i, \widetilde{\cos}\theta \rangle \tag{5.16b}$$

$$Q_D = \omega M_D i_D \langle i, \widetilde{\cos}\theta \rangle - \omega M_Q i_Q \langle i, \widetilde{\sin}\theta \rangle \tag{5.16c}$$

$T_D$ and $Q_D$ as calculated by (5.16a) and (5.16c) respectively will both be positive for $E < E_n$. The control signals are then added to the APL and RPL respectively as depicted in Figure 5.4. The virtual damper windings are here added to the system already equipped with the virtual resistor to further improve the dynamic response. It is however also possible to implement the virtual damper windings to the original Synchronverter without adding the virtual resistor, as the two implementations are entirely independent of each other. It should be noted that for the actual controller implementation, the damping power is added before the set-point saturation described in Section 3.1.5 to ensure that the set-points, including the contribution from the artificial damper windings, are within the operating capability of the converter.
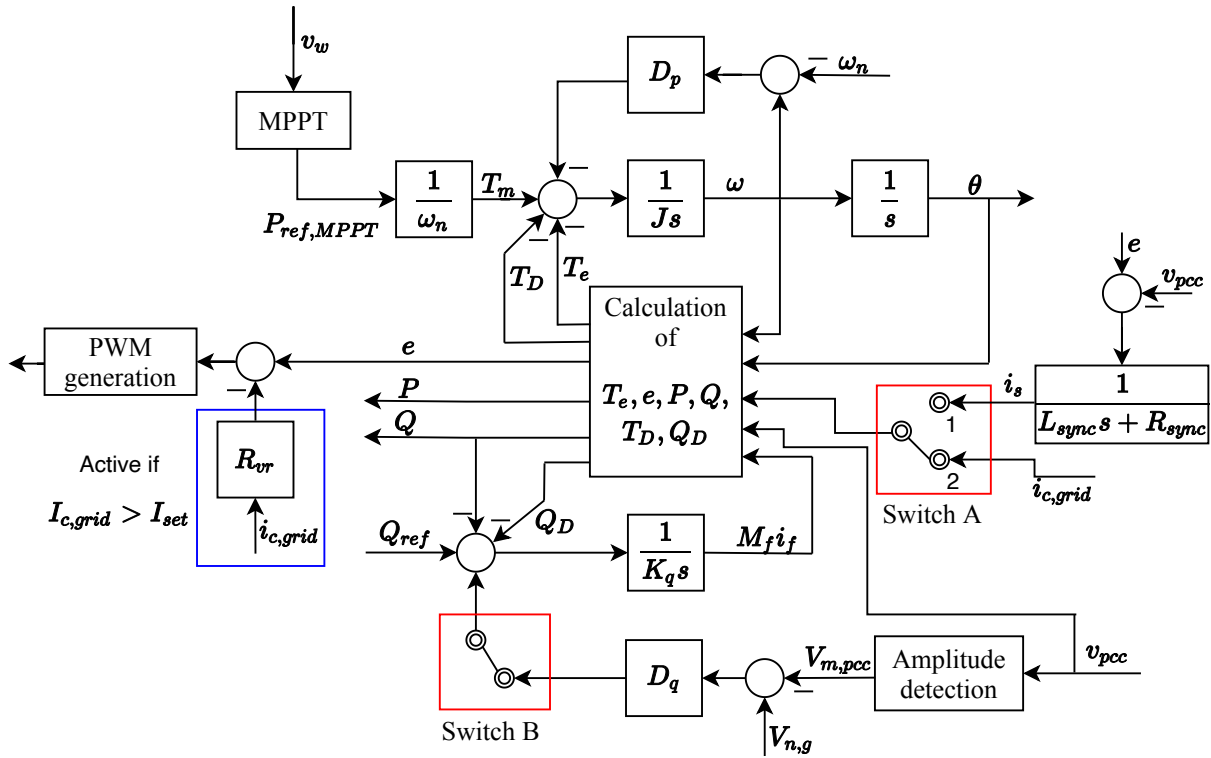
Figure 5.4: Enhanced control structure including virtual resistor and damper windings.

The virtual damper windings proposed in this section use the back-EMF of the VSM to implement damping, without the need for additional tuning. The mathematical model is modified to improve the dynamics under both small-signal disturbances causing oscillations, and improve stability when subjected to a large contingency. The method is however designed based on the assumption of the nominal voltage also being the reference voltage. If the converter is set to operate away from the nominal voltage, the enhanced control structure would introduce a steady-state deviation, and a subsequent need to be redesigned.

A similar method as the one described above was proposed in [69] for a High Voltage Direct Current (HVDC) system. However, the implementation into the control algorithm proposed here is vastly different and modified to improve damping during longer and more severe contingencies while still achieving the same advantages, all with less controller complexity. As such, when combined with the virtual resistor from Section 5.2.2, the implementation of both a virtual resistor and virtual damper windings comprise a novel control strategy, having the potential to drastically improve the dynamic performance of the Synchronverter control topology when subjected to a severe contingency.

## 5.3   Simulations and Results

Simulations have been carried out to validate the effectiveness and functioning of the enhanced control loops described in Chapter 5. In addition, for the system added with the power correction loop, the quasi-steady approximate Lyapunov approach is modified to include the changed fault dynamics to check whether the method can still provide adequate results for the stability limits when the loop is added to the system. The system parameters used in the simulation model are the same as for the original system. When discussing the performance of the enhanced systems, the two main objectives of the added control loops should be kept in mind; improve the transient stability limits of the system, and mitigate the excessively high post-fault converter current.

### 5.3.1   Results of Enhanced Control Loops: Power Correction Loop

Before adding the PCL to the system, the coefficient $M$ must be set based on (5.4). For this thesis $M$ is set so that the active power set-point is reduced by $25\%$ of base power for a $100\%$ reduction in grid voltage, $\Delta V = V_b$. Using this, $M$ can be calculated as in (5.17).

$$M = \frac{0.25 S_b}{\omega_n V_b} = 1.4125 \tag{5.17}$$

Furthermore, the voltage threshold activating the PCL is set to $V_{set} = 0.5$ p.u.. With $M = 1.4125$, the reduction in the active power set-point for the given reduction in grid voltage, $\Delta V = 0.9$ p.u., is calculated to be $\Delta P_{m,corr} = 225\,\text{kW} = 0.225$ p.u.. The PCL is added to the grid side controls in the Simulink model as depicted in Figure 5.1, and the Simulink model of the controller added with the PCL can be found in Appendix C.2, Figures C.9 and C.10.

Using the quasi-steady approximate Lyapunov approach on the system added with the PCL, the critical clearing time is found analytically to be $t_{cc} = 0.5663$ s, with a corresponding critical clearing angle $\delta_{cc} = 108.3255°$. Graphic illustrations of the analytic results are provided in Figure 5.5, where a clearing time equal to the CCT and a clearing time 15 ms above the CCT are used in Figure 5.5b.
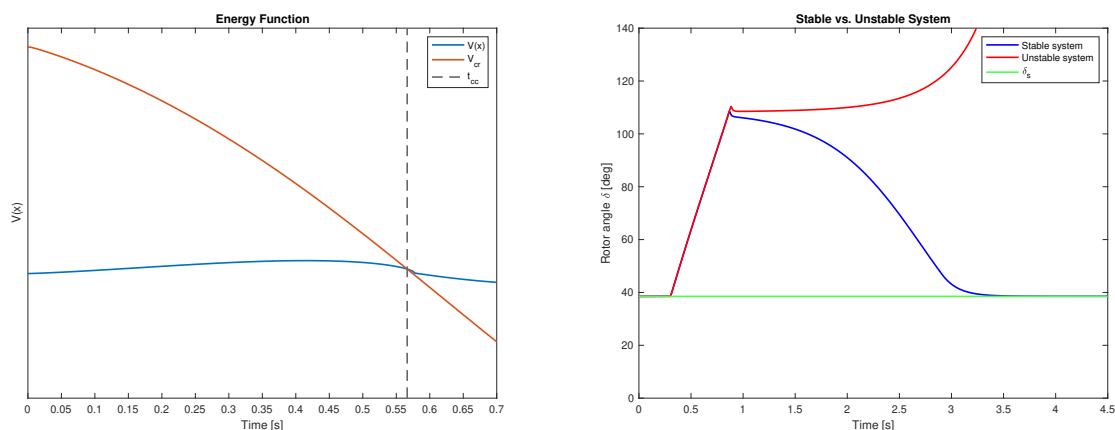


(a) Energy function vs. clearing time for system added with PCL.

(b) $\delta$ for stable and unstable analytical system added with PCL.

Figure 5.5: Analytical stability assessment of system added with PCL.

Furthermore, full forward numerical integration of the system added with the PCL yielded a critical clearing time equal to $t_{cc} = 0.5801$ s, with a corresponding critical clearing angle $\delta_{cc} = 110.0725°$. To see how the the PCL affects the dynamic response, and to find the actual CCT, the system added with the Power Correction Loop was simulated using the same procedure as in Section 4.6.6 until the actual CCT was obtained. Simulation results yielded a $t_{cc} = 0.6444$ s, with a corresponding critical clearing angle $\delta_{cc} = 112.4382°$, and the stability limits as found by the stability analysis of the system added with the PCL are summarised in Table 5.1.

Table 5.1: Stability limits for system added with power correction loop, using different types of assessment methods.

| Method | CCA | CCT | $\Delta$**CCT** [%] |
|---|---|---|---|
| Quasi-steady approx. Lyapunov | 108.3255° | 0.5663 s = 566.3 ms | 12.12% |
| Full Forward Integration | 110.0725° | 0.5801 s = 580.1 ms | 9.98% |
| Simulink Simulation | 112.4382° | 0.6444 s = 644.4 ms | 0% |

Using the quantification methods in (5.1) and (5.2), the improvement in the stability limit, $\mathcal{I}$, and the stability margin, $\mathcal{M}_{stab}$, as a result of the added power correction loop can be calculated as in (5.18a) and (5.18b). The results are further summarised for easy identification in Table 5.2.

$$\mathcal{I} = \left(\frac{0.6444 - 0.3861}{0.3861}\right) \cdot 100\% = 66.9\% \tag{5.18a}$$

$$\mathcal{M}_{stab} = \left(\frac{0.6444 - 0.3861}{0.6444}\right) \cdot 100\% = 40.08\% \tag{5.18b}$$

Table 5.2: Quantified stability improvement for PCL system.

| Parameter | Value |
|---|---|
| Stability limit improvement, $\mathcal{I}$ | 66.9% |
| Stability margin, $\mathcal{M}_{stab}$ | 40.08% |

As previously explained, the PCL has the major advantage of easy implementation in both the quasi-steady approximate Lyapunov method and the full-forward numerical integration, meaning analytical stability analysis can be carried out without heavy re-modelling of the analytical equations. This is possible because the PCL does not affect steady-state operation, nor the post-fault system, as the loop will only be active when the fault is on.

Implementing the PCL does however require additional hardware equipment, such as additional sensors and communication devices, to provide the control system with the grid voltage. This could potentially increase the CAPEX of a project by some minor amount, but will in most cases be far less expensive than installing e.g. braking resistors. Another factor is the potential delays that might occur in communications when the grid voltage is being communicated over longer distances. These delays are not taken into account in the analysis performed here but should be considered for a real application.

Looking at the obtained results in Figures 5.5a and 5.5b, many of the same observations that were pointed out for the original system also holds for the system added with the PCL. As such, they will not be treated in detail again, but it can be noted that the significant decrease in the critical value of the Lyapunov function can still be seen in Figure 5.5a, and that the stable system in Figure 5.5b is asymptotically stable.

When added with the power correction loop, the critical clearing time of the simulated system is improved by 258.3 ms compared to the original system, which yields an improvement in the stability limits, $\mathcal{I}$, equal to $66.9\%$ as seen from Table 5.2. Furthermore, the stability margin $\mathcal{M}_{stab}$ is found to be $40.8\%$, and the PCL thus achieves the first of the two objectives by indeed making the original system more stable. From the results of the stability analysis in Table 5.1 it is evident that even with the added power correction loop, the quasi-steady method provides adequate estimates for the system stability, having a deviation of $12.12\%$ from the CCT of the Simulink model. The full-forward numerical integration has, as expected, a slightly better accuracy deviating by only $9.98\%$. It can thus be concluded that the analytical analysis is still feasible for the system added with a PCL.

The critical clearing angles listed in Figures 5.1 provides some interesting insight into the system characteristics for both the Simulink model and the analytic model. When comparing the CCA obtained by each method in Table 5.1 to their respective counterparts in Table 4.11, they are found to be practically identical with the largest difference being $0.2330°$ for the full forward integration method. This means that the CCA of the system added with a PCL is the same as for the original system but with a $66.9\%$ improvement in the CCT. This observation can be seen in relation to the fact that the PCL affects the faulted system by decreasing the power imbalance yielding a smaller speed deviation $\Delta\omega$, while the available post-fault deceleration area remains unchanged. As such, it takes a longer time to inject the same amount of kinetic energy. With a smaller speed deviation, $\delta$ uses a longer time to reach the CCA, and thus the CCT is increased.

The response of the system added with the PCL when pushed to its critical clearing time will be discussed in detail in Section 5.3.4. It can however be mentioned already here that the system response is to a large extent identical to what was seen for the original system, only with a longer clearing time. This is especially true looking at Figure 5.11i, where the problem of the excessively high post-fault current is still present when the system is pushed to its limits, thus making the PCL system fail the second objective. It is however reasonable to believe that if simulated for a clearing time equal to the CCT of the original system, the response would indeed be far better, drastically reducing the operating time with a current above 1 per unit.

As a final remark it can be noted that the power correction coefficient $M$ was set to reduce the active power set-point by 25% of base power for a $100\%$ reduction in the grid voltage, yielding a reduction of 0.225 p.u. for the fault investigated. From the response in Figure 4.14d, it can be deduced that the difference between the set-point of 0.8 p.u. and the injected power is approximately 0.5 p.u. during fault for the original system. Based on this deduction, it can be argued that $M$ could have been tuned more aggressively, e.g. reducing the set-point closer to 0.4 p.u. for the same fault. This could potentially increase the stability limits beyond what was achieved here.

The response of the simulated system equipped with the PCL when fault is cleared at $t_{cc} = 0.6444$ is depicted in Figures 5.11 and 5.12 in Section 5.3.4, where the response is compared to the responses of the system equipped with a virtual resistor and the system equipped with both a virtual resistor and damper windings.

## 5.3.2 Results of Enhanced Control Loops: Virtual Resistor

The power correction loop had the large drawback of requiring additional infrastructure investments, and the Virtual Resistor (VR) was therefore proposed as an alternative, omitting the need for extra hardware installations altogether. The VR loop does however have the drawback of being far more difficult to implement into analytical models for use by methods, such as the quasi-steady approximate Lyapunov method, as the virtual resistor also changes the post-fault dynamics if the current is larger than $I_{set}$. While analytical modelling for the application of full-forward numerical integration is possible, this is kept outside of the scope of this thesis. Before adding the Virtual Resistor (VR) to the system, $R_{vr}$ must be chosen. For this thesis $R_{vr}$ is set to

$$R_{vr} = 0.2 \, \text{p.u.} = 0.0952 \, \Omega \tag{5.19}$$

Furthermore, the current threshold activating the VR loop is set to $I_{set} = 1$ p.u., and the Virtual Resistor is added to the grid side controller as depicted in Figure 5.2, with the actual Simulink implementation depicted in Appendix C.3, Figure C.11. The value of $R_{vr}$ was chosen without entering into detailed analysis maximising the potential of the control loop. Tuning the virtual resistor to the specific system could therefore improve upon the results found in this thesis. That being said, the idea behind the chosen $R_{vr} = 0.2$ p.u. is that at the point where the amplitude of the current passes $I_{set} = 1$ p.u. the imaginary active power consumed by the virtual resistor starts at $P_{R_{vr}} = 0.2$ p.u. with an even higher virtual power being consumed for higher currents.

The system added with the virtual resistor was simulated using the same procedure as in Section 4.6.6 until the CCT was obtained. Simulation results yielded a critical clearing time of $t_{cc} = 0.7606$ s, with a corresponding critical clearing angle $\delta_{cc} = 134.6213°$. Dynamic responses for the system equipped with a VR when simulated for a clearing time equal to the CCT are provided in Figures 5.6 and 5.7, while the stability limits are summarised in Table 5.3.

Table 5.3: Results of stability analysis by simulating the system added with a VR in MATLAB/Simulink.

| Parameter | Value |
|---|---|
| CCA, $\delta_{cc}$ | 134.6213° |
| CCT, $t_{cc}$ | 0.7606 s = 760.6 ms |

Lastly, $\mathcal{I}$ and $\mathcal{M}_{stab}$ for the system added with a VR loop are calculated in (5.20a) and (5.20b), and further summarised for easy identification in Table 5.4.

$$\mathcal{I} = \left( \frac{0.7606 - 0.3861}{0.3861} \right) \cdot 100\% = 97.00\% \tag{5.20a}$$

$$\mathcal{M}_{stab} = \left( \frac{0.7606 - 0.3861}{0.7606} \right) \cdot 100\% = 49.24\% \tag{5.20b}$$

The effect of the virtual resistor can be seen in Figure 5.6d, where the power injected by the converter as calculated by the control system, $P_{VR,c}$ is far higher than the actual injected power $P_{VR,act}$. This will, as expected, reduce the power imbalance in the swing equation of the VSM,

Table 5.4: Quantified stability improvement for VR system.

| Parameter | Value |
|---|---|
| Stability limit improvement, $\mathcal{I}$ | 97.00% |
| Stability margin, $\mathcal{M}_{stab}$ | 49.24% |

thus improving the angular stability. Furthermore, $\Delta P = P_{VR,c} - P_{VR,act}$ should equal the power consumed by the virtual resistor. Using $R_{vr} = 0.2$, the current amplitude found in Figure 5.6f and $P = RI^2$, this is found to be as expected. In addition, as explained in Section 5.2.2, the added VR loop will not affect the reactive power injection of the VSM. This theory is confirmed looking at Figure 5.6d where $Q_{VR,act}$ and the $Q_{VR,c}$ are identical.

The obtained stability limits summarised in Table 5.3 look very promising, with the CCT moved all the way up to $760.6$ ms at a CCA of $134.6213°$. Furthermore, the stability limit improvement, $\mathcal{I}$, and the stability margin, $\mathcal{M}_{stab}$, of $97.00\%$ and $49.24\%$ respectively are indeed very good. This testifies towards what seems like an extreme improvement of the system stability using nothing else than an additional, digitally implemented control loop, and it is therefore beyond doubt that the VR loop achieves objective number one of improving the system stability.
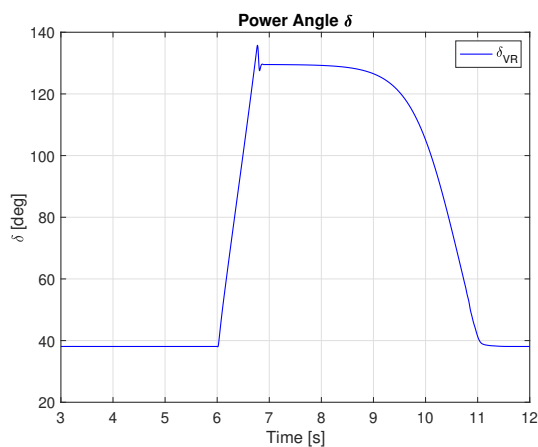


(a) Power angle $\delta$
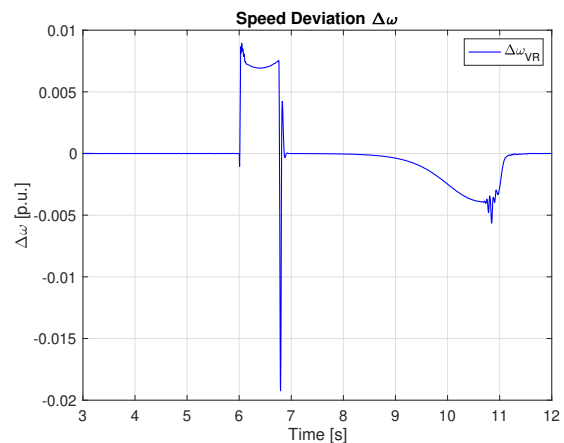
(b) Speed deviation $\Delta\omega$ of the VSM from the nominal grid frequency.
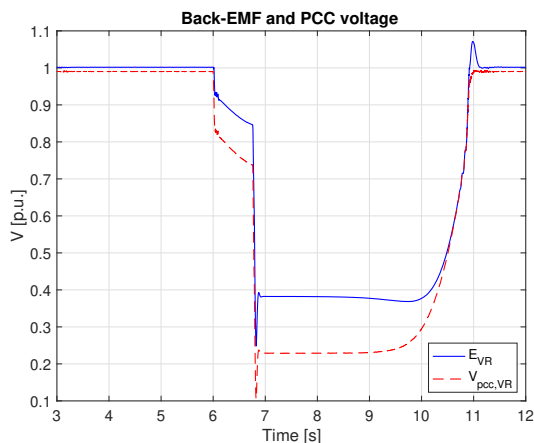
(c) Amplitudes of $E$ and $V_{pcc}$.
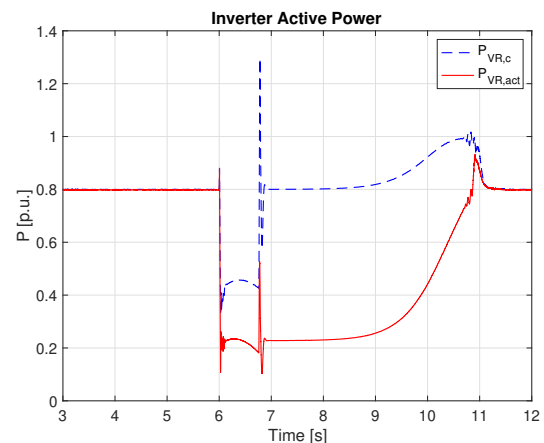
(d) Active power injection $P$ as calculated by the inverter and actual injection.
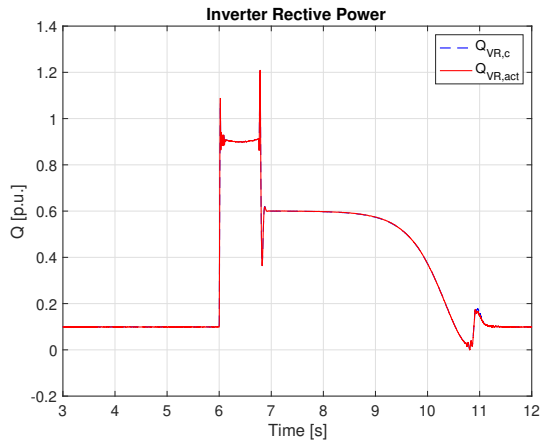
(e) Reactive power injection $Q$ as calculated by the inverter and actual injection.
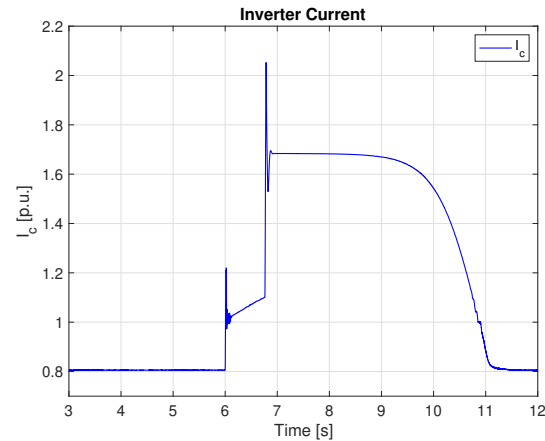


(f) Inverter current amplitude.

Figure 5.6: Grid side response for control system equipped with virtual resistor for $t_c = t_{cc,VR} = 0.7606$ s.

However, looking more closely at the system response in Figure 5.6 when pushed all the way to this high CCT, some major issues can be identified. The first indication of an undesirable system response can be seen already in Figure 5.6a where several seconds are needed for the power angle to return to the s.e.p.. Also, the characteristic of the rotor angle response is practically identical to the rotor angle response of the original system, an observation which also holds for the speed deviation in Figure 5.6b. Figure 5.6b does however reveal small oscillations in the frequency at the point where the VR loop is disabled.

The extremely low voltages seen in Figure 5.6c can be explained by recalling how the virtual resistor actually affects the system behaviour, namely by subtracting the voltage drop across $R_{vr}$ from the control signal $e$. Furthermore, the fact that the voltages are so low, and the relatively large voltage difference between $E$ and $V_{pcc}$ indicates that the converter current most likely is excessively high also for this enhanced control system, which is confirmed looking at Figure 5.6f. It should also be mentioned that voltages as low as $0.4$ p.u. are unfeasible even on its own, as converters typically have a rated operating range also for voltages.

The virtual resistor loop almost doubles the critical clearing time of the system, but in addition to not solving the problem with the post-fault current, the VR brings a new issue that can be observed in Figure 5.6d. During fault, the desired operation is achieved, effectively decreasing the power imbalance and improving the stability. However, after the fault is cleared the virtual resistor is still active due to the high current, resulting in the control system acting as it follows the power set-point without actually injecting the desired power. It takes as much as 4 seconds after the fault is cleared for the VSM to again deliver the desired active power. It can therefore be concluded that not only is the post-fault current slightly higher than for the original system, but the current is high without the system delivering the desired power.

When it comes to the rotor side response in Figure 5.7, the large drop seen in the DC link voltage for the original system at the time of fault-clearing is not present in Figure 5.7a. This can be seen in connection to the low active power in Figure 5.7b, which also reaffirms the low actual power injection observed in Figure 5.6d. The mechanical speed in Figure 5.7c is higher for a longer period, as expected, due to the low electromagnetic torque applied to the PMSG after fault-clearing. This also affects the turbine itself, which due to having a higher mechanical speed
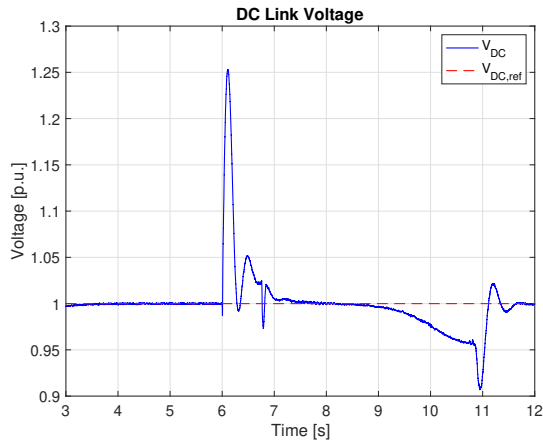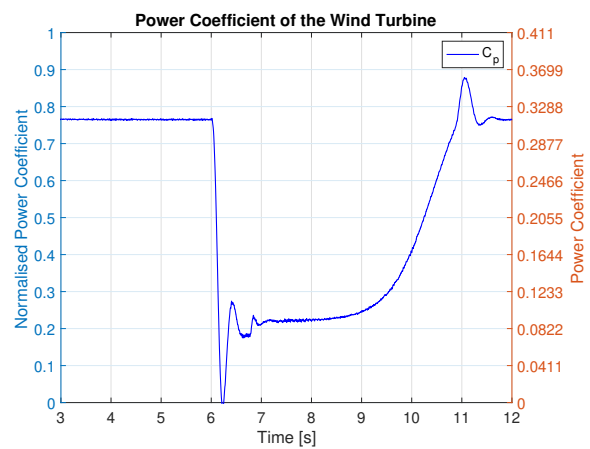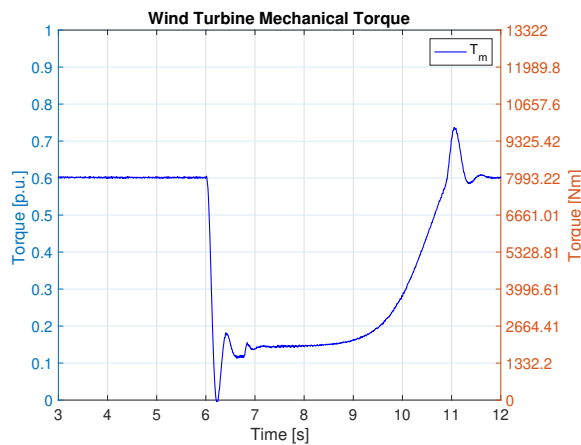
(a) DC link voltage.
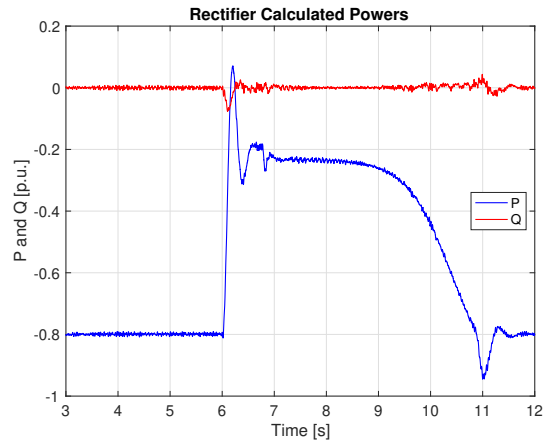


(b) Powers calculated by the rectifier control system.
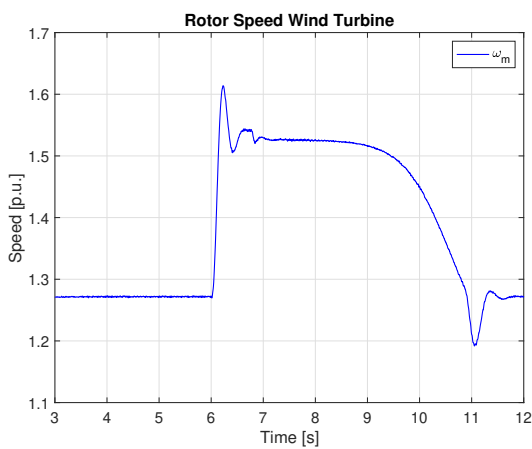


(c) Mechanical rotor speed of the wind turbine.



(d) Power coefficient of the wind turbine.



(e) Mechanical torque of the wind turbine.

Figure 5.7: Rotor side response for control system equipped with virtual resistor for $t_c = t_{cc,VR} = 0.7606$ s.

operates lower on the torque curve, and thus outputs a lower mechanical torque as seen in Figure 5.7e. Operating on the far right-hand side of the power/torque curves also implies a low power coefficient as seen in Figure 5.7d. However, as for the original system, the rotor side responses do not seem to affect the transient stability of the grid side, and the rectifier controller is able to achieve its controller objectives. The rotor side response is therefore concluded to be adequately

good.

To summarise, the system response when cleared at the CCT is to a large extent identical to what was seen for the original system, only with a longer clearing time and worsened active power injection post fault. The VR loop does however provide a better stability margin than the PCL, while still not solving the issue of the high post-fault current. As such, the first objective is achieved but not the second. It can be mentioned that the system added with the VR was also simulated for a $t_c = t_{cc,PCL} = 0.6444$ s, for which the results are depicted in Figures 5.11 and 5.12 in Section 5.3.4. The VR loop will hence be compared to the other enhanced control loops for that lower clearing time in Section 5.3.4.

### 5.3.3   Results of Enhanced Control Loops:  Virtual Resistor and Damper Windings

The artificial Damper Windings (DWs) were added to the system already equipped with the virtual resistor as depicted in Figure 5.4 using the explanation from Section 5.2.3. Furthermore, they were implemented into the Simulink model as shown in Appendix C.4, Figures C.12, C.13 and C.14. Recalling Section 5.2.3 these damper windings would yield control inputs based on the VSM's deviation from the nominal back-EMF $E_n$ to improve the transient stability, speed up the return to normal operation, and dampen out oscillations.

The damper windings require no additional tuning before implementation. As for the system only added with a virtual resistor, no analytical investigation of stability limits is carried out. However, to see the capabilities of the enhanced system equipped with both a VR and DWs, different scenarios were simulated in MATLAB/Simulink. First, the system from Section 5.2.2 equipped only with a VR was simulated for a clearing time $t_c = 0.6\,\text{s} = 600\,\text{ms}$ and the system response is depicted in Figure 5.8a. Then, the same system was added with the virtual DWs and simulated for the same clearing time, yielding the response in Figure 5.8b.
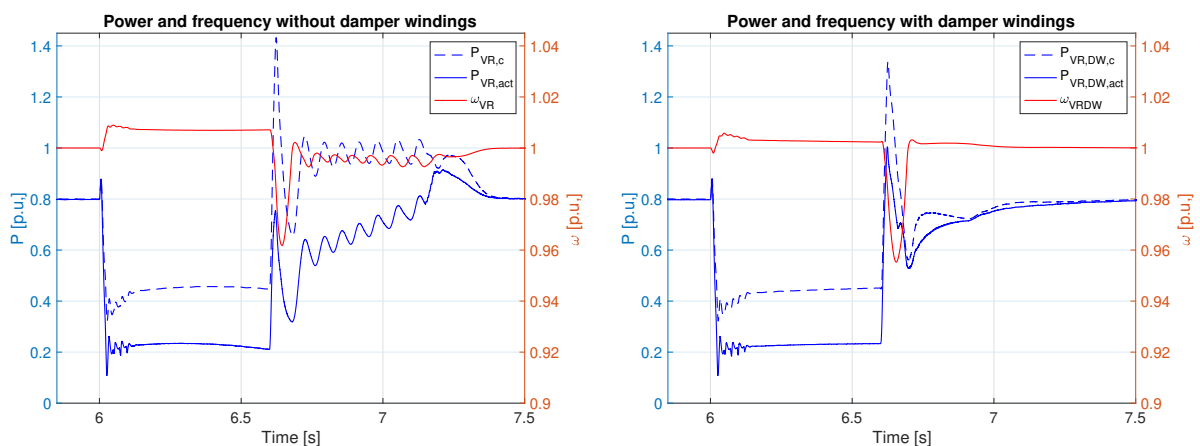


(a) $P$ and $\omega$ for system with virtual resistor, but   (b) $P$ and $\omega$ for system with both virtual resistor and
without damper windings.                              damper windings.

Figure 5.8: $P$ and $\omega$ for system with VR with/without damper windings for $t_c = 0.6$s.

From Figure 5.8a it is evident that the system only equipped with the virtual resistor is prone to experience oscillations when cleared at certain clearing times. These oscillations are not seen when the system is cleared e.g. at its CCT in Figure 5.6, but are clearly present for other clearing times such as the one used in Figure 5.8a. Adding the artificial damper windings clearly

improves the dynamical response as seen in Figure 5.8b, where the system reaches steady-state both faster and more controlled, as the post-fault oscillations in both $P$ and $\omega$ are dampened out. From an industrial perspective, the response in Figure 5.8b is undoubtedly more beneficial for system stability, and while the example depicted in Figure 5.8 is related to transient stability and a long clearing time of $600$ ms, it is feasible to conclude that the damper windings also drastically improve the dynamical response to small-signal disturbances. This is however not tested here.

No critical clearing time within the range of 4 seconds was found for the system added with both a VR and virtual DWs, but to demonstrate the capabilities of this enhanced control structure, the system was simulated for a clearing time $t_c = 1.5\,\text{s} = 1500\,\text{ms}$, and the responses are provided in Figures 5.9 and 5.10. Furthermore, also a clearing time $t_c = 3.0\,\text{s} = 3000\,\text{ms}$ was tested. As this is way above typical power system clearing times, and conclusions that can be drawn from this simulations might as well be drawn from the simulation using $t_c = 1.5\,\text{s}$, the responses when using $t_c = 3\,\text{s}$ are provided in Appendix D.2, Figures D.3 and D.4. It can however be noted that both $t_c = 1.5\,\text{s}$ and $t_c = 3\,\text{s}$ rendered the system stable.

Considering the fact that no critical clearing time was found for the system inside a range of 4 seconds, the performance of the enhanced control system is clearly beyond expectation. Both the clearing time of $t_c = 1.5$ s, depicted in Figures 5.9 and 5.10, and the clearing time of $t_c = 3.0$ s, attached in Appendix D.2, are far above typical power system clearing times, and it can be argued that such long-lasting contingencies are so rare that investigating an even higher clearing time will be unnecessary, or even uninteresting.

As such, it should also be mentioned that even the clearing time of $1.5$ s is used solely to demonstrate the capabilities of the system, as $t_c = 1.5$ s is also far higher than any commonly seen clearing time in the power system. Regardless, the first objective of the enhanced control loop is unquestionably achieved, improving the transient stability of the system with a substantial amount.

$\mathcal{I}$ and $\mathcal{M}_{stab}$ for a clearing time $t_c = 1.5\,\text{s}$ are calculated in (5.21a) and (5.21b), while results for $t_c = 3.0\,\text{s}$ are calculated in (5.21c) and (5.21d). The results are further summarised for easy identification in Table 5.5.

$$\mathcal{I}_{1.5s} = \left(\frac{1.5 - 0.3861}{0.3861}\right) \cdot 100\% = 288.50\% \tag{5.21a}$$

$$\mathcal{M}_{stab,1.5s} = \left(\frac{1.5 - 0.3861}{1.5}\right) \cdot 100\% = 74.26\% \tag{5.21b}$$

$$\mathcal{I}_{3.0s} = \left(\frac{3.0 - 0.3861}{0.3861}\right) \cdot 100\% = 677.00\% \tag{5.21c}$$

$$\mathcal{M}_{stab,3.0s} = \left(\frac{3.0 - 0.3861}{3.0}\right) \cdot 100\% = 87.13\% \tag{5.21d}$$

Looking at the quantified stability improvements in Table 5.5, the achieved improvement in the stability limits for both clearing times can be said to be extraordinary at $288.4\%$ and $677.0\%$ for $t_c = 1.5$ s and $t_c = 3.0$ s respectively. Also, the stability margins for the enhanced system when clearing the fault at the CCT of the original system are undoubtedly very high, but the difference in $\mathcal{M}_{stab}$ of only $12.87\%$ between the two clearing times is not that large taking into account that one clearing time is double the other one. As such, the improvement in the stability margin when

Table 5.5: Quantified stability improvement for VR/DW system.

| Parameter | Value |
|---|---|
| Stability limit improvement for $t_c = 1.5$ s: $\mathcal{I}_{1.5s}$ | 288.50% |
| Stability limit improvement for $t_c = 3.0$ s: $\mathcal{I}_{3.0s}$ | 677.0% |
| Stability margin for $t_c = 1.5$ s: $\mathcal{M}_{stab,1.5s}$ | 74.26% |
| Stability margin for $t_c = 3.0$ s: $\mathcal{M}_{stab,3.0s}$ | 87.13% |

doubling the clearing time is quite small, further emphasising that analysing the clearing time of 1.5 s is sufficient.
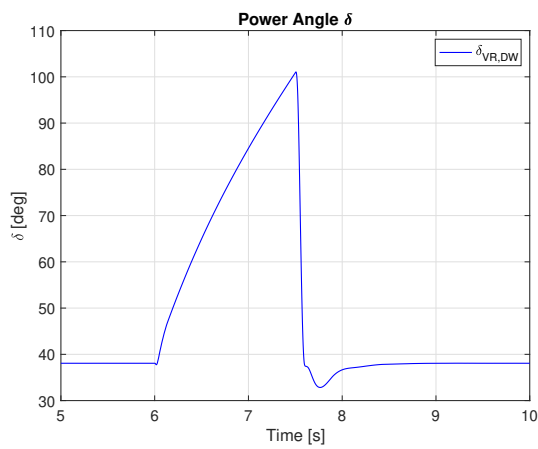


(a) Power angle $\delta$
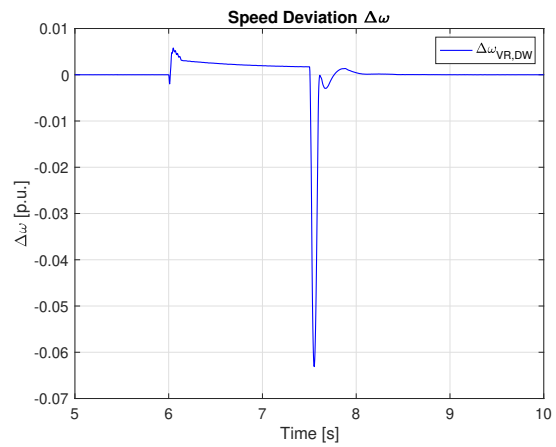


(b) Speed deviation $\Delta\omega$ of the VSM from the nominal grid frequency.
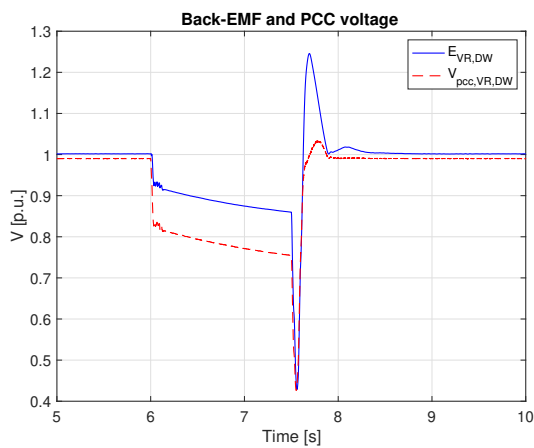


(c) Amplitudes of $E$ and $V_{pcc}$.
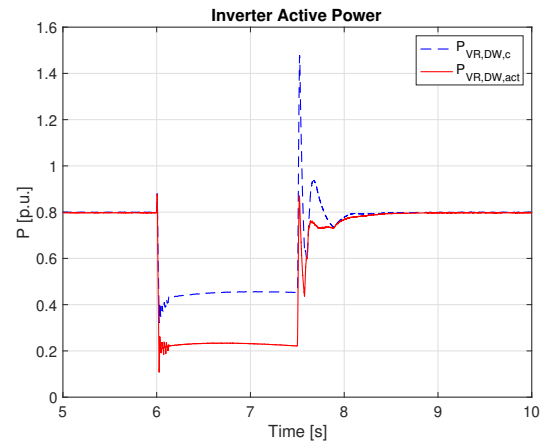


(d) Active power injection $P$ as calculated by the inverter and actual injection.

However, an extremely long clearing time is of little value if the operating scenario following clearing is unfeasible when cleared at this high clearing time. It is therefore important to see the long clearing time of 1.5 s in light of the dynamic responses depicted in Figures 5.9 and 5.10, where it can be noted that the first 5 seconds of the simulation are omitted from the plots. Starting with the response of the power angle depicted in Figure 5.9a, a distinct improvement
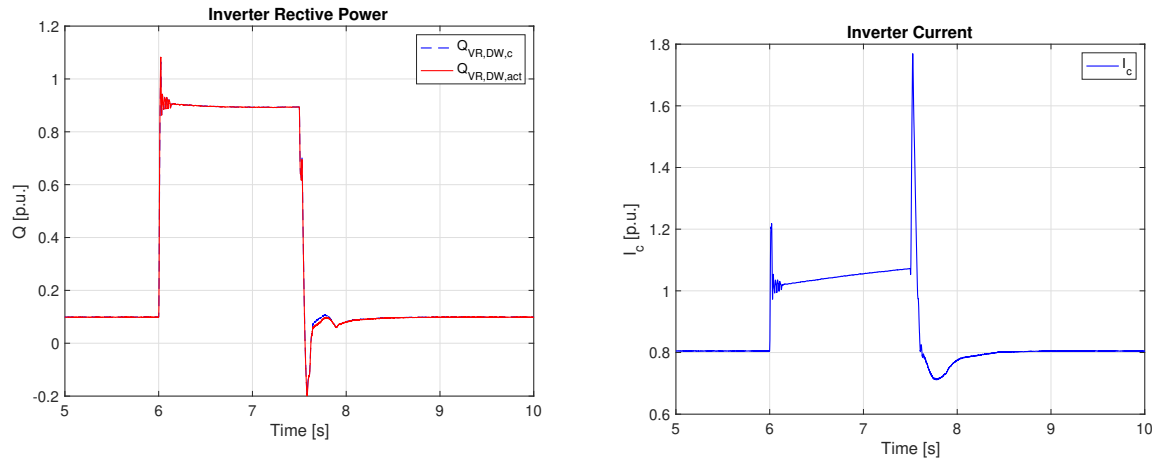
(e) Reactive power injection $Q$ as calculated by the inverter and actual injection.

(f) Inverter current amplitude.

Figure 5.9: Grid side response of VR/DW system using $t_c = 1.5$ s.

can be seen. Not only does the angle only reach $\approx 100°$ during the course of the $1.5$ s, but instantly drops down after fault-clearing, reaching steady-state around $0.5$ s after the fault is cleared. The response of $\delta$ must be seen in the context of $\Delta\omega$ seen in Figure 5.9b, which during fault is limited by the control system, largely influenced by the damper windings, to be in the range of $< 0.005$ p.u., while immediately after fault-clearing reaches as high as $-0.06$ per unit. This large, negative post-fault $\Delta\omega$ is what drives the power angle back to the s.e.p. so quickly.

Recalling the theory from Section 4.4.3, the back-EMF $E$ will not be controlled back to its nominal operating point before $\delta$ moves closer to its nominal operating point. The fact that the damper windings help to control the power angle back to its nominal value so quickly should thus render it possible for also $E$ to return to its nominal value more quickly. This is confirmed looking at Figure 5.9c, where after first dropping to $0.45$ p.u. due to the fault being cleared at the high power angle, the enhanced controller quickly controls $E$ back to $1.0$ p.u after a short overshoot. Thus, both $E$ and $V_{pcc}$ are seen to reach steady-state in less than $1$ second after clearing the fault. This should in theory imply that the response of the post-fault converter current is also far more feasible for the system enhanced with the damper windings than for the other system responses seen so far in the thesis.

The indication of an advantageous response of $I_c$ is indeed confirmed by looking at Figure 5.9f. Here it can be seen that the converter current, after a small transient, is kept below $1.1$ p.u. during the entire duration of the fault. Furthermore, after the fault is cleared, the converter current is below $1$ p.u. after only $80$ ms, which is very fast considering that the transient that takes place during this period reaches almost $1.8$ p.u.. Nonetheless, the current reaches steady state in a controlled manner approximately $1$ second after clearing the fault. This is a very competent response, and it can most definitely be concluded that the system added with both a virtual resistor and damper windings achieve also the second objective of the enhanced control loops, drastically mitigating the post-fault current to a feasible level of operation through controlling the power angle back to the s.e.p..

Moreover, the active power injected and active power calculated by the inverter in Figure 5.9d are both indications of the inverter operating as desired. During fault, the power calculated is higher than the actual power injection, thus slowing down the power angle acceleration. After clearing the fault, the synthesised virtual power injection, reaching up to $1.5$ p.u., help forcing the

power angle back down to the stable equilibrium point through the relationship governed by the swing equation. This happens at the same time as the actual injected power never exceeds 1 p.u., meaning the inverter does not inject more power than what is available from the wind turbine, nor does it violate the inverter power ratings. As observed for the other responses related to the VR/DW system, the active power is nicely controlled back to steady-state within the first second after clearing the fault. Moreover, the process of tracking the power reference is satisfactorily damped without high-frequent oscillations.

Lastly, a highly interesting observation related to the reactive power in Figure 5.9e should be discussed. Apart from the more obvious observations, such as the actual $Q$ and the calculated $Q$ being identical and the fact that also $Q$ reaches steady-state within the first second after fault, it can be noticed that $Q$ drops below zero for a very short period of time. This means that the inverter consumes reactive power for approximately 60 ms or 3 cycles. Such an operating scenario is however not uncommon, as voltage source converters have the inherent capability of both injecting and consuming power. It does however require the reactive power to be available from either the grid or Flexible AC Transmission Systems (FACTS) devices placed between the converter and the grid.

Looking at the responses of the rotor side in Figure 5.10, the common thread is that the system responses are very good. All the depicted responses reach steady-state within the first second after the fault is cleared, except for the DC link voltage which, due to its well-dampened response, uses an additional second. Moreover, it can be observed that the duration of the fault, i.e. 1.5 s, is so long that the rotor side variables are able to stabilise at their respective fault levels, and thus show no tendency to move towards more unstable operating points which may affect the grid side stability or the stability of the WECS as a whole. This, while not being treated in detail in this thesis, also testifies towards the robustness of the control system, having well-tuned parameters that are able to function far from their rated operation for a sustained period of time, without compromising the system stability.

Looking more closely at each of the responses belonging to the rotor side, the DC Link voltage in Figure 5.10a has the same spike at the initiation of the fault, due to the sudden drop in active power flowing through the DC link, as for all the other simulated systems. Furthermore, while the sudden drop in the DC voltage seen at the time of fault-clearing for the original system was not present for the system with only a VR, this drop is clearly present again when adding the DWs. This can be seen in relation with the inverter at the grid side quickly injecting the desired active power again post fault. This is also seen in Figure 5.10b, where the fast return of the active power to the pre-fault values after the fault is cleared is evident.

The speed in Figure 5.10c bear witness of the turbine being operated at quite high speeds, over 1.5 per unit, for the entire duration of the fault. As previously discussed, these high speeds effectively decrease the mechanical output torque of the turbine, as per the torque curve, and thus also yields a lower power coefficient. This is also confirmed looking at Figures 5.10e and 5.10d. An additional side effect of the substantial increase in the PMSG speed, which is not shown in any of the rotor side results, is an increase in the rotor side grid voltage. This is a direct consequence of equation (2.9a), and while not being investigated in detail, the large increase in speed could potentially yield a PMSG voltage which violates rotor side/rectifier ratings. This must however again be seen in light of the simplification of not having implemented any sort of turbine control, limiting the speed of the wind turbine. The rotor side responses are therefore concluded to be adequately good for the analysis carried out, yielding no unexpected results.
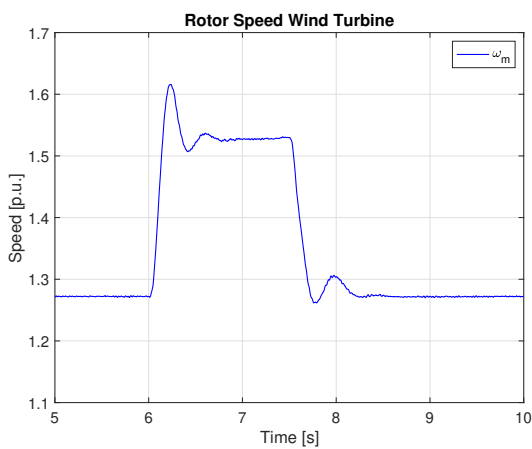
Based on the discussion above, the system response of the VR/DW system when cleared at
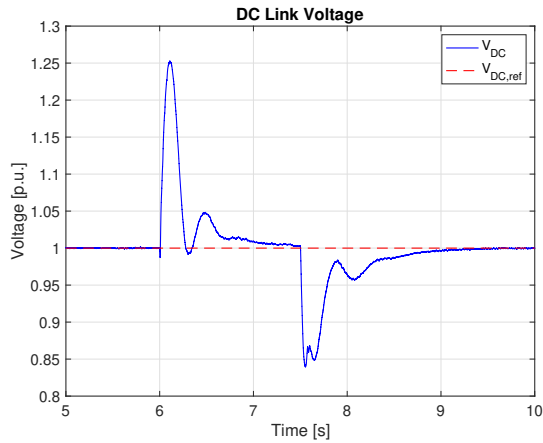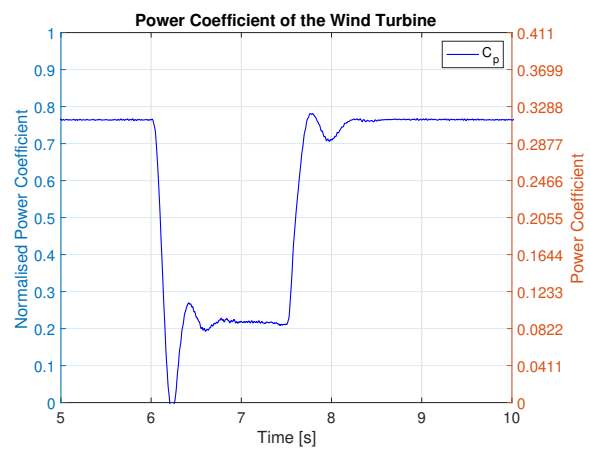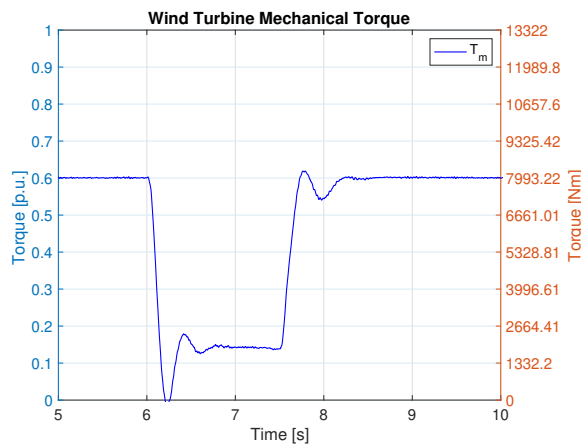
(a) DC link voltage.
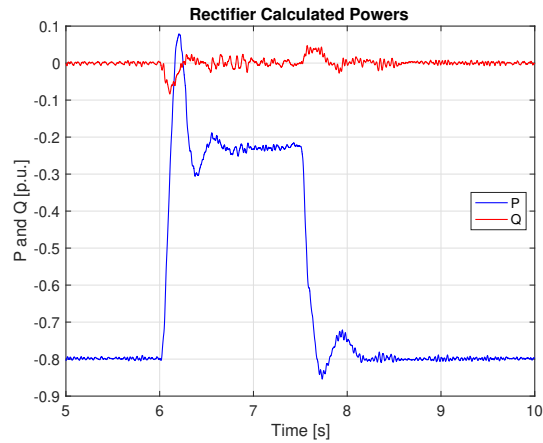


(b) Powers calculated by the rectifier control system.



(c) Mechanical rotor speed of the wind turbine.



(d) Power coefficient of the wind turbine.



(e) Mechanical torque of the wind turbine.

Figure 5.10: Rotor side response of VR/DW system using $t_c = 1.5$ s.

$t_c = 1.5$ s is irrefutably good. The system transient stability is improved beyond expectations, while also keeping the converter current well within its allowed operating area, thus making the enhanced control system achieve both of the main objectives even at this high clearing time. The implemented virtual damper windings also demonstrate an excellent ability to dampen out any high-frequent oscillations that might occur, possibly also improving the small-signal stability. As such the topology including both a VR and DWs can be concluded to be far superior to the two

other enhanced controller topologies discussed. This will however be further discussed using comparable results at a clearing time $t_c = t_{cc,PCL} = 0.6444$ s which is closer to clearing times commonly seen in the power system. This will be done in Section 5.3.4.

## 5.3.4   Comparable Results of the Enhanced Control Structures

The three enhanced control systems equipped with a power correction loop, a virtual resistor, and both a virtual resistor and damper windings are simulated for a clearing time equal to the CCT of the enhanced system with least stability margins, i.e. the system added with a PCL. Thus, the clearing time $t_c$ used for the comparable simulations in Figures 5.11 and 5.12 is set to $t_c = t_{cc,PCL} = 0.6444$ s, which is considerably closer to the clearing times typically seen in the power system than the clearing times used when simulating both the VR system and the VR/DW system. As such, these two enhanced systems can be evaluated for a more realistic fault scenario, providing system responses that are more likely to be seen in the system, and at the same time be compared to the PCL system which is pushed to its limits.

From Section 5.3.1 it is already known, and discussed, that the PCL system failed to mitigate the post-fault current when cleared at the CCT, as will be seen in the figures below. Also the system added with only the VR failed this objective when pushed to its CCT in Section 5.3.2. The comparison below is therefore of particular interest regarding the VR system as it will provide insight into how a lower, more realistic clearing time might yield a better accomplishment of reducing the operating time at excessively high currents.

For the comparable plots, the legend subscripts are defined as follows: $X_{PCL}$ denotes the system with power correction loop, $X_{VR}$ denotes the system with a virtual resistor, and $X_{VR,DW}$ denotes the system equipped with both a virtual resistor and damper windings. Furthermore, the subscript $X_{act}$ denotes the actual power injection for the two systems added with a VR, while $X_c$ either denotes the converter current or the powers calculated by the converter, depending on the plot.

From the discussions provided for each of the enhanced control system topologies respectively, it has already been established that all of the proposed systems are asymptotically stable for $t_c = t_{cc,PCL} = 0.6444$ s. While this clearing time is the critical clearing time for the system equipped with the PCL, the two other enhanced systems are known to be stable for clearing times even beyond this. The improvement in the CCT from the original system is however substantial already at $t_c = 0.6444$ s, and all systems are therefore concluded to achieve the controller objective of improving the transient rotor angle stability.

The main topic of interest will therefore be how well the different enhanced control structures handles this advanced clearing time. The response of the PCL system depicted in Figures 5.11 and 5.12 was described in Section 5.3.1 as being practically identical to what was seen for the original system, just with a longer CCT. Its resemblance to the original system will therefore not be further commented, but instead, the focus will be on the difference between the different enhanced systems and their performance.
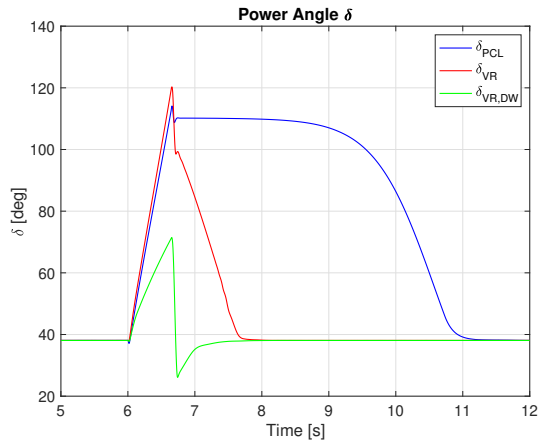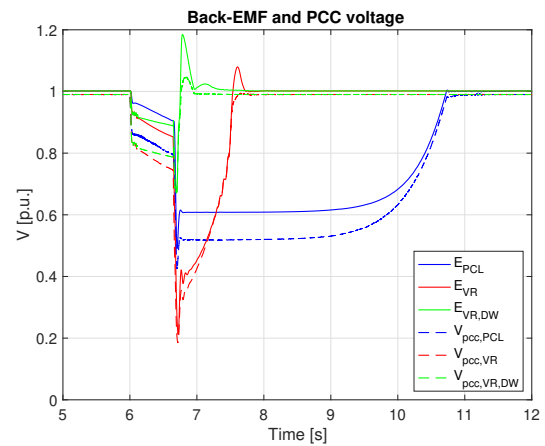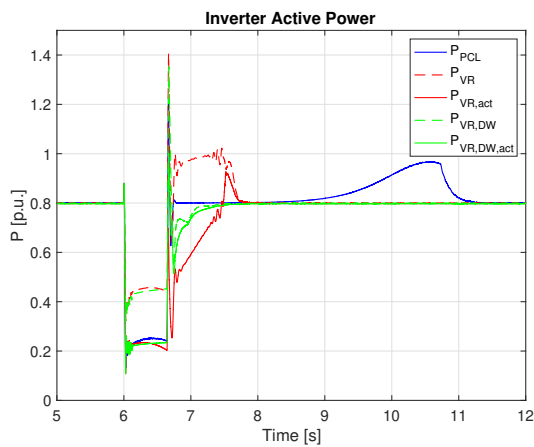
(a) Power angle $\delta$
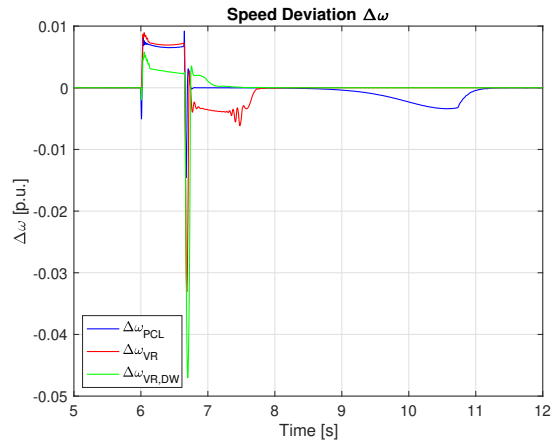


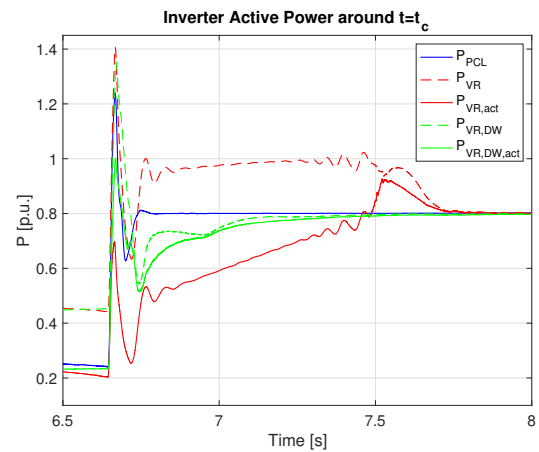(b) Speed deviation $\Delta\omega$ of the VSM from the nominal grid frequency.
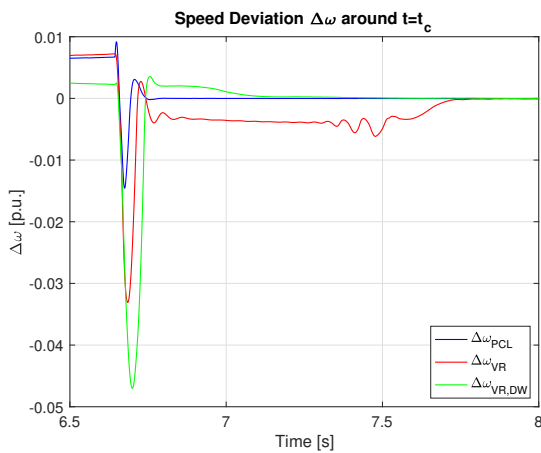


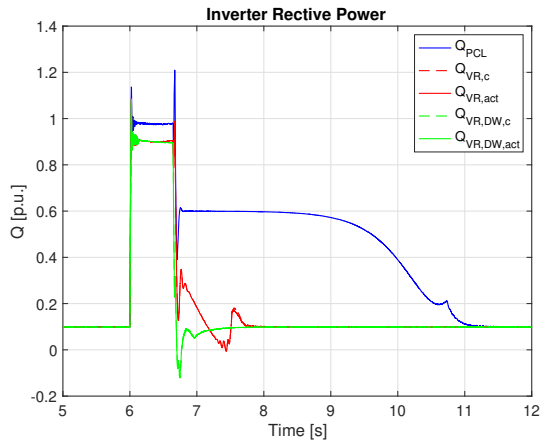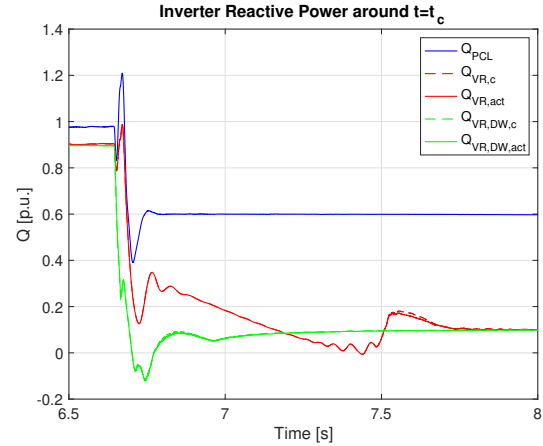(c) Speed deviation $\Delta\omega$ of the VSM from the nominal grid frequency around $t = t_c$.



(d) Amplitudes of $E$ and $V_{pcc}$.



(e) Active power injection $P$ as calculated by the inverter and actual injection.



(f) Active power injection $P$ as calculated by the inverter and actual injection around $t = t_c$.

(g) Reactive power injection $Q$ as calculated by the inverter and actual injection.

(h) Reactive power injection $Q$ as calculated by the inverter and actual injection around $t = t_c$.
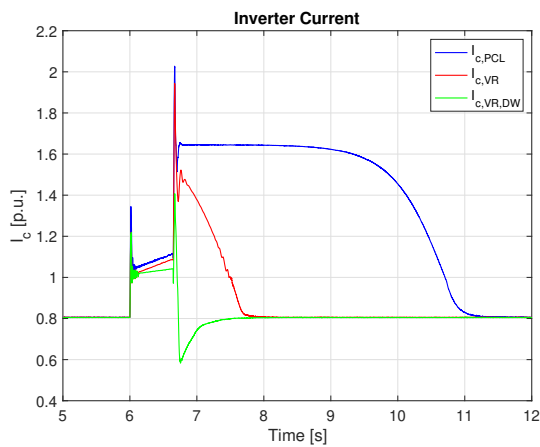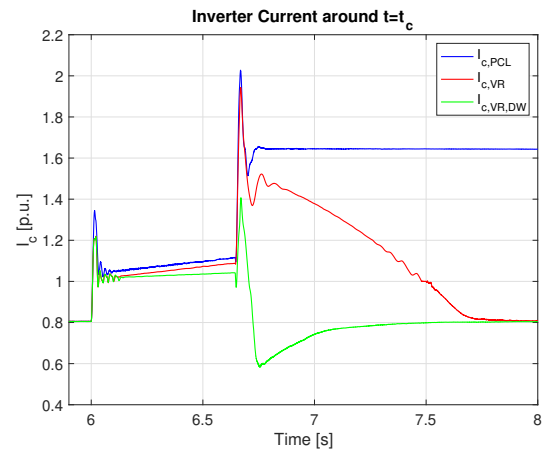


(i) Inverter current amplitude.

(j) Inverter current amplitude around $t = t_c$.

Figure 5.11: Grid side response of each of the enhanced control systems for $t_c = t_{cc,PCL} = 0.6444$ s.

The first sign of large differences in system behaviour between the three enhanced control loops is seen already in Figure 5.11a depicting $\delta$. While $\delta_{PCL}$ and $\delta_{VR}$ seem to have quite similar accelerations, and subsequently a relatively small difference in clearing angle, $\delta_{VR,DW}$ is cleared approximately $40°$ below the two other power angles. Furthermore, while $\delta_{PCL}$ and $\delta_{VR}$ appear to experience a linear increase, the increase in $\delta_{VR,DW}$ slows down with time. This effect can be explained by the impact of the damper windings which is dependant on the voltage deviation. As $E$ decreases, $T_D$ increases and thus slows down the rotor. This can also be seen in Figure 5.11b where $\Delta\omega_{VR,DW}$ is both smaller and decreases more than $\Delta\omega_{PCL}$ and $\Delta\omega_{VR}$ throughout the duration of the fault.

Another interesting observation in Figure 5.11a is how, even though being cleared at a higher angle, $\delta_{VR}$ drops and re-obtains steady-state faster than $\delta_{PCL}$. $\delta_{VR}$ and $\delta_{VR,DW}$ actually reach steady-state approximately at the same time, however via two very different post-fault responses. As such, both $\delta_{VR}$ and $\delta_{VR,DW}$ reach steady-state around 1 s after fault-clearing, while $\delta_{PCL}$ uses an additional 3.5 seconds.

The speed deviations of the three systems are depicted in Figure 5.11b, with Figure 5.11c portraying the same deviations with focus around the time of fault-clearing. Differences in the

deceleration process are clearly evident. $\Delta\omega_{PCL}$ has the smallest immediate post-fault drop and then returns quickly to approximately zero where it remains until the main process of returning the power angle to the e.p happens between 2 and 4 seconds after fault-clearing.

Both $\Delta\omega_{VR}$ and $\Delta\omega_{VR,DW}$, having control loops that function also after the fault is cleared, are seen to experience a higher deceleration. This is especially true for the system equipped with the damper windings, where the whole deceleration process takes place immediately at fault clearing, with a subsequent nicely dampened response, controlling the VSM frequency to again track the grid frequency. For $\Delta\omega_{VR}$ however, small oscillations can be seen around $t = 7.5$ seconds. These oscillations match the time where the converter current $I_{c,VR}$ drops below the current threshold $I_{set} = 1$ p.u., and as such it is possible that the VR, when implemented as a standalone addition, may have the undesirable effect of actually causing oscillations if the conditions are right.

It should be mentioned that the resemblance between $\Delta\omega_{PCL}$ and $\Delta\omega_{VR}$ can be attributed to the coincidental similarity between the contribution from the PCL, $\Delta P_{m,corr} = 0.225$ p.u., and the starting point of the power burned in the virtual resistor, $P_{R_{vr}} = 0.2$ p.u. at $I_c = 1$ per unit. Completely different results would have been obtained by changing $M$ or $R_{vr}$. The similarity does however make for a good comparison of the two systems.

As a side-note, a peculiar observation can be seen in Fig. 5.11c. Here, the drops in the different frequencies have a remarkable resemblance with frequency drops typically seen after major disturbances for systems having different amounts of inertia, and subsequent different Instantaneous Frequency Deviation (IFD) at the point called the frequency nadir in a typical investigation into frequency stability.

As expected, the large differences in how fast the power angle returns to the s.e.p. are followed by large differences in how fast the back-EMF returns to track the voltage reference, as seen in Figure 5.11d. The controller equipped with both a VR and DWs controls $E_{VR,DW}$ to track the reference voltage within half a second after fault-clearing, via a substantially smaller post-fault drop than the two other systems. $E_{VR}$, which tracks the voltage reference after approximately 1 second, has clearly the largest post-fault drop, reaching as low as $0.2$ per unit, while $E_{PCL}$ on the other hand, drops and stabilises just above $0.6$ p.u. for almost three seconds before being controlled to track the reference.

The active power injection is depicted in Figure 5.11e, with additional focus on the clearing time in Fig. 5.11f. From these figures, the controller responses could be argued to be adequately good for all three enhanced systems as all three controllers track the power reference within one second after fault-clearing. Furthermore, the system added with the PCL is actually the first to deliver $P \geq P_{ref}$ and can thus be argued to have the best response when it comes to active power injection. It should however be noticed that while the systems implemented with a VR have $P_{act}$ well within the converter ratings, the transient in $P_{PCL}$ seen at fault-clearing exceeds the rated power, going all the way up to $1.2$ per unit. During fault, the effect of the virtual resistor is clearly seen in Figure 5.11e for both the VR system and the VR/DW system, as the conceived power injection is almost twice the actual power injection. It can also be noted that the actual power injection during fault is quite similar for all three control systems.

As experienced in Section 5.3.2, the VR system has a large deviation between the actual power injection and the conceived power injection also post fault. The response is however far better for this lower clearing time than what was seen for its CCT in Figure 5.6d. Furthermore, the oscillations seen for the VR system in Figure 5.11c are also seen in Figure 5.11f. Finally, the

active powers belonging to the VR/DW system are seen to have a smaller discrepancy between the actual power and calculated power, and are significantly more dampened, than what is seen for the VR system.

Further, looking at Figures 5.11g and 5.11h, the reactive power responses are as expected. Firstly, the reactive powers calculated by the inverter and the actual reactive power injected are identical for the two systems equipped with the virtual resistor. Secondly, as seen in Section 5.3.3, the VR/DW system experience a very short period were the inverter consumes reactive power. Thirdly, oscillations are seen for the VR system at the same places in Figure 5.11h as in Figures 5.11c and 5.11f. Finally, the PCL does not change the post-fault dynamics, and the fact that this system stabilises at 0.6 p.u. immediately after fault-clearing is thus not unexpected when recalling the assumptions used in Section 4.6.5. As for the other responses, the VR system and the VR/DW system reaches steady-state approximately at the same time, while the PCL system uses additional seconds before again reaching steady-state.

The final response to be analysed for the grid side is the inverter current depicted in Figures 5.11i and 5.11j. Comparing Fig. 5.11i to Fig. 5.11d the relationship between low back-EMF and high current is clearly visible, highlighting the importance of quickly controlling the power angle back to the e.p. to facilitate the return of $E$ to its nominal value. Looking more closely at Figure 5.11i, $I_{c,PCL}$ is seen to not fall below 1 p.u. until four seconds after clearing the fault, where $I_{c,PCL} > 1.6$ p.u. for almost three seconds. $I_{c,VR}$ and $I_{c,VR,DW}$ on the other hand drops below 1 p.u. after only approx. 1 second and approx. 60 ms respectively. As such, it is beyond doubt that the PCL system fails the second controller objective for the simulated clearing time, while the VR/DW clearly achieves to mitigate the post-fault current. The VR system sits somewhat in between, having a vast improvement over the PCL system, but is not quite as good as the VR/DW system. It can however still be argued that the rapid decrease in $I_{c,VR}$ is sufficient, but this will of course vary from converter to converter depending on the ratings.

From Figure 5.11j it is also evident that the mostly inductive fault current is fairly similar for the three systems. It can therefore be concluded that none of the methods affects the fault current to a large extent, and thus none of the methods can be deemed as current limiting methods in the sense that their objective is to limit the fault current. This is however not what the enhanced loops are designed to do, and failure to alter the fault current is thus not deemed as failure to achieve a control objective. In addition to $I_{c,VR,DW}$ having a distinctively faster return below 1 p.u., it also has a significant smaller transient at $t = t_c$, reaching only 1.4 p.u. while both $I_{c,PCL}$ and $I_{c,VR}$ reaches currents as high as $1.9 - 2.0$ per unit. This even by itself could pose a threat to the converter switching devices, possibly forcing protection systems to trip, and thus disconnecting the entire WECS. Even though $I_{c,VR}$ and $I_{c,VR,DW}$ reach steady-state approx. at the same time, two vastly different paths to obtaining this steady-state are observed, and the response of $I_{c,VR,DW}$ is thus concluded to be far superior to the two other systems. With that being said, the response of $I_{c,VR}$ at this lower, more realistic clearing time is considerably better than what was seen in Fig. 5.6f.

Moving on to the rotor side responses depicted in Fig. 5.12, a common observation is that the responses during fault are identical for all three systems in all five plots depicting the rotor side. This further emphasises that the enhanced control loops have approximately identical actual active power injection at the grid side during fault. Large differences do however appear for the post-fault system, but as expected, these large differences are mainly due to the large differences in the post-fault active power injection at the grid side. All results in Fig. 5.12 can therefore be seen in light of the responses seen in Fig. 5.11e. As for the previously discussed rotor side
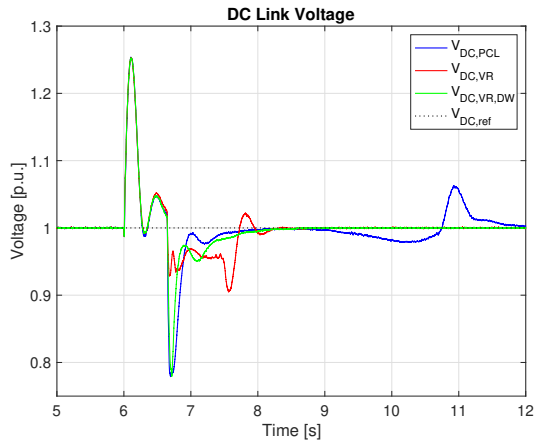
(a) DC link voltage.
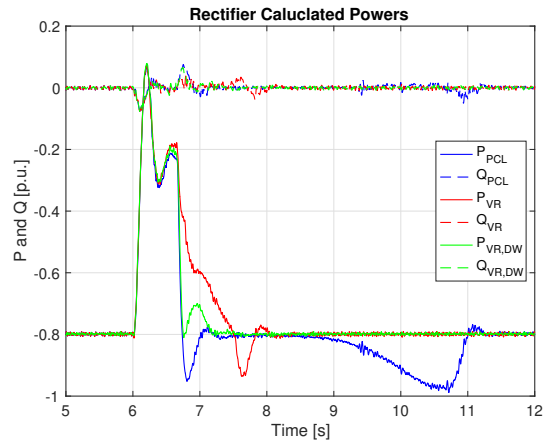


(b) Powers calculated by the rectifier control system.
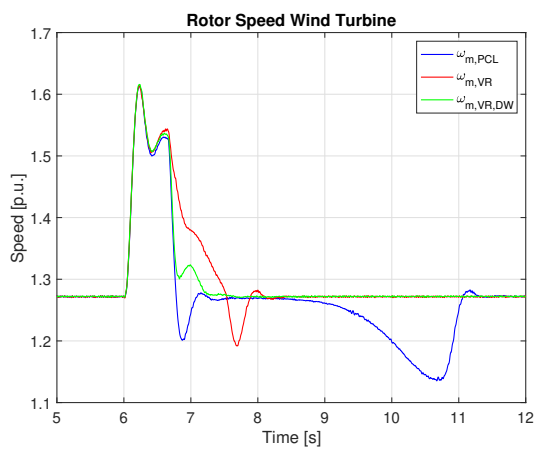


(c) Mechanical rotor speed of the wind turbine.
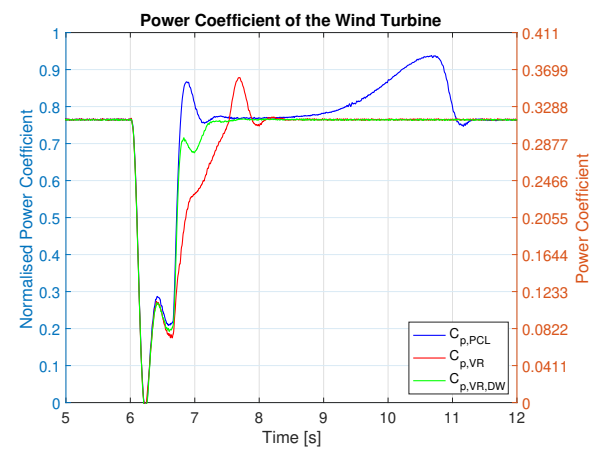


(d) Power coefficient of the wind turbine.
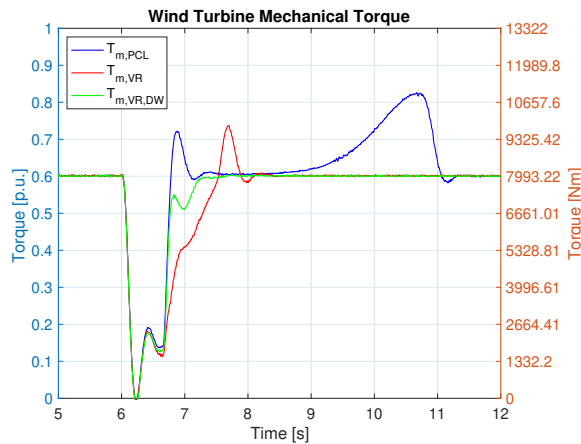


(e) Mechanical torque of the wind turbine.

Figure 5.12: Rotor side response of each of the enhanced control systems for $t_c = t_{cc,PCL} = 0.6444$ s.

results of the thesis, the rotor side variables do not seem to move towards instability during fault or post fault. In addition, none of the responses seems to impact the stability of the grid side.

Looking first at the DC link voltage in Fig. 5.12a, $V_{DC,PCL}$ and $V_{DC,VR,DW}$ are observed to have

similar responses, if disregarding the variations around $t = 10 - 11$ s, as the rectifier controller quickly tracks the voltage reference after a slightly over-dampened response. This stands in sharp contrast to $V_{DC,VR}$, which is significantly more oscillatory and has a larger deviation from the reference for a longer period of time. The active powers in Fig. 5.12b are highly linked with the turbine speeds in Figure 5.12c, which again affects the power coefficients and torques in Figures 5.12d and 5.12e.

Generally, the results are as expected, with the VR/DW system experiencing less time of operation away from nominal values, in addition to having less oscillations, thus potentially putting less wear and tear on the wind turbine and related components than the other control topologies. The transients in the active powers seen at $t = t_c$ in Fig. 5.11e have slightly lower amplitude when calculated for the rotor side in Fig. 5.12b. Beyond this, the active powers match what was seen for the actual active power injection at the grid side. The inverse relationship between the turbine speed and the torque/power coefficient, when operating on the right half side of the power curve, is also clearly visible.

Based on the analysis provided above, some main conclusions can be outlined for the enhanced control loops and their functioning. Before even being considered as a viable option for improving transient stability, it should be confirmed that the loop does not negatively impact the steady-state performance of the system. This is true for all three enhanced systems, as the grid side controller is able to track the power reference without steady-state deviation, and at the same time achieves all the controller objectives of the original Synchronverter when operating in steady-state.

As already concluded, all of the enhanced control structures achieve the first controller objective of improving the transient rotor angle stability of the system. The control system equipped with a VR and the system equipped with both a VR and artificial DWs does however, in addition to yielding better stability margins than the PCL system, have the large advantage of not requiring additional infrastructure investments, such as sensors and communication equipment. The PCL method would however most likely be far cheaper than e.g. braking resistors or any of the other traditional methods of improving the transient stability discussed in Section 5.1.

Large variability has been pointed out between the three enhanced loops in regards to fulfilment of the second controller objective. For the clearing time investigated above it is evident that the power correction loop fails to enable the system to operate at a sufficiently low current immediately after the fault is cleared. The system added with a virtual resistor provides a significant improvement over the PCL system, but has the same problem when pushed to its critical clearing time, and fulfilment of objective number two is thus conditional upon the clearing time being sufficiently low. Adding the artificial damper windings to the system equipped with the virtual resistor does however provide a response far superior to the two other system topologies, bringing the converter current down to acceptable levels in only 3 cycles for the clearing time investigated above, clearly satisfying both of the set objectives for the enhanced control loops.

Furthermore, adding the virtual DWs to the VR system requires close to zero additional cost as everything is implemented digitally in the controller. As such, it can be argued that there is no point in implementing the virtual resistor as a standalone addition. This is especially true when considering the observed oscillations most likely caused by implementing the VR, and the fact that the damper windings have the ability to dampen out oscillations and possibly also improve small-signal stability. As such, the proposed novel control structure, equipped with both a virtual resistor and artificial damper windings, is shown to be a large improvement over both the original Synchronverter and the two other enhanced control loops, yielding excellent performance for both long-lasting and shorter clearing times.

# Chapter 6

# Conclusions

*This chapter will outline conclusions for both the stability analysis carried out on the original system and the proposed control loops improving the transient stability. The conclusions will be tied to the objectives and targeted contribution of the thesis. Lastly, recommendations for future research will be proposed based on the findings and discussions provided by the investigations carried out in this thesis.*

## 6.1   Concluding Remarks

The Synchronverter control technology has been adapted to a wind energy conversion system using three-phase back-to-back converters for connection to the grid. The back-to-back converters are used as the wind turbine is a variable speed turbine using a directly driven PMSG, and while the rectifier controls the DC link voltage, the inverter controls the power injection to the grid based on the operating mode of the turbine.

An investigation into the system transient rotor angle stability has been carried out using different analytical methods to establish whether classical stability analysis known from the conventional synchronous generator is still applicable for the Synchronverter VSM, or if new methods must be applied. The analytical system model has also been compared to the simulation model to demonstrate the correctness of the analytical dynamic formulations. To validate the functioning and accuracy of the different analytical stability analysis methods, simulations have been carried out in the MATLAB/Simulink environment using de-loaded turbine mode to obtain the correct stability limits and the true system response. Enhanced control loops were then proposed to improve the stability of the system and advance the dynamic responses of the controllers. These new control loops were also simulated to verify their ability and performance related to a set of defined controller objectives.

The analytical methods of determining the stability limits of the system yielded large variations in precision and performance related to obtaining the desired Critical Clearing Angle (CCA) and Critical Clearing Time (CCT), and it has been shown that the more precise modelling technique used, the more precise are the results. The first methods to be tested were the Equal Area Criterion and the Transient Energy Function which were both based on the classical model of an unregulated system without damping. As expected, the two methods found identical CCAs, but while the CCT could not be found analytically by the EAC, the CCT found by the TEF was far

too conservative, deviating with $88.47\%$ from the real CCT. When adding the damping term to the model, the TEF gave a far too high estimate of the system stability with an estimate of the CCT $57.45\%$ above the real CCT, thus predicting an unstable system to be stable.

Through these results, two important characteristic properties were illustrated. Firstly the impact of the damping/frequency drooping on the dynamic response of the Synchronverter VSM is significant, especially if the inertia gain is tuned to be relatively small. This term can thus not be neglected in the analysis. Secondly, the deteriorating effect of the Reactive Power Loop (RPL) is drastically reducing the stability limits of the system to the point where dynamical formulations assuming an unregulated system is no longer applicable. This was shown to be true even for the inherently conservative Lyapunov energy function method. As such, the results clearly show that using an analytical model formulation based on the classical model known from the conventional SG, and applying traditional analysis methods, both with and without damping, does not adequately predict the stability limits of the Synchronverter VSM. Additional investigations were therefore carried out to obtain an adequate analysis method for the VSM.

The quasi-steady approximate Lyapunov method was then derived to include the effect of the RPL in the analysis. The method showed an excellent ability to predict the stability limits of the system with a high degree of precision, yielding a deviation of only $10.64\%$ or two cycles. Moreover, its precision with regard to the limits of the analytical system model, found using full forward numerical integration of the system dynamics, was even better, clearly demonstrating the capabilities of the quasi-steady method, which to a large degree render possible a faster and more precise analytical analysis of the VSM than previous methods.

The performances of the different analytical methods are closely tied to the correctness of the analytical model itself. While the classical model is highly imprecise, simulation results show that the simulation model and the mathematical model describing the full Synchronverter dynamics have almost identical responses. The two systems responded identically throughout both the pre-fault period and the fault-period. The relatively small difference in system response is found in the post-fault system and has been attributed to the already known simplifications of the analytical model. The deviation is however limited to a time delay in the response, and not the characteristic of the response itself. The deviation between the models is therefore considered to be as expected. Nevertheless, the analytical model has been shown to perform very well when analysing the transient rotor angle stability of the original Synchronverter system, and thus fulfils its desired purpose.

While the stability limits in the sense of rotor angle stability were clearly identified by the analysis, thus fulfilling the objective of the stability investigation, the simulation results showed that clearing the fault at the stability limit yielded an unfeasible operating scenario immediately after clearing the fault. This was due to the low back-EMF, which is a direct effect of the RPL, resulting in a converter current higher than $1.6$ per unit, effectively damaging the switching devices followed by disconnection of the converter. As clearing the fault at the stability limit results in an unfeasible operating condition, the actual stability limit, i.e. highest clearing time yielding a feasible post-fault operating scenario, is concluded to be far lower than the CCT of $386.1$ ms found in the simulation. The obvious disadvantage of the Synchronverter not being able to control the current was thus emphasised, and the need for measures improving the transient rotor angle stability was highlighted.

Three different enhanced control structures have been proposed to improve the stability and facilitate a feasible operating condition immediately after fault-clearing; a Power Correction Loop (PCL) system, a Virtual Resistor (VR) system and a system equipped with both a VR and

artificial Damper Windings (DWs). While the PCL needed extra hardware to function, the other two proposed systems were implemented digitally without the need for extra investments. An important feature was the possibility of implementing the enhanced loops without altering the steady-state characteristics of the Synchronverter. In this perspective, all three systems performed very well, with all controllers reaching steady-state without steady-state deviation.

All three systems are indeed fulfilling their primary objective of improving the rotor angle stability, with the PCL providing the least improvement in stability limits of $66.9\%$. Differences were however pointed out related to how quickly steady-state was achieved and how fast the controllers are able to track the references after the fault. This was tied to the simulation results revealing that, as for the original system, both the PCL and the VR yielded an excessively high converter current if cleared at their respective CCTs, thus failing to fulfil the second control objective of the enhanced loops.

These two enhanced loops were also shown to have a significantly poorer stability limit compared to the VR/DW system, which demonstrated an excellent ability to improve the transient stability far beyond common power system clearing times, and at the same time limit the operating time of excessively high post-fault currents to acceptable levels. This was shown for both an extremely long-lasting fault, and a fault-duration more typically seen in the power system. The damper windings are also shown to have the inherent capability of damping out high-frequent oscillations that might occur, possibly also improving small-signal rotor angle stability.

Even though having the significant disadvantage of requiring additional hardware equipment and yielding the least improvement in stability, the PCL was shown to be easily implemented into the quasi-steady approximate Lyapunov method for analytical investigation, yielding satisfyingly accurate predictions. This attribute is highly valued, as fast analytical investigations into system stability are preferable over time-consuming simulations. Furthermore, while not satisfyingly achieving both controller objectives when the fault is cleared at its CCT, the response of the VR system was shown to be far better when cleared at a lower clearing time, thus constituting a real improvement over the original system.

The same can be assumed for the PCL system, but the improvement over the original system would, in that case, be significantly smaller. However, fine-tuning the PCL coefficient $M$ and the VR $R_{vr}$ could have yielded better system responses, and potentially larger improvements, for these two systems. Apart from the high converter current and the lower CCT, the PCL system actually has a notably faster and more well-dampened controller response compared to the VR system, but when adding the artificial damper windings to the VR system, the proposed VR/DW controller is undoubtedly a far superior implementation over both of the other two enhanced loops.

It can therefore be concluded that traditional stability analysis methods known from the conventional synchronous generator are no longer viable for the Synchronverter virtual synchronous machine, and that a modified quasi-steady approximate Lyapunov method must be utilised to incorporate the deteriorating effect of the reactive power loop into the analysis. The quasi-steady method is proven to yield accurate stability predictions, and the simulation results obtained in this project verifies this conclusion.

The novel, enhanced Synchronverter control system, added with both a virtual resistor and artificial damper windings, is shown to yield exceptionally good system responses when subjected to a severe contingency, without changing the steady-state characteristics of the system. Furthermore, it demonstrates a fast and well-dampened return to reference values after fault-clearing without

excessively high converter currents. As such, the implementation is single handily improving the stability limit well above $1.5$ seconds, which in the context of rotor angle stability is considered extremely long. The enhanced Synchronverter is therefore confirmed as a promising method of connecting large-scale renewables, such as wind energy conversion systems, to the grid by offering improved stability over the current connection schemes.

The first main objective of this thesis was to investigate the transient stability of the original Synchronverter system. This was done with the aim of establishing the applicability of traditional stability analysis when investigating the transient rotor angle stability of a VSM, comparing the analytical results to simulation results, and if needed, outline a modified analysis method yielding viable stability predictions also for the VSM. The second main objective was to modify the Synchronverter control structure to improve the stability using enhanced control loops. This was done with the aim of proposing easily implemented control structures, requiring a minimum amount of both tuning and increase in controller complexity.

These objectives were closely linked to the targeted contributions, which were to first create an analytical model that could be used to investigate the Synchronverter dynamical response analytically, and provide a detailed comparison between the simulated system and the obtained analytical model. Then, a novel, enhanced Synchronverter control structure, using a virtual resistor and artificial damper windings, was to be proposed. The control structure should drastically improve the dynamic response of the Synchronverter control system when subjected to a contingency, and by this advancing the transient stability of a power system consisting of a VSM-connected wind turbine. Relating the above conclusions to the objectives and targeted contributions of the thesis, it is beyond doubt that the objectives are satisfyingly achieved, and that the targeted contributions have been made.

## 6.2   Further Work

Based on the results, discussions and conclusions in Chapters 4 and 5, as well as Section 6.1, several extensions, improvements and profoundly interesting complementary research topics to this thesis can be identified as subjects of possible future research. A list containing summaries of the most prominent topics that should be the subject of future work is provided below.

- The investigations in this thesis have been based on the major simplification of assuming static wind conditions, and subsequently constant power available from the wind turbine. Continuously changing wind speeds are however a major factor when investigating the stability of a power system dominated by intermittent wind power generation. As such, the stability of the system should be investigated for large variations in the wind speed such as a large increase or a sudden drop. Furthermore, also small variations using e.g. real weather data or low pass filtered noise with random variance, could be used to investigate how these small-signal disturbances affect the system, and as such make the system more realistic in its behaviour. This could also be tied to an investigation into small-signal rotor angle stability.

- The focus of both the specialisation project and this thesis has been on the Synchronverter VSM topology. However, there exist several other virtual synchronous machine topologies, and control systems based on droop control, that can be utilised for a WECS as in this thesis, having many of the same characteristics as the Synchronverter. Therefore, as stated in the specialisation project, a comparative analysis between different control methods, to identify benefits, weaknesses, and stability characteristics for each of them, should be carried out. Based on such an investigation it should be possible to make well-judged assessments of which control technology to apply for which types of systems, and how they differ in relation to system stability.

- While deriving three different methods of improving the transient stability by implementing new control loops to the grid side controller, new implementations to the rotor side controller was not investigated. It should be the topic of future work to look at how also the rotor side control system can participate in improving the stability and possibly increase the FRT capabilities of the system. This work should also include investigations on how to implement a current limiting scheme for the rotor side controller to limit the current injected onto the DC link. Furthermore, work can be done to fine-tune the PCL- and VR parameters, $M$ and $R_{vr}$, to yield the best results possible for a given system.

- The investigations carried out in this thesis revolved around a hypothetical SMIB system. While being adequate for the scope of this thesis, the system model should be expanded and modified in future work to analyse two distinctively different operating scenarios:

  - Expanding the system to consist of several converters/machines connected to a common grid, possibly also including inter-area connections between multiple groups of synchronised converters/machines. This would allow an investigation into how disturbances may cause oscillations between two or more converters/machines, or even inter-are oscillations. Such an expansion is also of interest to investigate the effect of implementing control algorithms such as the Power System Stabiliser (PSS) known from the conventional SG, into the VSM, and to perform a more thorough stability analysis, looking into how the Synchronverter behaves when operating in parallel with other generators. Load sharing capabilities and the effect of tripping parallel machines could also be investigated.

  – Expanding, and modifying, the system to comprise a microgrid fully equipped with both a VSM-based WECS and a Battery Energy Storage System (BESS). This would facilitate an investigation into the stability of the Synchronverter VSM when operated in islanded mode. Furthermore, offshore microgrids have gained significant interest due to Oil and Gas (O&G) companies investing in offshore wind farms in combination with Energy Storage System (ESS) as a complement to the already installed gas turbines to supply O&G installations with renewable energy[70]. Applying the Synchronverter VSM to such a topology, using real load scenarios and parameters gathered from a real-life installation, would create many highly interesting research topics such as power system stability, operating mode transitions and optimal control.

Within the scope of expanding the system model, the system should also be modelled closer to real-life applications. As such, system parameters should come from a real system, and the turbine model should be more advanced, including pitch control and braking systems etc., while also being scaled more closely to the large-scale wind power installations of several MW commonly seen today.

• In analysing the transient rotor angle stability, stability was only considered for the power angle range $[0, \pi]$, following the approach known from the conventional SG. This overlooks the fact that the converter has the ability to allow bidirectional power flow, and it is in [62] suggested that this characteristic allows the converter to ride thorough higher power angles to reach new, asymptotically stable equilibrium points if cleared inside certain time periods. This would allow for multiple CCTs to be found for the same system, possible yielding much higher stability limits, and more precise evaluations of the stability characteristics of the VSM. An investigation into how this can be applied to the Synchronverter and how it would affect a WECS system connected though back-to-back converters should therefore be carried out.

• The enhanced control structures proposed, and tested, to improve the transient rotor angle stability have not been tested for smaller voltage drops or frequency instabilities. As such, even though the enhanced systems have been shown to not affect the steady-state operation of the Synchronverter, simulations have not been carried out to re-test/verify the enhanced systems' ability to contribute with ancillary services such as frequency control for an operating scenario with grid frequencies deviating from the nominal frequency. The novel, enhanced Synchronverter controller with a virtual resistor and artificial damper windings should therefore in future research be tested for a larger variety of operating conditions to further verify its overall performance.

# Bibliography

[1]  IEA. (2019). World electricity generation by fuel, 1971-2017, [Online]. Available: `https://www.iea.org/data-and-statistics/charts/world-electricity-generation-by-fuel-1971-2017` (visited on 05/05/2020).

[2]  IEA. (2019). Renewables 2019, [Online]. Available: `https://www.iea.org/reports/renewables-2019` (visited on 05/05/2020).

[3]  European commission, 'A policy framework for climate and energy in the period from 2020 to 2030', European Union, 2014.

[4]  21st Conference of the Parties of the UNFCCC, 'United nations framework convention on climate change - paris agreement', United Nations, 2015.

[5]  H. Høstmark, 'Virtual synchronous machine based wind energy conversion system', Department of Electric Power Engineering, NTNU – Norwegian University of Science and Technology, Project report in TET4520, Dec. 2019, Unpublished Specialisation Project.

[6]  B. Parkin. (2019). Subsidy-free green power may be closer than you think in germany, [Online]. Available: `https://www.bloomberg.com/news/articles/2019-06-17/subsidy-free-green-power-may-be-closer-than-you-think-in-germany` (visited on 27/08/2019).

[7]  I. Komusanac, D. Fraile and G. Brindley, 'Wind energy in europe in 2018 - trends and statistics', Wind Europe, 2019.

[8]  Q. Zhong, 'Power-electronics-enabled autonomous power systems: Architecture and technical routes', *IEEE Transactions on Industrial Electronics*, vol. 64, no. 7, pp. 5907–5918, Jul. 2017, ISSN: 0278-0046. DOI: `10.1109/TIE.2017.2677339`.

[9]  ENTSO-e. (2012). Operational reserve ad hoc team report- final version, [Online]. Available: `https://www.entsoe.eu/fileadmin/user_upload/_library/resources/LCFR/2012-06-14_SOC-AhT-OR_Report_final_V9-3.pdf` (visited on 28/10/2019).

[10]  Z. C. J. Tian, 'Reactive power capability of the wind turbine with doubly fed induction generator', eng, 2013.

[11]  J. F. Manwell, J. G. McGowan and A. L. Rogers, *Wind Energy Explained: Theory, Design and Application*, Second edition. John Wiley and Sons, Ltd, 2010, ISBN: 978-0-470-01500-1.

[12] A. Betz, 'Wind-energie und ihre ausnutzung durch windmühlen', ger, Aus Naturwissenschaft und TEchnik, vol. H. 2, 1926.

[13] O. Anaya-Lara, *Lecture notes elk 12 - wind power in electric power systems*, Norwegian University of Science and Technology, 2019.

[14] S. Heier, *Grid integration of wind energy : onshore and offshore conversion systems*, eng, 3rd ed. Chichester, England: Wiley, 2014, ISBN: 1-118-70329-4.

[15] J. G. Slootweg, H. Polinder and W. L. Kling, 'Representing wind turbine electrical generating systems in fundamental frequency simulations', *IEEE Transactions on Energy Conversion*, vol. 18, no. 4, pp. 516–524, Dec. 2003, ISSN: 0885-8969. DOI: `10.1109/TEC.2003.816593`.

[16] Mathworks, *Variable pitch wind turbine model - simulink*. [Online]. Available: `https://se.mathworks.com/help/physmod/sps/powersys/ref/windturbine.html`.

[17] M. Abdullah, A. Yatim, C. Tan and R. Saidur, 'A review of maximum power point tracking algorithms for wind energy systems', *Renewable and Sustainable Energy Reviews*, vol. 16, no. 5, pp. 3220–3227, 2012, ISSN: 1364-0321. DOI: `https://doi.org/10.1016/j.rser.2012.02.016`. [Online]. Available: `http://www.sciencedirect.com/science/article/pii/S1364032112001098`.

[18] Q.-C. Zhong, Z. Ma, W.-L. Ming and G. C. Konstantopoulos, 'Grid-friendly wind power systems based on the synchronverter technology', *Energy Conversion and Management*, vol. 89, pp. 719–726, 2015, ISSN: 0196-8904. DOI: `https://doi.org/10.1016/j.enconman.2014.10.027`. [Online]. Available: `http://www.sciencedirect.com/science/article/pii/S019689041400908X`.

[19] A. Attya, J. Dominguez-Garcia and O. Anaya-Lara, 'A review on frequency support provision by wind power plants: Current and future challenges', *Renewable and Sustainable Energy Reviews*, vol. 81, pp. 2071–2087, 2018, ISSN: 1364-0321. DOI: `https://doi.org/10.1016/j.rser.2017.06.016`. [Online]. Available: `http://www.sciencedirect.com/science/article/pii/S1364032117309553`.

[20] O. Anaya-Lara, *Wind energy generation: modelling and control*, eng, 1st ed. Chichester: Wiley, 2009, ISBN: 9780470714331.

[21] J. A. Baroudi, V. Dinavahi and A. M. Knight, 'A review of power converter topologies for wind generators', *Renewable Energy*, vol. 32, no. 14, pp. 2369–2385, 2007, ISSN: 0960-1481. DOI: `https://doi.org/10.1016/j.renene.2006.12.002`. [Online]. Available: `http://www.sciencedirect.com/science/article/pii/S0960148106003430`.

[22] M. Amin, *Lecture notes elk 21 - electronics for control of power*, Norwegian University of Science and Technology, 2019.

[23] N. Mohan, *Power electronics : converters, applications, and design*, Third edition. John Wiley and Sons, Ltd, 2003, ISBN: 0471226939.

[24] Q. Zhong and T. Hornik, 'Introduction', in *Control of Power Inverters in Renewable Energy and Smart Grid Integration*. IEEE, 2012, pp. 1–61. DOI: `10.1002/9781118481806.ch1`. [Online]. Available: `https://ieeexplore.ieee.org/document/6381824`.

[25] Mathworks, *Pwm generator (2-level)*. [Online]. Available: `https://se.mathworks.com/help/physmod/sps/powersys/ref/pwmgenerator2level.html`.

[26] F. Rahman, 'Lecture 23 - three-phase spwm inverters - elec4614', University of New South Wales - School of Electrical Engineering and Telecommunications, 2019. [Online]. Available: `https://subjects.ee.unsw.edu.au/elec4614/Lecture%2023%20-%20Three-phase%20SPWM%20Inverters.pdf`.

[27] Q. Zhong and G. Weiss, 'Synchronverters: Inverters that mimic synchronous generators', *IEEE Transactions on Industrial Electronics*, vol. 58, no. 4, pp. 1259–1267, Apr. 2011, ISSN: 0278-0046. DOI: `10.1109/TIE.2010.2048839`.

[28] Q. Zhong and G. Weiss, 'Static synchronous generators for distributed generation and renewable energy', in *2009 IEEE/PES Power Systems Conference and Exposition*, Mar. 2009, pp. 1–6. DOI: `10.1109/PSCE.2009.4840013`.

[29] Z. Ma, 'Synchronverter-based control for wind power', PhD thesis, Loughborough University, Nov. 2012. [Online]. Available: `https://repository.lboro.ac.uk/articles/Synchronverter-based_control_for_wind_power/9218990`.

[30] Z. Ma and Q.-C. Zhong, 'Synchronverter-based control strategy for back-to-back converters in wind power applications', *IFAC Proceedings Volumes*, vol. 45, no. 21, pp. 349–354, 2012, 8th Power Plant and Power System Control Symposium, ISSN: 1474-6670. DOI: `https://doi.org/10.3182/20120902-4-FR-2032.00062`. [Online]. Available: `http://www.sciencedirect.com/science/article/pii/S1474667016319942`.

[31] Z. Ma, Q. Zhong and J. D. Yan, 'Synchronverter-based control strategies for three-phase pwm rectifiers', in *2012 7th IEEE Conference on Industrial Electronics and Applications (ICIEA)*, Jul. 2012, pp. 225–230. DOI: `10.1109/ICIEA.2012.6360727`.

[32] J. Machowski, J. W. Bialek and J. R. Bumby, *Power System Dynamics:Stability and Control*, eng, 2nd ed. Chichester, U.K.: John Wiley & Sons Ltd, 2008, ISBN: 978-0-470-72558-0.

[33] H. Dharmawardena and K. Uhlen, 'Modeling variable speed wind turbine for power system dynamic studies', in *2015 IEEE Students Conference on Engineering and Systems (SCES)*, Nov. 2015, pp. 1–6. DOI: `10.1109/SCES.2015.7506448`.

[34] M. Ghandhari, *Stability of Power Systems, An introduction*. Royal Institute of Technology, KTH, Stockholm, 2018.

[35] H. Beck and R. Hesse, 'Virtual synchronous machine', in *2007 9th International Conference on Electrical Power Quality and Utilisation*, Oct. 2007, pp. 1–6. DOI: `10.1109/EPQU.2007.4424220`.

[36] J. Driesen and K. Visscher, 'Virtual synchronous generators', in *2008 IEEE Power and Energy Society General Meeting - Conversion and Delivery of Electrical Energy in the 21st Century*, Jul. 2008, pp. 1–3. DOI: `10.1109/PES.2008.4596800`.

[37] M. Ashabani, F. D. Freijedo, S. Golestan and J. M. Guerrero, 'Inducverters: Pll-less converters with auto-synchronization and emulated inertia capability', *IEEE Transactions on Smart Grid*, vol. 7, no. 3, pp. 1660–1674, May 2016, ISSN: 1949-3061. DOI: `10.1109/TSG.2015.2468600`.

[38]  H. Alrajhi Alsiraji and R. El-Shatshat, 'Comprehensive assessment of virtual synchronous machine based voltage source converter controllers', *IET Generation, Transmission Distribution*, vol. 11, no. 7, pp. 1762–1769, 2017, ISSN: 1751-8695. DOI: `10.1049/iet-gtd.2016.1423`.

[39]  J. Liu, Y. Miura and T. Ise, 'Comparison of dynamic characteristics between virtual synchronous generator and droop control in inverter-based distributed generators', *IEEE Transactions on Power Electronics*, vol. 31, no. 5, pp. 3600–3611, May 2016, ISSN: 1941-0107. DOI: `10.1109/TPEL.2015.2465852`.

[40]  H. Lin, C. Jia, J. M. Guerrero and J. C. Vasquez, 'Angle stability analysis for voltage-controlled converters', *IEEE Transactions on Industrial Electronics*, vol. 64, no. 8, pp. 6265–6275, Aug. 2017, ISSN: 1557-9948. DOI: `10.1109/TIE.2017.2682022`.

[41]  M. D. Pedersen, *Lecture notes ttk4115 - linear systems theory*, Norwegian University of Science and Technology, 2018.

[42]  H. K. Khalil, *Nonlinear systems*, eng, 3rd ed., Pearson new international ed., ser. Always learning. Harlow: Pearson Education, 2014, ISBN: 9781292039213.

[43]  P. Kundur, J. Paserba, V. Ajjarapu, G. Andersson, A. Bose, C. Canizares, N. Hatziargyriou, D. Hill, A. Stankovic, C. Taylor, T. Van Cutsem and V. Vittal, 'Definition and classification of power system stability ieee/cigre joint task force on stability terms and definitions', *IEEE Transactions on Power Systems*, vol. 19, no. 3, pp. 1387–1401, Aug. 2004, ISSN: 0885-8950. DOI: `10.1109/TPWRS.2004.825981`.

[44]  P. Kundur, *Power System Stability and Control*, eng, 1st ed. New York: McGraw-Hill, 1994, ISBN: 0-07-035958-X.

[45]  M. Ghandhari and L. Söder, *Static Analysis of Power Systems*. Royal Institute of Technology, KTH, Stockholm, 2016.

[46]  M. Amin, *Small-signal Stability Characterization of Interaction Phenomena between HVDC System and Wind Farms*, eng. NTNU, 2017, ISBN: 978-82-326-2493-5. [Online]. Available: `http://hdl.handle.net/11250/2451148`.

[47]  G. Weiss and Q.-C. Zhong, 'Some problems with connecting renewable energy sources to the grid', Jul. 2010.

[48]  Q. Zhong and T. Hornik, 'Preliminaries', in *Control of Power Inverters in Renewable Energy and Smart Grid Integration*. IEEE, 2012, pp. 63–78. DOI: `10.1002/9781118481806.ch2`. [Online]. Available: `https://ieeexplore.ieee.org/document/6381813`.

[49]  Q. Zhong and T. Hornik, 'Conventional synchronisation techniques', in *Control of Power Inverters in Renewable Energy and Smart Grid Integration*. IEEE, 2012, pp. 360–378. DOI: `10.1002/9781118481806.ch22`. [Online]. Available: `https://ieeexplore.ieee.org/document/6381810`.

[50]  J. Svensson, 'Synchronisation methods for grid-connected voltage source converters', *IEE Proceedings - Generation, Transmission and Distribution*, vol. 148, no. 3, pp. 229–235, May 2001, ISSN: 1350-2360. DOI: `10.1049/ip-gtd:20010101`.

[51]  Q. Zhong, P. Nguyen, Z. Ma and W. Sheng, 'Self-synchronized synchronverters: Inverters without a dedicated synchronization unit', *IEEE Transactions on Power Electronics*, vol. 29, no. 2, pp. 617–630, Feb. 2014. DOI: `10.1109/TPEL.2013.2258684`.

[52]  Q. Zhong, Z. Ma and Phi-Long Nguyen, 'Pwm-controlled rectifiers without the need of an extra synchronisation unit', in *IECON 2012 - 38th Annual Conference on IEEE Industrial Electronics Society*, Oct. 2012, pp. 691–695. DOI: `10.1109/IECON.2012.6388668`.

[53]  O. Anaya-Lara, *Lecture notes - elk12 wind power in electric power systems*, Accessed: 24.10.2019.

[54]  M. Ribbens-Pavella, *Transient stability of power systems : theory and practice*, eng. Chichester: Wiley, 1994, ISBN: 0471942138.

[55]  P. M. Anderson and A. A. Fouad, *Power System Control and Stability*, eng, 2nd ed. John Wiley & Sons, 2002, ISBN: 9780471238621.

[56]  Z. Shuai, C. Shen, X. Liu, Z. Li and Z. J. Shen, 'Transient angle stability of virtual synchronous generators using lyapunov's direct method', *IEEE Transactions on Smart Grid*, vol. 10, no. 4, pp. 4648–4661, Jul. 2019, ISSN: 1949-3061. DOI: `10.1109/TSG.2018.2866122`.

[57]  D. P. Kothari, *Electric machines*, eng, 5th ed. Chennai: McGraw Hill Education (India), 2018, ISBN: 9789352606405.

[58]  Y. Xue, T. Van Custem and M. Ribbens-Pavella, 'Extended equal area criterion justifications, generalizations, applications', *IEEE Transactions on Power Systems*, vol. 4, no. 1, pp. 44–52, Feb. 1989, ISSN: 1558-0679. DOI: `10.1109/59.32456`.

[59]  M. Pai, *Energy function analysis for power system stability*, eng, New York, NY, 1989.

[60]  *Differential equations, linear algebra and its applications*, eng, 2nd ed. Harlow: Pearson, 2014, ISBN: 9781784480202.

[61]  Y.-H. Moon, B.-K. Choi and T.-H. Roh, 'Estimating the domain of attraction for power systems via a group of damping-reflected energy functions', *Automatica*, vol. 36, no. 3, pp. 419–425, 2000, ISSN: 0005-1098. DOI: `https://doi.org/10.1016/S0005-1098(99)00162-4`. [Online]. Available: `http://www.sciencedirect.com/science/article/pii/S0005109899001624`.

[62]  P. Li, Y. Wang, Y. Liu, H. Zhou, G. Gao and W. Lei, 'Transient stability analysis of virtual synchronous generator connected to an infinite bus', in *2019 IEEE Energy Conversion Congress and Exposition (ECCE)*, Sep. 2019, pp. 2099–2104. DOI: `10.1109/ECCE.2019.8913226`.

[63]  H. Sasaki, 'An approximate incorporation of field flux decay into transient stability analyses of multimachine power systems by the second method of lyapunov', *IEEE Transactions on Power Apparatus and Systems*, vol. PAS-98, no. 2, pp. 473–483, 1979.

[64]  Z. Shuai, C. Shen, X. Yin, X. Liu and Z. J. Shen, 'Fault analysis of inverter-interfaced distributed generators with different control schemes', *IEEE Transactions on Power Delivery*, vol. 33, no. 3, pp. 1223–1235, Jun. 2018, ISSN: 1937-4208. DOI: `10.1109/TPWRD.2017.2717388`.

[65]  T. Younis, M. Ismeil, E. Hussain and M. Orabi, 'Single-phase synchronverter with current-limitation for distributed generation', vol. 1, p. 8, May 2017.

[66]  H. Xin, L. Huang, L. Zhang, Z. Wang and J. Hu, 'Synchronous instability mechanism of p-f droop-controlled voltage source converter caused by current saturation', *IEEE Transactions on Power Systems*, vol. 31, no. 6, pp. 5206–5207, Nov. 2016, ISSN: 1558-0679. DOI: `10.1109/TPWRS.2016.2521325`.

[67]  Z. Shuai, W. Huang, C. Shen, J. Ge and Z. J. Shen, 'Characteristics and restraining method of fast transient inrush fault currents in synchronverters', *IEEE Transactions on Industrial Electronics*, vol. 64, no. 9, pp. 7487–7497, Sep. 2017, ISSN: 1557-9948. DOI: `10.1109/TIE.2017.2652362`.

[68]  M. Ebrahimi, S. A. Khajehoddin and M. Karimi-Ghartemani, 'An improved damping method for virtual synchronous machines', *IEEE Transactions on Sustainable Energy*, vol. 10, no. 3, pp. 1491–1500, Jul. 2019, ISSN: 1949-3037. DOI: `10.1109/TSTE.2019.2902033`.

[69]  A. Tebib and M. Boudour, 'An improved synchronverter based hvdc system considering damper windings effect', in *2018 International Conference on Electrical Sciences and Technologies in Maghreb (CISTEM)*, Oct. 2018, pp. 1–5. DOI: `10.1109/CISTEM.2018.8613381`.

[70]  Oljedirektoratet, 'Ressursrapport - funn og felt 2019', Oljedirektoratet, 2019.

# APPENDICES

# Per Unit Conversion

*This appendix contains the per unit system used in this thesis.*

It is common practice to use per unit (p.u.) values when analysing the power system, and the per unit system used in this thesis is therefore defined here. The base apparent power, $S_b$, is defined as the three-phase rated VSM power, while the base voltage, $V_b$, is defined as the rated phase-to-ground peak voltage of the grid, i.e $\sqrt{2}$ times the Root Mean Square (RMS) grid voltage. The rest of the base values are then defined below.

$$S_b = \text{Three-phase rated VSM power} \tag{A.1a}$$

$$V_b = \text{Rated grid phase-to-ground peak voltage} \tag{A.1b}$$

$$I_b = \frac{S_b}{\sqrt{\frac{3}{2}}V_b}\sqrt{\frac{2}{3}} \quad \text{(Base current defined as peak value of rated RMS current)} \tag{A.1c}$$

$$Z_b = \frac{V_b}{I_b} \quad \text{(Impedance base)} \tag{A.1d}$$

$$f_b = f_n \quad \text{(Frequency base defined as nominal grid frequency)} \tag{A.1e}$$

$$\omega_b = 2\pi f_b = \omega_n \tag{A.1f}$$

$$M_f i_{f,b} = \frac{V_b}{\omega_b} \quad \text{(Base Flux Excitation)} \tag{A.1g}$$

$$L_b = \frac{Z_b}{\omega_b} \quad \text{(Base inductance)} \tag{A.1h}$$

$$R_b = Z_b \quad \text{(Base resistance)} \tag{A.1i}$$

$$C_b = \frac{1}{\omega_b Z_b} \quad \text{(Base capacitance)} \tag{A.1j}$$

$$T_b = \frac{S_b}{\omega_b} \quad \text{(Base torque electrical system)} \tag{A.1k}$$

$$V_{DC,b} = 2V_b \quad \text{(Base DC link voltage)} \tag{A.1l}$$

$$T_{b,wind} = \frac{P_{rated,turbine}}{\omega_{rated,turbine}} \quad \text{(Base torque wind turbine)} \tag{A.1m}$$

Using the base values, all quantities can be represented in per unit by dividing the quantity by its base value, e.g. $V_{pu} = \frac{V}{V_b}$.

# B

# System Parameters

## B.1 Base Values for Per Unit Calculations

Table B.1: Base Values for Per Unit Calculations.

| Parameter | Value |
|---|---|
| Electrical system base power, $S_b$ | 1.0 MVA |
| Electrical system base frequency, $f_b$ | 50 Hz |
| Electrical system base frequency, $\omega_b$ | $2\pi f_b = 100\pi$ rad/s |
| Electrical system base torque, $T_b$ | 3183.1 Nm |
| Wind turbine mechanical base power, $P_{mech,b}$ | 1.0603 MW |
| Wind turbine mechanical base rotational speed, $\omega_{m,b}$ | 79.59 rad/s |
| Wind turbine mechanical base torque, $P_{mech,b}$ | 13322 Nm |
| Base AC voltage, $V_b$ | 563.3826 V |
| Base AC current, $I_b$ | 1183.3 A |
| Base impedance, $Z_b$ | 0.4761 Ω |
| Base inductance, $L_b$ | 0.0015 H |
| Base resistance, $R_b$ | 0.4761 Ω |
| Base capacitance, $C_b$ | 0.0067 F |
| Base DC voltage, $V_{DC,b}$ | 1126.8 V |
| Base DC current, $I_b$ | 887.4963 A |
| Base resistance DC link, $R_{DC,b}$ | 1.2696 Ω |
| Base capacitance DC link, $C_{DC,b}$ | 0.0025 F |
| Base flux excitation, $M_f i_{f,b}$ | 1.7933 Vs |

## B.2   Wind Turbine and PMSG Parameters

Table B.2: Turbine parameters.

| Parameter | Value |
|---|---|
| Turbine radius, $R$ | 1.2 m |
| Number of turbines, aggregated model | 550 |
| Air density, $\rho$ | 1.2 kg/m$^3$ |
| Optimal tip speed ratio, $\lambda_{opt}$ | 7.95 |
| Maximum power coefficient, $C_{p,max}$ | 0.411 |
| Rated wind speed, $v_{w,rated}$ | 12 m/s |
| Aggregated rated mechanical power, $P_{mech,rated}$ | 1.0603 MW |

Table B.3: PMSG parameters.

| Parameter | Value |
|---|---|
| Number of pole pairs PMSG, $p$ | 2 |
| Permanent magnet flux, $\Psi$ | 1.7933 Vs |
| Inertia of the PMSG, $J$ | 5.4713 kgm$^2$ |
| Friction factor of the PMSG, $D$ | 0 Nms |

## B.3   Power Grid Parameters

Table B.4: Grid parameters.

| Parameter | Absolute Value | Per Unit Value |
|---|---|---|
| Grid inductance, $L_g$ | 1.1 mH | 0.7 |
| Grid resistance, $R_g$ | 0.0476 $\Omega$ | 0.1 |
| Filter capacitance, $C$ | 494.75 μF | 0.074 |
| Parallel resistance, $R_C$ | 1000 $\Omega$ | 2100.4 |
| "Stator"/filter inductance, $L_s$ | 0.15155 mH | 0.1 |
| Grid side "stator"/filter resistance, $R_s$ | 0.4761 m$\Omega$ | 0.001 |
| Rotor side resistance, $R_{s,rotor}$ | 0.0024 $\Omega$ | 0.005 |
| DC link capacitance, $C_{DC}$ | 0.1003 F | 40 |
| Chopper resistance, $R_{chopper}$ | 2.1583 $\Omega$ | 1.7 |
| Breaker resistance, $R_B$ | 0.001 $\Omega$ | 0.0021 |

Table B.5: Electrical parameters.

| Parameter | Value |
|---|---|
| Rated power, $S_{rated}$ | 1.0 MVA |
| Nominal Line-Line voltage, $V_{gn,L-L}$ | 690 V |
| Nominal DC link voltage, $V_{DC,ref}$ | 1126.8 V |
| Nominal DC link current, $I_{n,DC}$ | 177.5 A |
| Nominal grid frequency, $f_n$ | 50 Hz |

# B.4   Synchronverter Parameters

Table B.6: Inverter Controller Parameters.

| Parameter | Value |
|---|---|
| $J$ | 2 |
| $K_q$ | 40000 |
| $D_p$ | 506.6059 |
| $D_q$ | 17750 |
| Virtual synchronising resistance, $R_{sync}$ | 0.0476 $\Omega$ |
| Virtual synchronising inductance, $L_{sync}$ | 0.53042 mH |
| Virtual resistor (enhanced loop), $R_{vr}$ | 0.0952$\Omega$ = 0.2 p.u. |
| PCL coefficient (enhanced loop), $M$ | 1.4125 |
| Switching frequency, $f_s$ | 5kHz |

Table B.7: Rectifier Controller Parameters

| Parameter | Value |
|---|---|
| $J_m$ | 4.0528 |
| $K_{qm}$ | 223050 |
| $K_{p,dc}$ | 18.3624 |
| $K_{i,dc}$ | 45.9061 |
| $D_{pm}$ | 2026.4 |
| Switching frequency, $f_s$ | 5kHz |
| Virtual synchronising resistance, $R_{sync}$ | 0.0024 $\Omega$ |
| Virtual synchronising inductance, $L_{sync}$ | 0.75774 mH |

# Appendix C

# Simulink Models

## C.1 Original System

### C.1.1 Full Original System
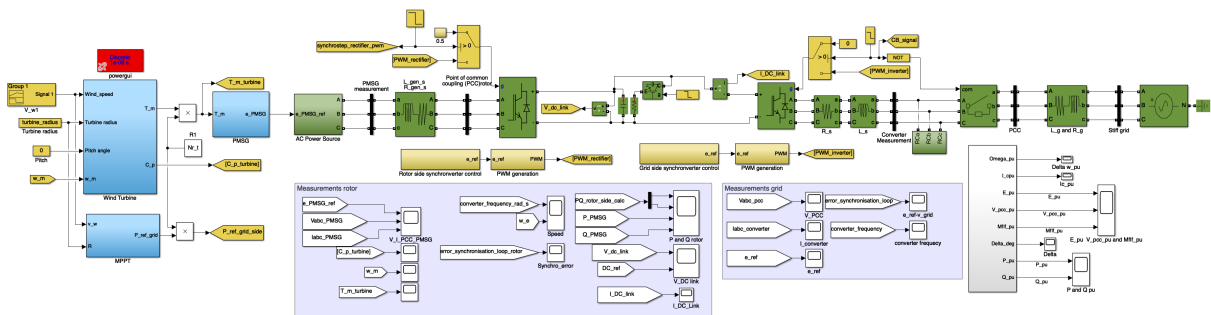


Figure C.1: Full system Simulink model.

### C.1.2 Wind turbine
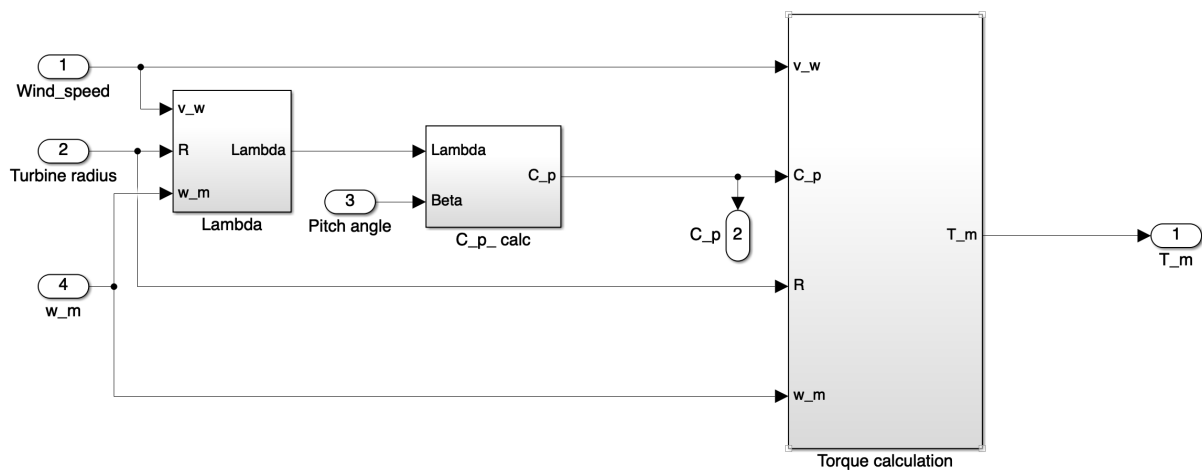


Figure C.2: Wind turbine Simulink model.

## C.1.3 Drive Train and PMSG
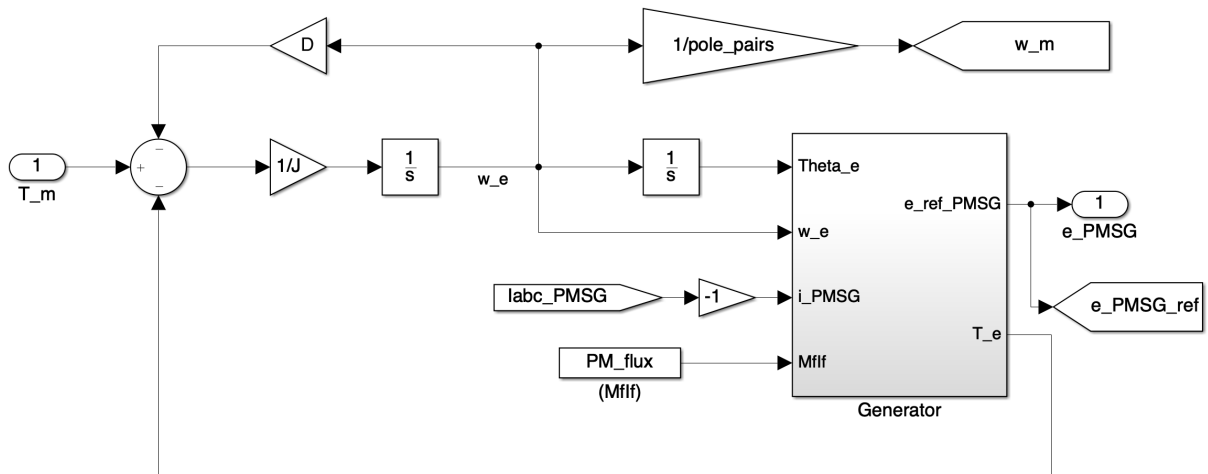


Figure C.3: Drive train and PMSG Simulink model.
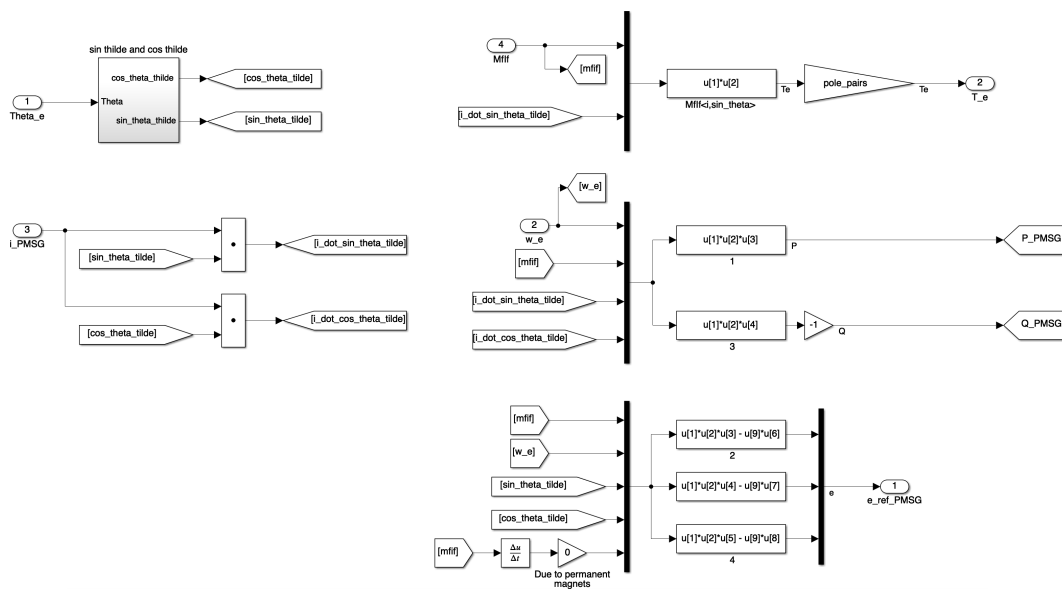


Figure C.4: PMSG Generator Simulink model.

## C.1.4   Grid Side Controller
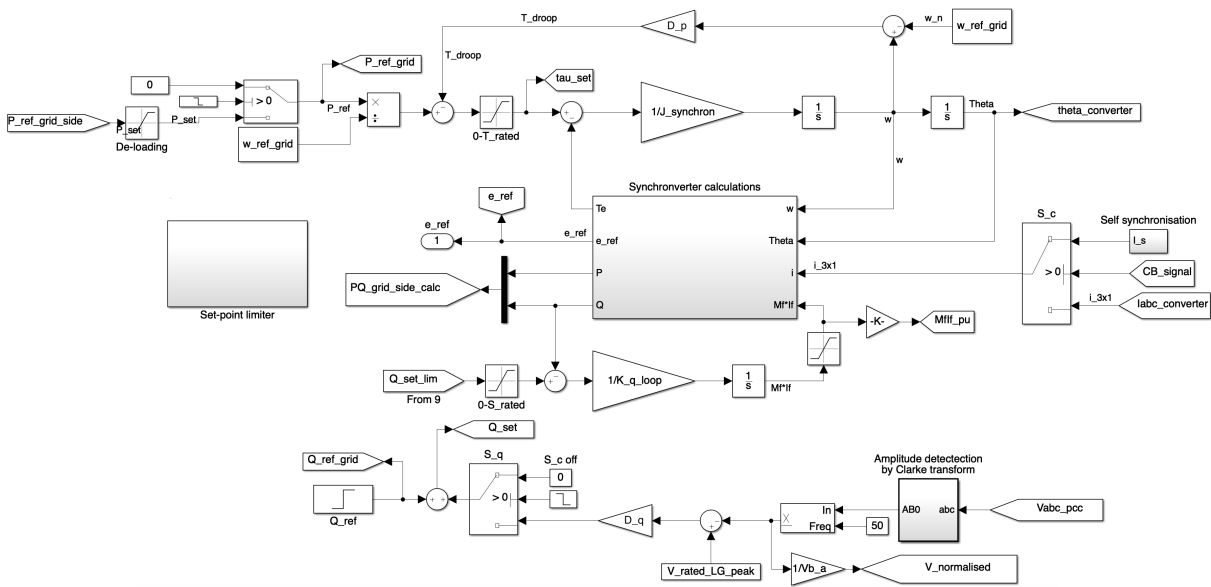


Figure C.5: Original grid side inverter control Simulink model.
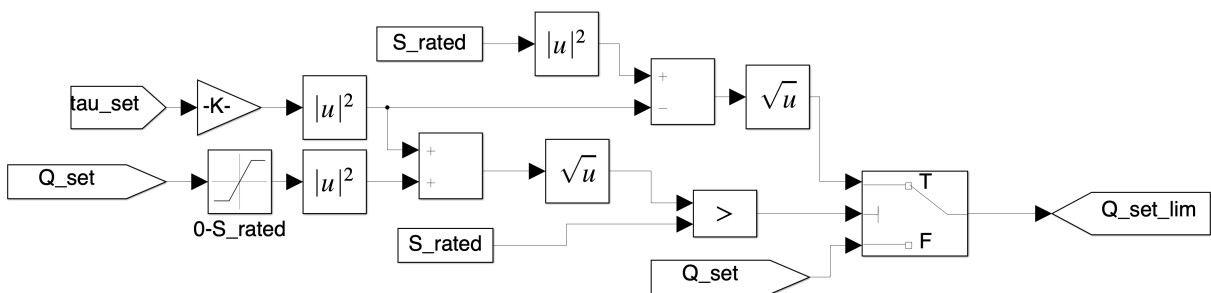


Figure C.6: Simulink implementation of set-point limiter.
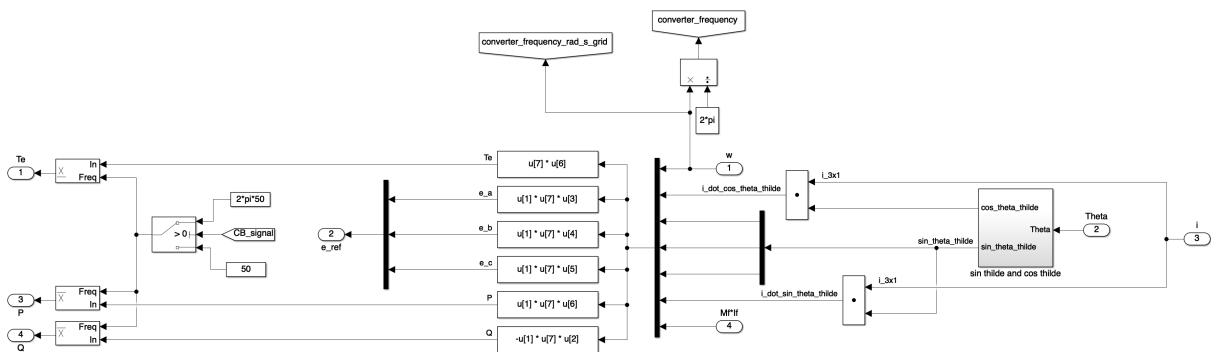


Figure C.7: Synchronverter core constituting the Synchronverter calculations.

## C.1.5   Rotor Side Controller
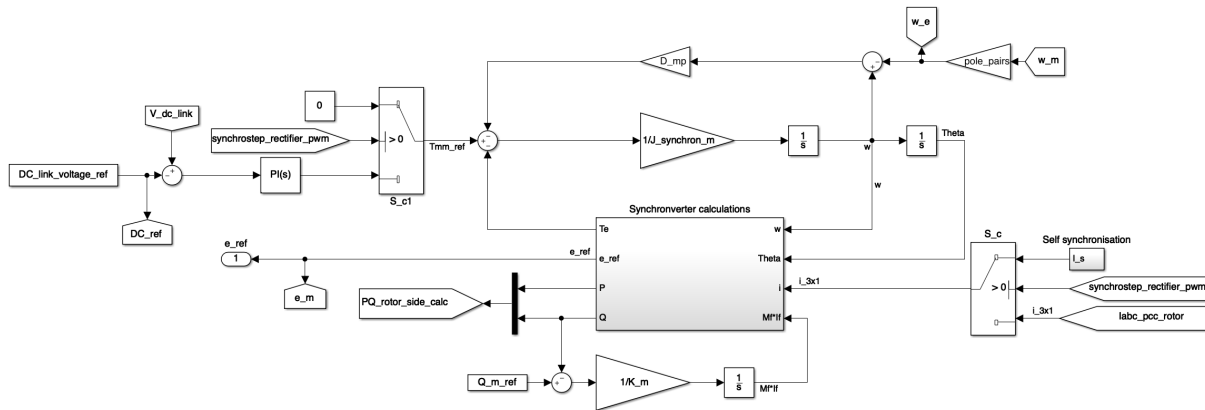


Figure C.8: Original rotor side rectifier control Simulink model.

# C.2   Grid Side Controller Including Power Correction Loop
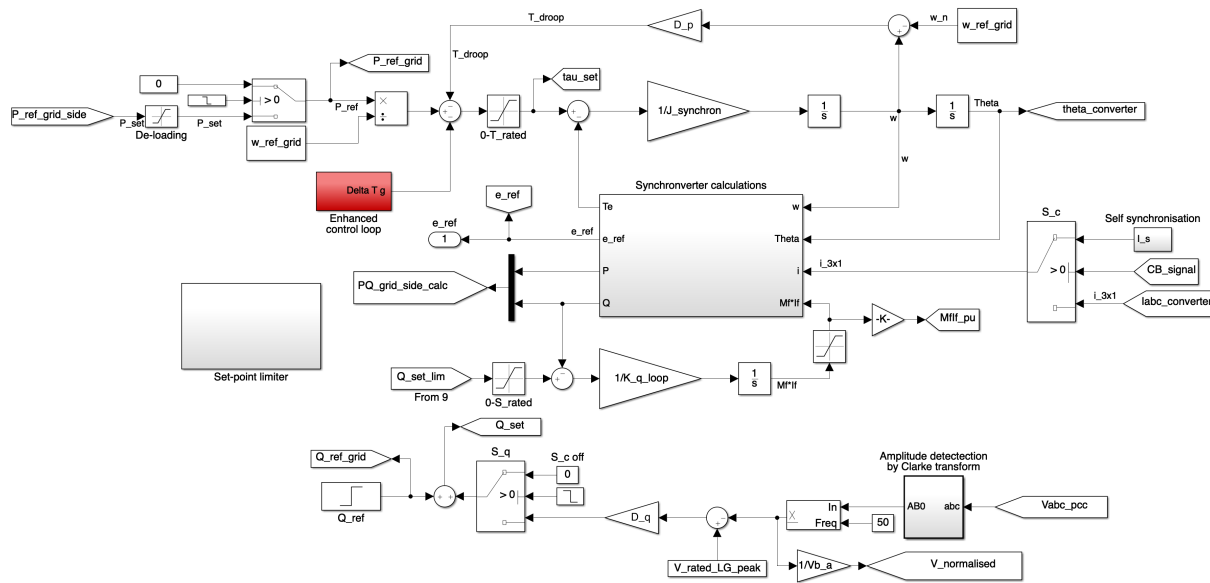


Figure C.9: Grid side inverter control equipped with a power correction loop Simulink model.
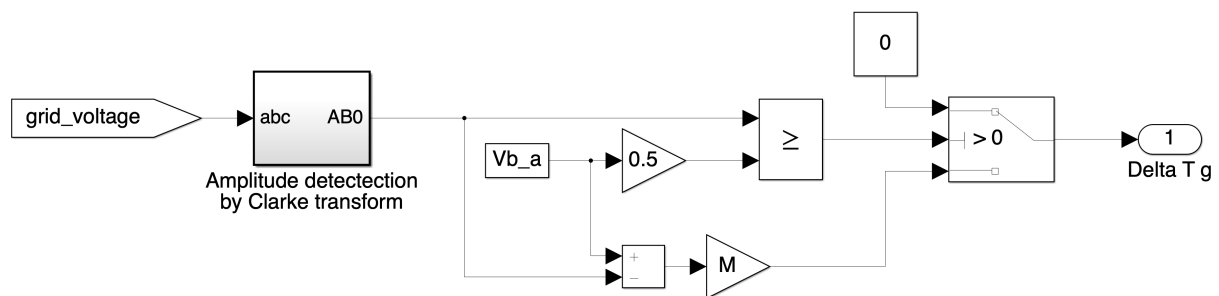


Figure C.10: PCL core calculations.

## C.3    Grid Side Controller Including Virtual Resistor
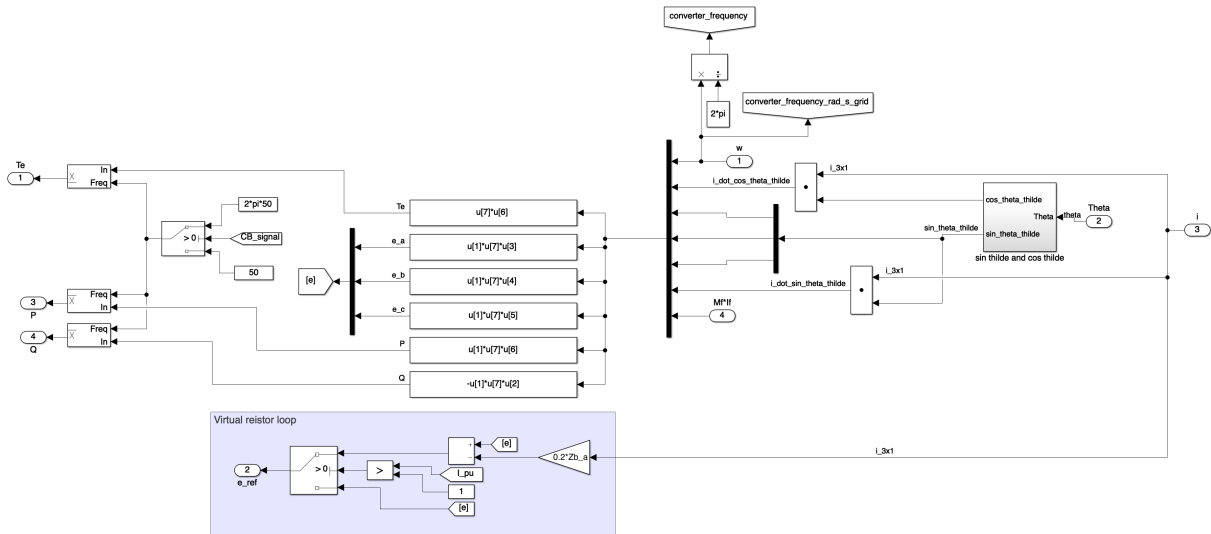


Figure C.11: Grid side inverter control equipped with a virtual resistor loop, Simulink model of core calculations.

## C.4    Grid Side Controller Including Virtual Resistor and Damper Windings
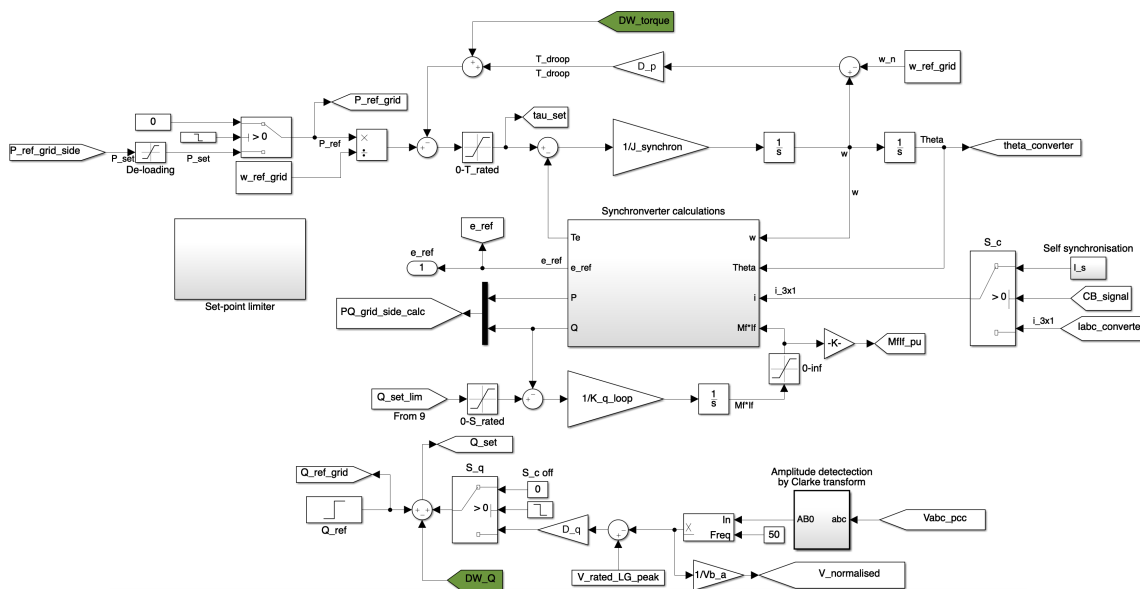


Figure C.12: Grid side inverter control equipped with both a virtual resistor and damper windings Simulink model.
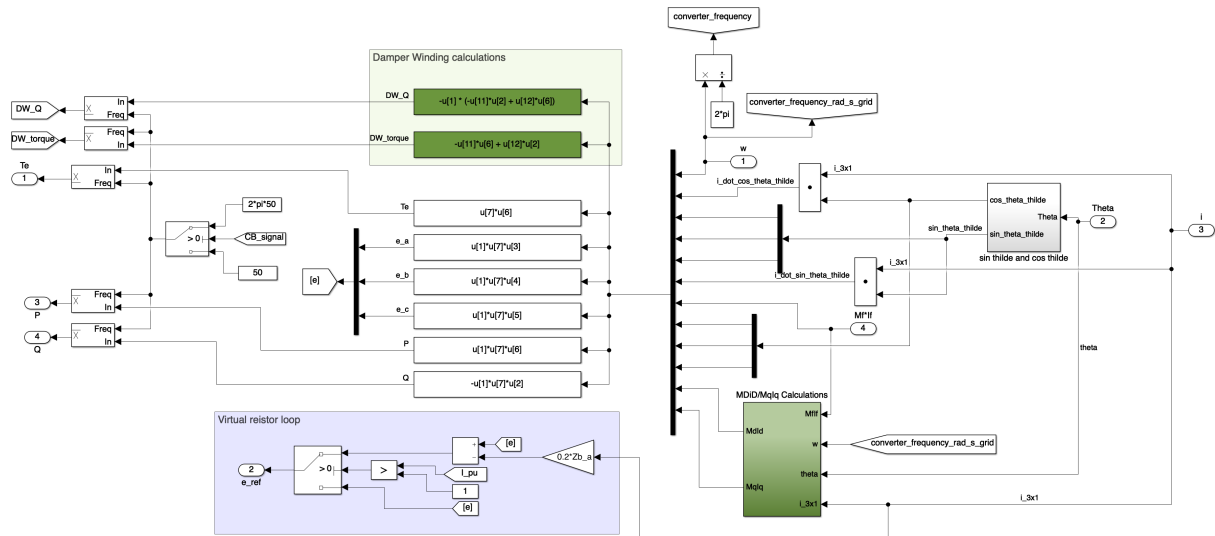
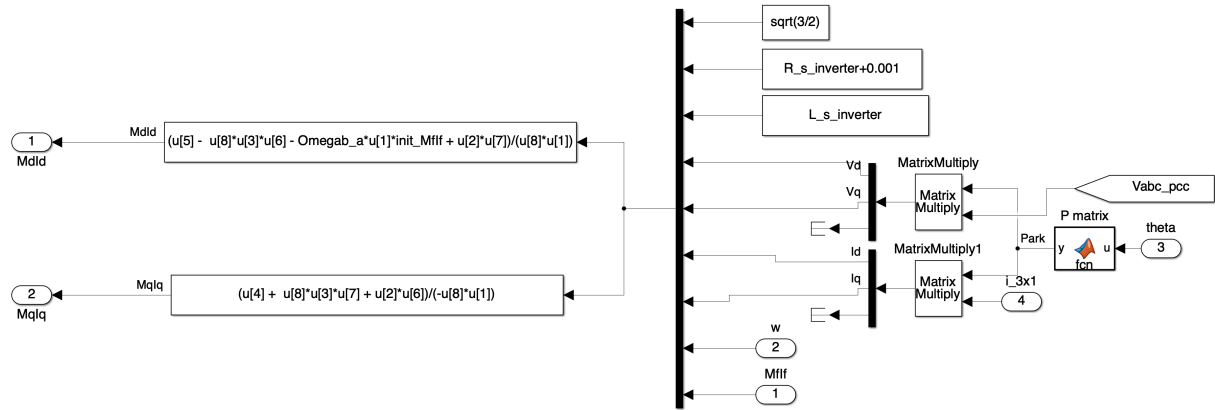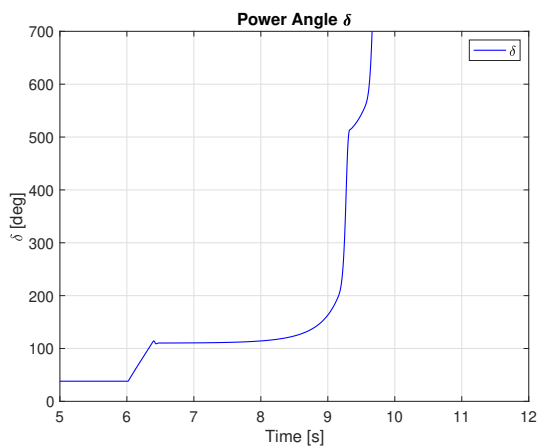Figure C.13: Core calculations including a VR and virtual DWs.



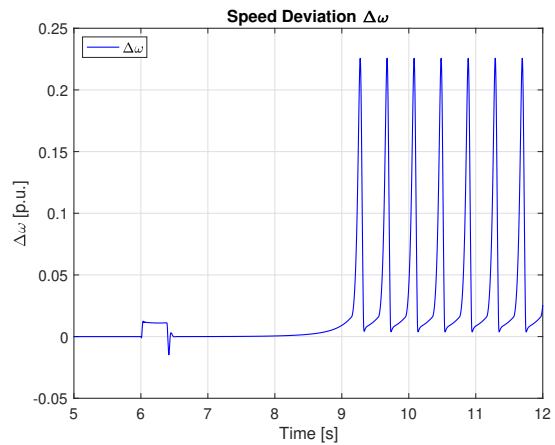Figure C.14: $M_D i_D$ and $M_Q i_Q$ calculations.

# Appendix D

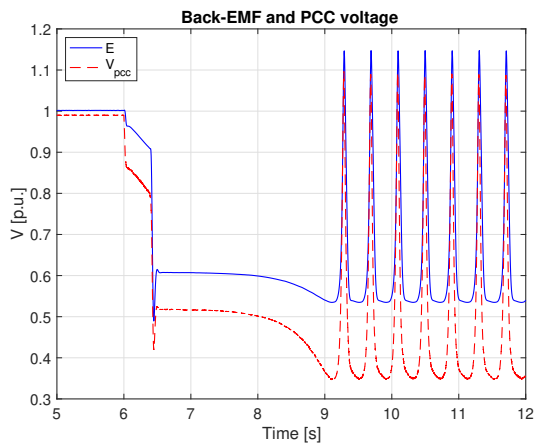# Additional Simulation Results

## D.1 Unstable Original System

Simulation results for the original system using a clearing time $t_c = 0.3866$, which is 0.5 ms above the critical clearing time $t_{cc}$, are provided in Figures D.1 and D.2.



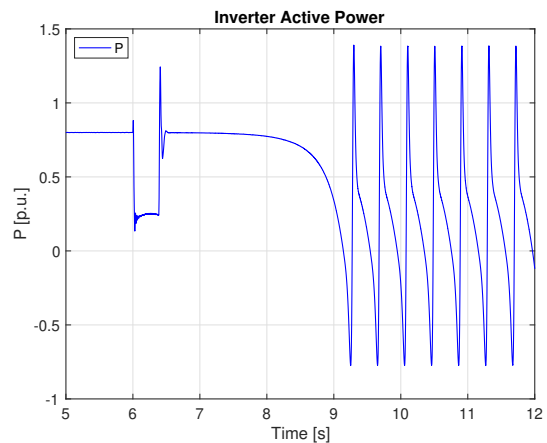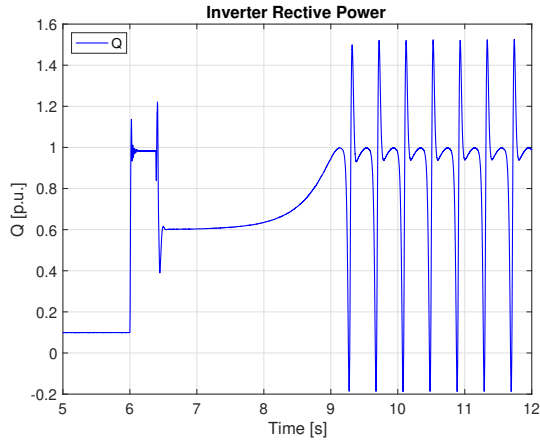(a) Power angle $\delta$



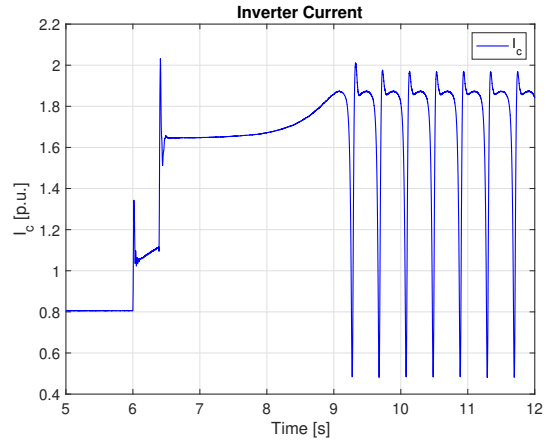(b) Speed deviation $\Delta\omega$ of the VSM from the nominal grid frequency.



(c) Amplitudes of $E$ and $V_{pcc}$.


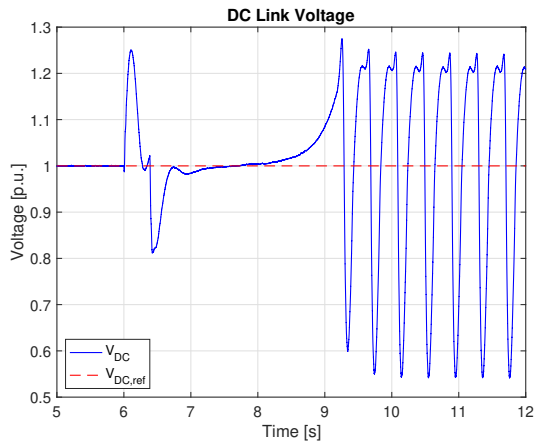
(d) Active power injection $P$ by inverter.

(e) Reactive power injection $Q$ by inverter.



(f) Inverter current amplitude.

Figure D.1: Grid side response of original system when fault is cleared at $t_c > t_{cc}$.



(a) DC link voltage.
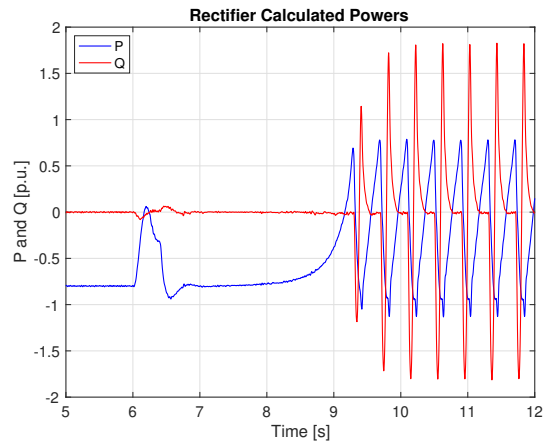


(b) Powers calculated by the rectifier control system.
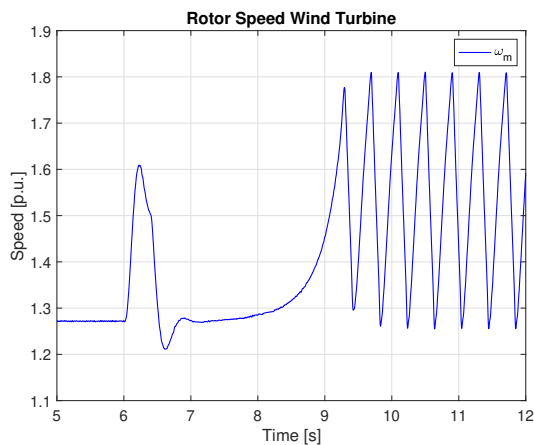


(c) Mechanical rotor speed of the wind turbine.
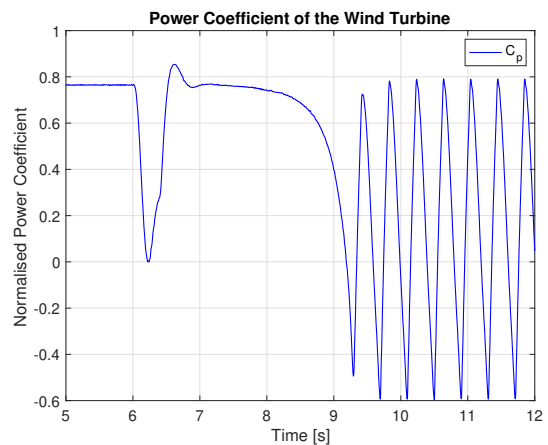


(d) Power coefficient of the wind turbine.
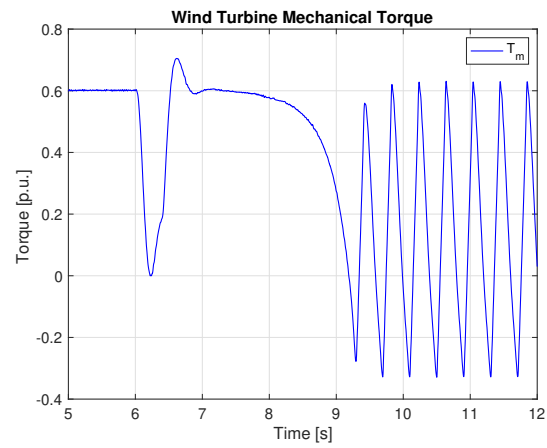
(e) Mechanical torque of the wind turbine.

Figure D.2: Rotor side response of original system when fault is cleared at $t_c > t_{cc}$.

## D.2 System with VR and DWs: Prolonged Clearing Time

Simulation results for the enhanced system equipped with both a virtual resistor and artificial damper windings are provided in Figures D.3 and D.4. The clearing time is set to $t_c = 3$ s.



(a) Power angle $\delta$

(b) Speed deviation $\Delta\omega$ of the VSM from the nominal grid frequency.
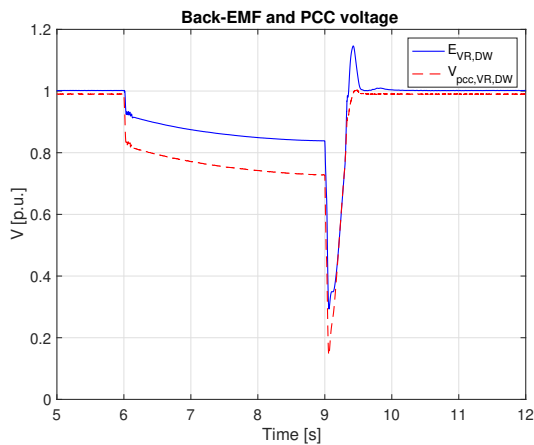
(c) Amplitudes of $E$ and $V_{pcc}$.
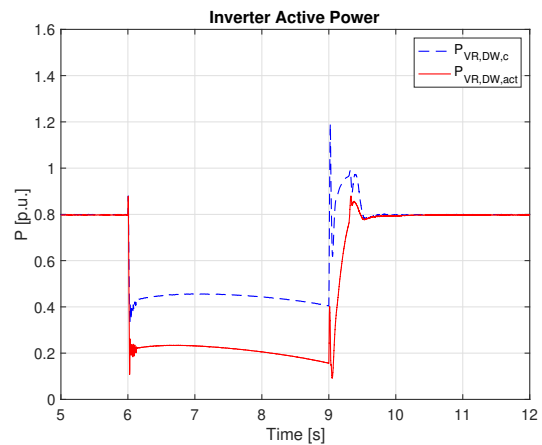
(d) Active power injection $P$ by inverter.
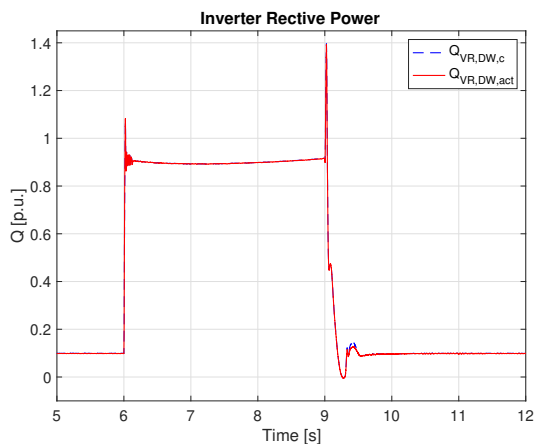
(e) Reactive power injection $Q$ by inverter.
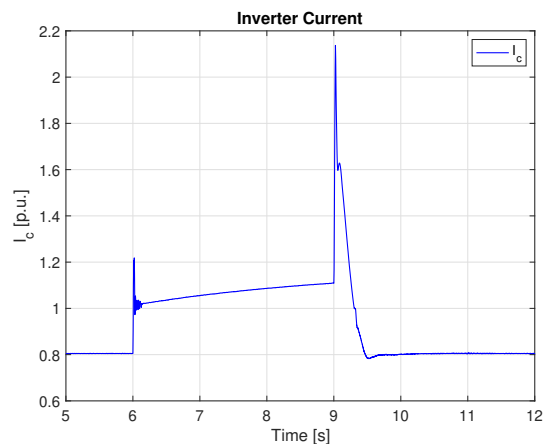
(f) Inverter current amplitude.

Figure D.3: Grid side response of system equipped with both VR and DWs when fault is cleared at $t_c = 3.0$ s.
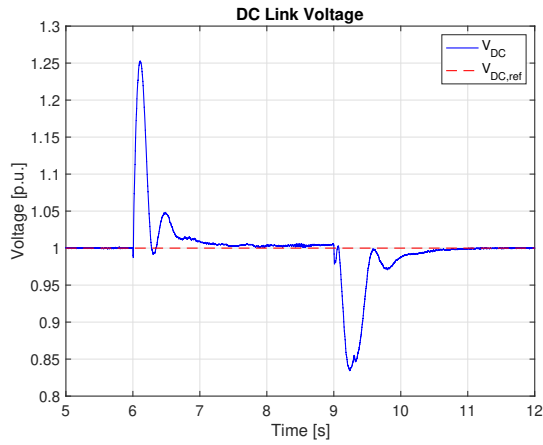
(a) DC link voltage.
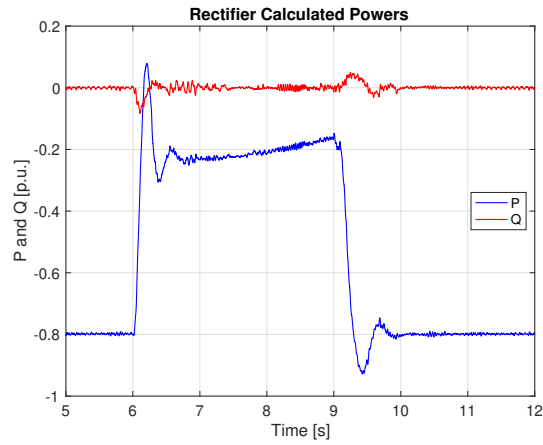


(b) Powers calculated by the rectifier control system.
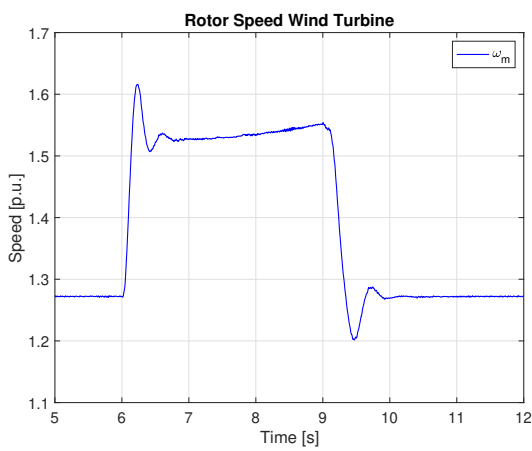


(c) Mechanical rotor speed of the wind turbine.
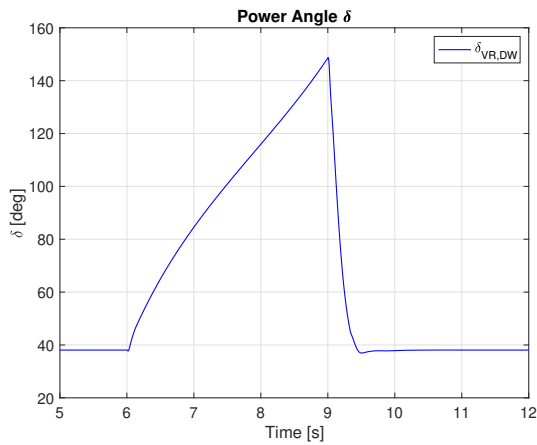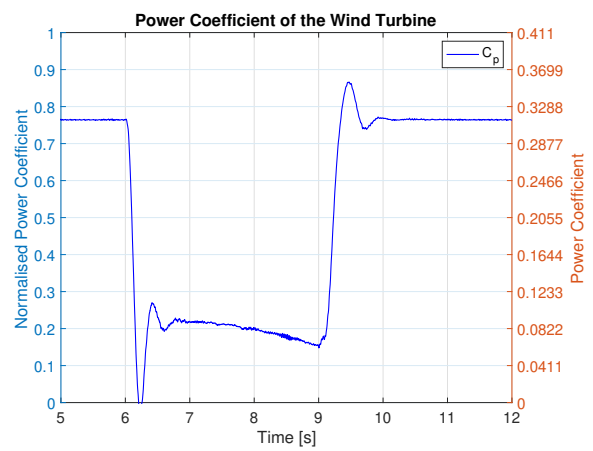


(d) Power coefficient of the wind turbine.

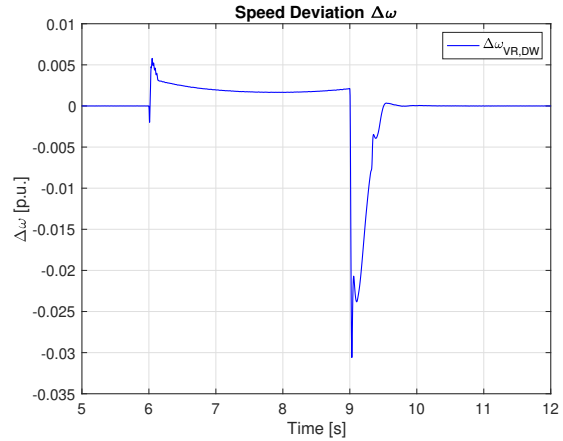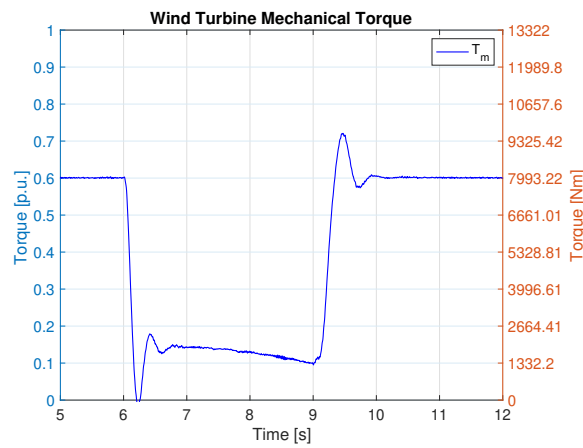

(e) Mechanical torque of the wind turbine.

Figure D.4: Rotor side response of system equipped with both VR and DWs when fault is cleared at $t_c = 3.0$ s.

# Appendix E

# Scientific Paper

This appendix contains the full version of the paper that was written based on the specialisation project report in [5]. The paper was written parallel to the thesis work, and submitted for journal publication to form the contribution to the scientific community from the work carried out in the specialisation project. The paper is attached in its entirety with both appendices and it own bibliography, and is currently in major revision.

# Small-signal Modelling and Tuning of Synchronverter-based wind energy conversion systems

Henrik Høstmark, Mohammad Amin
Department of Electric Power Engineering, NTNU
7491 Trondheim, Norway, email: mohammad.amin@ntnu.no

**Abstract:** The Synchronverter technique is an example of a virtual synchronous machine-based control method for PWM controlled power electronic converters that enable converters to mimic the behavior of a synchronous generator (SG). It is based on the well-established mathematical model of an SG and should equip converter connected generation with the capabilities of providing the grid with ancillary services such as frequency/voltage support due to the inherent capabilities of the SG. In this paper, the Synchronverter control method is applied to a wind energy conversion system (WECS) connected to the grid using back-to-back converters. The mathematical models of the control system for both the rectifier side and the inverter side are elaborated and used to derive the required transfer functions. A tuning procedure is proposed, using the transfer functions of the system, to enable a fast and easy adaption of the control method to power systems with different parameters. Simulations have been performed to validate both the functioning of the proposed tuning procedure and the ability of the WECS to provide the grid with ancillary services. The results are promising, showing the controllers yielding fast and accurate responses to contingencies and changes in power set-points without steady-state deviations.

**Keywords:** Wind Energy, Synchronverter, Frequency response, Back-to-back converters

## 1  Introduction

In recent years the power system has started the transition from a centralized structure dominated by conventional generation, to a distributed structure, dominated by converter connected, renewable generation. In this transition, one of the most promising and fastest-growing energy sources is wind power, which is often connected to the grid using power electronic converters due to its intermittent- and uncontrollable nature. The increased interest in wind power can be accredited to political, economical and technical reasons as new climate policies favors renewable energy, the Levelized cost of electricity for wind power in Germany, Britain and France drops below coal-fired electricity and more efficient turbines are being developed, all leading to wind power to become the leading energy technology in Europe measured by installed capacity in 2019 [1–3].

Modern wind turbines are divided into two categories based on the operating type; fixed speed wind turbines and variable speed wind turbines. Variable speed turbines are preferred due to more control flexibility and improved system efficiency and power quality [4,5]. The most used topologies for variable speed wind turbines are doubly-fed induction generators and fully-rated converter wind turbines with permanent magnet synchronous generators, and both of these topologies often use PWM controlled back-to-back converters for connection to the grid [6].

The new system topology, dominated by converter connected generation, creates new challenges related to system stability in the form of less inertia and easily adjustable energy sources. This requires new types of grid control and grid regulation, resulting in more and more countries establishing new grid codes and requirements for what types of support functions a unit connected through power electronics must be able to supply. This is especially important for maintaining the security and stability of the power grid also in a future with less conventional generation and higher penetration of renewables.

A proposed solution to these challenges is to control converters, both rectifiers and inverters, to mimic synchronous machines. One such virtual synchronous machine (VSM) is the Synchronverter first proposed by Zhong and Weiss [7,8]. The use of VSMs seems like a promising method of enabling converter connected generation to provide the grid with ancillary services, such as inertial response and frequency control, formerly only provided by conventional synchronous machines. While the concept of controlling back-to-back converters as Synchronverters when connecting wind power to the grid was first proposed by Ma and Zhong [9], the concept was only proven for a relatively small system. The proposed solution should therefore be applied to a larger system with more realistic parameters. To enable this, an easy and precise method of adapting controller parameters to any given system should be proposed. Besides, the proposed solution by Ma et al [6,9] uses sinusoidal tracking

algorithms to enable synchronization with the grid, which can have a negative impact on controller performance. Several methods of choosing parameters for Synchronverter controlled converters exist in the literature.

In the original Synchronverter, Zhong and Weiss [8] chooses parameters using empirical formulas and pre-chosen time constants, meaning trial and error must be applied when choosing the parameters used in the formulas. To counter this, Wu et al [10] proposes a general tuning algorithm for virtual synchronous machines that can be modified and adapted to the syncrhonverter. Dong and Chen [11] proposes an enhanced self-synchronization technique using a virtual resistance branch and a damping correction loop with parameters chosen based entirely on the trial and error method, while Rosso et al [12] and Dong and Chen [13] find parameters based on the linearized system state-space model. Dong and Chen [14] also proposes a method to directly compute controller parameter values in a Synchronverter augmented with a damping correction. Here, avoidance of trial-and-error procedures and achievement of precise pole placement is obtained, but the work focus only on the Active Power Loop (APL) of inverter control. Also, Zhang et al [15] proposes a parameter design method that includes the effects of low-pass filters. However, the authors focus only on single-phase synchronverter controlled inverters.

Lastly, Wei et al [16] obtains a small-signal model of a Synchronverter controlled inverter and then uses the "optimal second-order system" method, choosing the dampening ratio of the system, and then use the Eigen equation to find eigenvalues yielding the desired response. However, again the authors do not look at rectifier controls. Therefore, based on the literature and to the best of the authors' knowledge, no work has been done on finding the transfer functions and developing a method of choosing controller parameters for Synchronverter controlled rectifiers, and adapting this to back-to-back converters integrating a large scale wind turbine.

In this paper, a tuning method of Synchronverter controller parameters for back-to-back converters is proposed. More specifically the contribution devolves around tuning the control system for the rectifier side of the back-to-back converters. Using the transfer functions of the control systems a procedure is developed to enable a fast and easy adaption of the Synchronverter to wind power systems with different parameters. Based on the small-signal model of a synchronverter controlled inverter, the small-signal model of a Synchronverter controlled rectifier is established, and a method of tuning the PI controller is proposed to ensure fast a precise control of the DC link voltage. The basis for the proposed method is a large scale wind energy conversion system connected to the grid through back-to-back converters. Here, the rotor side rectifier controls the DC link voltage and the grid side inverter controls the injected active- and reactive power to the grid based on the maximum power point of the wind turbine and reactive power consumption at the grid. The transfer functions are obtained using a small signal model based on the mathematical model of the control system and the block diagrams. To validate the functioning of the tuning procedure, a fictitious system is implemented in the MATLAB/Simulink environment and tested for different voltage and frequency events to ensure that the controls behave as designed.

The rest of the paper is structured as follows: The basics of a Synchronverter based wind energy conversion system and the Synchronverter control technology are outlined in Section 2. The transfer functions and the tuning procedure are explained in Section 3, before simulation results are provided in Section 5. Finally, this work is concluded in Section 6.

## 2 Synchronverter-based WECS

In this paper, a full-scale type-four WECS is investigated, which is connected to the ac grid through a two-level voltage source converter (VSC). The system is shown in Fig. 1. Synchronverter control technology has been adopted for both the grid side converter and the rotor side converter. The control architectures of the converters are as follows. 1) The grid side converter is used to regulate the active power and reactive power injection to the grid. The maximum power tracking algorithm has been implemented to the grid side converter. 2) The rotor side converter is used to control the voltage of the WECS dc-bus.

### 2.1 Control of the grid side converter

The implementation of grid side converter controller is based on the synchronverter proposed by Zhong and Weiss [8]. An idealized three-phase round rotor SG is recalled for the purpose of implementing the synchronverter control strategy [19]. The stator winding is assumed to be a concentrated coil having self-inductance $L$ and mutual-inductance $M$ with a typical value of $1/2L$. The field winding is assumed to be a concentrated coil having self-inductance $L_f$. The phase terminal voltage, $v_{abc} = [v_a \ v_b \ v_c]^T$ can be written as

$$v_{abc} = -R_s i_{abc} - L_s \frac{di_{abc}}{dt} + e_{abc} \tag{1}$$

where, $i_{abc} = [i_a \ i_b \ i_c]^T$ is the stator phase currents vector; $R_s$ and $L_s = L + M$ are the stator winding resistance and inductance, respectively and $e_{abc} = [e_a \ e_b \ e_c]^T$ is the back electromotive force (EMF) due to
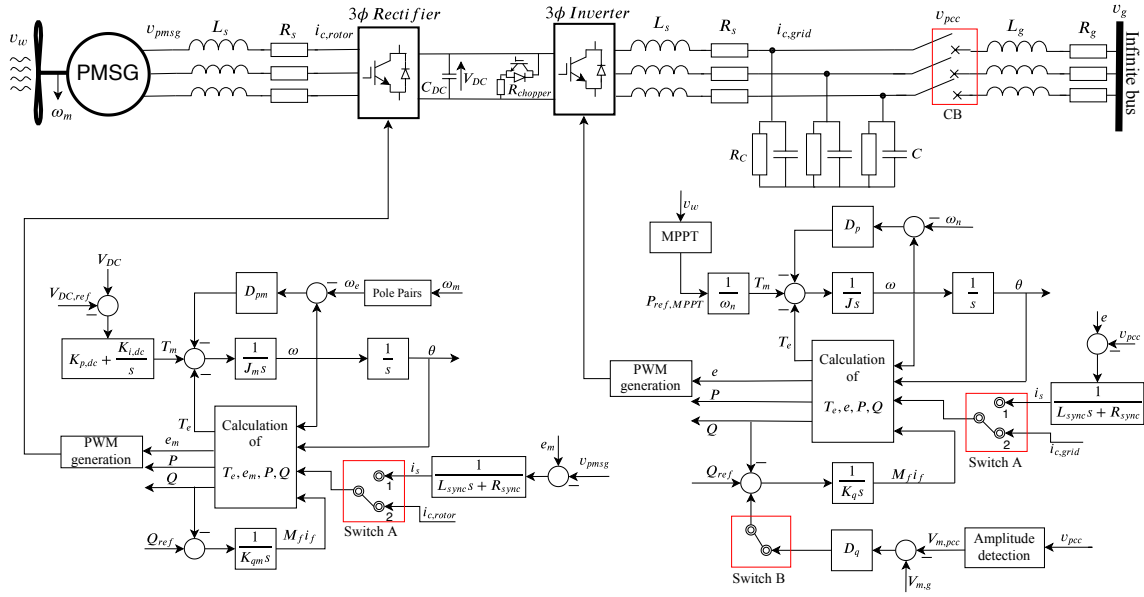
2

Figure 1: System topology of a wind turbine connected to the grid through back-to-back converters, including control systems modified from [9, 17, 18].

the rotor movement and can be given by

$$e_{abc} = M_f i_f \omega \widetilde{\sin}\theta \tag{2}$$

where $M_f i_f$ is the flux field; $\omega$ is the speed; $\theta$ is the rotor angle and

$$\widetilde{\sin}\theta = [sin\theta \ \ sin(\theta - \frac{2\pi}{3}) \ \ sin(\theta + \frac{2\pi}{3})].$$

The mechanical part of the machine can be written by

$$J\dot{\omega}_g = T_m - T_e - D_p\omega \tag{3}$$

where $J$ is the moment of inertia of all the parts rotating with rotor; $T_m$ is the mechanical torque; $T_e$ is the electromagnetic torque and $D_p$ is a damping factor. The electromagnetic torque, $T_e$ can be found from the energy stored in the magnetic field of the machine and can be given by

$$T_e = M_f i_f \left\langle i_{abc}, \widetilde{\sin}\theta \right\rangle \tag{4}$$

where $\langle \cdot, \cdot \rangle$ denotes the conventional inner product in $\mathbb{R}^3$. The active power, $P$ and reactive power, $Q$ generated by SG can be given by, respectively

$$P = M_f i_f \omega \left\langle i_{abc}, \widetilde{\sin}\theta \right\rangle \tag{5}$$

$$Q = -M_f i_f \omega \left\langle i_{abc}, \widetilde{\cos}\theta \right\rangle . \tag{6}$$

The synchronverter concept is developed based on the SG model (1)-(6).

The swing equation for the grid-side synchronverter can be given in (2) where the mechanical torque, $T_m$ is a control input obtained through the maximum power point tracking (MPPT) algorithm as described by Ma et al [6] and the electrical torque, $T_e$ depends on $i_{abc}$ and $\theta_g$ according to (4). To have similar behaviour as an SG, a frequency droop control loop is included, hence, the swing equation of the grid side-converter can be given by

$$J\dot{\omega}_g = P_{ref,MPPT}/\omega_n - T_e - D_p(\omega - \omega_n) \tag{7}$$

where $P_{ref,MPPT}$ is reference active power obtained through the MPPT algorithm [6].

The electrical circuit of the grid-side WECS inverter including the synchronverter controller is given in Fig. 1. The voltage in (2) corresponds to the back EMF of the virtual rotor. The inverter switches are operated such that over a switching period, the converter outputs are to be equal to $e_{abc}$ as given in (2) and it is achieved by a PWM technique.

3

In order to regulate the field excitation, $M_f i_f$, the reactive power is controlled by a voltage droop control loop using voltage droop coefficient, $D_q$. The control of reactive power is shown in the lower part of Fig. 1 where the inner loop is the voltage (amplitude) loop and outer loop is the reactive power loop. The magnetic field excitation, $M_f i_f$ and reactive power reference, $Q_{ref}$ can be given by

$$M_f i_f = \frac{1}{K_q s}(Q_{ref} - Q + D_q(V_{m,g} - V_{m,pcc}) \tag{8}$$

where $V_{m,pcc}$ is the output voltage magnitude and $V_{m,g}$ is the reference voltage magnitude.

The control structure of the grid side controller is depicted to the right in Fig. 1, where the active and reactive drooping coefficients are denoted $D_p$ and $D_q$ respectively. The structure is modified from Ma et al [17] and utilizes the inherent synchronization ability of the synchronous machine to achieve self-synchronization with the grid. The main objective of the grid side inverter is to feed the correct amount of power into the grid, based on the MPPT of the turbine, frequency- and voltage situation of the grid.

## 2.2 Control of rotor-side converter

Controlling a three-phase rectifier as a Synchronverter was first proposed by Ma et al [20], and later added with the self-synchronization ability [18]. The control structure of the rotor side controller is depicted to the left in Fig. 1 and is modified from Ma et al [20]. Here the active drooping coefficient is denoted $D_{pm}$, and the core of the rotor side rectifier controller is the same as for the grid side, however now with the converter current defined in the opposite direction. The main objective of the rotor side rectifier is to keep the DC link voltage at its reference voltage and at the same time keep the power factor at the rotor side as close to unity as possible.

The swing equation for the rotor-side synchronverter can be given by

$$J_m \dot{\omega} = T_m - T_e - D_{pm}(\omega - \omega_e) \tag{9}$$

where $\omega_e$ is the frequency of the generated voltage of the PMSG. The mechanical torque, $T_m$ is the control input. Hence, the WECS dc-link voltage can be controlled by controlling the mechanical torque and it is generated by PI-controller as shown in Fig. 1 and can be given by

$$T_m = (K_{p,dc} + \frac{K_{i,dc}}{s})(V_{DC} - V_{DC,ref}) \tag{10}$$

where $K_{p,dc}$ and $K_{i,dc}$ are the proportional and integral gain of the dc voltage controller, respectively.

# 3 Small-signal modeling and tuning of the control-loops

The control structure presented in Fig. 1 can now be used to develop a small-signal model, yielding the block diagrams of the Synchronverter for both the grid-side converter and rotor side converter control.

## 3.1 Grid-side synchronverter

The converter controller consist of two control channels; one for the active power and one for the reactive power. Therefore the first objective is to find the transfer function from the active power reference $P_{ref}$ to the actual power $P$, and the transfer function from the reactive power reference $Q_{ref}$ to the actual power $Q$. It is known that for a grid-connected synchronous machine the powers can be calculated as

$$P = \frac{3V_{pcc}V_g}{X_s}\sin\delta \tag{11a}$$

$$Q = \frac{3(V_{pcc} - V_g\cos\delta)V_{pcc}}{X_s} \tag{11b}$$

where the parameters used are related to the Synchronverter, and it is assumed that the grid impedance $Z_g = R_g + jX_g$ is mainly inductive, i.e. $X_s = \omega_n L_g >> R_g$. Using $v_g = V_g \angle 0°$ implies $\delta = \theta - \theta_g = \theta$, i.e. the power angle of the system is the angle of the PCC voltage.

To develop the small-signal model, the variables are defined as

$$x = x_n + \Delta x \tag{12}$$

where $x_n$ denotes the nominal value, while the small deviation is denoted $\Delta x$. It can be assumed $\Delta V_g = 0$ and $\Delta \omega_g = 0$ when developing the small-signal model. Applying the approximations $sin\delta_n \approx \delta_n$, $sin\Delta\delta \approx \Delta\delta$,

<div align="center">4</div>

$cos\delta_n \approx 1$ and $cos\Delta\delta \approx 1$, and in addition neglect the constant terms and higher order varying terms, (11a) and (11b) can be rewritten into the Laplace domain as in (13a) and (13b) [10].

$$\Delta P = \frac{3V_{pcc,n}V_{gn}}{X_s}\Delta\delta(s) + \frac{3V_{gn}\delta_n}{X_s}\Delta V_{pcc}(s) \tag{13a}$$

$$\Delta Q = \frac{3V_{pcc,n}}{X_s}\Delta V_{pcc}(s) + \frac{3V_{pcc,n}V_{gn}\delta_n}{X_s}\Delta\delta(s) \tag{13b}$$

Further, using the approximation that the small signal feedback voltage amplitude is approximately equal to the small signal back-emf amplitude, i.e. $\Delta V_{pcc} \approx \Delta E$, and equations (13a) and (13b), the control system from the grid side in figure 1 can be presented in block diagram as shown in figure 2. Note that for the block diagrams the definitions $K_p = \frac{1}{J}$ and $K_{qi} = \frac{1}{K_q}$ are used.
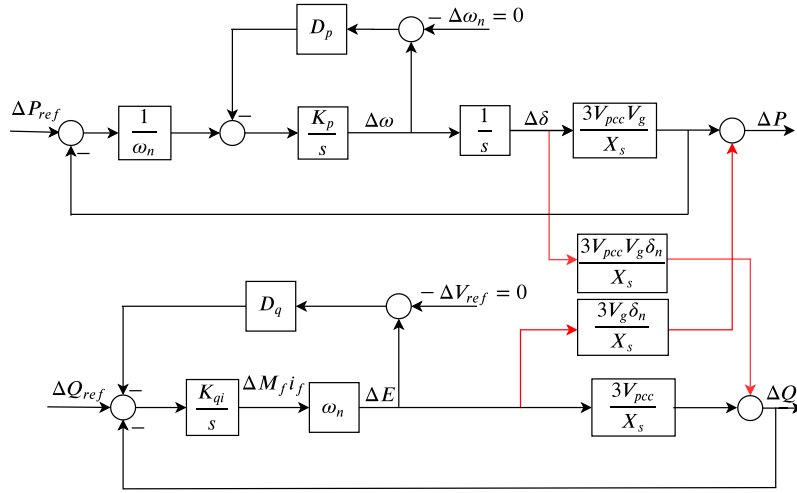


Figure 2: Block diagram of the coupled grid side control system.

As can be seen from both the block diagram and the small-signal power equations the active power loop (APL) and reactive power loop (RPL) are coupled. The coupling is coming from (13a) and (13b) where both $\Delta P$ and $\Delta Q$ are depending on $\Delta\delta$ coming from the APL and $\Delta V_{pcc} = \Delta E$ coming from the RPL. The loops must therefore be de-coupled to simplify the system analysis.

If the coupling is omitted the two loops can be simplified as in figures 3 and 4, from which the two open loop gains $T_{APL,grid}$ and $T_{RPL,grid}$ can be easily identified in (14a) and (14b).
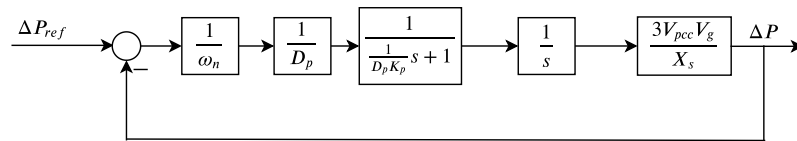


Figure 3: Simplified block diagram of the grid side APL when coupling is omitted.
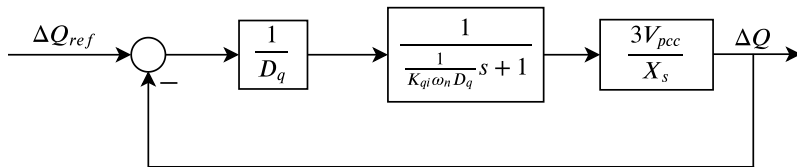


Figure 4: Simplified block diagram of the grid side RPL when coupling is omitted.

5

$$T_p(s) = \frac{1}{\omega_n} \cdot \frac{1}{D_p} \cdot \frac{1}{\frac{1}{D_p K_p} s + 1} \cdot \frac{1}{s} \cdot \frac{3V_{pcc,n} V_{gn}}{X_s} \tag{14a}$$

$$T_q(s) = \frac{1}{D_q} \cdot \frac{1}{\frac{1}{K_{qi} \omega_n D_q} s + 1} \cdot \frac{3V_{pcc,n}}{X_s}. \tag{14b}$$

Now, by setting $\Delta Q$ to zero in Fig. 2, it can be shown that the loop gain of the APL including the coupling will be

$$T_{pc}(s) = T_p(s)\Big(1 - \frac{T_q(s)}{1 + T_q(s)} \delta_n^2\Big). \tag{15}$$

Similarly, by setting $\Delta P$ to zero in figure 2, it can be shown that the loop gain of the RPL including the coupling will be

$$T_{qc}(s) = T_q(s)\Big(1 - \frac{T_p(s)}{1 + T_p(s)} \delta_n^2\Big). \tag{16}$$

The APL and RPL, in the upper and lower part of Fig. 2, are coupled due to the inherent nature of the VSM, as both and P and Q are related to V and $\delta$. This coupling brings difficulty to parameter design. For simplification of the tuning procedure, the loops can be considered decoupled [10] which simplifies to

$$T_{pc} \approx T_p$$

$$T_{qc} \approx T_q$$

and the controller parameters can therefore be designed separately for the active power loop and reactive power loop from the decoupled structure.

### 3.1.1 Active Power Loop

The parameters for the APL can now be tuned based on the transfer function given in (14). As seen in Fig. 3 there are essentially two parameters that needs to be tuned in the APL; $D_p$ and $K_p$. The drooping coefficients are often treated as a result of grid code requirements, where a 100% change in active or reactive power is required for a certain amount of change in frequency or voltage respectively. Therefore using a pre-selected drooping percentage $\Delta p\%$ the droop coefficient $D_p$ can be set as

$$D_p = \frac{\frac{P_n}{\omega_n}}{\omega_n \cdot \Delta p_\%} \tag{17}$$

The next parameter is $K_p = \frac{1}{J}$. It is known that the amplitude of the open loop APL gain is unity at the gain crossover frequency and this can be used to express $K_p$ as a function of the crossover frequency $f_{pc}$. The magnitude of the transfer function at crossover can be given by

$$|T_p(j2\pi f_{pc})| = \frac{3V_{pcc,n} V_{gn}}{X_s \omega_n D_p} \frac{1}{\left|\frac{j2\pi f_{pc}}{D_p K_p} + 1\right|} \frac{1}{|j2\pi f_{pc}|} = 1$$

which gives the value of $K_p$ as

$$K_p = \frac{2\pi f_{pc}}{D_p \sqrt{\left(\frac{3V_{pcc,n} V_{gn}}{2\pi f_{pc} X_s \omega_n D_p}\right)^2 - 1}} \tag{18}$$

It is, in addition to optimise stability and controller performance, important to attenuate the Double Line-Frequency Ripples (DLFR) in the output voltage caused by the instantaneous power outputs during periods of unbalanced grid voltages. To ensure that the DLFR is attenuated properly the magnitude of the loop gain should also be assessed at the the frequency $2f_n$, i.e.:

$$|T_p(j2\pi \cdot 2f_n)| = \frac{3V_{pcc,n} V_{gn}}{X_s \omega_n D_p} \cdot \frac{1}{\left|\frac{j4\pi f_n}{D_p K_p} + 1\right|} \cdot \frac{1}{|j4\pi f_n|}$$

This expression can be simplified using the approximation

$$\frac{1}{\left|\frac{j4\pi f_n}{D_p K_p} + 1\right|} \approx \frac{1}{\left|\frac{j4\pi f_n}{D_p K_p}\right|}$$

6

due to the fact that the cutoff frequency $\frac{D_p K_p}{2\pi}$ of the first order filter in $T_p$ is way below $2f_n$, yielding

$$|T_p(j2\pi \cdot 2f_n)| \approx \frac{3V_{pcc,n}V_{gn}K_p}{16\pi^2 f_n^2 X_s \omega_n} \leq a_p \qquad (19)$$

where $a_p$ is the maximum desired magnitude at $f = 2f_n$. The criteria in (20) can thus be found using (19).

$$K_p \leq \frac{16\pi^2 f_n^2 X_s \omega_n a_p}{3V_{pcc,n}V_{gn}} = K_{p,max} \qquad (20)$$

To ensure a robust controller with good stability, the phase margin should also be taken into consideration when tuning the parameters. The desired phase margin for the open-loop gain is defined as $PM_{desired}$, yielding the criteria in (21).

$$PM = 180° + \angle T_{APL,grid}(j2\pi f_{pc}) \geq PM_{desired} \qquad (21)$$

The part of (14a) governing the angle will be

$$\frac{1}{\frac{1}{D_p K_p}s + 1} \cdot \frac{1}{s}$$

where $\frac{1}{s}$ automatically translate to $-90°$, yielding

$$90° - \arctan \frac{\Im(\frac{1}{D_p K_p}j2\pi f_{pc} + 1)}{\Re(\frac{1}{D_p K_p}j2\pi f_{pc} + 1)} = 90° - \arctan \frac{\frac{2\pi f_{pc}}{D_p K_p}}{1}$$

The angle should be larger, or equal, to the desired phase margin, i.e. $\geq PM_{desired}$. Based on the above the minimum value of $K_p$ can thus be calculated in (22).

$$K_p \geq \frac{2\pi f_{pc}}{D_p}\tan(PM_{desired}) = K_{p,min} \qquad (22)$$

Using (18), (20) and (22), $K_{p,min}$, $K_{p,max}$ and $K_p$ can be plotted as functions of the crossover frequency $f_{pc}$, and any value of $K_p(f_{pc})$ lying within the two curves $K_{p,min}$ and $K_{p,max}$ will satisfy the tuning criteria for the APL. It is usually beneficial to chose the value for $K_p$ in the higher area of the valid range to improve controller performance to have a faster response in response to a disturbance.

### 3.1.2   Reactive Power Loop

From Fig. 4 it can be deduced that there are two parameters that should be designed for the RPL; $D_q$ and $K_{qi}$. As for the drooping coefficient of the APL, the drooping coefficient of the RPL will be a result of grid code requirements. Using a drooping percentage $\Delta q\%$ the droop coefficient $D_q$ can be set as:

$$D_q = \frac{Q_n}{\sqrt{2}V_{gn,L-G} \cdot \Delta q\%}. \qquad (23)$$

The final parameter to be decided for the grid side controller is $K_{qi} = \frac{1}{K_q}$, and the tuning procedure will be similar as for $K_p$. From the loop gain in (14b) it can be seen that the denominator only consist of $s$ to the power of 1, i.e. its a first order denominator. This implies that the phase of the RPL reaches a minimum of $-90°$ and thus the phase margin will always be $90°$ or more, meaning no lower limit for $K_{qi}$ is needed. As was the case for the APL the DLFR must be attenuated properly also for the RPL, creating the need to assess the magnitude of the loop gain at the the frequency $f = 2f_n$, i.e.:

$$|T_q(j2\pi \cdot 2f_n)| = \frac{3V_{pcc,n}}{D_q X_s} \cdot \frac{1}{\left|\frac{j4\pi f_n}{D_q K_{qi}\omega_n} + 1\right|}$$

which can be simplified using the approximation

$$\frac{1}{\left|\frac{j4\pi f_n}{D_q K_{qi}\omega_n} + 1\right|} \approx \frac{1}{\left|\frac{j4\pi f_n}{D_q K_{qi}\omega_n}\right|}$$

as the cutoff frequency $\frac{D_q K_{qi}\omega_n}{2\pi}$ of the first order filter in $T_{RPL,grid}$ is way below $2f_n$, yielding

$$|T_q(j2\pi \cdot 2f_n)| \approx \frac{3V_{pcc,n}K_{qi}\omega_n}{4\pi f_n X_s} \leq a_q$$

where $a_q$ is the maximum desired magnitude at $f = 2f_n$. The criteria in (24) can thus be found using the relation above.

$$K_{qi} \leq \frac{4\pi f_n X_s a_q}{3V_{pcc,n}\omega_n} = K_{qi,max} \qquad (24)$$

7

## 3.2 Small-signal modeling of the rotor-side Synchronverter

The rotor-side synchronverter also consists of two control channels; one for the dc voltage control and one for the reactive power control. It is therefore necessary to find the transfer function from the DC voltage reference $V_{DC,ref}$ to the actual voltage $V_{DC}$, and the transfer function from the reactive power reference $Q_{ref}$ to the actual power $Q$. Also for the rotor side rectifier controller, a small signal model will be used, and as the method of de-coupling the APL and RPL will be very much the same as for the grid side controller, the procedure will not be repeated here.

The inner loops of the rectifier upper control channel are essentially identical to the grid side APL, with the only difference being that the active power will be negative. For the outer DC voltage loop, the mechanical torque will be created by the PI controller. To find the outer loop in the small-signal model, the deviations around the steady-state values are defined in (25a) and (25b). The objective is here to find the transfer function from $\Delta P$ to $\Delta V_{DC}$.

$$V_{DC} = V_{DC,n} + \Delta V_{DC} \tag{25a}$$

$$I_{DC} = I_{n,DC} + \Delta I_{DC} \tag{25b}$$

Using the nominal plus the small signal values of $P$, (25a) and (25b) can be used to yield the following result:

$$P_n + \Delta P = (V_{DC,n} + \Delta V_{DC})(I_{n,DC} + \Delta I_{DC}) \tag{26}$$

When ignoring the DC term, the second order term, and applying the approximation $\Delta I \approx 0$ the transfer function from $\Delta P$ to $\Delta V_{DC}$ can be found in (27b) based on (27a).

$$\Delta P = \Delta V_{DC} I_{n,DC} \implies \Delta V_{DC} = \frac{\Delta P}{I_{n,DC}} \tag{27a}$$

$$H_{P-V_{DC}} = \frac{1}{I_{n,DC}} \tag{27b}$$

Using the transfer function above, and the fact that the active power will be negative, the rotor-side control system can be presented in the small-signal form through block diagrams as shown in figures 5 and 6 for the DC voltage control and reactive power control channels respectively. Note that they are assumed to already be de-coupled, and that the definitions $K_{pm} = \frac{1}{J_m}$ and $K_{qi,m} = \frac{1}{K_{qm}}$ are used.
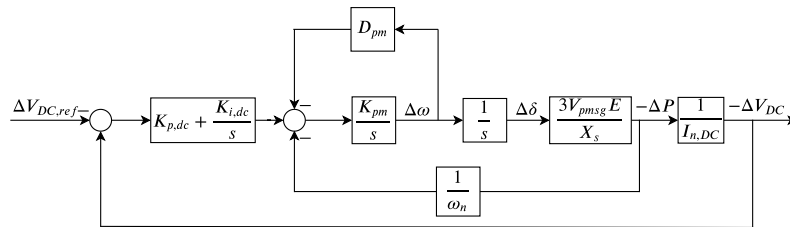


Figure 5: Block diagram of the upper control channel for a Synchronverter based rectifier control system.
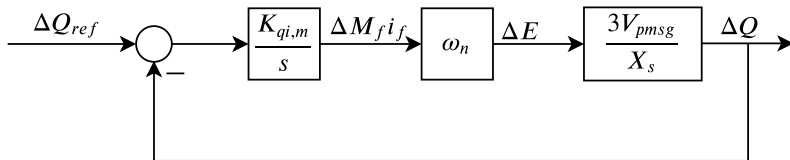


Figure 6: Block diagram of the lower control channel for a Synchronverter based rectifier control system.

As seen in Fig. 5 the block diagram is not represented in its standard form as the reference is coming in negative and the feedback is positive. For simplified system analysis, the fact that $\Delta P$ is negative can be taken advantage of by multiplying the loop gain with minus one, essentially switching the signs of both the feedback and reference and at the same time obtaining a positive $\Delta V_{DC}$. This yields the simplified version of the block diagram representing the upper control channel in Fig. 7.

8
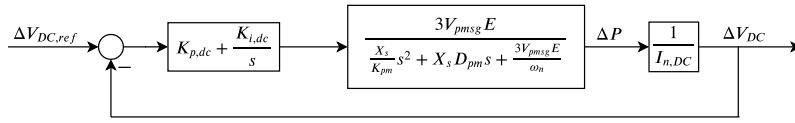
Figure 7: Simplified upper control channel block diagram on standard form.

From figures 7 and 6 the two open loop gains $T_{DC,rotor}$ and $T_{RPL,rotor}$ can be easily identified in (28) and (29).

$$T_{DC} = (K_{p,dc} + \frac{K_{i,dc}}{s}) \cdot \Big( \frac{3V_{pmsg}E}{\frac{X_s}{K_{pm}}s^2 + X_s D_{pm}s + \frac{3V_{pmsg}E}{\omega_n}} \Big) \cdot \frac{1}{I_{n,DC}} = G \cdot H \tag{28}$$

$$T_{q,r} = \frac{K_{qi,m}}{s} \cdot \omega_n \cdot \frac{3V_{pmsg}}{X_s} \tag{29}$$

In (28), $G$ and $H$ are defined as

$$G = (K_{p,dc} + \frac{K_{i,dc}}{s})$$

$$H = \Big( \frac{3V_{pmsg}E}{\frac{X_s}{K_{pm}}s^2 + X_s D_{pm}s + \frac{3V_{pmsg}E}{\omega_n}} \cdot \frac{1}{I_{n,DC}} \Big)$$

### 3.2.1   Tuning the DC voltage PI Controller

$D_{pm}$ has the exact same definition as $D_p$ and thus does not need to be re-tuned for the rotor side. For simplicity reasons and to limit the scope of this research, the parameters $K_{pm}$ and $K_{qi,m}$ are set equal to their grid side counterparts $K_p$ and $K_{qi}$. The RPL of the rotor side controller has thus no further parameters that need to be decided, and the focus can be shifted to the DC voltage control loop.

Here, only the parameters for the PI controller creating the reference torque based on the DC voltage deviation needs to be designed. Different methods can be applied to tune a PI controller, and many of them are essentially different methods of applying the *trial and error* method. One example of such a method is the process of selecting a crossover frequency $\omega_c$ and then use the trial and error method to chose the proportional gain $K_{p,dc}$ and the integral gain $K_{i,dc}$ such that the amplitude of the loop gain at the selected crossover frequency is unity, i.e.

$$|T_{DC,rotor}(j\omega_c)| = 1$$

Another trial and error method is to use the step response of the closed-loop system, in combination with a Bode diagram of the open-loop gain, to find parameters that yield both a fast and precise response and have acceptable stability margins. However, the procedures using the trial and error method are inherently time-consuming and provides no guarantee of finding the parameters yielding the best possible controller performance. It is therefore beneficial to find a starting point close to the optimal parameters by use of a faster and more precise tuning procedure so that any additional use of the trial and error method will be limited to a minimum.

The idea will be to set the closed-loop transfer function approximately equal to a first-order filter. The open-loop gain of the DC voltage control loop is given in (28) and by closing the loop with a feedback gain equal to 1, the closed-loop can be found as:

$$\frac{G \cdot H}{1 + G \cdot H}$$

Setting the closed-loop equal to a first-order low-pass filter as

$$\frac{G \cdot H}{1 + G \cdot H} = \frac{\alpha}{s + \alpha} \tag{30}$$

where $\alpha$ is the corner frequency of the first order filter, also known as the bandwidth. From (30) it can be derived that

$$G \cdot H \approx \frac{\alpha}{s}$$

which yields the relation seen in (31).

$$(K_{p,dc} + \frac{K_{i,dc}}{s}) \cdot \Big( \frac{3V_{pmsg}E}{\frac{X_s I_{n,DC}}{K_{pm}}s^2 + X_s I_{n,DC} D_{pm}s + \frac{3V_{pmsg}EI_{n,DC}}{\omega_n}} \Big) \approx \frac{\alpha}{s} \tag{31}$$

9

Using (31) and applying mathematical derivations, (32) is obtained.

It can quickly be deduced that as the controller used is a PI controller and not a PID controller, i.e. $G$ does not have a derivative part, the fraction multiplied with $s$ in (32) must be set to zero. This approximation will have an impact on the design process as will be discussed later. Neglecting the derivative part and comparing the two sides of (32) the desired gains can be approximated in (33a) and (33b).

$$K_{p,dc} = \alpha \frac{X_s I_{n,DC} D_{pm}}{3 V_{pmsg} E} \tag{33a}$$

$$K_{i,dc} = \alpha \frac{I_{n,DC}}{\omega_n} \tag{33b}$$

Now, by selecting a corner frequency $\alpha$ yielding an acceptable bandwidth, the above-calculated controller gains can be used as a starting point for further manual tuning using the trial and error method. Since the procedure above is based on approximations, the bandwidth of the actual control loop will not necessarily be equal to $\alpha$. It is therefore important to apply manual tuning after obtaining the initial parameters to ensure that both the bandwidth and phase margin are acceptable.

## 4 Tuning example

Before simulations can be carried out, the controller parameters need to be designed based on the outlined tuning method. The system parameters are listed in Table 2, and these parameters will be used in the tuning procedure.

First, $D_p = D_{pm}$ and $D_q$ are set using (17) and (23), resulting in (34a) and (34b). For the purpose of this paper the grid code requirements from the standard EN50438 will be used, meaning $p_{change,\%} = 2\%$ and $p_{change,\%} = 10\%$ [10].

$$D_p = D_{pm} = \frac{\frac{200kW}{2\pi \cdot 50}}{2\pi \cdot 50 \cdot 0.02} = 101.3212 \tag{34a}$$

$$D_q = \frac{200kVAr}{\sqrt{\frac{2}{3}} \cdot 690 \cdot 0.1} = 3550 \tag{34b}$$

Next, $K_p = K_{pm}$ are to be determined. Here, a maximum magnitude at double the line frequency, $a_p = 0.1$ and $a_q = 0.1$ will be used. Equations (18), (20) and (22) along with the simplifications that $V_{pcc} \approx V_g$ and $E \approx V_{pmsg}$, can then be utilised to obtain Fig. 8. From Fig. 8 a value of $K_p$ can be chosen in the higher area of the satisfactory curve, and here $K_p = 4$ is chosen. The controller parameter $J = J_m$ can then be calculated as

$$J = J_m = \frac{1}{K_p} = 0.25 \tag{35}$$

$K_{qi}$ is chosen close to $K_{qi,max} = 3.9837 \cdot 10^{-5}$ calculated from (24), and is thus chosen to be $K_{qi} = 3.8 \cdot 10^{-5}$. The controller parameters $K_q = K_{qm}$ is then calculated as:

$$K_q = K_{qm} = \frac{1}{K_{qi}} = 26316 \tag{36}$$

Bode plots of the APL and RPL of the grid side controller are depicted in figures 9a and 9b respectively.

As seen from Fig. 9a and 9b the magnitude at double the line frequency, i.e. 100 Hz, is indeed found to be $-20dB$, and thus the criteria of $a_p = 0.1$ and $a_q = 0.1$ is achieved.

Finally, the parameters of the PI controller needs to be tuned. Equations (33a) and (33b) are used to obtain initial values for $K_{p,dc}$ and $K_{i,dc}$. In these initial calculations $\alpha$ is set to $\alpha = 220$ rad/s $\approx 35$Hz, resulting in $K_{p,dc} = 1.9783 \approx 2.0$ and $K_{i,dc} = 124.2995 \approx 124.3$. Using these initial values the phase margin of the open-loop is found to be below 60°, and the bandwidth of the closed-loop is be found to be $56.29\,Hz$. A common rule of thumb for bandwidth is that the bandwidth of the most inner loop should be 3-10 times lower than the switching frequency and then 3-10 times lower for the next loop etc. Looking at Fig. 5, the DC voltage loop is the third loop after the frequency loop and power loop. Therefore using the rule of thumb, a bandwidth of 56

$$\left(K_{p,dc} + \frac{K_{i,dc}}{s}\right) \approx \alpha \frac{X_s I_{n,DC}}{3 V_{pmsg} E K_{pm}} s + \alpha \frac{X_s I_{n,DC} D_{pm}}{3 V_{pmsg} E} + \alpha \frac{I_{n,DC}}{\omega_n s} \tag{32}$$

10
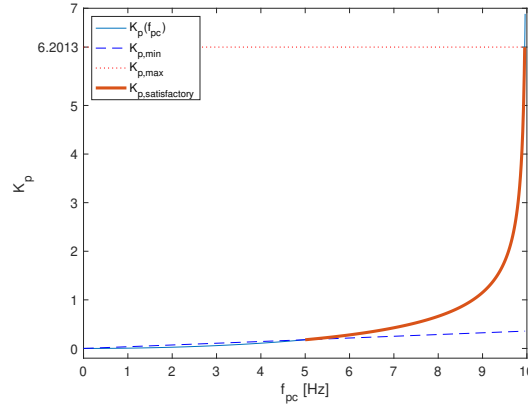
Figure 8: Plot showing valid range of $K_p$.
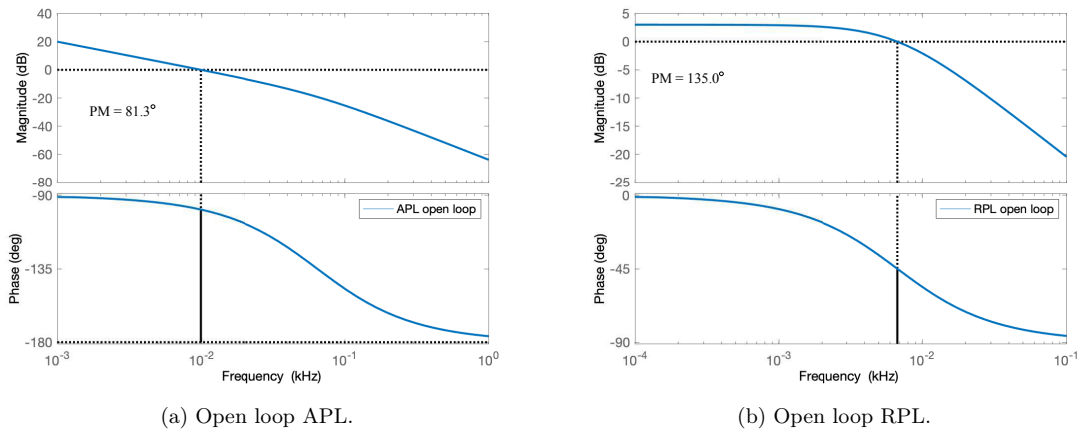


(a) Open loop APL.

(b) Open loop RPL.

Figure 9: Bode plots for grid side controller.

Hz is just within the recommended range, and thus deemed as acceptable for now. In this paper, a minimum phase margin of 65° is desired for stability, and therefore additional tuning must be applied.

Two options arises to improve stability; decrease the proportional gain or decrease the integral gain. First $K_{p,dc}$ is decreased to $K_{p,dc} = 1.5$, while $K_{i,dc}$ is kept unchanged, resulting in a system where the phase margin is approximately unchanged, while the bandwidth is found to have decreased to $46.40\,Hz$. Therefore, the next step is to try to decrease $K_{i,dc}$ to $K_{i,dc} = 100$, while keeping $K_{p,dc}$ unchanged from the initial value. This yields a system with an improved phase margin equal to 62.8°, while the bandwidth is found to be approximately the same at $55.06\,Hz$.

Based on these results additional tuning is applied by further decreasing $K_{i,dc}$, ultimately yielding the final controller parameters $K_{p,dc} = 2.0$ and $K_{i,dc} = 82.5$. The Bode plot of the open loop DC voltage loop with the final parameters is depicted in Fig. 10a, where it is also compared to the the Bode plot using the initial values. The phase margin is 65.1° and the bandwidth of the closed loop is found to be $54.61\,Hz$. In addition, the Bode plot of the RPL of the rotor side is depicted in Fig. 10b, and the controller parameters are provided in Table 1.

Table 1: Controller Parameters.

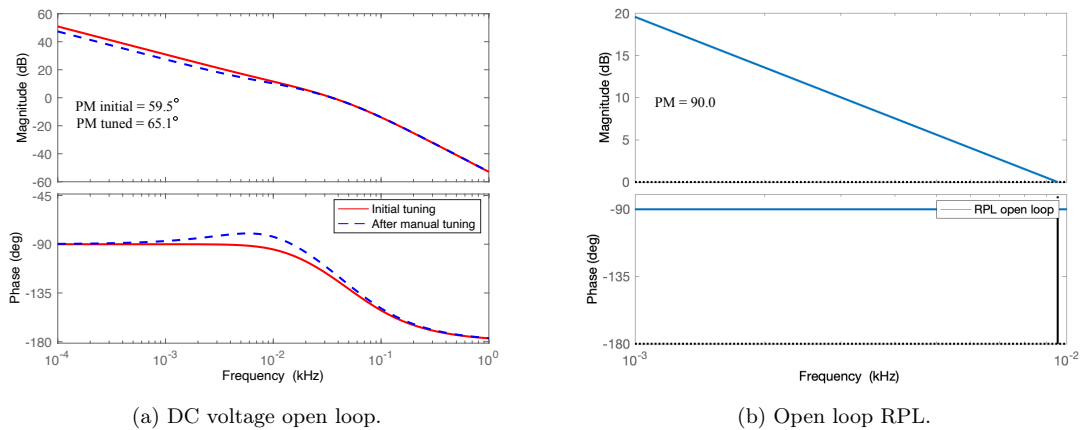| Parameter | Value | Parameter | Value |
|---|---|---|---|
| $J = J_m$ | 0.25 | $K_q = K_{qm}$ | 26316 |
| $D_p = D_{pm}$ | 101.3212 | $D_q$ | 3550 |
| $K_{p,dc}$ | 2.0 | $K_{i,dc}$ | 82.5 |

11

(a) DC voltage open loop.  (b) Open loop RPL.

Figure 10: Bode plots for rotor side controller.

# 5 Simulation Results

In order to show the effectiveness and functioning of the tuned control parameters, simulations have been carried out using MATLAB/Simulink association with SimPower System tool box. The investigated synchronverter-based WECS is shown in figure 1 which consist of a wind turbine rated at $200\,kW$. The rated voltage of both the PMSG and the infinite bus is $690V$ line to line with gird frequency $50Hz$ and the DC link voltage is $1126.8V$.

The simulations were carried out using the fixed step solver *ode3* with a sample time $T_s = 1 \cdot 10^{-6}s = 1\mu s$. The plots depicting the response of the rotor side controller are shown in figures 11a to 11d, while the plots depicting the response of the grid side controller are shown in figures 12a to 12d. Note that the first 0.7 seconds representing the synchronisation period is omitted from the plots. The simulation has the following sequence of events:

1. The simulation was started at $t = 0$ with all IGBTs off and the circuit breaker in the open position. The initial wind speed is $12\,m/s$. In the DC link a resistance equal to $2 \cdot R_{chopper}$ was connected to obtain the DC voltage, and the virtual synchronisation currents were fed to the controllers. The IGBTs on the rotor side was started at $t = 0.2$ with $V_{DC,ref} = 1126.8\,V$ and $Q_{ref,rotor} = 0$. Switch A in the rotor side controller was turned to position 2 to feed the real current to the controller.

2. The IGBTs on the grid side was started at $t = 0.5$ with $P_{ref} = Q_{ref} = 0$, and the voltage droop disabled, i.e. switch B open. Switch A in the grid side controller was turned to position 2 to feed the real current to the controller.

3. The circuit breaker was closed at $t = 0.8$ connecting the grid side converter to the grid. $P_{ref}$ was changed to reflect the MPPT at $t = 1.5$, and the chopper resistance was disconnected to send all available power to the grid side.

4. The wind speed was changed to $10\,m/s$ at $t = 2.5$, to $12\,m/s$ at $t = 3.5$, to $14\,m/s$ at $t = 4.5$, and to $12\,m/s$ at $t = 5.5$

5. $Q_{ref,grid}$ was changed to $100\,kVAr$ at $t = 6.5$. Switch B was closed at $t = 8.0$, enabling the voltage droop loop of the grid side.

6. Grid frequency increase by 0.1 Hz from $t = 9.5$ to $t = 10.5$. Grid voltage decrease by 0.05 p.u. from $t = 11.5$ to $t = 12.5$ and increase by 0.05 p.u. from $t = 13.5$ to $t = 14.5$

7. Simulation was ended at $t = 15.5$

## 5.1 Performance of the Rotor Side converter

Figure 11a shows the DC link voltage of the WECS. The rotor side controller is able to maintain the DC link voltage at the reference voltage during the entire simulation. Small transients are seen at the occurrence of events, but the controller quickly tracks the reference again after each event. The variations in the DC voltage at steady state vary inside the range from 1100 to 1150 volts, meaning the variation is always less than 50 V in steady state. Fig. Fig. 11b shows the active power and reactive power of the rotor side converter. As can

12

(a) DC link voltage.

(b) Powers calculated by the rectifier.

(c) Rectifier frequency vs PMSG stator frequency.
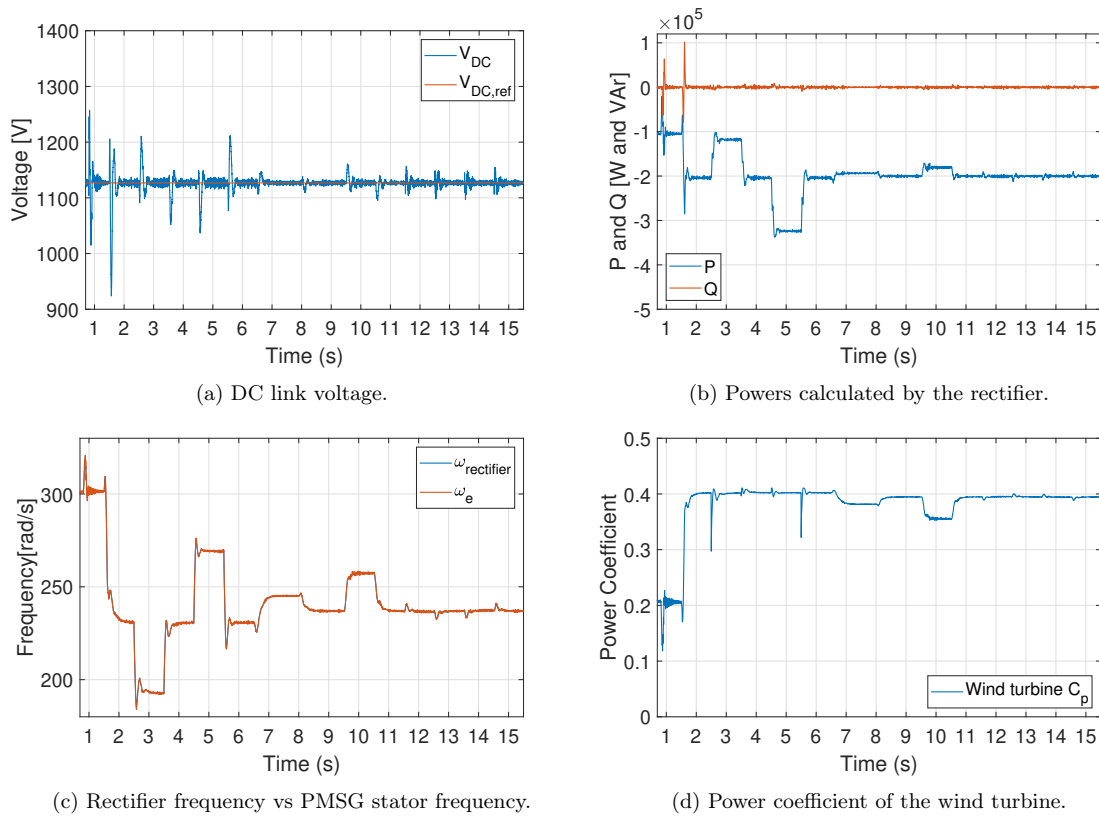
(d) Power coefficient of the wind turbine.

Figure 11: Rotor Side Simulation Results

be seen from Fig. 11b, the reactive power was approximately zero during the entire simulation run, meaning the current drawn by the rectifier was in phase with the voltage, and that the desired unity power factor was achieved by the rotor side controller.

Fig. 11c shows the electrical frequency of PMSG and rectifier. As can be seen, the converter speed tracks the electrical speed very well during the entire operation. Figure 11c also shows that the frequency event has a direct impact on the turbine, effectively speeding up the turbine as less power is extracted at the same wind speed. The voltage events, on the other hand, had very little to zero impact on turbine performance.

These observations are supported by looking at the power coefficient of the turbine in Fig. 11d. It is here clear that the frequency event in A decreased the power coefficient as less power is extracted at the same wind speed, while the power coefficient remains unchanged during the voltage events. Figure 11d also clearly shows that the grid side controller is able to follow the MPPT very closely as the power coefficient of the turbine is very close to the maximum power coefficient $C_{p,max} = 0.411$ during normal operations.

## 5.2   Performance of the Grid Side converter

Figure 12a depicts the active power injected into the grid by the grid side converter. It is obvious that the power follows the reference very well with very small transients during events. This can also be seen in relation to the high power coefficient as discussed above, and the MPPT-operation is thus achieved by the inverter. The active power is maintained very well also during changes in reactive power injection, and the converter is able to maintain the active power injection also during the voltage events. For the frequency event, i.e. a frequency increase of 0.1 Hz, the frequency droop is working as expected and the converter decreases the power injected into the grid from the MPPT set-point. More specifically, the injected power is decreased by $\approx 20kW = 10\%$ of rated power when the frequency is increased by 0.2%. This change is in line with the designed criteria for the droop; 100% change in active power for 2% change in frequency. When the frequency returns to the rated value, the power injection is increased back to the MPPT set-point.

The reactive power of the grid side converter is shown in Fig. 12b. As depicted in Fig. 12b, as long as $Q_{ref,grid} = 0$ the reactive power injected is zero at steady state. Small transients can be seen during changes

13

(a) Active power injected by the inverter.


(b) Reactive power injected by the inverter.


(c) Inverter frequency.
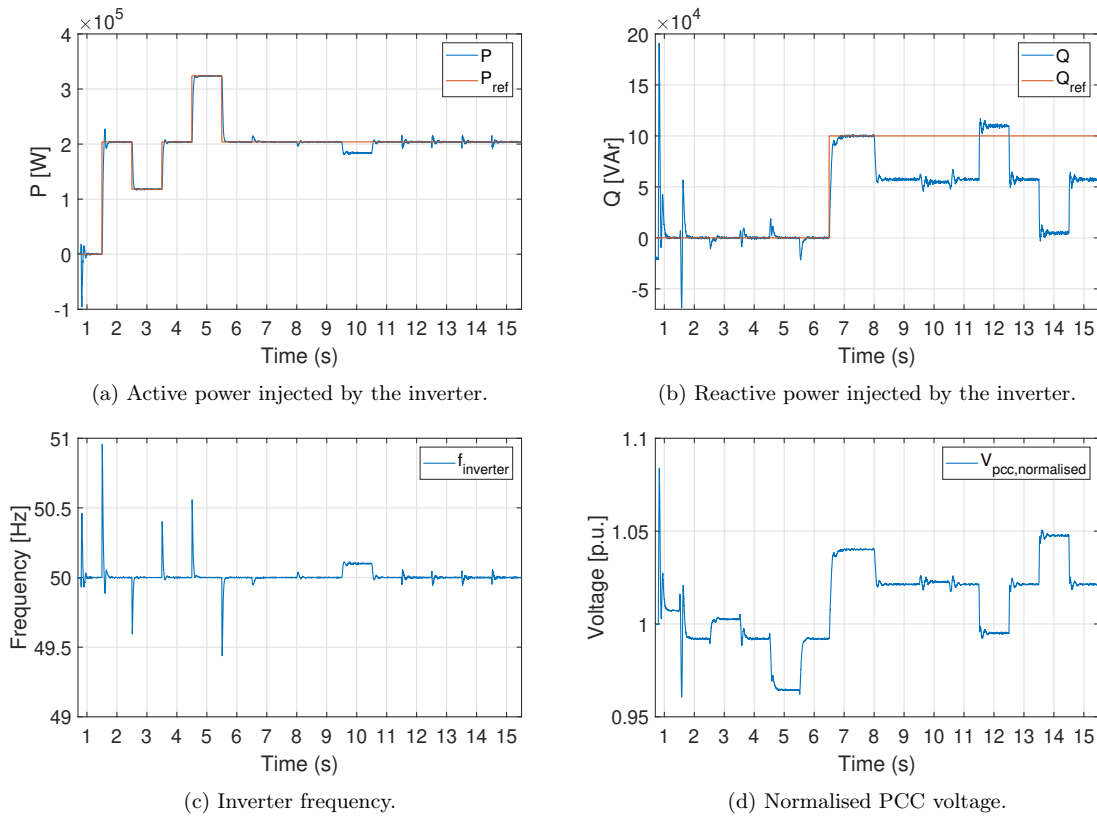

(d) Normalised PCC voltage.

Figure 12: Grid Side Simulation Results

in the active power injection, but the reactive power is quickly controlled back to zero. Also after $Q_{ref,grid}$ was changed, the converter quickly controls the injected reactive power to follow the reference. When the voltage droop is enabled at $t = 8$, the injected reactive power is reduced from the set-point as the PCC voltage is higher than the rated voltage. During the voltage events, two opposite control reactions are seen. As expected, when the grid voltage decrease the controller increases the reactive power input to counter the voltage drop in the grid. Opposite, when the grid voltage increase the controller decreases the reactive power input to counter the voltage increase in the grid.

Looking more closely at the results, during the voltage dip the voltage $V_{PCC}$ seen in Fig. 12d decreases from $\approx 1.021$ to $\approx 0.995$ p.u., i.e. a decrease in the PCC voltage equal to 2.6% of nominal voltage. As seen in Fig. 12b the controller then increases the injected reactive power with approximately 52.5kVAr. This means that there is a change of 52.5kVAr for a change of 2.6% in the voltage. Looking at the designed voltage droop, this is totally in line with expected controller behavior; 100% = 200kVAr change in injected reactive power for 10% change in voltage. The same observations holds for the voltage increase, but with the exact opposite controller reaction, i.e. reducing injected reactive power in accordance with the designed voltage droop.

Also, the grid side converter follows the frequency of the grid which it is connected to very well, as seen in Fig. 12c. Transients are seen during events, but the frequency is quickly controlled back to following the grid frequency. This can be seen also during the frequency increase in A, where the converter frequency has an identical increase. Also, during the voltage events in B and C, the converter is able to track the grid frequency without large deviations.

## 5.3   Simplifications and Limitations of the Tuning procedure

The simulation model used as well as the tuning procedure proposed in this paper have a number of obvious simplifications and limitations that need to be addressed. It is therefore of interest to discuss the validity of some of the obtained results.

Based on the discussion above it is beyond doubt that the proposed procedure is working, and based on the performance of the control system the controller parameters can be said to be adequately tuned. More

14

specifically, looking at the responses of the DC link voltage and the active and reactive power injections to the grid, their responses are extremely fast while still maintaining stability over the entire operating range. In addition, all references are reached and maintained very well without steady-state deviations. From Fig. 11a it can be seen that the DC link voltage is slightly under-dampened with a very fast settling time after the transients occur during events in the simulation. Small oscillations around the voltage reference can be seen, but these are well within the acceptable deviation limit of 5% (a 5% deviation from the DC voltage reference equals a deviation of approximately 56 V). From the grid side results, the active power seems to have a very small overshoot with no further oscillations, while the reactive power is slightly over-dampened when tracking its reference. When the voltage droop activates the response seems to go from slightly over-dampened to slightly under-dampened, resulting in very small oscillations before settling at the reference. The settling time is however very fast and the response is therefore deemed as satisfying.

However, there are still some factors that should be discussed. Firstly the tuning procedure is based on the line frequency average model using the average powers instead of the instantaneous powers, and the small-signal model used to identify the block diagrams for the control channels will thus not be valid for frequencies high above the nominal frequency. A model that is valid for all frequency ranges could in the future be developed to better accommodate these high frequencies. Secondly, it is possible that the performance of the rectifier could be even better if the simplifications $J_m = J$ and $K_{qm} = K_q$ were avoided. Designing these parameters separately for the rotor side controller instead of putting them equal to their grid side counterparts could help to decrease the fluctuations in the DC link voltage around the reference.

A major simplification is done in the process of tuning the PI controller. More specifically when neglecting the derivative term in (32). The consequence of this simplification can be observed in the bode plot in figure 10a, where the bandwidth of the initial closed-loop is found to be 56.29 Hz instead of the chosen $\alpha = 220$ rad/s $\approx 35$ Hz. Based on this it can be deducted that the closed-loop system with parameters that are tuned based on this simplification yields a bandwidth that is higher than the selected $\alpha$ in the tuning process. As a curiosity, the selected 35 Hz is found to be the crossover frequency in this initial Bode plot. Had the controller been a PID controller on the other hand, the derivative gain in the controller could be set equal to the part which is neglected in the simplification, yielding a closed-loop bandwidth actual equal to $\alpha$. This is however not done as PID controllers tend to be more sensitive against noise and thus less suitable for large industrial applications.

Also, during the tuning procedure, the bandwidth between 50 and 60 Hz for the DC voltage control loop is deemed as acceptable, and no further investigation or tuning steps were done to perfect the bandwidth. In retrospect, a more thorough analysis of the bandwidth should be implemented into the tuning procedure for the PI controller, to ensure controller speed without interference. This adds to the thought that since so many simplifications are made throughout the tuning process, there are a lot of uncertainties related to the stability margins of the system. It can therefore also be discussed if the phase margin of 65° for the DC voltage control loop is actually enough to ensure the stability of the rectifier, as the actual phase margin of the controller could be lower.

## 6    Conclusions

This paper presents the tuning of a synchronverter based wind energy conversion system. The proposed procedure offers a fast process where system parameters can be easily changed, resulting in new controller parameters without time-consuming calculations. Based on the results and discussion above it can be concluded that the established tuning procedure has shown to yield a well-functioning control system with fast and accurate responses, thus achieving the desired functioning. Simulation results are presented to show the effectiveness of the proposed tuning. It is shown that the performance of the tuning procedure is closely tied to the performance of the controllers, which are indeed fulfilling their objectives related to providing ancillary services to the grid. It is also important that the controllers are fast and react quickly to changes, especially during frequency events where time is of the essence to prevent cascade failures. In this perspective, the tuning performs excellent as the rising times of both the active and reactive powers during changes are very fast, and the DC voltage is kept well within its allowed deviation area. Discussions revolving the simplifications used during the tuning procedure are provided, and based on this it can be concluded that, for the sake of this research, the established tuning procedure is satisfactory. However, imperfections have been pointed out, and thus more work can be done to further perfect the tuning procedure.

## References

[1] European-Commission. A policy framework for climate and energy in the period from 2020 to 2030. Technical report, European Union, 2014.

15

[2] Brian Parkin. Subsidy-free green power may be closer than you think in germany, 2019. Available at https://www.bloomberg.com/news/articles/2019-06-17/subsidy-free-green-power-may-be-closer-than-you-think-in-germany, Collected 2019-08-27.

[3] Ivan Komusanac, Daniel Fraile, and Guy Brindley. Wind energy in europe in 2018 - trends and statistics. Technical report, Wind Europe, 2019.

[4] James F. Manwell, Jon G. McGowan, and Anthony L. Rogers. *Wind Energy Explained: Theory, Design and Application.* John Wiley and Sons, Ltd, 2 edition, 2010.

[5] Olimpo Anaya-Lara. Lecture notes elk12 - wind power in electric power systems - ntnu, 2019. Unpublished.

[6] Qing-Chang Zhong, Zhenyu Ma, Wen-Long Ming, and George C. Konstantopoulos. Grid-friendly wind power systems based on the synchronverter technology. *Energy Conversion and Management*, 89:719 – 726, 2015.

[7] Q. Zhong and G. Weiss. Static synchronous generators for distributed generation and renewable energy. In *2009 IEEE/PES Power Systems Conference and Exposition*, pages 1–6, 3 2009.

[8] Q. Zhong and G. Weiss. Synchronverters: Inverters that mimic synchronous generators. *IEEE Transactions on Industrial Electronics*, 58(4):1259–1267, 4 2011.

[9] Zhenyu Ma and Qing-Chang Zhong. Synchronverter-based control strategy for back-to-back converters in wind power applications. *IFAC Proceedings Volumes*, 45(21):349 – 354, 2012. 8th Power Plant and Power System Control Symposium.

[10] H. Wu, X. Ruan, D. Yang, X. Chen, W. Zhao, Z. Lv, and Q. Zhong. Small-signal modeling and parameters design for virtual synchronous generators. *IEEE Transactions on Industrial Electronics*, 63(7):4292–4303, 7 2016.

[11] S. Dong and Y. C. Chen. A fast self-synchronizing synchronverter design with easily tuneable parameters. In *2018 IEEE Power Energy Society General Meeting (PESGM)*, pages 1–5, 8 2018.

[12] R. Rosso, J. Cassoli, S. Engelken, G. Buticchi, and M. Liserre. Analysis and design of lcl filter based synchronverter. In *2017 IEEE Energy Conversion Congress and Exposition (ECCE)*, pages 5587–5594, 10 2017.

[13] S. Dong and Y. C. Chen. Adjusting synchronverter dynamic response speed via damping correction loop. *IEEE Transactions on Energy Conversion*, 32(2):608–619, 6 2017.

[14] S. Dong and Y. C. Chen. A method to directly compute synchronverter parameters for desired dynamic response. *IEEE Transactions on Energy Conversion*, 33(2):814–825, 6 2018.

[15] H. Li, X. Zhang, T. Shao, T. Zheng, X. You, H. Yi, and Z. Li. Single-phase synchronverter dynamic optimization and parameters design. In *IECON 2017 - 43rd Annual Conference of the IEEE Industrial Electronics Society*, pages 7866–7871, 10 2017.

[16] Zhou Wei, Chen Jie, and Gong Chunying. Small signal modeling and analysis of synchronverters. In *2015 IEEE 2nd International Future Energy Electronics Conference (IFEEC)*, pages 1–5, 11 2015.

[17] Q. Zhong, P. Nguyen, Z. Ma, and W. Sheng. Self-synchronized synchronverters: Inverters without a dedicated synchronization unit. *IEEE Transactions on Power Electronics*, 29(2):617–630, 2 2014.

[18] Q. Zhong, Z. Ma, and Phi-Long Nguyen. Pwm-controlled rectifiers without the need of an extra synchronisation unit. In *IECON 2012 - 38th Annual Conference on IEEE Industrial Electronics Society*, pages 691–695, 10 2012.

[19] J. J. Grainger and W. D. Stevenson. *Power System Analysis.* New York: McGraw-Hill, 1994.

[20] Z. Ma, Q. Zhong, and J. D. Yan. Synchronverter-based control strategies for three-phase pwm rectifiers. In *2012 7th IEEE Conference on Industrial Electronics and Applications (ICIEA)*, pages 225–230, 7 2012.

[21] Siegfried Heier. *Grid integration of wind energy : onshore and offshore conversion systems.* Wiley, Chichester, England, 3rd ed. edition, 2014.

[22] J. G. Slootweg, H. Polinder, and W. L. Kling. Representing wind turbine electrical generating systems in fundamental frequency simulations. *IEEE Transactions on Energy Conversion*, 18(4):516–524, 12 2003.

16

Table 2: System Parameters of the Test System.

| Parameter | Value |
|-----------|-------|
| Turbine radius, $R$ | $12.5\,m$ |
| Rated wind speed, $v_{w,rated}$ | $12\ m/s$ |
| Maximum power coefficient, $C_{p,max}$ | $0.411$ |
| Optimal tip speed ratio, $\lambda_{opt}$ | $7.95$ |
| Air density, $\rho$ | $1.2\,kg/m^3$ |
| Rated power, $S_{rated}$ | $200\,kVA$ |
| Switching frequency, $f_s$ | $5\,kHz$ |
| Nominal grid frequency, $f_n$ | $50\,Hz$ |
| Nominal Line-Line voltage, $V_{gn,L-L}$ | $690\,V$ |
| Nominal DC link voltage, $V_{DC,ref}$ | $1126.8\,V$ |
| Nominal DC link current, $I_{n,DC}$ | $177.5\,A$ |
| Number of pole pairs PMSG, $p$ | $28$ |
| Permanent magnet flux, $\Psi$ | $1.7933\,Vs$ |
| Inertia of the PMSG, $J$ | $10\,kgm^2$ |
| Friction factor of the PMSG, $D$ | $0\,Nms$ |
| DC link capacitance, $C_{DC}$ | $10\,mF$ |
| Chopper resistance, $R_{chopper}$ | $6.3891\,\Omega$ |
| "Stator" inductance, $L_s$ | $0.75774\,mH$ |
| "Stator" resistance, $R_s$ | $0.0024\,\Omega$ |
| Grid inductance, $L_g$ | $0.75774\,mH$ |
| Grid resistance, $R_g$ | $0.0024\,\Omega$ |
| Filter capacitance, $C$ | $98.95\,\mu F$ |
| Parallel resistance, $R_C$ | $1000\,\Omega$ |
| Virtual inductance, $L_{sync}$ | $3\,mH$ |
| Virtual resistance, $R_{sync}$ | $24\,\mu\Omega$ |

# A  Appendix

## A.1  System Parameters

## A.2  Maximum Power point Tracking

A part of the objective for the grid side inverter is to follow the maximum power point tracking (MPPT) of the wind turbine. The power available from the turbine can be found using the simplified turbine model by Heier [21]. Here, the kinetic energy in the airflow that can be converted into mechanical power, $P_m$, is given by (37) where $\rho$ is the density of the air, $R$ is the turbine radius, $v_w$ is the wind speed and $C_p$ is the power coefficient.

$$P_m = \frac{1}{2}\rho\pi R^2 v_w^3 C_p(\lambda,\beta) \tag{37}$$

The power coefficient, $C_p$, is dependent on the pitch angle of the turbine blades, $\beta$, and the tip speed ratio $\lambda$. $\lambda$ is defined in (38), where $\omega_m$ is the rotational speed of the rotor.

$$\lambda = \frac{\omega_m R}{v_w} \tag{38}$$

All wind turbine designs have their own specific expression describing $C_p$. However, according to Slootweg et al [22], these expressions does not have large differences and can therefore be approximated by an analytic

17

function. Therefore the model in (39) is used [21].

$$C_p(\lambda, \beta) = 0.5(\frac{116}{\lambda_i} - 0.4\beta - 5)e^{\frac{-21}{\lambda_i}} \tag{39}$$

Here $\lambda_i$ is defined as in (40).

$$\frac{1}{\lambda_i} = \frac{1}{\lambda + 0.08\beta} - \frac{0.035}{\beta^3 + 1} \tag{40}$$

Based on the model outlined above, the turbine needs to maintain its optimal tip speed ratio, $\lambda_{opt}$, at any given wind speed to extract maximum power out of the airflow. The maximum power of the turbine, $P_{m,opt}$, can then be calculated directly in (41) based on the wind speed and the maximum power coefficient, $C_{p,max}(\lambda_{opt}, \beta)$.

$$P_{m,opt} = \frac{1}{2}\rho\pi R^2 v_w^3 C_{p,max} \tag{41}$$

To account for losses, the power set point of the inverter is set slightly lower than the MPPT value as

$$P_{ref,MPPT} = 0.95 P_{m,opt}. \tag{42}$$

18

Henrik Høstmark

Transient Stability Assessment of Virtual Synchronous Machine based Wind Energy Conversion System

# NTNU
Norwegian University of
Science and Technology